

Valorization of carbon dioxide

Mechanistic aspects of hydrogenation and hydroformylation reactions over supported alkali modified gold and rhodium catalysts

Dissertation

Zur Erlangung des akademischen Grades
doctor rerum naturalium (Dr. rer. nat.)

der mathematisch-naturwissenschaftlichen Fakultät
der Universität Rostock

vorgelegt von

M.Sc. Denise Heyl

Geboren am 22. August 1990 in Burgstädt

Rostock 2018

1. Gutachterin: Prof. Dr. Angelika Brückner

Leibniz-Institut für Katalyse e.V. an der Universität Rostock

2. Gutachter: Prof. Dr. Ralf Ludwig

Institut für Chemie, Universität Rostock

Datum der Einreichung: 27. April 2018

Datum der Verteidigung: 16. Oktober 2018

Zusammenfassung

Die Reduktion des Ausstoßes von Kohlendioxid (CO_2), als das mit über 80% am meisten freigesetzte Treibhausgas, ist notwendig, um den Anstieg der globalen Temperatur zu begrenzen. Gleichzeitig ist es sinnvoll, CO_2 als Rohstoff für chemische Prozesse einzusetzen, und es in wertvollere Produkte umzuwandeln. In dieser Arbeit wurden zwei katalytische Reaktionen untersucht: die Hydrierung von CO_2 zu Kohlenmonoxid (CO) bzw. Methan (CH_4) an modifizierten Rhodium-Katalysatoren und die Bildung von 1-Propanol, 1-Butanol, *iso*-Butanol aus CO_2 , Ethen/Propen und Wasserstoff (H_2) an Alkali-modifizierten Gold-Katalysatoren. Dabei standen mechanistische Aspekte im Vordergrund, insbesondere Untersuchungen zum spezifischen Einfluss der Katalysatorkomponenten (Edelmetall, Alkalimetall und Träger) auf die Katalysatoraktivität und -selektivität sowie den Reaktionsmechanismus.

Bei der CO_2 -Hydrierung zu CO und CH_4 an mit Kalium modifizierten Rh/ Al_2O_3 -Katalysatoren konnte mittels *operando*-DRIFT-Spektroskopie unter Verwendung von isoto-penmarkiertem CO_2 die Rolle des Kaliums aufgeklärt werden, die darin besteht, dass die Adsorption von CO_2 befördert, die starke CO-Adsorption und damit Weiterreaktion zu CH_4 jedoch vermindert wird. Darüber hinaus konnten aktive und nicht aktive Formiat-Spezies nachgewiesen werden, wobei erstere als Intermediat für die CO-Bildung identifiziert wurden.

Die in der vorliegenden Arbeit vorgestellte „grüne“ Synthese von C_3/C_4 -Alkoholen aus CO_2 , H_2 und Olefinen stellt einen vielversprechenden Ansatz zur Verwertung von CO_2 dar. Goldkatalysatoren mit TiO_2 und SiO_2 als Träger sind für diese Reaktion geeignet, wenn sie mit Alkalimetallen (K oder Cs) modifiziert werden. Die Untersuchung des Einflusses von Alkalimetall einerseits und Träger andererseits auf die Katalysatorleistung sowie die Aufklärung ihrer Funktion in der katalytischen Reaktion war ein Kernthema dieser Dissertation. Unter Verwendung von Hochdruck-*in situ* und *operando*-FTIR-spektroskopischen Experimenten sowie zeitaufgelösten Produktanalysen im Vakuum (TAP) wurde die Wechselwirkung zwischen Reaktanden und Katalysatoroberfläche untersucht. Dadurch konnten mögliche Adsorbate identifiziert und entsprechende Reaktionswege vorgeschlagen werden.

In der 1-Propanol-Synthese zeigte sich, dass mit TiO_2 -basierten Katalysatoren eine höhere Ausbeute (maximal 6% bei 225 °C) als mit SiO_2 -basierten Katalysatoren erzielt werden konnte, was auf eine einfachere Aktivierung von CO_2 an TiO_2 -basierten Katalysatoren zurückzuführen ist. Außerdem konnte mittels CO-Adsorptionsversuchen gezeigt werden, dass intermediäre Au-CO Spezies, die für die Hydroformylierung notwendig sind, an diesen Katalysatoren stabiler sind. Alkalimetalle beeinflussen sowohl die Alkoholdesorption als auch die Reduktion von AuO_x -Spezies zu metallischem Gold in der Aktivierungsphase. Neben der Reduktion von AuO_x -Spezies im Aktivierungsprozess mit $\text{CO}_2 + \text{H}_2$ werden auch die aus der Präparation verbliebene Nitrate durch Reduktion entfernt.

Auch die 1-Butanolsynthese aus CO_2 , H_2 und Propen wurde an den Goldkatalysatoren untersucht. Es zeigt sich, dass der C_4 -Alkohol prinzipiell hergestellt werden kann, jedoch mit deutlich geringeren Ausbeuten als in der Propanol-Synthese, was zum einen thermodynamisch bedingt ist, aber auch an einer stärkeren Produktadsorption liegt.

Abstract

The reduction of emissions of carbon dioxide (CO_2), which is with more than 80% the most released greenhouse gas, is necessary to limit the rising global temperatures. Besides the reduction of CO_2 emissions, the use of CO_2 as feedstock in chemical processes for the production of value-added products can also help to decrease its atmospheric concentration. In this regard, two catalytic processes were investigated in this thesis: the hydrogenation of CO_2 to carbon monoxide (CO) and methane (CH_4) over modified rhodium catalysts and the formation of 1-propanol, 1-butanol and *iso*-butanol from CO_2 , ethene/propene, and hydrogen on alkali-modified gold catalysts. The work was focused on studies concerning the influence of the catalyst components (noble metal, alkali metal and support material) on the catalyst activity and selectivity as well as the reaction mechanisms.

In the CO_2 hydrogenation to CO and CH_4 over Rh/ Al_2O_3 catalysts modified with potassium the role of potassium in the catalytic reaction could be elucidated by *operando* DRIFT spectroscopy using isotopic labeled CO_2 . The adsorption of CO_2 is facilitated in the presence of potassium, while the strong adsorption of the formed CO is inhibited which decreases its further reduction to CH_4 , and, thus, increases CO selectivity. Furthermore, the formation of active and non-active formate species has been detected, where the first of which was proved to be an intermediate species for CO formation.

The presented “green” synthesis of C_3/C_4 -alcohols from CO_2 , H_2 , and olefins is a very promising reaction, which offers a potential route for the sustainable production of alcohols from mainly CO_2 and H_2 . Supported gold catalysts with TiO_2 and SiO_2 as support are suitable catalysts for the 1-propanol synthesis if they are modified with alkali metals (K or Cs). The elucidation of the influence of the alkali metal as well as the support materials on the catalyst performance as well as their role in the catalytic reaction pathway was a key issue of the thesis.

High-pressure *in situ* and *operando* FTIR spectroscopic experiments as well as TAP (temporal analysis of products) measurements were carried out to investigate the interaction between the reactants and the catalysts surface. Based on these studies, different reaction intermediates were identified (*e.g.* propionyl and propoxy species) and mechanisms were proposed for the alcohol synthesis, depending on the support material and alkali metal dopants.

In general, higher yields of 1-propanol (maximum 6% at 225 °C) were obtained over titania-based catalysts. This is mainly caused by the fact that CO_2 can be easier activated over titania- than silica-supported catalysts. Furthermore, it could be shown by CO adsorption experiments that the formed Au-CO species, which are important for the hydroformylation step, are more stable adsorbed on titania-based catalysts. The alkali metals facilitate desorption of the alcohols and favor the reduction of AuO_x particles to metallic gold in the activation process. Besides the reduction of AuO_x species during the activation process with $\text{CO}_2 + \text{H}_2$ also the nitrate species remained from the preparation were removed by reduction.

The synthesis of 1-butanol from propene, CO_2 and H_2 over supported gold catalysts was studied, too. In principle, 1-butanol can be formed, but with essential lower yields compared to the propanol synthesis, which is caused by thermodynamics and a stronger product adsorption.

Danksagung

Verantwortlich dafür, dass dieses ganze Werk überhaupt seinen Anfang nehmen konnte und ich die Möglichkeit erhielt, dieses spannende und zukunftsweisende Thema zu erforschen ist **Prof. Dr. Angelika Brückner**. Ihr danke ich für die Aufnahme in den Arbeitskreis *Katalytische in situ-Studien* und die manchmal sehr fordernde, aber auch zielstrebige Zusammenarbeit. Des Weiteren möchte ich mich herzlich dafür bedanken, dass ich in meiner Doktorandenzeit so viele schöne Orte bereisen durfte um meine Ergebnisse zu präsentieren, neue Dinge zu lernen, aber doch auch immer ein wenig mehr von der Welt zu erkunden.

Mein besonderer Dank gilt **Dr. Ursula Bentrup**, die mir seit meiner Masterarbeit vertrauensvoll zur Seite stand. Ich konnte von Ihr sehr viel lernen, aber Sie gab mir auch die Freiheit, eigene Ideen zu verfolgen und neben meiner Forschungsarbeit auch ehrenamtliche Aufgaben zu erledigen.

Außerdem möchte ich mich bei **PD Dr. Evgenii V. Kondratenko** bedanken, der maßgeblich an der umfangreichen Planung und Ausarbeitung des Themas beteiligt war und mich bei der Auswertung und Interpretation der Ergebnisse unterstützt hat. Trotz dessen, dass ich nicht offiziell der Arbeitsgruppe *Katalysatorentwicklung und Reaktionstechnik* angehörte, möchte ich zusätzlich **Dr. David Linke** und **Dr. Uwe Rodemerck** danken, dass ich Ihre „Hardware“ nutzen durfte und mich jederzeit mit Fragen willkommen fühlte. In dem Zusammenhang sei auch **Martina Marschall, Karin Buchholz, Dr. Martin Fait, Matthias Albrecht, Andreas Schröder und der restlichen Arbeitsgruppe** gedankt, an die ich mich bei kleineren technischen oder organisatorischen Problemen immer wenden konnte.

Des Weiteren bedanke ich mich außerordentlich bei **Dr. Stefan J. Ahlers**, ohne den ich im ersten Jahr meiner Doktorandenzeit wahrscheinlich manchmal verzweifelt wäre. Er zeigte mir wie ich mit der für mich neuen Technik umzugehen hatte und ließ mir später auch immer ein offenes Ohr, selbst während seiner eigenen stressigen Schreibphase.

Für die Zuarbeiten im analytischen und wissenschaftlichen Bereich danke ich **Dr. Vita Kondratenko** (TAP-Messungen), **Dr. Marga-Martina Pohl** (TEM-Messungen), **Dr. Henrik Lund** (XRD-Messungen), **Anja Simmula** und **Karin Struve** (ICP-OES-Messungen).

Christine Rautenberg danke ich für die vielen IR-Experimente und TG-DSC-Messungen, die sie für mich durchgeführt hat. Außerdem für die stets schnelle und zuverlässige Hilfe in allen erdenklichen Bereichen und die schöne Zeit in Caen.

Weiterhin ist die Arbeit der Personen, die im wissenschaftlichen Alltag nicht unbedingt im Mittelpunkt stehen, aber ohne die ich oft nicht weitergekommen wäre, her-

vorzuheben. Damit meine ich die technischen Mitarbeiter und Werkstattmenschen, besonders **Andreas Hutter, Thomas Rall, Dr. Detlef Salzwedel und Axel Radtke**.

Und natürlich waren auch die Menschen wichtig, die nicht direkt mit meiner Arbeit zu tun hatten, aber sehr viel dazu beigetragen haben, dass ich die Zeit am Likat genießen konnte, weil sie mir zuhörten und Ratschläge oder Zerstreuung gaben. Das sind **Sven Adomeit, Dr. Andrea Bellmann, Dr. Jana Engeldinger, Dr. Kathleen Grabow, Reni Grauke, Dr. Dirk Hollmann, Sonja Keller, Saskia Möller, Dr. Roxana Pérez-Velez, Dr. Nils Rockstroh, Dr. Huyen Thanh Vuong und Christoph Wulf**. Und auch allen anderen Arbeitsgruppenmitgliedern danke ich für das Zuhören in den Seminaren.

Den größten Dank möchte ich jedoch meiner Familie aussprechen. **Mama und Papa**, dass ihr mir überhaupt die Möglichkeit für eine solche Ausbildung gegeben habt und mir keinerlei Vorschriften gemacht, sondern jegliche Freiheit vertrauensvoll gewährt habt. Meinen **Großeltern** danke ich für ihre mir entgegen gebrachte Liebe und ihre stete Unterstützung auf meinem bisherigen Weg. **Teresa** danke ich für das große Geschenk, Marie und Sophie in mein Leben gebracht zu haben und außerdem immer eine gute Zuhörerin zu sein. Und ich bin unglaublich dankbar, dass **Marie und Sophie** so viel Sonnenschein in mein Leben bringen, mich motivieren, die Zukunft zu gestalten und sie zu einem besseren Ort zu machen.

Doch ohne **Harald** wäre alles nicht halb so schön, ich würde mich nicht so zuversichtlich neuen Aufgaben zuwenden und danke Dir deshalb für deine tägliche Unterstützung, deine Liebe und dein ausgesprochen großes Herz.

*“Valorization of carbon dioxide:
Mechanistic aspects of hydrogenation and hydroformylation reactions over
supported alkali modified gold and rhodium catalysts “*

List of Tables	viii
List of Figures.....	viii
List of Figures in the Appendix.....	xii
List of Schemes	xiv
List of Abbreviations.....	xv
Units of Measurement.....	xvi
1 Motivation and Objective.....	1
2 State of the Art	4
2.1 Carbon dioxide as recyclable feedstock	4
2.1.1 Capture and Utilization	4
2.2 Hydrogenation and reduction processes.....	5
2.2.1 Supported catalysts for CO ₂ hydrogenation.....	7
2.2.2 Discussed mechanisms for CO ₂ hydrogenation	8
2.3 Alcohol formation from carbon dioxide, hydrogen and olefins.....	13
2.3.1 Hydroformylation and hydrogenation	13
2.4 <i>In situ</i> and <i>operando</i> FTIR spectroscopy.....	17
2.4.1 Reaction intermediates and surface adsorbates	17
2.4.2 Isotopic transient technique	20
3 Experiments and Methods.....	22
3.1 Preparation of gold catalysts for alcohol formation.....	22
3.2 Preparation of rhodium catalysts for CO ₂ hydrogenation	23
3.3 <i>Ex situ</i> analysis and characterization of the catalysts	23
3.4 Measurements with TAP reactor.....	26
3.5 Catalytic tests.....	27
3.6 <i>In situ</i> and <i>operando</i> studies.....	29
3.6.1 Low-temperature CO adsorption.....	29
3.6.2 <i>Operando</i> DRIFTS/MS study: determination of adsorbates reactivity in CO ₂ hydrogenation with ¹³ CO ₂ over rhodium catalysts.....	30
3.6.3 High pressure FTIR spectroscopic experiments with gold catalysts in transmission mode	31
4 Results and Discussion.....	33
4.1 Rhodium catalysts for CO ₂ hydrogenation.....	33
4.1.1 Catalyst preparation and characterization.....	33
4.1.2 Catalytic activity of modified rhodium catalysts	34
4.1.3 <i>In situ</i> DRIFTS analysis of CO ₂ hydrogenation	36

4.1.4	<i>Operando</i> DIRFITS/MS study: determination of adsorbates reactivity in CO ₂ hydrogenation over rhodium catalysts with isotopic transient technique.....	39
4.1.5	Proposed reaction mechanism for CO ₂ hydrogenation over different supported Rh catalyst, modified with K and Ni.....	41
4.1.6	Summary of results for CO ₂ hydrogenation over modified Rh catalysts	44
4.2	Alkali metal promoted gold catalysts for alcohol formation from CO ₂ , H ₂ and C ₂ –C ₃ olefins	45
4.2.1	Catalyst preparation and characterization	45
4.2.2	Catalytic testing of modified Au catalysts in 1–propanol synthesis at 20 bar.....	49
4.2.3	Influence of time on stream on catalysts surface and Au nanoparticles.....	56
4.2.4	<i>In situ</i> CO adsorption at low temperature	58
4.2.5	Study of the influence of different pre–treatments on CO adsorption and simultaneous thermal analysis.....	60
4.2.6	Mechanistic <i>in situ</i> and <i>operando</i> studies at high pressure.....	67
4.2.7	Interaction of educts with the catalyst surface determined by TAP experiments.....	78
4.2.8	Structure–reactivity relationship in 1–propanol synthesis over modified Au catalysts	81
4.2.9	Catalytic testing of modified Au catalysts in butanol synthesis at 8 bar.....	87
4.2.10	<i>In situ</i> FTIR studies of butanol formation	90
4.2.11	Conclusion of butanol synthesis over modified Au catalysts	93
5	Summary and Outlook	94
6	Literature	98
	Appendix.....	I
	Curriculum Vitae	XIII

List of Tables

Table 1. Infrared absorption bands and assignments for possible adsorbate species formed in CO ₂ containing feed.	18
Table 2. Infrared absorption bands and assignments for possible species formed in hydroformylation (CO + H ₂ + olefin) or hydrogenation feed (C ₂ H ₄ + H ₂).	20
Table 3. Used supporting materials and their water absorption capacity for IWI.	23
Table 4. Rh, Ni, and K contents and surface area of alumina supported rhodium catalysts for CO ₂ hydrogenation.	33
Table 5. Gold and alkali metal loading of fresh and used SiO ₂ and TiO ₂ based catalysts for alcohol formation, used ones from 1-propanol formation.	46
Table 6. Fresh and used alkali containing gold catalysts for alcohol synthesis and their surface areas and Au NP sizes, determined by TEM and XRD.	48
Table 7. Correlation between different feed notations.	49
Table 8. Comparison of values for CO ₂ conversion and CO yield between catalytic test (Hector reactor) and <i>operando</i> IR/GC coupling.	72

List of Figures

Figure 1. Total world energy consumption by energy source, 1990-2040 (reproduced from [1]).	1
Figure 2. Sources of carbon dioxide [3, 6, 31-32].	4
Figure 3. Proposed mechanism of electrocatalytic CO ₂ reduction in aqueous solution and main reaction products. Reproduced from [42].	5
Figure 4. Equilibrium distribution upon CO ₂ reduction at atmospheric pressure and different temperatures using a H ₂ /CO ₂ = 4 feed. Reproduced from [43].	6
Figure 5. Proposed dissociative reaction mechanism for CO ₂ hydrogenation over redox active support (V _O = oxygen vacancy); displaying different intermediates and products, depending on the noble metal size (red = oxygen, black = carbon, light blue = hydrogen).	8
Figure 6. Proposed associative reaction mechanism for CO ₂ hydrogenation over Pt/CeO ₂ catalyst in analogy to Goguet <i>et al.</i> [73]; CO is formed directly from reactive carbonates (red = oxygen, black = carbon, light blue = hydrogen, V _O = oxygen vacancy).	10
Figure 7. HECTOR reactor with on-line GC and the 50 parallel operated stainless steel fixed bed reactors framed in red.	27
Figure 8. FTIR cell for low-temperature CO adsorption.	29
Figure 9. DRIFTS cell with Praying mantis™ accessory and beam path (red lines), implemented in a Nicolet 6700 FTIR spectrometer, the upper lid is closed during the experiment.	30
Figure 10. High pressure <i>in situ</i> FTIR cell (ISRI) in Nicolet iS10™ spectrometer, connected with HECTOR reactor for gas supply and GC analysis, the gas outlet was heated during <i>operando</i> experiments.	31

Figure 11. Open high pressure <i>in situ</i> FTIR cell (ISRI) with sample inside.....	31
Figure 12. Yields of CO/CH ₄ and CO ₂ conversion at 350 °C before (a) and after (b) high-temperature treatment (750 °C), reaction conditions: $p = 1$ bar, $\tau = 1.67$ g _{cat} ·min·L ⁻¹ , CO ₂ :H ₂ :N ₂ = 1:1:3.....	34
Figure 13. <i>In situ</i> DRIFTS spectra of different rhodium/alumina catalysts (pre-treated in He at 400 °C) after 30 min admission of the hydrogenation feed (CO ₂ :H ₂ :He= 1:1:3) at 250 °C (red) and 350 °C (blue).....	36
Figure 14. <i>In situ</i> DRIFT spectra of different Rh catalysts and pure alumina support recorded at 300 °C after 30 min exposure to 20 vol % CO ₂ /He (a) and subsequent short (1 min) admission of 20 vol % H ₂ /He (b).....	38
Figure 15. <i>In situ</i> DRIFTS spectra of selected Rh catalysts after 30 min exposure to ¹² CO ₂ /H ₂ /He (black) and ¹³ CO ₂ /H ₂ /He (red) at 300 °C.	40
Figure 16. Time-dependent normalized band intensities of ¹² C-containing and ¹³ C- containing Rh carbonyl and formate species recorded on Rh/A and Rh,K,Ni/A catalysts at 300 °C after switching from ¹² CO ₂ /H ₂ /He = 1/1/3 to the respective ¹³ CO ₂ /H ₂ /He feed.	41
Figure 17. Online-MS signals of product formation over Rh/A and Rh,K,Ni/A after switching from ¹² CO ₂ /H ₂ /He to ¹³ CO ₂ /H ₂ /He at 300°C, corresponding data to IR spectra in Figure A. 8....	41
Figure 18. Principal intermediate stages in gold deposition precipitation from chloroauric acid in water and fresh, calcined catalysts (a) 2K,Au/TiO ₂ (b) 2K,Au/SiO ₂	45
Figure 19. HR-TEM images of fresh (a) Au/TiO ₂ and (b) 5.9Cs,Au/TiO ₂	47
Figure 20. ABF-TEM images and gold particle size distribution of fresh (a) 5Cs,Au/SiO ₂ and (b) 5.9Cs,Au/TiO ₂	47
Figure 21. ABF-TEM images and the respective gold particle size distribution of (a) Au/TiO ₂ , (b) 6K,Au/TiO ₂ (c) 5.9Cs,Au/TiO ₂	48
Figure 22. Yield of 1-propanol (derived from CO ₂) over different alkali metal modified (a) Au/TiO ₂ and (b) Au/SiO ₂ catalysts and varied feed compositions, calculation on CO ₂ basis (T = 200 °C, $p = 20$ bar, $\tau = 43$ g _{cat} ·min·L ⁻¹).	49
Figure 23. Selectivity of CO (grey), 1-propanol (red) and 1-propanal (green) at different feed compositions (CO ₂ :H ₂ :C ₂ H ₄ :N ₂), calculation on CO ₂ basis (T = 200 °C, $p = 20$ bar, $\tau = 43$ g _{cat} ·min·L ⁻¹).....	50
Figure 24. Conversion of CO ₂ over different alkali modified Au/SiO ₂ and Au/TiO ₂ catalysts at 200 °C under different CO ₂ :H ₂ :C ₂ H ₄ :N ₂ feeds ($p = 20$ bar, $\tau = 43$ g _{cat} ·min·L ⁻¹)......	51
Figure 25. Conversion of ethene over different alkali modified Au/SiO ₂ and Au/TiO ₂ catalysts at 200 °C under different CO ₂ :H ₂ :C ₂ H ₄ :N ₂ feeds ($p = 20$ bar, $\tau = 43$ g _{cat} ·min·L ⁻¹)......	51
Figure 26. Influence of temperature on conversion (black) of CO ₂ (●) and C ₂ H ₄ (▲) as well as selectivity to 1-propanol calculated on the basis of CO ₂ (●) and C ₂ H ₄ (▲); (CO ₂ :H ₂ :C ₂ H ₄ :N ₂ = 1:1:1:1, $p = 20$ bar, $\tau = 43$ g _{cat} ·min·L ⁻¹)......	53
Figure 27. Yield of 1-propanol, calculated on CO ₂ basis, obtained over different alkali modified Au/SiO ₂ and Au/TiO ₂ catalysts at 225 °C with feed of CO ₂ :H ₂ :C ₂ H ₄ :N ₂ = 1:1:1:1, ($p = 20$ bar, $\tau = 43$ g _{cat} ·min·L ⁻¹)......	54

Figure 28. Yield of 1-propanol, calculated on CO ₂ basis, obtained over different alkali modified Au/SiO ₂ and Au/TiO ₂ catalysts at 250 °C with feed of CO ₂ :H ₂ :C ₂ H ₄ :N ₂ = 1:1:1:1, (p = 20 bar, τ = 43 g _{Cat} ·min·L ⁻¹).....	54
Figure 29. Selectivity to 1-propanol (red), 1-propanal (green) and CO (black) calculated on CO ₂ basis over Au/SiO ₂ and Au/TiO ₂ catalysts promoted with Cs versus contact time τ ; the upper row in CO ₂ :H ₂ :C ₂ H ₄ :N ₂ = 1:1:1:1 feed and the lower row in 1:2:4:1 feed (p = 20 bar, T = 200 °C).	55
Figure 30. Comparison between (a) fresh and (b) used 5K,Au/SiO ₂	56
Figure 31. HR-TEM images of fresh (a-d) and used (e-h) TiO ₂ catalysts; (a,e) Au/TiO ₂ , (b-c, f-g) 6K,Au/TiO ₂ (d,h) 5.9Cs,Au/TiO ₂	57
Figure 32. HR-TEM images of 5Cs,Au/SiO ₂ used in propanol synthesis in (a) annular bright field and (b) high-angle annular dark field mode, the red arrow points to the area of carbon over layer on Au NP, which possesses a starting short range order.	57
Figure 33. FTIR spectra of CO adsorption on fresh Au/TiO ₂ (left) and Au/SiO ₂ (right) catalysts with different K loadings. Solid lined spectra were taken after five pulses of 5 vol % CO in He, dashed lines show spectra after subsequent evacuation (p = 1 bar, T = -160 °C).....	58
Figure 34. FTIR spectra of CO adsorption and subsequent desorption from -160 °C to -120 °C over fresh and used samples of 2Cs,2Au/TiO ₂ and 2K,2Au/SiO ₂ . (p = 1 bar).....	60
Figure 35. FTIR spectra of CO adsorption on 2K,2Au/TiO ₂ catalyst with different pre-treatments: He, 200 °C (blue), 10%CO ₂ +H ₂ + He, 250 °C, 1 bar (yellow), 10%CO ₂ +H ₂ +N ₂ at 10 bar, 250 °C (red). Spectra were taken after dosing of 5 vol % CO in He at -160 °C, subsequent evacuation and heating to -150 °C.....	61
Figure 36. FTIR spectra of CO adsorption on fresh 5K,2Au/TiO ₂ catalyst with different pre-treatments: He, 200 °C (blue), 10%CO ₂ +H ₂ + He, 250 °C, 1 bar (yellow), 10%CO ₂ +H ₂ +N ₂ at 10 bar, 250 °C (red). Spectra were taken after dosing of 5 vol % CO in He at -160 °C, subsequent evacuation and heating to -150 °C	61
Figure 37. FTIR spectra in the ν OH/CH and ν OCO region of 2K,2Au/TiO ₂ during CO adsorption experiments with different pre-treatments: (red) He at 200 °C, (blue) CO ₂ +H ₂ +He, 250 °C, 1 bar, (green) CO ₂ +H ₂ +N ₂ at 10 bar, 250 °C. Spectra were taken after five pulses of 5 vol % CO in He and subsequent evacuation (p = 1 bar, T = -160 °C) except the grey spectra, which shows the pure catalysts without any treatment at RT.	62
Figure 38. FTIR spectra in the ν OH/CH and ν OCO region of 5K,2Au/TiO ₂ during CO adsorption experiments with different pre-treatments: (red) He at 200 °C, (blue) CO ₂ +H ₂ +He, 250 °C, 1 bar, (green) CO ₂ +H ₂ +N ₂ at 10 bar, 250 °C. Spectra were taken after five pulses of 5 vol % CO in He and subsequent evacuation (p = 1 bar, T = -160 °C) except the grey spectra, which shows the pure catalysts without any treatment at RT.	63
Figure 39. Simultaneous thermal analysis (TG-DSC-MS) of 5K,Au/TiO ₂ and 5K,Au/SiO ₂ in a gas mixture of 20% CO ₂ + 20% H ₂ + He (heating rate = 5 K min ⁻¹).....	65
Figure 40. FTIR spectra of Au/TiO ₂ (left) and Au/SiO ₂ (right) catalysts: fresh and untreated at room temperature (dashed line) and after heating in N ₂ , 250 °C, 1 bar (solid line).	67
Figure 41. FTIR spectra of Au/TiO ₂ catalysts in high-pressure <i>operando</i> study of 1-propanol synthesis, Top: after 14 h in activation feed with CO ₂ :H ₂ :C ₂ H ₄ :N ₂ = 4:2:1:1 at 250 °C (dark spectra) and after 5 h in feed of 1:1:1:1 at 200 °C (bright spectra), (p = 10 bar, total flow	

rate = 6.6 ml·min ⁻¹), Bottom: spectra recorded after reaction and flushing with nitrogen at 200 °C, p = 1 bar.....	68
Figure 42. FTIR spectra of Au/SiO ₂ catalysts in high–pressure <i>operando</i> study of 1–propanol synthesis, Top: after 15 h in activation feed with CO ₂ :H ₂ :C ₂ H ₄ :N ₂ = 4:2:1:1 at 250 °C (dark spectra) and after 5 h in feed of 1:1:1:1 at 200 °C (bright spectra), (p = 10 bar, total flow rate = 6.6 ml·min ⁻¹), Bottom: spectra recorded after reaction and flushing with nitrogen at 200 °C, p = 1 bar.....	70
Figure 43. FTIR spectra of ethene adsorption (blue), ethene hydrogenation (green) as well as complete feed (grey) and subsequent nitrogen flushing at 1 bar , pre–treatment only in nitrogen (yellow) at 250 °C for 60 min on 2Cs,Au/TiO ₂ (T = 200 °C, p = 10 bar).	75
Figure 44. FTIR spectra of Au catalysts after CO ₂ +H ₂ exposure, ethene hydrogenation and reaction in CO ₂ :H ₂ :C ₂ H ₄ = 1:1:1 for 60 min at 10 bar and subsequent nitrogen flushing (T = 200 °C, p = 1 bar).....	76
Figure 45. Dimensionless response signals after pulsing of H ₂ :Ar = 1:1 over fresh (a) and used (c) 2Cs,Au/SiO ₂ as well as fresh (b) and used (d) 2K,Au/SiO ₂ at 200 °C.....	78
Figure 46. Dimensionless response signals after pulsing of H ₂ :Ar = 1:1 over fresh (a) and used (c) 2Cs,Au/TiO ₂ as well as fresh (b) and used (d) 2K,Au/TiO ₂ at 200 °C.....	78
Figure 47. Dimensionless response signals after pulsing of CO ₂ :Ar = 1:1 over fresh (a) and used (c) 2Cs,Au/SiO ₂ as well as fresh (b) and used (d) 2K,Au/SiO ₂ at 200 °C.....	79
Figure 48. Dimensionless response signals after pulsing of CO ₂ :Ar = 1:1 over fresh (a) and used (c) 2Cs,Au/TiO ₂ as well as fresh (b) and used (d) 2K,Au/TiO ₂ at 200 °C.....	79
Figure 49. Dimensionless response signals after pulsing of CO:Ar = 1:1 over fresh (a) and used (c) 2Cs,Au/SiO ₂ as well as fresh (b) and used (d) 2K,Au/SiO ₂ at 200 °C.....	80
Figure 50. Dimensionless response signals after pulsing of CO:Ar = 1:1 over fresh (a) and used (c) 2Cs,Au/TiO ₂ as well as fresh (b) and used (d) 2K,Au/TiO ₂ at 200 °C.....	80
Figure 51. Correlation of Au NP size with the ratio of Au ⁶⁺ /Au ⁰ , determined by CO adsorption after pre–treatment in CO ₂ +H ₂ at 1 bar (integrated area of CO bands), and conversion of CO ₂ at 200 °C in CO ₂ :H ₂ :C ₂ H ₄ :N ₂ = 1:1:1:1 feed (p = 20 bar).	84
Figure 52. Correlation of Au NP size with the ratio of Au ⁶⁺ /Au ⁰ , determined by CO adsorption after pre–treatment in CO ₂ +H ₂ at 1 bar (integrated area of CO bands), and conversion of C ₂ H ₄ and selectivity to C ₂ H ₆ at 200 °C in CO ₂ :H ₂ :C ₂ H ₄ :N ₂ = 1:1:1:1 feed (p = 20 bar).....	84
Figure 53. Conversion of ethene (a) or propene (b) and CO ₂ in propanol (c) and butanol (d) synthesis, respectively, with different feeds of CO ₂ :H ₂ :C ₂ H ₄ /C ₃ H ₆ :N ₂ (p = 8 bar, T = 200 °C, τ = 43 g _{Cat} ·min·L ⁻¹).	87
Figure 54. Yield of 1–butanol (green) and <i>iso</i> –butanol (red), calculated on CO ₂ basis, at 8 bar over different Au/SiO ₂ and Au/TiO ₂ catalysts with feed of CO ₂ :H ₂ :C ₃ H ₆ :N ₂ = 1:1:1:1 (T = 200 °C, τ = 43 g _{Cat} ·min·L ⁻¹).	88
Figure 55. Yield of 1–propanol, calculated on CO ₂ basis, at 8 bar over different Au/SiO ₂ and Au/TiO ₂ catalysts at varied feeds of CO ₂ :H ₂ :C ₂ H ₄ :N ₂ (T = 200 °C, τ = 43 g _{Cat} ·min·L ⁻¹).	88
Figure 56. Selectivity to obtained products in alcohol synthesis, calculated on CO ₂ basis, at 8 bar with a feed of CO ₂ :H ₂ :C ₂ H ₄ /C ₃ H ₆ :N ₂ = 1:3:3:1 (T = 200 °C, τ = 43 g _{Cat} ·min·L ⁻¹).....	89

Figure 57. Selectivity to obtained products in alcohol synthesis, calculated on C_3H_6 basis, at 8 bar with a feed of $CO_2:H_2:C_3H_6:N_2 = 1:1:1:1$ ($T = 200\text{ }^{\circ}C$, $\tau = 43\text{ g}_{cat}\cdot\text{min}\cdot L^{-1}$).....	89
Figure 58. Normalized FTIR spectra of four selected catalysts after 2 h in $CO_2:H_2:C_3H_6 = 1:1:1$ stream ($T = 200\text{ }^{\circ}C$, $p = 8\text{ bar}$) and spectra of $C_3H_6 + CO_2$ in the empty cell (black dashed line).....	90
Figure 59. FTIR spectra of gold catalysts in nitrogen flow after 4 h in $CO_2+H_2+C_3H_6 = 1:1:1$ feed for butanol synthesis ($p = 8\text{ bar}$, $T = 200\text{ }^{\circ}C$).	92
Figure 60. Reaction energy of RWGS reaction, ethene and propene hydroformylation in dependence of temperature.	93
Figure 61. Possible future reaction scheme for alcohol and olefin production from CO_2 and H_2 , MTO = methanol-to-olefin process.	96

List of Figures in the Appendix

Figure A. 1 STEM images of the fresh Rh/A and Rh,K,Ni/A catalysts. The latter shows a superlattice structure of high contrast atoms forming a surface decoration.....	IV
Figure A. 2 STEM images of the Rh/A and Rh,K,Ni/A catalysts after CO_2 hydrogenation reaction showing agglomeration of the Rh particles (<i>cf.</i> Figure A. 1). On the right side, EDX analysis detected also particles with both Rh and Ni. Such particles were also found in the Rh,Ni/A catalyst.....	IV
Figure A. 3. Temperature dependent conversion of CO_2 over different rhodium catalysts, reaction condition: $p = 1\text{ bar}$, $\tau = 1.67\text{ g}_{cat}\cdot\text{min}\cdot L^{-1}$, $CO_2/H_2/N_2 = 1/1/3$	V
Figure A. 4. Temperature dependent yield of CO over different rhodium catalysts, reaction condition: $p = 1\text{ bar}$, $\tau = 1.67\text{ g}_{cat}\cdot\text{min}\cdot L^{-1}$, $CO_2/H_2/N_2 = 1/1/3$	V
Figure A. 5. Temperature dependent yield of CH_4 over different rhodium catalysts, reaction condition: $p = 1\text{ bar}$, $\tau = 1.67\text{ g}_{cat}\cdot\text{min}\cdot L^{-1}$, $CO_2/H_2/N_2 = 1/1/3$	V
Figure A. 6. <i>In situ</i> DRIFTS spectra of CO adsorbed on different Rh catalysts. The spectra were recorded after 30 min admission of the hydrogenation feed ($CO_2/H_2/He = 1/1/3$) at the labelled temperatures.....	VI
Figure A. 7. Temperature programmed reduction of modified Rh catalysts. Displayed is the hydrogen consumption and water evolution, measured by MS during heating of 50 mg of the sample in a mixture of 5 % H_2 in Ar (heating rate = 10 K/min). The samples were previously heated in Ar up to 700 $^{\circ}C$	VI
Figure A. 8. Time-resolved <i>in situ</i> DRIFT spectra of Rh/A and Rh,K,Ni/A obtained after switching from $^{12}CO_2/H_2/He$ (after 30 min, red) to $^{13}CO_2/H_2/He$ at 300 $^{\circ}C$ (each time multi-coloured).	VI
Figure A. 9. Powder XRD pattern of fresh SiO_2 based gold catalysts with different alkali metal loadings, the red dashed line marks the reflex, which was used for gold NP size determination; assignment of reflexes: cubic gold (red), $CsNO_3$ (black), KNO_3 (green).....	VII
Figure A. 10. Powder XRD pattern of fresh TiO_2 based catalysts with different alkali metal loadings; assignment of reflexes: $CsNO_3$ (black), TiO_2 anatase (light blue).....	VII

- Figure A. 11.** Selectivity of 1-propanol (red) and ethane (yellow) obtained over different alkali modified Au/SiO₂ and Au/TiO₂ catalysts at 200 °C with different feed composition of CO₂:H₂:C₂H₄:N₂, (p = 20 bar, τ = 43 g_{Cat}·min·L⁻¹).....VIII
- Figure A. 12.** Selectivity of 1-propanol (red) and CO (black) calculated on the basis of CO₂ at different reaction temperatures obtained over various alkali modified Au/SiO₂ and Au/TiO₂ catalysts with feed of CO₂:H₂:C₂H₄:N₂ = 1:1:1:1, (p = 20 bar, τ = 43 g_{Cat}·min·L⁻¹).VIII
- Figure A. 13.** FTIR spectra of CO adsorption on fresh Au/TiO₂ and Au/SiO₂ catalysts with different Cs loadings. Solid lined spectra were taken after five pulses of 5 vol % CO in He, dashed lines show spectra after subsequent evacuation (p = 1 bar, T = -160 °C).....IX
- Figure A. 14.** FTIR spectra of CO adsorption on 2K and 5K,2Au/SiO₂ catalysts with different pre-treatments: (grey) in He at 200 °C, (black) CO₂+H₂+He, 250 °C, 1 bar. Solid lined spectra were taken after five pulses of 5 vol % CO in He, dashed lines show spectra after subsequent evacuation (p = 1 bar, T = -160 °C).....IX
- Figure A. 15.** FTIR spectra of 5K,2Au/SiO₂ and 5K,2Au/TiO₂ catalysts after CO₂+H₂+He pre-treatment at 250 °C, 1 bar and cooling to -160 °C (solid lines) and after five pulses of 5 vol % CO in He (dashed lines).....IX
- Figure A. 16.** Selectivity to obtained products in alcohol synthesis, calculated on C₃H₆ basis, at 8 bar with a feed of CO₂:H₂:C₃H₆:N₂ = 1:3:3:1 (T = 200 °C, τ = 43 g_{Cat}·min·L⁻¹).....IX
- Figure A. 17.** Simultaneous thermal analysis (TG-DSC-MS) of 5K,Au/TiO₂ and 5K,Au/SiO₂ in air (heating rate = 5 K min⁻¹).X
- Figure A. 18.** High pressure FTIR spectra of time dependent ethane evolution and simultaneous changes in formate/carbonate band region over 2Cs,Au/TiO₂ and 2Cs,Au/SiO₂ in 10% ethene + N₂ flow (blue lines), (200 °C, 10 bar) after 60 min exposure to CO₂+H₂ (dotted black line), (250 °C, 10 bar).....X
- Figure A. 19.** FTIR spectra of stepwise reaction procedure over 2Cs,Au/SiO₂ and 2Cs,Au/TiO₂: 1) CO₂+H₂ (250 °C), 2) C₂H₄ (200 °C), 3) C₂H₄+H₂ (200 °C), 4) CO₂+H₂+C₂H₄ (200 °C) spectra are taken after 60 min of exposure (p = 10 bar).....XI
- Figure A. 20.** Dimensionless response signals after pulsing of C₂H₄:Ar = 1:1 over fresh (a) and used (c) 2Cs,Au/SiO₂ as well as fresh (b) and used (d) 2K,Au/SiO₂ at 200 °C.....XI
- Figure A. 21.** Dimensionless response signals after pulsing of C₂H₄:Ar = 1:1 over fresh (a) and used (c) 2Cs,Au/TiO₂ as well as fresh (b) and used (d) 2K,Au/TiO₂ at 200 °C.....XII

List of Schemes

Scheme 1. Proposed reaction steps of 1-propanol synthesis.....	13
Scheme 2. Simplified reaction scheme of 1-butanol/ <i>n</i> -butanol and 2-butanol/ <i>iso</i> -butanol formation.	13
Scheme 3. Mechanism of ethene hydroformylation over metal (M) supported catalysts with proposed intermediates.[95].....	14
Scheme 4. Surface Rh carbonyl species on Rh/A and their characteristic IR absorption bands [154].	36
Scheme 5. Identified species and proposed reaction mechanism for CO ₂ hydrogenation over Rh/A and Rh,Ni/A.....	42
Scheme 6. Identified species and proposed reaction mechanism for CO ₂ hydrogenation over Rh,K,Ni/A.....	43
Scheme 7. Possible adsorbate species in ethene hydroformylation and hydrogenation with corresponding band positions.	69
Scheme 8. Proposed reaction mechanism of 1-propanol formation from CO ₂ , ethene and hydrogen over alkali modified Au/SiO ₂ catalysts.....	83
Scheme 9. Proposed reaction mechanism of 1-propanol formation over 2Cs,Au/TiO ₂	86

List of Abbreviations

(ad)	Adsorbed species
CCS	Carbon capture and storage
DP	Deposition–precipitation (preparation method)
DRM	Dry reforming of methane
DRIFTS	Diffuse reflectance infrared Fourier transform spectroscopy
DSC	Differential scanning calorimetry
EDX	Energy dispersive X-ray spectroscopy
FTIR	Fourier transform infrared spectroscopy
GC	Gas chromatography
ICP-OES	Inductively coupled plasma optical emission spectrometry
IWI	Incipient wetness impregnation
MS	Mass spectrometry/spectrometer
NP	Nano particle
PP	Polypropylene
P25	Mixed-phase TiO ₂ (ca. 80% anatase and 20% rutile)
Ref.	Reference
RT	Room temperature
RWGS	Reverse water-gas shift
SMSI	Strong metal-support interaction
SSITKA	Steady-state isotopic transient kinetic analysis
TAP	Temporal analysis of products
TEM	Transmission electron microscopy
TG	Thermogravimetry
TPR	Temperature programmed reduction
UV/vis	Ultraviolet/visible (light)
USY	Ultra-stable Y zeolite
WGS	Water-gas shift
Wt%	Weight percent
XPS	X-Ray photoelectron spectroscopy
XRD	X-Ray diffraction

Units of Measurement

Generally, the common measurement units of the International System of Units (SI) were utilized throughout this work. All derived units, which were used in this document, and their expression in terms of SI base units are given below.

Quantity	Unit	Name	Conversion to SI units
Angle	°	Degree	$1^\circ = \pi/2$
	rad	radian	$1 \text{ rad} = 180^\circ / \pi$
Pressure	bar	bar	$1 \text{ bar} = 10^5 \text{ Pa} = 10^5 \text{ N} \cdot \text{m}^{-2}$
Energy	BTU	British Thermal Unit	$1 \text{ BTU} \approx 1055 \text{ J}$
	J	Joule	$1 \text{ J} = 1 \text{ kg} \cdot \text{m}^2 \cdot \text{s}^{-2}$
Temperature	°C	degree Celsius	$x^\circ \text{C} = (x + 273.15) \text{ K}$
Wavenumber	cm^{-1}	reciprocal centimeter	$1 \text{ cm}^{-1} = 100 \text{ m}^{-1}$
Time	h	hour	$1 \text{ h} = 3600 \text{ s}$
	min	minute	$1 \text{ min} = 60 \text{ s}$

1 Motivation and Objective

Our current economy strongly depends on fossil raw materials used not only for production of fuels, but also for the chemical and goods industry. Declining natural resources but simultaneously increasing energy and commodity demands are characteristic for the last and also coming decades (Figure 1) [1]. However, technical options for mining as well as natural reproduction of these fossil resources, like natural gas, crude oil and coal are limited. Furthermore, politicians started to take action against climate change caused by steadily increasing concentration of greenhouse gases. As a consequence, the European commission has set up an *Energy Roadmap 2050* [2], in which they urged to transform the current economy into a “low-carbon economy” and reduce “greenhouse gas emission to 80-95% below 1990 levels”.

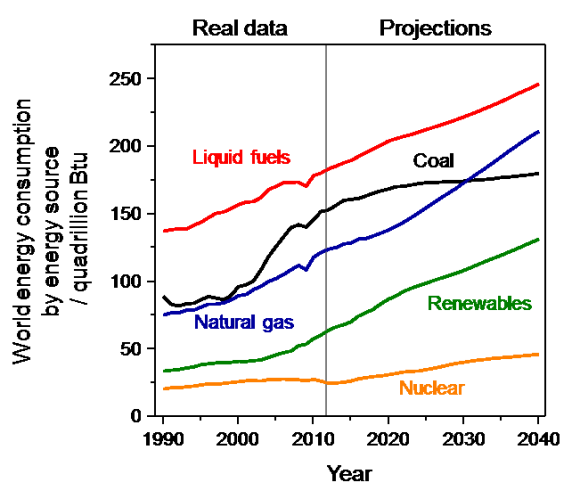


Figure 1. Total world energy consumption by energy source, 1990-2040 (reproduced from [1]).

In this regard, CO₂, which is the most abundant greenhouse gas, is considered to be an alternative carbon source for the future [3-7]. Being present nearly everywhere in the atmosphere makes CO₂ an attractive building block, assuming cheap and effective capture and supply methods [8-10]. The utilization of this greenhouse gas can help to decrease the concentration in the atmosphere. Moreover, the exploitation of natural resources will also be minimized when CO₂ is used in long term applications and not only in the production of fuels, like methane which would again result in CO₂ emission upon burning for energy generation [11].

By means of catalysis, a value-adding transformation of CO₂ into chemicals can be achieved. As CO₂ is, however, thermodynamically very stable ($\Delta H^\circ = -393$ kJ/mol), high energetic molecules are essential for its transformations. Unsaturated hydrocarbons, ammonia or hydrogen are quite often used for that purpose. However, only a few reactions are commercialized at the moment, *e.g.* methane, methanol and formic acid synthesis, formation of cyclic carbonates and some polymers [6, 12-14]. Another interesting approach is the conversion of CO₂ into CO, which can be achieved via dry reforming of methane (DRM) (Eq.1.1) [15-17] or through reverse water–gas shift reaction (RWGS) as shown in Eq. 1.2.



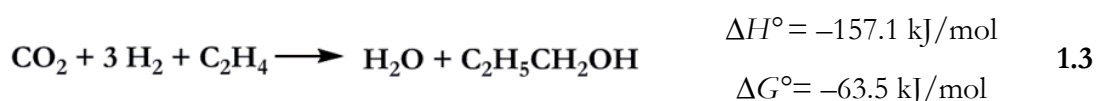
The obtained carbon monoxide can then be used in various other established reactions, which are mainly based on the so called synthesis gas, *i.e.* a mixture of CO and H₂ [18]. For example, higher hydrocarbons and alcohols can be produced via Fischer–Tropsch synthesis, which uses the synthesis gas mixture and iron or cobalt based catalysts [19–20]. Furthermore, the bulk chemical methanol can be synthesized from CO with mixed copper/zinc/aluminum catalysts [21]. Both reactions are recognized as opportunities for a more sustainable liquid hydrocarbon manufacturing.

The most striking argument for RWGS [12, 22] compared to DRM is, that it is energetically more favorable, but nevertheless needs high temperatures, and in principle, fossil resources are not necessary for the reaction if H₂ would be produced from water. On the other hand, depending on reaction conditions and catalyst, a considerable amount of carbon dioxide is completely reduced to methane instead of stopping at the carbon monoxide reduction level. Although methane is an attractive product for energy generation it would be more favorable, when RWGS catalysts worked selectively towards CO. And thus, it is important to understand the reaction mechanisms at a molecular level, to develop more suitable catalysts.

Therefore, it is the aim of the first part of this thesis to focus on the carbon dioxide reduction over supported rhodium catalysts, which were promoted with potassium and nickel. For gaining mechanistic insight into the reaction, we used *in situ* and *operando* infra-red (IR) spectroscopy to elucidate how methane and carbon monoxide were formed.

As already mentioned, a permanent reduction of the carbon dioxide concentration in the atmosphere can only be reached, when it is bound in large amounts for a long time. This can be realized, when products are manufactured, that are used over a long period. An important commodity for that purpose is polypropylene, a plastic from which manifold everyday objects can be made of [21]. Currently polypropylene (PP), the world’s second most traded polymer after polyethylene, is mainly made from propene generated from crude oil, but alternative production routes like the methanol–to–olefin process are gaining more and more importance and are still under research. Beside biotechnological approaches for propene production, which are for example pursued by Novozymes/Braskem [23], the dehydration of sustainably produced 1–propanol to propene can also be a key step prior to its polymerization.

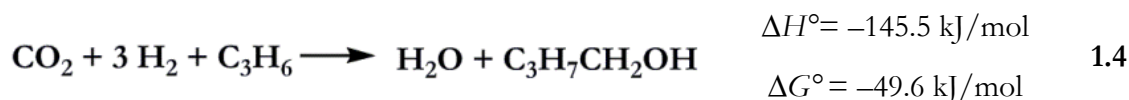
This novel “green” 1–propanol formation is the second subject of this thesis. As depicted in Eq. 1.3, educts for this reaction are carbon dioxide, hydrogen and ethene.



The innovative direct 1–propanol synthesis from CO₂, H₂ and C₂H₄ over alkali promoted gold catalysts was recently developed in the group of E.V. Kondratenko [24–28] and exhibited interesting and promising results, which initiated further studies in the frame of my thesis. TiO₂ (rutile and anatase phase) as well as SiO₂ were tested in the previous experiments as supporting material for gold nanoparticles (NP) and alkali promoters. While TiO₂ based Au-

catalysts show a higher CO₂ conversion, SiO₂ supported ones are superior in terms of 1-propanol selectivity, which can further be increased by addition of alkali promoters, but the precise role of the alkali dopants and the supporting material was not completely clear. Deep mechanistic studies on the role of the supporting material and the promoter have, however, not been performed, but are relevant for further catalyst development. To close this gap, *in situ* spectroscopic studies and other analytical tools were used in this thesis to evaluate the adsorption behavior of the reactants and to enable a more detailed insight into factors affecting catalyst activity and selectivity. Since 1-propanol synthesis is typically performed at high pressure due to thermodynamic requirements, an important objective of this thesis was to develop a suitable FTIR spectroscopic setup that persists under high pressure.

Motivated by the positive results for 1-propanol synthesis, the obvious next step was to evaluate if 1-butanol formation from CO₂, H₂ and propene (Eq. 1.4) is also feasible, because 1-butanol is also a common base chemical and can, for example, be used as solvent or next generation biofuel. The new synthesis route could replace the current petrochemical production and compete with the indeed sustainable but critical plant-based biobutanol production [29-30], which would limit the available land for food production. The IR spectroscopic investigation of this reaction should further help to detect differences in the reaction of ethene or propene, respectively.



In summary, this work focuses on three aspects:

- (1) *In situ* and *operando* IR studies to elucidate the role of support and dopants (K, Ni) in the CO₂ hydrogenation reaction with Rh/Al₂O₃ catalysts.
- (2) Development of alkali modified Au/TiO₂ and Au/SiO₂ catalysts for the 1-propanol synthesis and mechanistic studies comprising high-pressure *in situ* IR experiments and temporal analysis of product in vacuum with micro-second resolution to unravel the influence of promoters (K, Cs) and supports.
- (3) First attempts in 1-butanol formation over Au/TiO₂ and Au/SiO₂ catalysts from propene, hydrogen and carbon dioxide and comparative IR studies to unravel possible intermediates and differences to 1-propanol synthesis.

2 State of the Art

2.1 Carbon dioxide as recyclable feedstock

2.1.1 Capture and Utilization

Carbon dioxide is the final product of every combustion of organic matter, not toxic, but harmful for our climate in larger atmospheric concentration due to its greenhouse effect. That is, why many attempts have been made to reduce its concentration in the atmosphere. For example by techniques like carbon capture and storage (CCS) [33] or mineralization [34-35], which were installed at combustion intensive industry sites, but are often not widely accepted by the community, due to unlikely but possible harmful impacts on the eco- or geosystem [36]. An obviously more attractive route would be the recycling, thus utilization of already atmospheric CO₂ to create valuable products. Large-volume options for hypothetical capture strategies are displayed in Figure 2. Most often, gaseous CO₂ of high purity and partial pressure is necessary. Since the majority of applications are conducted as catalytic reactions, impurities would poison or at least decrease the activity of the catalyst. Therefore, prior to application, the separation and purification process is of special interest. Various carbon-capture processes have been developed, which are mainly based on ad- and absorption, membrane separation or chemical looping [8-9, 37-39].

The utilization of carbon dioxide itself is in focus of numerous review articles, published by Peters *et al.* [6], Wang *et al.* [12], Quadrelli *et al.* [4], and Kondratenko *et al.* [13] to name only a few of the notable works, which try to give a resume of the most often studied and promising reactions and catalysts. Carbon dioxide is converted only in few large scale processes up to now, which are urea synthesis,

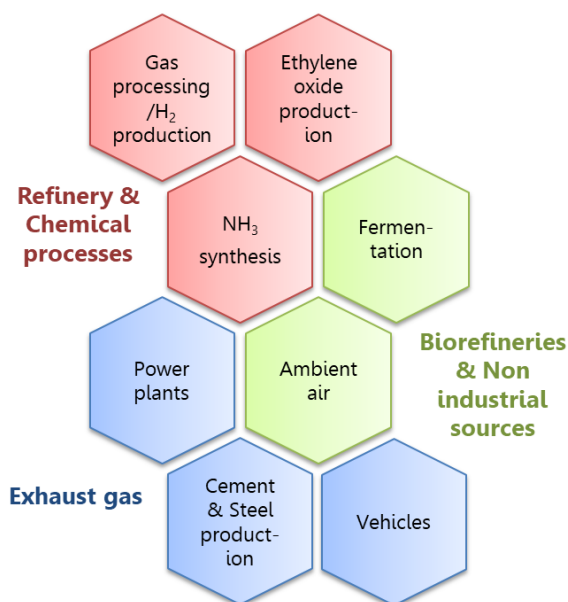
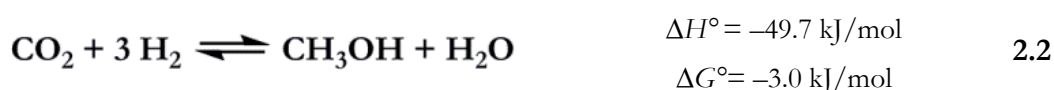


Figure 2. Sources of carbon dioxide [3, 6, 31-32].

salicylic acid production (precursor for aspirin synthesis) and methanol formation [32], but several new reaction routes are considered to be economically and chemically feasible in the near future. Von der Assen *et al.* [10] and Otto *et al.* [40] summarized and evaluated different approaches for CO₂ transformations. For assessing new processes, criteria like the duration and amount of CO₂ fixation, sustainability of the used educts, energy efficiency of the reaction and also the value of the product and its market capacity have to be taken into account. Two of the promising reactions are discussed in this thesis, the direct hydrogenation and the 1-propanol synthesis, using ethene together with hydrogen.

2.2 Hydrogenation and reduction processes

The direct reduction of CO₂ can result in CO (Eq. 1.2), CH₄ (Eq. 2.1), methanol (Eq. 2.2) or other hydrocarbons, depending on the conditions, stoichiometry and catalysts used. Beside the typical catalytic transformation with classical homogeneous or heterogeneous catalysts, also photo- or electrocatalytic reactions have been studied in the past [13]. Photocatalytic processes have the advantage of using light (UV/vis) for driving the reaction forward and avoiding any other energy source (*e.g.* high temperature), which would decrease the sustainability of the reaction. Unfortunately, the so called “solar fuels”, which are often heterogeneously produced using solid catalysts such as semiconductors like TiO₂, ZrO₂, β-Ga₂O₃, or hydroxides of Zn were not obtained in satisfactory rates [41]. Moreover, the majority of the studied photocatalysts did not perform well with natural solar light, but required UV irradiation with $\lambda < 400$ nm, which make them less attractive, because a separate light source is necessary.



Heterogeneous electrocatalytic CO₂ reduction is also conducted with a big variety of catalytic systems, which can be classified in terms of utilized electrode material, electrolyte, and also the applied potential [42]. Depending on the chosen condition, possible products of this so called artificial photosynthesis range from CO over CH₄ to methanol, formaldehyde or other chemicals as visualized in Figure 3. The first step of all these reactions is the adsorption of CO₂ at the surface of the catalyst, which can be solid catalysts supported on carbon paper or film-coated electrodes. This electrode surface delivers electrons to the adsorbed CO₂ molecule, which forms a CO₂^{•-}_(ad) (ad = adsorbed species) intermediate on many main-group elements. This species can then react with protons from the electrolyte, which are often aqueous solutions, producing a formate species HCO₂[•]_(ad). It is frequently observed, that this intermediate is not very stable, due to its unpaired electron, therefore it is transformed into HCO₂⁻ and readily desorbs from most surfaces as formic acid. If the bonding is stronger, another electron and proton can react with the adsorbate and CO_(ad) is formed. Depending on the ability to stabilize this intermediate, a further hydrogenation to methane or methanol is possible, or CO desorbs.

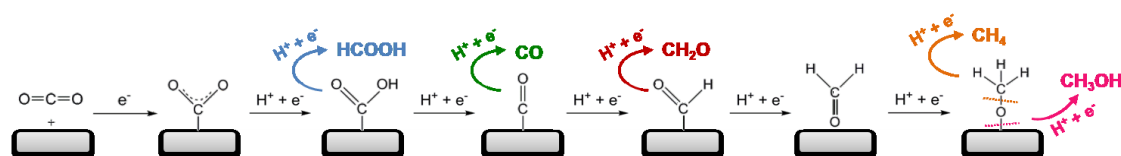


Figure 3. Proposed mechanism of electrocatalytic CO₂ reduction in aqueous solution and main reaction products. Reproduced from [42].

Catalysts, which contain only gold are not able to stabilize the $\text{CO}_{(\text{ad})}$ intermediate strong enough for further hydrogenation and are therefore more selective in CO production, compared for example with copper catalysts. Kim *et al.* [44] studied the behavior of bimetallic gold-copper NP with different transition metal ratios. They found that, when comparing Au_3Cu with AuCu and AuCu_3 catalysts, the adsorption of the intermediate CO^* is strongest at AuCu_3 and thus the main product is methane, compared to Au_3Cu where carbon monoxide is mainly formed. Even though much effort was made to develop active materials and study the mechanisms, present reactor setups and electrode production facilities are not capable for upscaling. That is why electrocatalytic CO_2 treatment is not yet industrially applied.

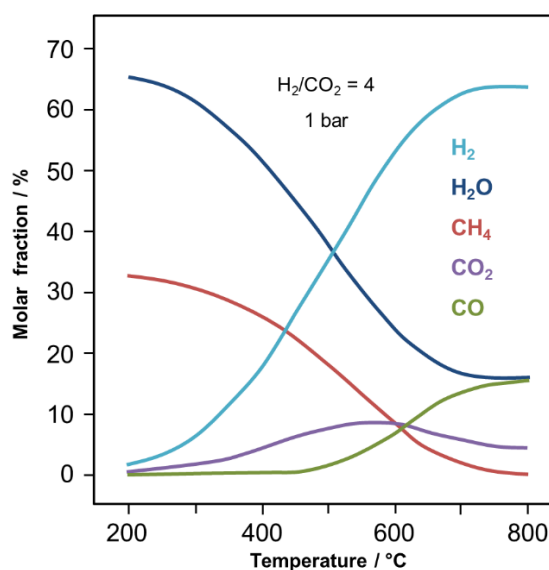


Figure 4. Equilibrium distribution upon CO_2 reduction at atmospheric pressure and different temperatures using a $\text{H}_2/\text{CO}_2 = 4$ feed. Reproduced from [43].

Conventional heterogeneous catalysts are in short-term perspective the most promising solids for large-scale application. However, to activate the thermodynamically very stable CO_2 molecule, neither light nor electric current can be used to deliver the mandatory energy. Thus, an appropriate reaction partner is required, who carries the demanded energy. Hydrogen is such a high energetic material and is already widely used for reduction reactions with CO_2 , both in homogeneous [45] and heterogeneous catalysis [12, 46]. Additionally, hydrogen has the advantage, that it could be in the future a sustainable reaction partner, if the production routes via water electrolysis or photo reduction become competitive compared to conventional fossil sources (coal gasification, methane steam - or naphtha reforming) [47]. However, high pressures and temperatures are quite often inevitable for satisfactory yields and selectivities. Thermodynamic calculations [43] for equilibrium composition in CO_2 hydrogenation indicate a strong influence of the temperature, as illustrated in Figure 4. With a stoichiometric ratio of $\text{H}_2/\text{CO}_2 = 4$ one would expect that CH_4 is the main product, but at temperatures higher than 500 °C, CO becomes the predominant reaction product. Additionally, Gao *et al.* [43] calculated the CO_2 conversion, CH_4 selectivity as well as CH_4 yield with varying pressures and H_2/CO_2 ratios. Generally, a significant enhancement of all values could be achieved at temperatures larger than 400 °C. For example, CO_2 conversion is increased at 500 °C from 70% to more than 90%, when the pressure is raised from 1 to 30 atm. according to Le Chatelier's principle, since the volume is reduced during the reaction. Regarding that, for accelerating the endothermic RWGS reaction, higher temperatures are beneficial.

In contrast, elevated temperatures are unfavorable for many supported catalyst, because the active metal (nano)-particles tend to sinter. This is not optimal, since a large number of ap-

plications require small NPs (< 10 nm). Moreover, coke formation is also a problem in reactions containing carbonaceous reactants. Especially, in reactions, where carbon monoxide is formed, the Boudouard reaction (Eq. 2.3) [48] can occur as an undesired side-reaction at a wide temperature range and forms carbon deposits on the surface, which also leads to deactivation of the catalyst.



2.2.1 Supported catalysts for CO₂ hydrogenation

Heterogeneous catalysts for the RWGS reaction are typically based on Cu, Pt or Rh. These metals are most often supported on TiO₂, SiO₂, CeO₂ or Al₂O₃, but also on Nb₂O₅ or ZrO₂. [49-50] Since noble metals like Pt and Rh have a higher ability to activate dihydrogen compared to Cu, a lower H₂/CO₂ ratio and lower metal loadings are preferable for high CO selectivity, otherwise methanation is favored. In all cases, a high dispersion of the active metal enhances the activity, because this enlarges the metal-support interface, where hydrogen spillover can take place and special intermediates are formed. The metal oxide supports also strongly influence the activity and play a role in the mechanism of the reaction. A systematic study of the impact of metals (Rh, Ru, Pd, Pt) and supports (TiO₂, Al₂O₃) on activity in CO₂ hydrogenation is given by Panagiotopoulou [51].

An earlier study of the activities of Au NPs supported on TiO₂ (P25; mixed-phase of ca. 80% anatase and 20% rutile [52]), Al₂O₃, Fe₂O₃, and ZnO was carried out by Sakurai *et al.* [53]. Au/TiO₂ showed the best performance, reaching thermodynamic equilibrium already at 200 °C. The Japanese researchers also recognized an effect of the preparation method. Coprecipitated and impregnated gold-catalysts clearly exhibited lower activity compared to the most active one, which was prepared by deposition-precipitation (DP). With this catalyst CO selectivities of 86% and > 99% could be achieved at 250 °C and pressures of 5 and 0.1 MPa, respectively. At 5 MPa, the remaining CO₂ molecules were transformed into methanol (4%) and methane (10%). A similar trend was observed by Kyriakou *et al.* [54] by comparing Au/TiO₂ (P25) with Au/Al₂O₃. Activity tests from 250 to 400 °C demonstrated the superior metal-support interaction of Au and TiO₂, since CO selectivity was nearly 100% for various H₂/CO₂ ratios, while the CO₂ conversion increases with rising partial pressure of H₂. Pure TiO₂ and Au/Al₂O₃ were found to be almost inactive.

A direct linkage between metal loading, particle size and selectivity was demonstrated by Kusama *et al.* [55] for Rh/SiO₂ catalysts. By increasing the weight percentage of rhodium from 1% to 10%, the particle size also grew from 3.3 to 5.3 nm (calculated on the basis of TEM measurements). Accordingly, the CH₄ selectivity increased from 11.0 to 96.5%, while CO selectivity decreased from 85.1 to 0.7%. This gives evidence that smaller metal nanoparticles or isolated sites produce CO more likely than CH₄.

Supported catalysts for selective methanation can generally be divided in two groups: (i) noble metal catalysts with Ru, Rh, and Pd and (ii) transition metals, most often Ni, but also

Co, Fe or Mo. Metal oxides are mainly used as supporting material and are quite often the same, which are applied for RWGS [56-57].

In recent years, chemical promotion with alkali metals emerged as an useful tool to tune the performance of supported catalysts for CO₂ hydrogenation.[58] For improving the selectivity towards CO, several groups found that the addition of Li [59] or K [60-62] can be beneficial, independent of the utilized supporting material or active metal. To explain these effects, a more detailed view on the reaction mechanism is necessary and will be given in the next paragraph. Generally, promoters can influence the active sites either electronically or structurally [63]. While electronic promoters donate or pull electronic density towards or from the active site, respectively, and therefore strengthen or weaken the chemisorptive bond of adsorbates, structural promoters give rise to a more dispersed active phase.

2.2.2 Discussed mechanisms for CO₂ hydrogenation

For gaining mechanistic insight into certain reactions *operando* or *in situ* spectroscopy is applied, since these techniques offer information on the interaction between the working catalyst and the reactants, intermediates and possibly formed products. Chapter 2.4 and 3.6 give a more detailed description of these specific spectroscopic techniques.

There is a lively discussion in literature, whether CO₂ hydrogenation proceeds via (i) an associative mechanism where oxygenate species act as intermediates or (ii) a mechanism, where CO₂ directly dissociates to CO_(ad) and O_(ad) [49, 64]. The direct dissociation can also be referred to a redox-process where the active metal or the support is oxidized.

Karelovic and Ruiz [65] found evidence for this second mechanism over Rh/TiO₂ catalysts from *operando*-DRIFTS measurements. Even at low temperature (50 °C), where RWGS is thermodynamically not favored, CO₂ dissociates to CO_(ad) on the pre-reduced surface, forming Rh carbonyl (Rh–CO) and Rh carbonyl hydride (Rh–H_nCO) species as depicted in Figure 5. The latter one was later ascribed as the probable active intermediate for further hydrogenation to methane. The authors proposed that formates are only spectator species, which do not significantly contribute to the product formation. However, no explanation was given, how the oxidation of the catalyst by CO₂ affects the support or the active metal.

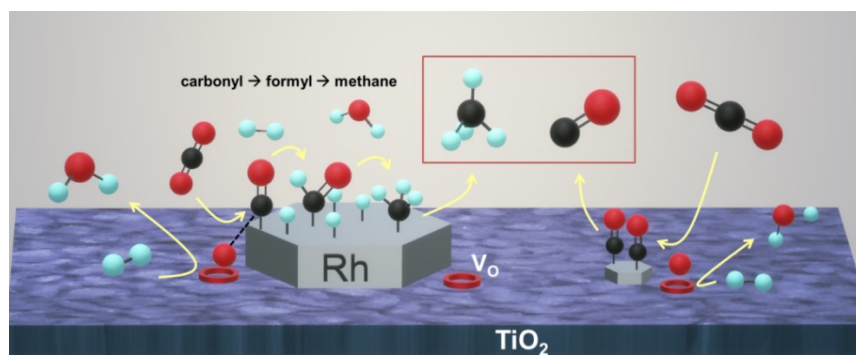


Figure 5. Proposed dissociative reaction mechanism for CO₂ hydrogenation over redox active support (V_O = oxygen vacancy); displaying different intermediates and products, depending on the noble metal size (red = oxygen, black = carbon, light blue = hydrogen).

This unsolved question on the redox behavior of the catalyst was discussed in publications of the Behm group, who studied oxygen mobility on Au/TiO₂ [66] and Au/CeO₂ [67-68] catalysts. Ceria is known for its excellent oxygen storage capacity [69] and is therefore an attractive support for redox reactions. Moreover, Widmann and Behm [66] were able to prove via temporal analysis of products (TAP) reactor experiments for CO oxidation, that titania can also act as an oxygen carrier, when gold is present on the surface. They propose an “Au-assisted Mars-van Krevelen mechanism”, where lattice oxygen atoms can participate in the reaction, when they are positioned at the perimeter of Au NP and TiO₂. Similar active atomic oxygen species are claimed to be created upon CO₂ adsorption and further dissociation on Au/CeO₂ catalysts, which were previously reduced with either H₂ or CO, forming surface oxygen vacancies on the support. Comparing TiO₂ and CeO₂ based Au-catalysts, Behm *et al.* [68] stated, that the amount of active oxygen on the surface is roughly ten times higher on CeO₂ than on TiO₂ under similar conditions. This indicates that on CeO₂ active oxygen deposition or removal is not only possible close to perimeter sites of Au NP, but also directly on the support. Most probably, those oxygen vacancies have a high mobility and can help to activate the CO₂ molecule in abstracting an oxygen atom, creating the active species.

However, RWGS and methanation can be also conducted over noble metal catalysts on supports, which have markedly lower oxygen mobility than CeO₂, like Al₂O₃ or SiO₂. In this case the associative mechanism seems more realistic. Benitez *et al.* [70] observed formate species and carbonyls by applying *in situ* DRIFTS experiments with Rh/Al₂O₃ catalysts in CO₂ methanation feed (H₂/CO₂ = 4/1). They claimed that the formates are only reactive when situated at the interface of Rh and support, forming carbonyls, which can be further hydrogenated to methane. Formates on the support are unreactive. The same intermediates were found by Wu *et al.* [71] on Ni/SiO₂ catalysts and Westermann *et al.* [72] on Ni impregnated USY zeolites. Those groups proposed that methane is generated via hydrogenation of *in situ* formed carbonyls on the active metal. The selectivity of the catalysts seems to be dependent on the metal particle size. Apparently, larger particles offer more adsorption sites for CO and H₂, respectively. Having both carbon and hydrogen in close vicinity, reaction to methane is facilitated, but on smaller particles, where CO and H₂ are competing for the same sites, CO accumulates on the surface and hinders the activation of H₂, because the cleavage of the C–O bond is assumed to be the rate-determining step of the methanation [55].

On the other hand, Goguet *et al.* [73] carried out *operando* DRIFTS/MS measurements under steady-state isotopic transient kinetic analysis (SSITKA) conditions in order to elucidate the mechanism of CO₂ hydrogenation over Pt/CeO₂ catalysts. They found that formates are not the main reaction intermediates in RWGS (Figure 6). Instead, carbonates, which are formed at the active oxygen sites of CeO₂, have been proofed to be the most important intermediates for CO formation. Carbonyls and formates were also present on the surface but did not contribute significantly to the product formation. Methane formation was only observed in trace amounts.

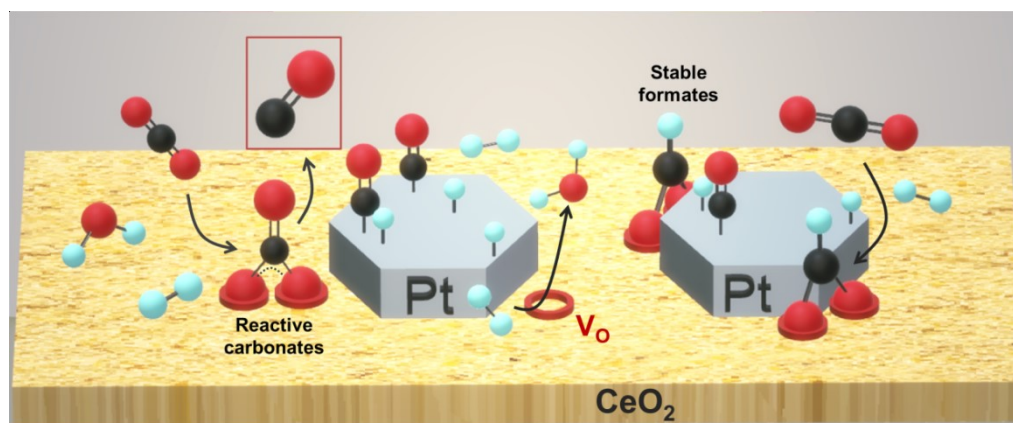


Figure 6. Proposed associative reaction mechanism for CO₂ hydrogenation over Pt/CeO₂ catalyst in analogy to Goguet *et al.* [73]; CO is formed directly from reactive carbonates (red = oxygen, black = carbon, light blue = hydrogen, V_O = oxygen vacancy).

Ceria-zirconia supported Ni catalysts were also studied in CO₂ hydrogenation by Ussa Al-dana *et al.* [74]. While CO formation was explained by a redox-like mechanism as discussed above, methanation was found to proceed not via carbonyl intermediates. It was stated that CO₂ is adsorbed as carbonate or hydrogen carbonate species, depending on the available site (oxygen or hydroxyl, respectively) on the support. Those carbonates are further transformed into formate, but remain on the support, close to the Ni, where the hydrogen is activated and can spill over to the carbon, probably forming methoxy species, but they could not be detected in IR spectra.

Comparing theoretically the associative and the dissociative mechanism, Pan *et al.* [75] calculated in a density functional theory (DFT) study the energy levels of elementary steps in the CO₂ methanation over Ni/Al₂O₃. If hydroxyls are present on the alumina surface, intermediate carbonyls are identified to be kinetically and thermodynamically favored. When there are no hydroxyls, carbonyl formation is kinetically hindered and formates are the dominant intermediates. One can criticize in this study, that in the calculation formates were supposed to be located only on the nickel, not on alumina. Many other studies [70, 73, 76] describe the formates as present on the support, so those results can only roughly be compared.

Influence of alkali metal promoters

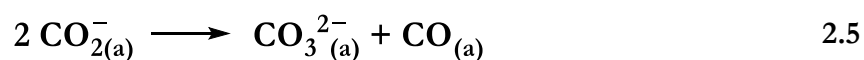
As already mentioned, alkali promotion is a topic of rising interest in heterogeneously catalyzed CO₂ hydrogenation [63]. Especially for the RWGS reaction [61-62, 77-78] and FT synthesis [79-81], potassium addition was demonstrated to be beneficial for altering the catalysts performance. In both systems methane production could be suppressed, which leads to a higher selectivity towards CO or higher hydrocarbons, respectively. Several possible explanations are given in literature, for both electronic and structural reasons responsible for the influence of alkali metals on the catalysts surface and hence the mechanism of the reaction. Jordan *et al.* [82] studied CO adsorption on Al₂O₃ and the impact of alkalization with FTIR spectroscopy. Their experiments revealed that the normally generated hydrogencarbonates on Al₂O₃ were not formed when K is present. Those hydrogencarbonates typically adsorb on Lewis acid sites, which have basic OH-groups in close proximity. Instead, on the alkalized

surface, carbonates are created. This is due to the increase of basicity of surface O^{2-} sites and coverage of basic OH-groups upon potassium addition.

The exchange of protons of Si–OH groups by K^+ was found to occur also on K,Cu/SiO₂ catalysts. Millar *et al.* [83] reported, that the presence of potassium weakens the CO adsorption on copper, by inducing a positive charge at the copper, which decreases the stabilizing backdonation of electrons from the copper into the $2\pi^*_{CO}$ orbital.[84] Moreover, the oxygen ions in dispersed K₂O species supply electrons for the formation of carboxylate (CO_2^-) in CO₂ adsorption at interfacial sites of copper and potassium. In reaction with hydrogen, these carboxylates are transformed into monodentate formates.

These findings on the important role of OH groups, are in contrast to results of Yang *et al.* [60], who examined promotional effects on Pt/zeolite catalysts for the RWGS reaction. Solid-state impregnation of the zeolites with potassium promoted the adsorption and activation of CO₂. Active sites were Pt–O(OH)–K species, at which hydrogencarbonates were created and transformed into formates, which later release CO. Similar oxygen–linked gold species were found for alkali–promoted Au/zeolite catalysts. Flytzani-Stephanopoulos and co-workers [85] stated, that those mononuclear Au–O(OH)–K species and not Au NP are the active sites for WGS. These active gold sites are highly dispersed and positively charged, which is directly induced by alkali promotion. Moreover, the activity of these catalysts is proportional to the number of surface OH–groups and not to the number of gold atoms.

Potassium can also influence the activity of the active metal directly, without the contribution of the support. This was demonstrated by Farkas and Solymosi [86], by applying Auger electron spectroscopy and high-resolution electron energy loss spectroscopy. An Au(111) crystal surface was doped with metallic potassium and then exposed to CO₂ gas atmosphere. Whereas CO₂ adsorption on the clean Au surface was negligible, addition of alkali metal resulted in the formation of CO_2^- (Eq. 2.4). Moreover, the authors claimed that two of the CO_2^- species can disproportionate to adsorbed carbonyl and carbonate on the catalysts surface (Eq. 2.5).



The gold atoms at step positions gained enhanced mobility and charge could be easily transferred to the adsorbed molecule. This additional electron density, which is located in the empty π orbital of the carbon dioxide leads to a strengthening of the gold-carbon bond and the simultaneous weakening of the carbon–oxygen bond, facilitating the scission of that bond and the generation of carbonyls.

In a more recent paper of Solymosi and co-workers [87], the enhancing effect of electron donating supports for CO₂ activation was underlined for Au catalysts. The analysis of different supports revealed that semiconducting oxides, like TiO₂ or CeO₂ performed superior to

non-semiconducting ones like SiO_2 . The authors concluded that promoting the catalyst with alkali metals has the same effect and leads to the formation of CO.

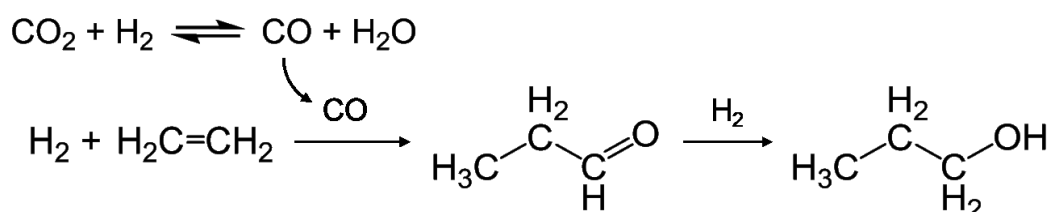
In summary, several research groups agree that the addition of alkali metals to different oxidic supports or also noble metals leads to a stronger CO_2 adsorption [88]. Moreover, it enables the scission of one CO bond, but the further CO hydrogenation seems to be hindered, as the desorption of CO is facilitated in the presence of alkali metals. This is often explained with electronic properties of these alkali metals. The electron donating ability of K_2O , which is further enhanced by other (noble) metals (Cu/Au), enables the reduction of CO_2 to CO. Moreover, Lewis acidity is altered compared to the unpromoted surface, but it is not totally clear if the impact is more pronounced for the support (*e.g.* basicity of O_2^-) or the electron density on the active metal.

However, it was often observed, that beside the electronic influences, also the type of surface intermediate was changed. This suggests that also the supporting material plays a crucial role and not only the alkali promoter. Furthermore, the amount of OH-groups on the support is important. Additionally, alkali ions cause mobility of the transition or noble metals, resulting in dispersed single atoms or at least degradation of larger NP, which is advantageous in that case.

Against this background it was one aim of this work to investigate, if the structure of the Au and Rh particles on the catalysts surface is changed by alkali metal promotion and furthermore, if the electronic properties are altered thereby.

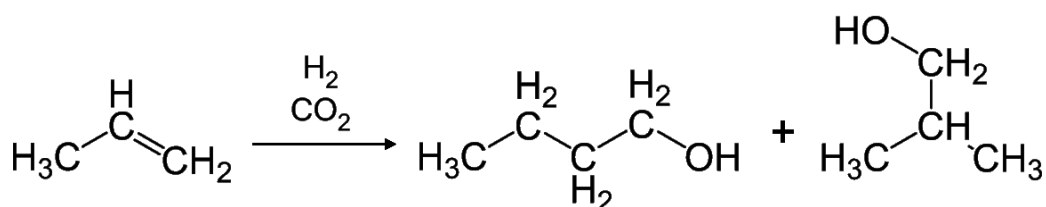
2.3 Alcohol formation from carbon dioxide, hydrogen and olefins

As already mentioned in the first chapter, this thesis aims at the further development and deeper understanding of a novel 1-propanol and 1-butanol synthesis from sustainable or at least non-fossil-based molecules. The new “green” synthesis of 1-propanol was found to comprise three reaction steps (Scheme 1) [24]. It starts with the already described RWGS reaction, providing CO for hydroformylation with an olefin, which is the second part. This gives rise to the respective aldehyde 1-propanal, which is in the last step hydrogenated yielding the desired alcohol 1-propanol.



Scheme 1. Proposed reaction steps of 1-propanol synthesis.

Concerning the respective reaction with propene, two aspects have to be considered: (i) the insertion of the CO in the hydroformylation step can also occur on the secondary carbon of propene, yielding *iso*-butanal and later *iso*-butanol (Scheme 2) and (ii) the reaction has to be studied under lower pressure than the 1-propanol synthesis (20 bar), because the vapor pressure of propene reaches only 9.3 bar at 25 °C [89]. It was therefore assessed to study the butanol synthesis at 8 bar.



Scheme 2. Simplified reaction scheme of 1-butanol/*n*-butanol and *iso*-butanol formation.

In the following, some aspects of hydroformylation and hydrogenation are discussed.

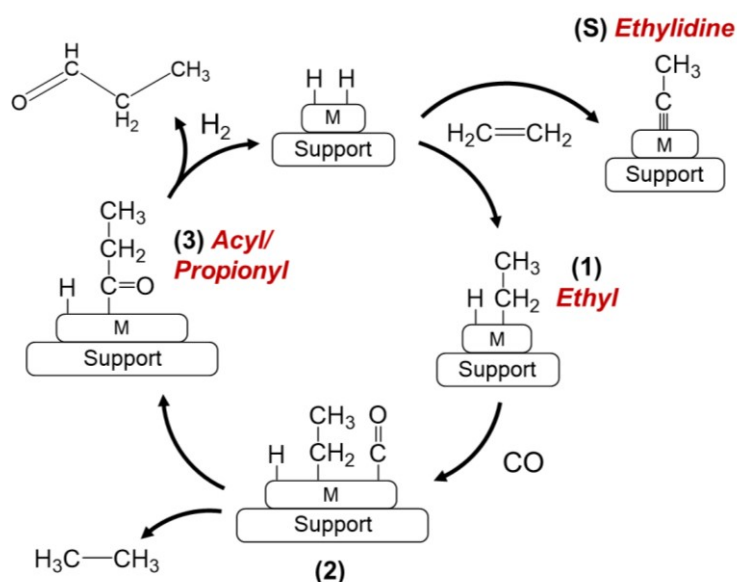
2.3.1 Hydroformylation and hydrogenation

The addition of a CO molecule to a carbon–carbon double bond of an olefin together with hydrogen is called hydroformylation, and aldehydes are the products. The respective homogeneous catalytic reaction is applied already industrially, very often catalysed by rhodium and cobalt complexes [90]. The resulting alcohol can further be dehydrogenated, which gives rise to a homologue olefin production sequence.

Homogeneous catalysts are difficult to recover after reaction, but especially in the case of noble metal complexes, this is economically important. Therefore, a heterogeneous or heterogenized hydroformylation catalyst would be more attractive in numerous cases [91]. Sev-

eral approaches were tested for hydroformylation of small olefins, for example the immobilisation of rhodium carbonyl complexes on silica [92], platinum group metal phosphides on silica [93] or silica-supported ruthenium catalyst [94]. More easy to prepare are typical heterogeneous catalysts like Rh/Al₂O₃ [95-96], Rh/SiO₂ [97-99] or Rh/zeolite [100]. A severe problem of most of these catalysts is the domination of olefin hydrogenation over hydroformylation, especially for rhodium-based ones. The mechanism for this reaction was already described by Horiuti and Polanyi in 1934 [101]. It was found that the size of metal particles has a drastic influence on the chemoselectivity. Thus edges and corners of small crystallites promote hydroformylation [91]. For example, a particle size of 5 nm was optimum for Rh/SiO₂. [98]

It is discussed for the heterogeneously catalyzed hydroformylation reaction mechanism as depicted in Scheme 3, that primarily ethene adsorbs as ethyl species (**1**, C₂H_{5(ad)}) on the active metal. Depending on the neighboring adsorbate (**2**), which can be either hydrogen or carbonyl, the subsequent product would be ethane or an acyl species (**3**, C₂H₅CO_(ad)), respectively. The acyl species can then be hydrogenated to form propanal or after an additional hydrogenation step propanol [99, 102]. Besides, adsorbing ethene can also form an ethylidene species (**S**), which is described as spectator species only that does not participate in the reaction, but is slowly hydrogenated to ethane [103].



Scheme 3. Mechanism of ethene hydroformylation over metal (M) supported catalysts with proposed intermediates.[95]

Moreover, Williams *et al.* [104] unraveled that adsorbed CO can inhibit the hydrogenation of ethene over a rhodium foil covered with titania-overlayers. For the reaction studied in this work, that would mean, those catalysts with a high ability to form *in situ* CO from CO₂, hydrogenation could be suppressed. Beside the generation of oxo-products, also higher hydrocarbons can be formed during reaction, in analogy to FT synthesis. By means of isotopically labeled ¹³CO and unlabeled ethene, Jordan and Bell [105] studied the interaction of those molecules with hydrogen over a Ru/SiO₂ catalyst. It was observed that ethene can undergo three different reactions with hydrogen: (i) hydrogenolysis to form CH₄, (ii) hydrogenation to ethane and (iii) homologation to C₄₊ hydrocarbons. Rising partial pressure of CO enhanced hydroformylation and strongly suppressed hydrogenation of ethene. It is worth mentioning that only 10% of the produced methane stems from CO and nearly no labelled carbon can

be found in higher hydrocarbons. This means that C₄-olefins are most probably formed by dimerization of C₂H₄ [104], while C₅-products can be formed by a reaction of CH₂ units, deriving from CO hydrogenation or partial hydrogenolysis of C₂H₄ with a C₄-olefin.

In case of propene hydroformylation, also regioselectivity is of major importance. The ratio of normal (*n*) to *iso*-butanol formation is assumed to be dependent on the chosen metal, where Rh and Ni produce more *n*-alcohol and Pd more *iso*-alcohol [106]. The ratio seems also scalable by adjusting the flow rate of reactants [91]. For homogeneous catalysts, the regioselectivity is mainly tuned by adjusting the ligands on the metal center. Then partial pressures of CO or hydrogen do not play a role in the range of 8 to 15 bar [107]. Controlling the selectivity by using zeolites as support was not successful, because the reaction was found to proceed only on the outer surface of the zeolite and not in the pores [100].

Gold catalyzed hydroformylation has been only rarely explored. Liu *et al.* [108] reported the liquid phase transformation of higher olefins over a cobalt oxide supported gold catalyst. At temperatures of 100–140 °C and pressures of 3–5 MPa, selectivities of 85% to the desired aldehydes were reached. Internal insertion of CO, leading to branched products, was proved to be much slower than the terminal insertion, obtaining the linear aldehyde. The authors claimed that the role of gold was just to activate the hydrogen, which spills over and reduces the cobalt in the support.

Nevertheless, the studies of Ahlers *et al.* [24] unraveled, that the choice of gold as active metal in the alcohol formation from CO₂, H₂ and olefins is superior, compared to other (noble) metals. Olefin hydrogenation, which is the most undesired reaction, since olefins are expensive educts, is strongly dominating over rhodium and ruthenium-based catalysts. Besides, conversion of carbon dioxide is negligible at those noble metals and propanol formation could not be observed. Copper based catalysts showed a certain carbon dioxide conversion, but the selectivity of CO was much higher than that of 1-propanol. Moreover, cobalt catalysts presented a higher conversion of carbon dioxide, but the good FT-activity of cobalt converted the *in situ* formed carbon monoxide preferentially to higher hydrocarbons. The gold-based catalysts displayed the best conversion of carbon dioxide together with the highest yield of propanol. Therefore, this work focuses on gold catalysts for hydroformylation in combination with CO₂ and aldehyde hydrogenation.

Influence of alkali metal promoters

By modification of the supported metal catalysts with alkali metals, several groups noticed an improvement of selectivity. The C₃-oxygenate selectivity in ethene hydroformylation with carbon monoxide over Rh/SiO₂ catalysts was increased from 23 to 33% when potassium chloride was added [98]. At the same time, activity of both hydrogenation and hydroformylation reactions was decreased, but the rate of hydrogenation was lowered more significantly. The opposite was observed for the turnover frequency of propene hydroformylation over different sodium-modified metal catalysts (Rh, Pd, Pt, Ni) supported on SiO₂ [106]. While activation energy for this reaction was decreased, regioselectivity to *n*- or *iso*-butanal was not affected. Comparing the effect of different alkali metals on Rh/SiO₂ catalysts in propene

hydroformylation, Sordelli *et al.* [97] could prove that all alkali metals enhance the CO insertion rate, but activity strongly decreased with rising size of the alkali metal. They explain this finding with the polarizing power of the atoms. Lithium, which has the largest polarizing power, accelerates therefore hydroformylation the best.

In general, the effect of alkali addition on the performance of different heterogeneous catalysts for small olefin hydroformylation has been only rarely studied spectroscopically, especially at elevated pressure [92]. Very often, only carbonyl band formation and stability were discussed, while the alkyl or acyl intermediates were not described or even observed. Therefore, it is one objective of this work to establish a setup which enables high-pressure FTIR spectroscopic studies of ethene and propene hydroformylation and evaluate the data with special emphasis on the alkali metal promotion effect.

2.4 In situ and operando FTIR spectroscopy

Catalytic reactions can be sub-divided into different elemental reaction steps. A thorough investigation of those steps is essential for the understanding of the overall process and rational catalyst design. To gain this mechanistic insight, *in situ* and *operando* spectroscopy turned out to be useful tools for achieving those goals [109-111]. By applying *in situ* spectroscopy, it is possible to obtain evidence about the nature of active sites and their role in the reaction [112]. The power of *operando* spectroscopy is that, in addition to the spectroscopic data, activity measurements show the catalysts performance [113].

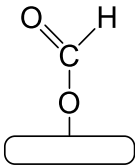
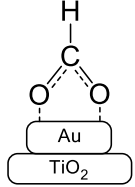
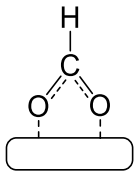
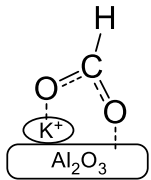
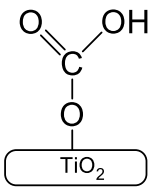
For heterogeneous catalysts it is crucial how and where educts and products of the reaction are adsorbed on the catalysts surface [114]. Infrared (IR) spectroscopy can be properly applied to evaluate those interactions [115-118]. Depending on the desired information, several techniques of sample preparation and analysis have been developed. The classic transmission IR spectroscopy can be used, when the solid catalyst is pressed into a self-supporting disc, being very thin, that the IR beam can go through it (for a detailed description of the preparation and analysis technique see Chapter 3.6). For a realistic reactor-like performance, catalyst particles are placed in a DRIFTS cell, where the reaction gas mixture can flow through the catalyst bed. Here, the IR beam is reflected on the surface of the catalyst, and afterwards collected by a mirror-system that re-focuses the beam and guides it to the detector. This method is especially useful for very dark materials that would totally absorb the beam in transmittance mode or for samples that are very difficult to press into brittle wafers. Different cell designs are available with the possibility to heat the catalyst and also to work under higher pressures, so that a realistic reactor behavior is enabled [115].

Evaluation of the effluent gas composition can be realized by mass spectrometry (MS) or gas chromatography (GC). The advantage of MS is the time-dependent online observation of the gas stream, by analyzing dedicated mass/charge numbers. So the change in composition is directly measureable. On the other hand a quantitative analysis is more accurate with GC. By calculation of conversion, yield and selectivity activity information is available.

2.4.1 Reaction intermediates and surface adsorbates

As already mentioned, the alcohol formation from CO₂, hydrogen and olefins is a totally new process and no detailed mechanism or reaction steps were so far described in literature before the work of Ahlers *et al.* [24-25], but the proposed mechanism presented in that work suggests that a comparison with spectroscopic data from RWGS reaction, hydroformylation and hydrogenation is advisable. For that purpose, Table 1 summarizes possible adsorbates and their corresponding FTIR absorption bands, which can be formed on the catalyst surface under admission of CO₂ and H₂. The same band assignments can be used for analyzing the RWGS reaction over Rh/Al₃O₃.

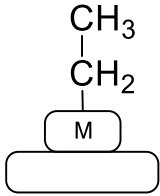
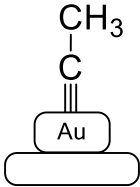
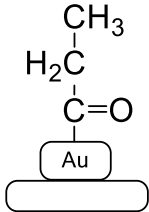
Table 1. Infrared absorption bands and assignments for possible adsorbate species formed in CO₂ containing feed.

Species			IR absorption wave-length / cm ⁻¹	Material	Ref.
Formate HCOO⁻			2795 (ν CH) 1575 (ν _{as} CO) 1375 (δ CH) 1342 (ν _s CO)	KHCO ₂	[119]
	No specified structure		2870 (ν CH) 1580 (ν _{as} CO) 1365 (ν _s CO)	TiO ₂	[120]
			1598 (ν _{as} CO) 1380 (ν _s CO)	Au/SiO ₂	[87]
			1592 1392 1378	Rh/Al ₂ O ₃	[70]
	Mono-dentate		2978 2904 1583–1578	Cu/SiO ₂	[117]
	Bidentate		2950 1632 1312	Au/TiO ₂	[121]
			2936 2856 1552 (ν _{as} COO) 1354 (ν _s COO)	Cu(I)/SiO ₂	[122]
			2777–2682 1600–1595 1370–1360 1355–1350	K/Al ₂ O ₃	[82]
Hydrogen carbonate/ Bicarbonate HOCO₂⁻			1555 (ν C=O) 1420 (ν _{as} COO) 1220 (ν _s COO)	TiO ₂	[120]

Species			IR absorption wave-length / cm^{-1}	Material	Ref.
Carbonate CO_3^{2-}	Bidentate		1550–1540 1360–1350	K/ Al_2O_3	[82]
			1670/1580 1243/1320	TiO_2	[120]
	Monodentate		1550 1356	TiO_2	[123]
Carboxylate CO_2^-	Interfacial		1541 ($\nu_{\text{as}} \text{COO}$) 1351 ($\nu_{\text{s}} \text{COO}$)	$\text{K}^+, \text{Cu}_2\text{O}/\text{SiO}_2$	[83]
			1510 ($\nu_{\text{as}} \text{COO}$) 1366 ($\nu_{\text{s}} \text{COO}$)		
Formyl species HCO-			1760	Ru/ Al_2O_3	[124]
Methoxy species $\text{H}_3\text{CO-}$			2926 ($\nu_{\text{as}} \text{CH}$) 2815 ($\nu_{\text{s}} \text{CH}$)	Cu/ SiO_2	[122]
			2957 2857	Rh/ Al_2O_3	[95]

For comparing the bands measured during FTIR experiments in ethene containing gas flow, Table 2 lists literature data for different adsorbates and intermediates observed in hydroformylation (with CO) or hydrogenation feed.

Table 2. Infrared absorption bands and assignments for possible species formed in hydroformylation ($\text{CO} + \text{H}_2 + \text{olefin}$) or hydrogenation feed ($\text{C}_2\text{H}_4 + \text{H}_2$).

Species		IR absorption wave-length / cm^{-1}	Material	Ref.
Ethyl ($\text{C}_2\text{H}_5\text{-M}^*$)		2876 2855 1190	Rh/ Al_2O_3	[95]
		1200	Pt/ Al_2O_3	[103]
Ethylidyne ($\text{CH}_3\text{C-M}^*$)		2878 1337	Rh/ Al_2O_3	[95]
		2880 1339	Pt/ Al_2O_3	[103]
Propionyl/Acyl species ($\text{C}_2\text{H}_5\text{-C(=O)M}^*$)		1678	Rh/ SiO_2	[99]
		2869 1675	Rh/ Al_2O_3	[95]
adsorbed Propanal		1722	Rh/ SiO_2	[99]
		1737	Rh/ Al_2O_3	[95]

M^* = supported metal (*e.g.* Rh, Au)

2.4.2 Isotopic transient technique

Beside the normal *in situ* and *operando* examinations of the reaction in different gas mixtures, by which the formation of adsorbates and products can be followed, some more sophisticated techniques were developed to study the reactivity and hence the role of single adsorbate species in the reaction mechanism. The so called “spectrokinetic” approach enables the understanding of relations between the reactivity of adsorbates, which can be followed by FTIR spectroscopy, and product formation, analyzed by on-line MS [125-126]. For that purpose, isotopic transient techniques, also in steady-state (SSITKA, [127-128]), were introduced. The aim of that technique is to switch, after reaching steady-state in normal gas flow, to an isotopically labelled gas feed and monitor the changes in FTIR band position and

intensity and also the different mass/charge traces, which are representative for both the original product molecule and also the new ones with labelled atoms.

Isotopic labelling, for example with $^{13}\text{CO}_2$, changes the mass of the carbon atom in the molecule. This is evidenced by the wavenumber position ν of the FTIR band, because the energy demanded for vibrating (Eq. 2.6) is directly related to the reduced mass of the molecule (Eq. 2.7).

$$\nu = \frac{1}{2\pi} \sqrt{\frac{k}{\mu}} \quad 2.6$$

$$\mu = \frac{m_1 m_2}{m_1 + m_2} \quad 2.7$$

With k = spring constant of the molecular bond and m = mass of the single atoms.

The band position of ^{13}C containing species is then shifted to approximately 40 to 50 cm^{-1} lower wavenumbers compared to the original ^{12}C containing species [125]. By comparing the time dependent behavior of band heights or areas after switching to the labelled feed, the discrimination between reactive intermediates and spectator species, which do not mainly contribute to the product formation, can be realized. The bands of spectator species change slower than those of active species. With this method, the spectator role of formates in RWGS over Pt/CeO₂ was evidenced [73, 129].

This method was applied for the investigation of different Rh/Al₂O₃ catalysts in RWGS reaction.

3 Experiments and Methods

All chemicals used for the preparation and experiments as well as their sources are listed in the appendix in Table A. 1. Moreover, additional figures, denoted with Figure A.x. are also located in the appendix

3.1 Preparation of gold catalysts for alcohol formation

Generally, all catalysts were prepared with 2 wt % of gold. Therefore, in the following chapters, the abbreviation $\text{Au}/\text{M}_x\text{O}_y$ is always used instead of the whole description. The alkali metal loading was varied from 0 to 5 mol %. This unit is chosen for a better comparison with regard to the different size and weight of potassium and cesium, the unit is in the following not additionally listed. The resulting catalysts names are for example given as: $x\text{K}, \text{Au}/\text{TiO}_2$, which means 2 wt % Au and x mol % K. The preparation methods were adopted from the work of Ahlers [24] Supported gold particles were prepared by deposition precipitation of $\text{Au}(\text{OH})_3$ from HAuCl_4 with ammonia solution (25%). The alkali metal doping was subsequently carried out following the incipient wetness impregnation method (IWI) [130].

Caution: It may happen that during preparation of gold NP from HAuCl_4 with ammonia solution, some explosive compounds are formed [131]. Special attention has to be paid in handling of the dried powders after precipitation. It has to be avoided to directly treat the hot samples from the drying oven. After calcination, the catalysts can be considered safe.

Preparation of (K/Cs), Au/TiO₂: The TiO_2 anatase was calcined in air at 500 °C for 8 h before preparation. 2 g of the supporting material was suspended in 200 ml of distilled water and stirred for 10 min. The bright yellow aqueous chloroauric acid ($\text{HAuCl}_4 \cdot x \text{H}_2\text{O}$) was added dropwise with a micro liter pipette. This suspension was further stirred for 30 min at room temperature. After that, the deposition–precipitation (DP) was carried out under stirring with ammonia solution (25%) until a pH value of 10 was reached. An altering for 10 min followed. Then the solution was filtered by a fine frit and the precipitate was washed several times with cold distilled water until the filtrate was negatively tested for chloride ions with AgNO_3 . The remaining catalyst precursor in the frit was then transferred into a small porcelain cup and dried over night at 80 °C. If alkali metal addition was performed, the dried powder was impregnated with the corresponding alkali nitrate solution. The appropriate amount of alkali metal nitrate was dissolved in the volume of distilled water, which is needed for wetting the entire surface of the supporting material (see Table 3). Then it was added dropwise to the dry precursor, which was placed in a vortex mixer (Desyre Mix, Fa. Zinsser Analytic) at 800 rpm (revolution per minute). Retaining this movement, the impregnated samples were then heated to 80 °C and again dried for 10 h in the mixer. The final calcination was carried out in a muffle oven in air at 250 °C for 4 h with a heating ramp of 3 K min^{-1} . For preparation of particles, the calcined samples were pressed and sieved to obtain a size of 250 – 450 μm .

Preparation of (K/Cs), Au/SiO₂: The preparation of SiO₂ – supported catalysts was slightly different than that with TiO₂, because precipitation of gold particles is more difficult on the less acidic surface of SiO₂ [132]. This can cause incomplete precipitation of gold. Therefore, after adding the HAuCl₄ solution to the suspended SiO₂ the mixture was heated under continuous stirring to 70 °C, this temperature was held for 1 h. After reaching room temperature again, the ammonia solution was added for precipitation. The washing and drying procedure was the same as for the TiO₂ based catalysts, but after that and before impregnation with alkali metals, the samples were intermediately calcined in air at 250 °C for 4 h. The impregnation, final calcination and particle preparation was the same, as described above for the TiO₂ catalysts.

Table 3. Used supporting materials and their water absorption capacity for IWI.

Supporting material	Water absorption capacity / mL g ⁻¹	S _{BET} / m ² g ⁻¹
TiO ₂ anatase	0.85	58
SiO ₂	1.9	315

3.2 Preparation of rhodium catalysts for CO₂ hydrogenation

The γ – alumina supported rhodium catalysts were prepared by IWI. Generally, rhodium loading was adjusted to 0.5 wt %, nickel to 3 wt % and potassium to 2 wt %. Depending on the desired composition, RhCl₃·3 H₂O, KNO₃ and Ni(NO₃)₂·6 H₂O were together dissolved in a small amount of distilled water. If dissolution was difficult, the mixture was gently heated. The solution was then dropwise added to the untreated Al₂O₃ powder (in the following denoted as A), stirred with a glass bar and then altered for 10 min. After 24 h drying at 120 °C, the samples were subsequently calcined in inert gas atmosphere (Ar) at 700 °C for 5 h. Finally, the catalyst was pressed and sieved to obtain particles the size of 315 – 710 μ m.

3.3 *Ex situ* analysis and characterization of the catalysts

For characterizing the catalysts, different *ex situ* analysis methods were used. The composition of the samples was analyzed by optical emission spectrometry with inductively coupled plasma (ICP-OES). The phases and crystallite sizes were determined with powder XRD. The specific surface areas of the samples were measured according to the method of Brunauer, Emmett and Teller (BET) [133]. To gain insight into the size and shape of noble metal particles and the surface morphology in general, transmission electron microscopy (TEM) was carried out. For understanding of the thermal degradation of the fresh catalyst during calcination or the activation process, the samples were analyzed with so called simultaneous thermal analysis (STA), which is a combination of DSC and TG. The volatile components, which were released from the samples, were then measured with MS.

ICP-OES

The amounts of Rh, Ni, K and Au were analyzed with a Varian 715–ES ICP emission spectrometer. 20–30 mg of the sample were mixed with 6 mL aqua regia and 2 mL hydrofluoric acid and digested in a microwave–assisted sample preparation system “Multiwave Pro” from Anton Paar at 200 °C and a maximum pressure of 50 bar. The obtained solution was filled up to 100 ml and then measured.

Powder XRD

XRD powder pattern were recorded either on a Panalytical X'Pert diffractometer equipped with a Xcelerator detector or on a Panalytical Empyrean diffractometer equipped with a PIXcel 3D detector system, both used with automatic divergence slits and Cu $k\alpha_1/\alpha_2$ radiation (40 kV, 40 mA; $\lambda = 0.015406$ nm, 0.0154443 nm). Cu β –radiation was excluded by using nickel filter foil. The measurements were performed in 0.0167° steps and 25 s of data collecting time per step. The samples were mounted on silicon zero background holders. Peak positions and profile were fitted with Pseudo-Voigt function using the HighScore Plus software package (Panalytical). Phase identification was done by using the PDF-2 database of the International Center of Diffraction Data (ICDD).

Gold crystallite size (d) was calculated by applying the Scherrer equation (Eq. 3.1) using the integral breadth under the assumption of spherically shaped crystallites [134].

$$d = \frac{K \cdot \lambda}{B(2\theta) \cdot \cos(\theta)} \quad 3.1$$

K is set to 1.0747. λ is the wavelength of the X–ray. For gold, reflexes at $\theta = 19.1$, 22.2, 32.3 and 38.8° were used and averaged to calculate the crystallite size.

Simultaneous thermal analysis (STA)

The STA is a combination of thermogravimetry and differential scanning calorimetry. During the measurement in which the sample is heated and exposed to a certain gas atmosphere, mass and heat flow changes, which indicate exo- or endothermic processes, are detected. The device (Sensys TG–DSC from Setaram) analyzes differences between the sample, which is placed in a small aluminum crucible and an empty crucible. In case of the gold catalysts, the sample was weighed in the crucible and then placed on the balance. Then it was heated with 5 K min^{−1} up to 600 °C. For comparing the behavior in different media, the sample was exposed to two different gas flows i) air and ii) 20 vol % CO₂ + H₂. The exhaust of the device was coupled with a MS (OmniStar, Pfeiffer Vacuum GmbH) to detect different emerging products.

Surface area determination with BET method

The specific surface areas of fresh as well as used catalysts were measured with a BEL-SORP-mini II (Fa. BEL Japan, Inc.). The porous materials were pre-treated at 200 °C for 2 h in vacuum. The recording of adsorption isotherm by N₂ physisorption was subsequently carried out at -196 °C in the relative pressure range of $0.05 < P/P^0 < 0.30$.

Transmission electron microscopy and EDXS

The TEM measurements were performed at 200 kV with an aberration-corrected JEM-ARM200F (JEOL, Corrector: CEOS). The microscope is equipped with a JED-2300 (JEOL) energy-dispersive x-ray-spectrometer (EDXS) for chemical analysis. The aberration corrected STEM (High-Angle Annular Dark Field (HAADF) and Annular Bright Field (ABF)) imaging was performed under the following conditions. HAADF and ABF measurements both were executed with a spot size of approximately 0.13 nm, a convergence angle of 30–36° and collection semi-angles for HAADF and ABF of 90–170 mrad and 11–22 mrad respectively. Preparation of the TEM sample: The sample was deposited without any pretreatment on a holey carbon supported Cu-grid (mesh 300) and transferred to the microscope.

A maximum of 100 particles was measured and evaluated with the software ImageJ for calculating the particle size distribution of gold NP [135].

3.4 Measurements with TAP reactor

The adsorption and desorption behavior of CO₂, CO, C₂H₄ and H₂ was tested over fresh and used (270 h on stream at 200 – 250 °C K using feeds containing CO₂, H₂ and C₂H₄) catalysts in a TAP-2 reactor (temporal analysis of products). This technique was developed by Gleaves *et al.* [136-137] in the 80s and later also described in detail elsewhere [138-140]. The analysis of gas phase components was carried out with a quadrupole mass spectrometer (HAL RC 301, Hiden Analytical) directly at the reactor outlet with 100 μ s resolution.

70 mg of catalyst sample were filled into the quartz reactor (i.d. = 6 mm, length = 40 mm) for each measurement. The catalyst bed was fixed within the isothermal zone of the reactor between two quartz particle (grain size = 250 – 350 μ m) layers. Fresh catalysts were treated in a flow of H₂ (3 mL·min⁻¹) and Ar (9 mL·min⁻¹) for 1 h at 250 °C prior to evacuation (10⁻⁵ Pa) and cooling to 200 °C. Used catalysts were only heated in vacuum (10⁻⁵ Pa) for 30 min at 200 °C before pulsing.

A 1:1 mixture of reactant and inert gas was used in the pulse experiments carried out at 200 °C. The pulse size N was adjusted to approximately 10¹⁵ Ar atoms, what should exclude intermolecular interactions in the gas phase (Knudsen diffusion). This guarantees that only interactions between reactants and catalyst surface are analyzed. Each pulse was repeated 10 times for each atomic mass unit to calculate an averaged pulse signal, to obtain a better signal to noise ratio.

Experimental data were transformed into dimensionless flow (f) and time (τ^*) in order to determine the type (reversible versus irreversible) of adsorption of H₂, CO, C₂H₄ or CO₂. In addition, the effect of the molecular weight of pulsed components on their diffusivity could be excluded [140].

$$\tau^* = \frac{t \cdot D_{Knudsen}^{eff}}{L^2} \quad 3.2$$

$$f = F \frac{L^2}{N \cdot D_{Knudsen}^{eff}} \quad 3.3$$

3.5 Catalytic tests

Activity and selectivity tests of the catalysts were carried out in an in-house developed setup named HECTOR (heterogeneous catalyst evaluator, Figure 7). Gas components were analyzed by on-line GC.

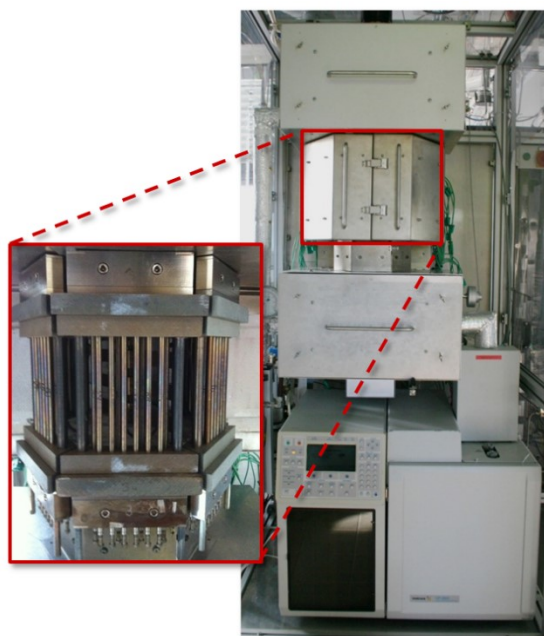


Figure 7. HECTOR reactor with on-line GC and the 50 parallel operated stainless steel fixed bed reactors framed in red.

directed to a GC, the rest was exhausted. The pressure in the system was adjusted by an electronic pressure controller (Brooks Instruments) at the common outlet for all reactors. Optionally, the mass flow in each reactor could be measured with a mass flow meter (Brooks Instruments). The GC measurements were performed in the beginning with a Varian instrument (CP-3800), later with an Agilent (7890B) device. Both were equipped with a HP-Plot Q column for the flame ionization detector (FID) and both HP-Plot Q and Molsieve 5A column for thermal conductivity detector (TCD). The detailed protocol and oven program is listed in the appendix (Table A. 2 – Table A. 5).

In every experiment, 300 mg of the catalyst were mixed with the same (in case SiO_2 -based catalysts) or threefold (in case of TiO_2 -based catalysts) amount of SiC ($> 450 \mu\text{m}$) and filled in the reactor. Then the samples were covered with a 1 cm thick layer of SiC to ensure plug flow and to preheat feed gases. In the beginning of the experiment, the pressure was raised under nitrogen flow (6.6 mL min^{-1} per reactor) to 20 bar in case of experiments with ethene and to 8 bars for the propene measurements. Some additional ethene measurements at 8 bar were also carried out for comparing with the propene data. After reaching the respective pressure and a temperature of 250°C , a mixture of $\text{CO}_2\text{:H}_2\text{:C}_2\text{H}_4/\text{C}_3\text{H}_6\text{:N}_2$ with a ratio of 4:2:1:1 was admitted to the samples. Feeds with a composition of $\text{CO}_2\text{:H}_2\text{:C}_2\text{H}_4/\text{C}_3\text{H}_6\text{:N}_2 = 1:1:1:1$; 1:2:4:1 and 1:3:3:1 were also tested. Temperatures from 175°C to 275°C and flow

Alcohol formation from CO_2 , H_2 and olefins with gold catalysts: Digital mass flow controllers (Brooks Instruments) dosed the preset amount of CO_2 , H_2 , $\text{C}_2\text{H}_4/\text{C}_3\text{H}_6$ and N_2 . In the upper chamber of the reactor, the gases were preheated and the total flow was equally distributed between 50 fixed-bed tubular reactors (inner diameter of 4 mm). Each reactor is equipped with an inert spring that holds a mesh serving as a holder for catalyst particles ($250 - 450 \mu\text{m}$). The mesh was positioned so that the catalyst bed stayed in the isothermal zone. The reactors were then put together in five blocks, each consisting of ten reactors. An additional external reactor served as bypass. In the lower chamber, multiport valves selected one of the product gas flows, which was

rates from 6.6 to 26.4 mL min⁻¹ were additionally included, which results in modified contact times of 11 to 45 g min L⁻¹. The data acquisition contained three GC measurements for every sample and condition, which were later averaged.

CO₂ hydrogenation with rhodium catalysts: Generally, the same reactor setup was used for these experiments, but instead of stainless steel reactors, quartz reactors were used. 50 mg of the catalyst (particle size = 315–710 μm) mixed with 125 mg of inert SiC were filled into each reactor and covered with circa 2 cm of the inert material. In the beginning the reactors were heated under nitrogen flow (18 mL min⁻¹ per reactor) up to 400 °C for activation. Then the catalytic test was performed at ambient pressure starting with T = 250 °C, then 300 °C and 350 °C with feed of CO₂:H₂:N₂ = 1:1:3 (30 mL min⁻¹ per reactor). After a complete test cycle, the catalysts underwent a high-temperature treatment with the same gas mixture of CO₂ and H₂ at 750 °C. Subsequently, the same test procedure from 250 to 350 °C was repeated.

Procedure for evaluation of catalytic tests: Yields Y of the respective products k were calculated with respect to the original molecule (*e.g.* CO from CO₂, propanol and propanal from CO₂ and C₂H₄). By considering the stoichiometric factors (v_i and v_k) Y can be calculated following equation 3.4.

$$Y(k, i) = \frac{\dot{n}_k - \dot{n}_{k,0}}{\dot{n}_{i,0}} \cdot \frac{v_i}{v_k} \cdot 100\% \quad 3.4$$

With \dot{n}_k and \dot{n}_i being molar flows of products and reactants, respectively. Index 0 describes the feed concentration at reactor inlet. By summing up the yields $Y(k, i)$ of all products, conversion of reactant i can be calculated following equation 3.5.

$$X(i) = \sum_k Y(k, i) \quad 3.5$$

The selectivity was derived from equation 3.6.

$$S(k, i) = \frac{Y(k, i)}{X(i)} \cdot 100\% \quad 3.6$$

Two different selectivities exist for the studied alcohol formation reactions, one relating to CO₂ and one relating to C₂H₄ or C₃H₆, respectively.

3.6 In situ and operando studies

The interaction of reactants or probe molecules with the surface of the catalyst was studied with different FTIR spectroscopic techniques, which are described in the following section. Theoretical aspects of the methods and probable adsorbates were already discussed in Chapter 2.4.

3.6.1 Low-temperature CO adsorption

The adsorption of CO and simultaneous recording of FTIR spectra is a widely used method to characterize surfaces, to determine the state of supported metals as well as acid and basic sites [117, 141]. Since the surface complexes formed upon CO adsorption are very unstable, it is common to use low temperatures for the experiment. Depending on the influence of the adsorption site on the binding of the CO molecule, the IR band shifts to wavenumbers, which differ from the frequency of gaseous CO at 2143 cm^{-1} .

For the experiment, 50 mg of the sample were pressed into a self-supporting disc with a diameter of 20 mm and placed in the reaction cell (see Figure 8), which was enclosed by a cooling jacket (Specac). The performed CO adsorption experiments can be divided into three groups concerning the pre-treatment. The total gas flow was always 20 mL min^{-1} :

- i) pre-treatment in inert gas (He, $200\text{ }^{\circ}\text{C}$, 30 min, 1 bar)
- ii) gas mixture of 10 vol % CO_2 +10 vol % H_2 +He ($250\text{ }^{\circ}\text{C}$, 60 min, 1 bar) and
- iii) external pre-treatment with 10 vol % CO_2 +10 vol % H_2 + N_2 ($250\text{ }^{\circ}\text{C}$, 60 min, 10 bar).

In case of the external pre-treatment, which was carried out in the high pressure cell from ISRI (Chapter 3.6.3), an extra heating ($200\text{ }^{\circ}\text{C}$, He) was performed after transfer of the sample. Then generally after the respective pre-treatment, the sample was cooled down to $55\text{ }^{\circ}\text{C}$. Evacuation of the cell jacket was performed at that point to avoid water condensation. The cell was then cooled down to $-160\text{ }^{\circ}\text{C}$ with liquid nitrogen. After five pulses of CO (5 vol % in He), the cell was evacuated. Finally, the desorption process was monitored as the cell was slowly heated to RT again under vacuum. FTIR measurements were carried out by a Nicolet iS10 (Thermo Scientific).

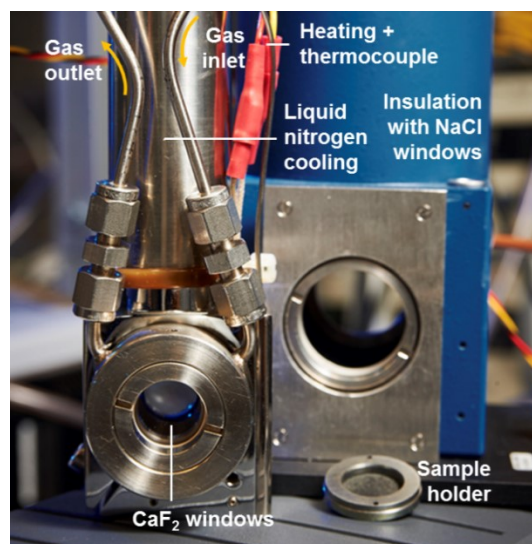


Figure 8. FTIR cell for low-temperature CO adsorption.

3.6.2 *Operando* DRIFTS/MS study: determination of adsorbates reactivity in CO₂ hydrogenation with ¹³CO₂ over rhodium catalysts

As already mentioned in chapter 2.4.2, isotopic labelling experiments can offer detailed insights into reaction mechanism, when adsorbates reactivity is monitored with FTIR spectroscopy and product formation with MS. The experiments were performed using a Nicolet 6700 (Thermo Scientific), which was equipped with a MCT detector, a mirror system (Praying Mantis™, Harrick) accessory as well as a high temperature DRIFT cell with CaF₂ windows (Harrick), as depicted in Figure 9. The outlet was connected to the MS (OmniStar with Prisma Plus™, Pfeiffer Vacuum GmbH), which consists of a filament (Y₂O₃/Ir) as electron collision ionizer, a quadrupole mass analyzer and a Faraday cup as detector. The signals were detected as ion current in dependence of time. To reduce background signals, FTIR measurements with KBr in helium flow at the utilized temperatures were carried out prior to the catalyst measurements.

The catalyst particles (315–710 μm) were filled into the DRIFTS cell, which practically acts as a heatable fixed-bed flow reactor, where the gas flows from below the sample through the particle bed. After pre-treatment in He at 400 °C for 30 min, the samples were cooled down to the initial reaction temperature of 250 °C under He flow. During the cooling process, base spectra were recorded, which were later subtracted for clearer baseline. Then the reaction gas mixture was admitted to the sample (20 vol % CO₂ + 20 vol % H₂ + 5 vol % Ar + 55 vol % He) in a total gas flow of 30 mL min⁻¹. The Ar signal was used as internal standard for MS analytics. The temperature was raised sequentially up to 350 °C under this gas stream.

This unlabeled feed was used to reach steady state [129]. By means of a fast switching four-way valve (Vici, Valco Instruments), the normal feed was then exchanged by the labelled feed containing ¹³CO₂ instead of ¹²CO₂. The remaining gases were constantly flowing, maintaining the flow rate of 30 mL min⁻¹. During the whole time, MS signals ($m/z = 15, 17, 28, 29, 44$, and 45) were recorded and later normalized with the Ar signal. The CO signal ($m/z = 28$) was corrected with respect to the fragmentation of CO₂, which was determined in separate experiments.

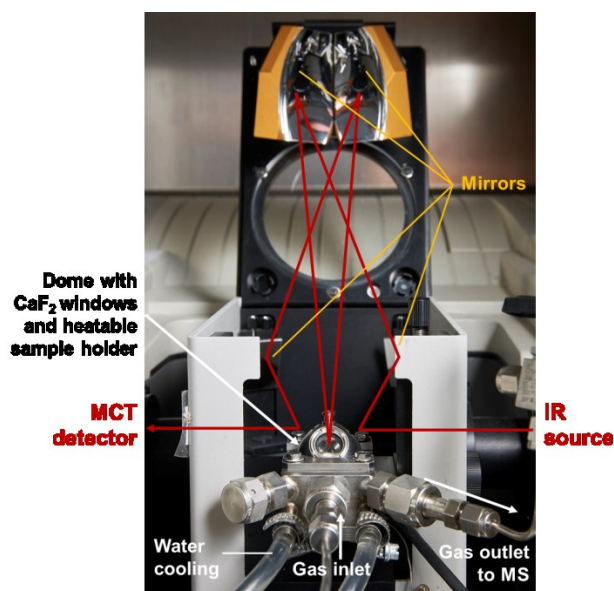


Figure 9. DRIFTS cell with Praying mantis™ accessory and beam path (red lines), implemented in a Nicolet 6700 FTIR spectrometer, the upper lid is closed during the experiment.

3.6.3 High pressure FTIR spectroscopic experiments with gold catalysts in transmission mode

Because the alcohol formation from carbon dioxide, hydrogen and olefins was carried out at pressures up to 20 bar in the catalytic tests, also *in situ* FTIR spectroscopic studies were reasonably done at elevated pressures. The cell equipment from ISRI (In-situ Research Instruments, Figure 10/Figure 11) was not constructed for experiments at more than 15 bar [142], but a sufficient tightness was given at 10 bar, so the *in situ* experiments were performed at this highest possible pressure.

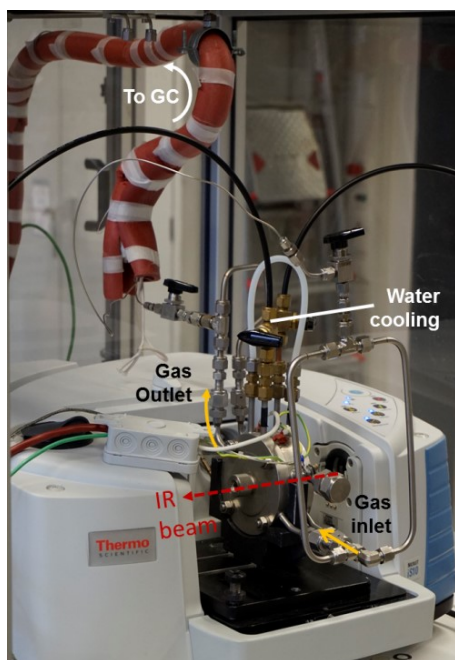


Figure 10. High pressure *in situ* FTIR cell (ISRI) in Nicolet iS10TM spectrometer, connected with HECTOR reactor for gas supply and GC analysis, the gas outlet was heated during operando experiments.

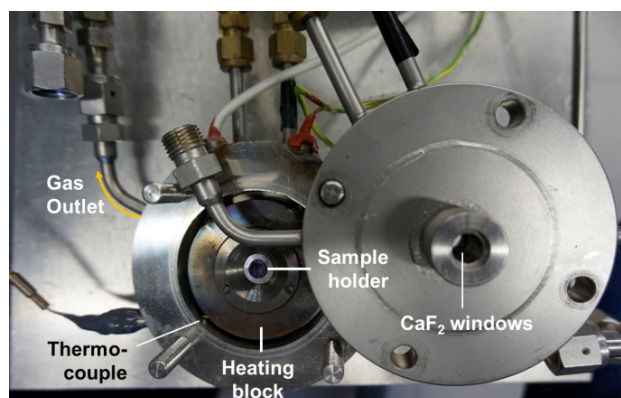


Figure 11. Open high pressure *in situ* FTIR cell (ISRI) with sample inside.

The FTIR spectroscopic experiments were carried out under real flow conditions, so that a comparison with reactor data is possible. Beside studies with complete feed ($\text{CO}_2 + \text{H}_2 + \text{C}_2\text{H}_4/\text{C}_3\text{H}_6 + \text{N}_2$), also CO_2 and ethene/propene adsorption or respective reactions with hydrogen were evaluated. Experiments with propene were performed at 8 bar as before in the catalytic tests. For studying the activation effect, also long time tests were executed with over-night activation at 250 °C ($\text{CO}_2:\text{H}_2:\text{C}_2\text{H}_4/\text{C}_3\text{H}_6:\text{N}_2 = 4:2:1:1$) and subsequent normal reaction feed of 1:1:1:1 composition at 200 °C. During those experiments, the gas outlet was analysed by GC (method was the same as in the catalytic tests).

Generally, 50 mg of the sample were pressed into a wafer (diameter = 20 mm) and placed in the stainless-steel cell. The heating block of the cell directly surrounds the sample holder and is equipped with a thermocouple, which measures the temperature at the sample (see Figure 11).

The educt gas stream is admitted to the sample wafer from both sites and leaves the cell at the opposite. The outlet was heated during the experiments to avoid condensation in the lines. In principal, both inlet and outlet were connected to the HECTOR reactor system, which supplied the gases, monitored and adjusted the pressure. The IR cell connection was installed at one valve in the lower part of HECTOR, which selects the gas streams for the GC analysis. The educt gases passed an empty reactor and flowed through the IR cell, like an extension of the reactor line.

In every case, background spectra were recorded without the cell and sample in the IR beam. Then the untreated sample was measured. The catalysts were always pre-treated at 250 °C in nitrogen flow for at least 30 min. Generally, the gas flow was 6.6 ml min⁻¹. Then the pressure was raised under nitrogen flow to 10 bar (C₂H₄) or 8 bar (C₃H₆). After reaching the pressure, the nitrogen stream was exchanged by a 10 vol % H₂ + N₂ flow, which reduced the catalyst for 60 min at 250 °C. After the pre-treatment, a mixture of CO₂ and H₂, each with 10 vol %, plus nitrogen, was filled into the cell and FTIR spectra were taken at 10, 30 and 60 min at 250 °C. Then the cell was cooled down to 200 °C and a feed of CO₂:H₂:C₂H₄/C₃H₆ = 1:1:1 (each 10 vol % + N₂) was passed into it. At the end of each experiment, the cell was flushed with nitrogen while the pressure was lowered to 1 bar again. And finally, the last spectrum was taken when temperature reached RT again.

For the long time activation tests, there was no reductive pre-treatment with hydrogen, but directly exposure to the activation feed (CO₂:H₂:C₂H₄/C₃H₆:N₂ = 4:2:1:1), which was used in the catalytic test. Additional experiments without pressure rising were also carried out.

4 Results and Discussion

4.1 Rhodium catalysts for CO₂ hydrogenation

4.1.1 Catalyst preparation and characterization

Rhodium was chosen as active metal, due to its high hydrogenation ability and activity in RWGS reaction [55, 143-144]. For reducing the price of possible catalysts, alternative noble metals should be tested. For this reason, nickel was added to the catalyst and its effect on catalysts performance and formation of intermediates has been evaluated. The potential ability of potassium to drive selectivity from CO₂ to CO was already discussed in the introduction (see chapter 2.2).

The contents of rhodium, potassium and nickel of the prepared catalysts were characterized by ICP-OES and the surface area was analyzed by nitrogen adsorption (BET method). Results are presented in Table 4. Additional TEM measurements (Figure A. 1, appendix) revealed that the rhodium is homogeneously and atomically distributed over the surface, only small agglomerates were formed after usage (Figure A. 2). This was also confirmed by powder XRD by which crystalline rhodium phases could not be detected. This indicates that the rhodium particles are too small to give sharp reflections, according to Scherrers Equation (Eq. 3.1).

Table 4. Rh, Ni, and K contents and surface area of alumina supported rhodium catalysts for CO₂ hydrogenation.

Catalyst	Rh / wt %	K / wt %	Ni / wt %	S _{BET} / m ² g ⁻¹
Rh/A	0.45	–	–	141
Rh,K/A	0.40	1.47	–	139
Rh,Ni/A	0.34	–	2.30	117
Rh,K,Ni/A	0.50	2.07	3.10	134

In principal, the preparation method was suitable to produce catalysts with small rhodium particles, which are said to be helpful for CO rather than methane formation, since hydrogen and CO do not have enough space to co-exist together on the Rh particle [55]. The position of potassium could not be determined by TEM since the contrast, which is directly related to the mass of the analyzed atom, is too low [145]. Nickel was sometimes described to be incorporated as Ni²⁺ into the alumina lattice, when the calcination temperature was higher than 500 °C, which was also reached in the preparation of the Rh catalysts with Ni. Thus, special surface compounds can be formed, like spinel type NiAl₂O₄ [146-149]. The Ni position on the surface could be detected by using EDX mapping technique. With this method, discrimination between Rh and Ni, which is difficult by only evaluating the contrast of the particles, is possible (Figure A. 2). The formation of agglomerates, which consist of both Rh and Ni indicates the existence of alloy like compounds or at least an intimate contact between these

metals, which should also directly influence the redox behavior of the catalyst [149-150]. Compared to pure supported nickel catalysts, the prepared samples with rhodium and nickel are reducible at lower temperatures, since the rhodium facilitates nickel reduction by activating the hydrogen [147].

4.1.2 Catalytic activity of modified rhodium catalysts

The catalytic test data of the supported rhodium catalysts in CO₂ hydrogenation at 350 °C is displayed in Figure 12. Conversion of CO₂ is generally lower than 14%, where Rh/A showed the highest conversion before (11%) and Rh,Ni/A the highest after the high temperature treatment (12%). The yield of CO or CH₄ is very different depending on the catalyst. Only the double-modified catalyst Rh,K,Ni/A is more selective for CO formation, all others produce mostly methane or roughly equal amounts of CO and CH₄.

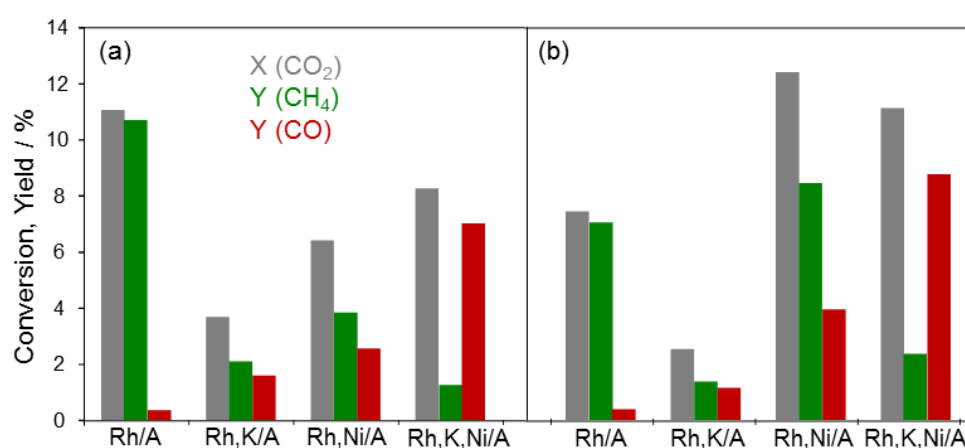


Figure 12. Yields of CO/CH₄ and CO₂ conversion at 350 °C before (a) and after (b) high-temperature treatment (750 °C), reaction conditions: $p = 1$ bar, $\tau = 1.67$ g_{cat}·min·L⁻¹, CO₂:H₂:N₂ = 1:1:3.

The high-temperature treatment at 750 °C led to an enhanced activity for all Ni containing catalysts, which can be seen in Figure 12,b. The reason for this behaviour is most probably the deeper reduction of the surface Ni-species, which might be NiAl₂O₄ [149]. The reducibility of the samples was further investigated by temperature programmed reduction with hydrogen in a separate experiment. The resulting profiles are displayed in Figure A. 7. Those catalysts, that contained nickel, started to consume hydrogen at temperatures higher than 700°C, which is consistent with the finding, that those catalysts obtain higher conversion after the high-temperature treatment at 750 °C, since Ni is then, at least partially, reduced. This resulted also in a distinctly higher yield of methane for the Rh,Ni/A catalyst. This is not a surprising result, since Ni is well known for its superior methanation ability [56-57]. In combination with Rh, which readily activates hydrogen, methanation is further promoted. This is underlined by the fact that these experiments are not carried out under excess of hydrogen or even in stoichiometric ratio. Nevertheless, the Rh,K,Ni/A catalysts is still selective in CO formation after this high-temperature treatment. Its higher CO₂ conversion compared

to the results displayed in Figure 12, a demonstrates the stability of this catalysts and underlines its peculiar different behaviour, compared to the other samples.

During the high-temperature treatment at 750 °C, conversion of CO₂ was ~50% for all catalyst (not shown here), which correlates with equilibrium conversion. According to this and thermodynamic constrains (see Figure 4), CO selectivity was nearly 100% over all samples under those conditions. Additional experimental results, reflecting the temperature dependent behaviour of the catalysts are shown in Figure A. 3 to Figure A. 5. These data result from measurements before the high-temperature treatment and show that the activity of all catalysts at 250 °C is negligible and best conversion and also yields are obtained at 350 °C. This can be well understood by consulting the thermodynamic data in Figure 4.

A comparison of activity data with literature is difficult, because either catalyst composition or reaction conditions are differing from our data and are principally very diverse [49]. Beuls *et al.* [151] studied low-temperature CO₂ hydrogenation over 1 wt % Rh/ γ -Al₂O₃ catalyst and obtained a conversion of about 25% at ambient pressure and 25 °C. While working with excess hydrogen and pre-reduced catalysts, methane selectivity was 100% in those experiments. By using a feed mixture of CO₂:H₂ = 1:4 testing of 2 wt % Rh/ γ -Al₂O₃, the same group found a CO₂ conversion of 6.2 % at 200 °C [152]. The results for the present study are comparable. However, it should be noted, our focus was on mechanistic understanding of the reaction and not on the optimization of the catalysts performance.

However, a really surprising result was the high CO yield of the Rh,K,Ni/A catalyst, by simultaneous low methane yield. Although some other groups reported on such effect of alkali promoters, [60-61, 77, 153] this influence could not be expected, when Ni is also present, because Ni is predominantly known for its activity in methanation [74, 144]. For example over catalysts with Ni supported on silica or ceria-zirconia oxide obtained a maximum CO selectivity of 14.5 % at 350 °C was obtained [74]. The prepared Rh,K,Ni/A catalysts exhibits an obviously higher CO selectivity. The following chapters address the elucidation of reasons for this behaviour, which were extensively studied by *in situ* DRIFTS experiments combined with isotopic labelling techniques.

4.1.3 *In situ* DRIFTS analysis of CO₂ hydrogenation

For gaining mechanistic insight into the hydrogenation of CO₂ over the monometallic and modified rhodium catalysts, *in situ* FTIR experiments were carried out. The particular catalysts were exposed to a 1:1 mixture of 20% CO₂ and 20% H₂, which was diluted with He. The recorded spectra after 30 min reaction are presented in Figure 13 for temperatures of 250 and 350 °C, respectively.

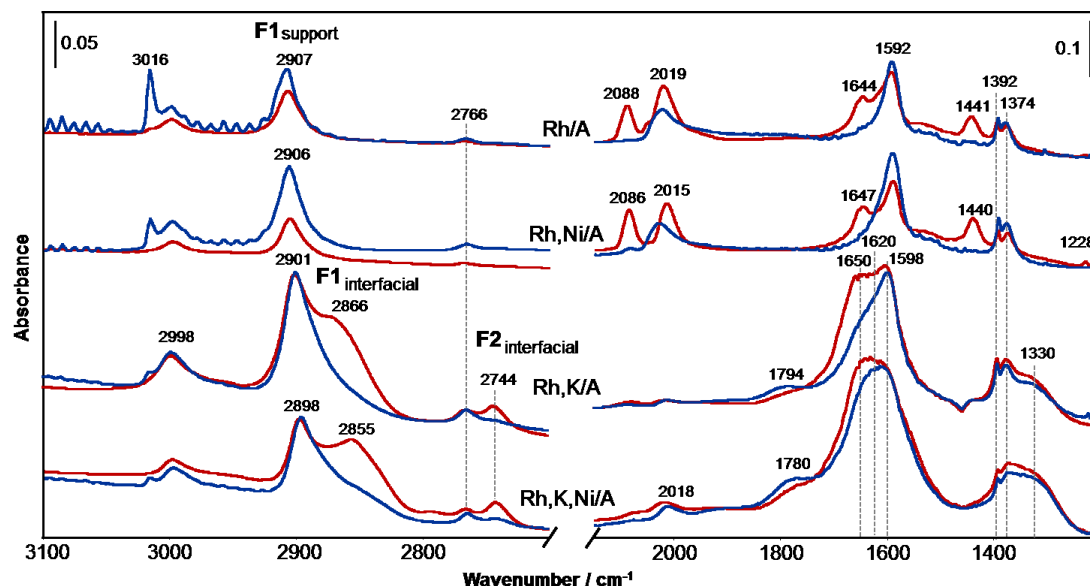
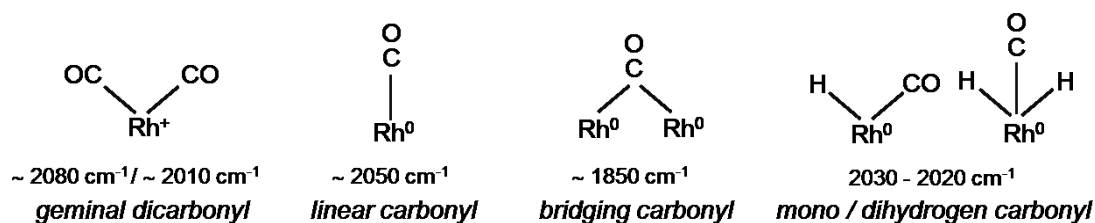


Figure 13. *In situ* DRIFTS spectra of different rhodium/alumina catalysts (pre-treated in He at 400 °C) after 30 min admission of the hydrogenation feed (CO₂:H₂:He=1:1:3) at 250 °C (red) and 350 °C (blue).

In the higher wavenumber region (3100–2800 cm⁻¹) CH-stretching bands (ν C–H) appear. The very characteristic band at 3016 cm⁻¹ with rotational bands on both sides, stems from gaseous methane formed during the reaction [124]. The bands between 2998 and 2744 cm⁻¹ result from different adsorbed formate species (ν C–H) [117, 120]. In the region around 2088–2015 cm⁻¹ typically Rh carbonyl bands can be detected (see Scheme 4) [154-155], and O–C–O stretching bands from adsorbed carbonate and formate species are observable from 1650 to 1200 cm⁻¹ (see Table 1) [120].



Scheme 4. Surface Rh carbonyl species on Rh/A and their characteristic IR absorption bands [154].

Obviously, there are distinct differences between the spectra of catalysts with and without K. On Rh/A and Rh,Ni/A a certain amount of methane is formed at 350 °C and Rh carbonyl bands are clearly observable. Potassium containing catalysts show only small bands arising from these species. In general, the spectra recorded at 250 °C are different from those taken at 350 °C. This is especially visible for Rh carbonyl bands of Rh/A and Rh,Ni/A. Both exhibit bands of geminal dicarbonyl species $\text{Rh}^+-(\text{CO})_2$ at 250 °C ($\sim 2088/\sim 2019 \text{ cm}^{-1}$), but linear carbonyl Rh^0-CO bands at 350 °C ($\sim 2020 \text{ cm}^{-1}$). Furthermore, bands of hydrogen carbonate species (1647/1644, 1441/1440 and 1228 cm^{-1}) [120] are only detectable at 250 °C.

The spectra of K-containing catalysts display broad intensive bands at 1620 and 1330 cm^{-1} which are characteristic for adsorbed bidentate carbonate species. Those adsorbates are relatively stable also at 350 °C. In contrast to Rh/A and Rh,Ni/A catalysts, Rh carbonyl bands have only very low intensity on the K-containing catalysts. On the other hand, bands at 2866/2855, 2744, and 1650 cm^{-1} are seen at 250 °C in addition to the bands at 2998, 2901/2898, 1598, 1392, and 1374 cm^{-1} , which are observable at both 250 and 350 °C. These latter bands stem probably from stable formates, which are adsorbed on the alumina support [82, 156]. The other bands, which are only visible at 250 °C are presumably also assignable to formates, but at another location on the surface. Since potassium is present on the catalyst, it seems likely that also potassium formate is existing, which should give rise to bands at 2833, 1590, and $1385/1350 \text{ cm}^{-1}$ [156]. However, it is also conceivable that some formates are located at the vicinity of potassium and alumina, which would be in accordance with the shift of the bands compared to the pure potassium formate bands. Such an influence of alkali promotion on formate adsorption has been reported in high-pressure CO₂ hydrogenation over modified Cu/Al₂O₃ catalysts [157]. Moreover, chelating formates were found upon CO adsorption on potassium modified alumina, with bands at 2777–2682, 1600–1595, 1370–1360, and $1355\text{--}1350 \text{ cm}^{-1}$ [82]. These formates form bridges between K⁺ and the alumina support (see Table 1).

Taking these findings into account, we assume that two formate species are formed: (i) formates adsorbed on pure alumina support (F1) and (ii) formates adsorbed on the support but interacting with the neighboring K (F2). The latter ones seem to be more labile or reactive, since they are not visible after flushing with He, which was performed after hydrogenation reaction at 250 °C and also not at higher temperatures. The spectra of alkali containing catalysts show another characteristic band in the C=O stretching region located at 1794 or 1780 cm^{-1} , respectively. This not very intensive band was already assigned to unstable formyl species (HCO) observed at Ru/Al₂O₃ catalysts in methanation of CO and CO₂ [124].

By inspecting the Rh carbonyl band changes with temperature in Figure A. 6, it is obvious that Rh particles on the catalysts were reduced with increasing temperature and time on stream. This is indicated by transformation of the prominent two bands of Rh^+ geminal dicarbonyl (~ 2088 and 2019 cm^{-1}), which are present at 250 °C into linear carbonyl band at around 2020 cm^{-1} at higher temperatures [154, 158]. Such Rh carbonyl bands were observed on K-containing catalysts already at lower temperatures. Nevertheless, the Rh^0-CO bands are mostly shifted to lower wavenumbers. Normally those linear carbonyls appear at around

2050 cm^{-1} (see Scheme 4) [143]. This shift indicates a weakened bonding of the adsorbed CO. Considering that under CO_2 hydrogenation conditions, hydrogen atoms are occupying the surface of Rh particles, which hinders normal linear CO adsorption, it is probable that H and CO are adsorbed at the same Rh sites, forming Rh^0 mono or dihydrogen carbonyls. The chemisorbed hydrogen is electron donating and thus, Rh π backdonation into the antibonding orbital of the CO lowers its bond order, which results in a decreased IR frequency according to equation 2.6 [84]. Moreover, the distinctly lower intensity of Rh carbonyl bands for Rh,K/A and Rh,K,Ni/A is associated with a low coverage of CO and leads to the conclusion that the carbonyls are less stable than on the catalysts without alkali metal.

Evaluation of CO_2 hydrogenation by stepwise feeding of reactants

For studying the role and reactivity of carbonate species on the catalysts in CO_2 hydrogenation, transient experiments were carried out. Therefore, the catalysts and also the pure alumina support were pre-treated in CO_2 (20%)/He at 300 °C and subsequently exposed to a reductive mixture of H_2 (20%)/He at the same temperature. The respective spectra for the four catalysts and also the support are depicted in Figure 14. After 30 min CO_2 adsorption, characteristic bands of adsorbed hydrogen carbonate (1647/1440/1228 cm^{-1}), which is formed on hydroxyl groups of the support, and also monodentate carbonate (1527 cm^{-1}) can be monitored on the support, as well as on Rh/A, and Rh,Ni/A (Figure 14a) [120]. The other spectra of catalysts with alkali metal are dominated by broad bands of bidentate and monodentate carbonate species. As expected, dissociative adsorption of CO_2 did not proceed under these conditions. However, shortly after switching to the reductive feed (H_2 /He), the evolution of Rh carbonyl bands at 2072-2088/2007-2015 cm^{-1} could immediately be observed (Figure 14b). Apparently, methane formation (3016 cm^{-1}) was further detected for Rh/A and Rh,K/A, and also on Rh,Ni/A, but less pronounced.

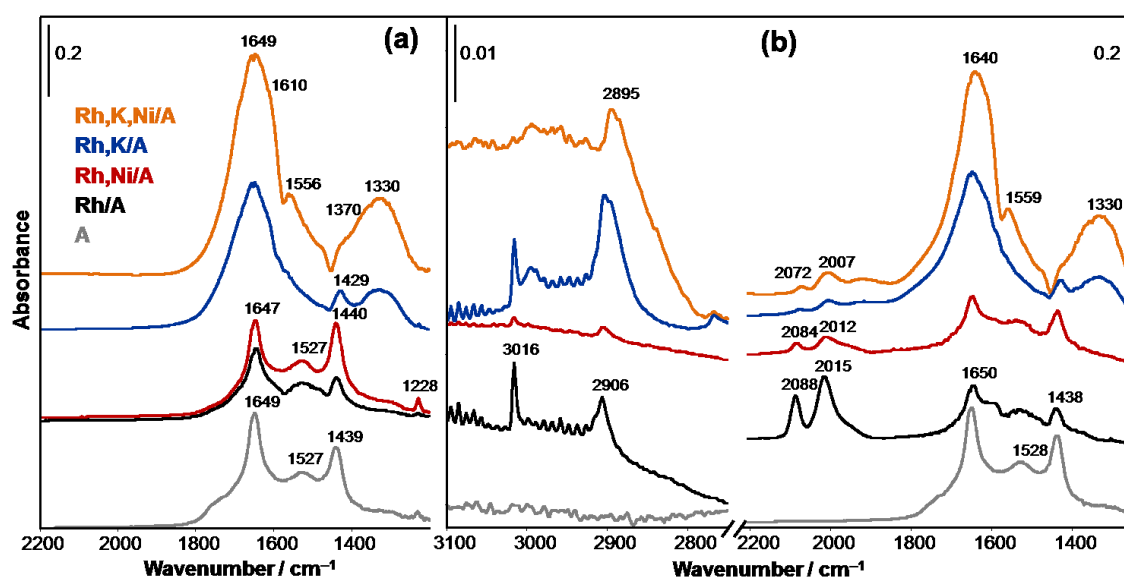


Figure 14. *In situ* DRIFT spectra of different Rh catalysts and pure alumina support recorded at 300 °C after 30 min exposure to 20 vol % CO_2 /He (a) and subsequent short (1 min) admission of 20 vol % H_2 /He (b).

The emergence of a band around 2900 cm⁻¹ on all Rh-containing samples indicates formate formation [73]. Since the intensity of hydrogen carbonate and carbonate bands decrease simultaneously, it has to be assumed, that formates and CO are formed from these adsorbed species upon exposure to the reductive feed.

As already reported [143, 152, 159] Rh activates dihydrogen and enables its dissociative adsorption. Therefore, hydrogen activated by Rh particles can spill over to the neighboring acceptor site on the support, where the already adsorbed hydrogen carbonate species can react with it. Hence, the emerging formates (F1) are mainly situated on the support.

Concluding these findings, *in situ* DRIFTS studies showed that the modification of the alumina supported Rh catalysts altered the adsorption of CO₂ and indicated that also the reaction pathway of CO₂ hydrogenation is changed. CO₂ is adsorbed as hydrogen carbonate on the OH-groups of alumina on Rh/A and Rh,Ni/A catalysts. These hydrogen carbonates are not stable upon heating or exposure to hydrogen, by which they are transformed into monodentate carbonates. Simultaneously, not alkali modified catalysts showed higher carbonyl band intensities, mainly at oxidized Rh particles. Furthermore, support bound formates were found, which are most probably not reactive. On the other hand, modification of the Rh catalysts with potassium hindered the formation of hydrogen carbonates, which is caused by the covering of the hydroxyl groups by K. Instead, mono- and bidentate carbonates were formed. Moreover, carbonyl bands were found to be less intensive on the K modified samples and revealed that the Rh particles are mostly in reduced state. The adsorption of CO was evidenced to be less strong on the samples with alkali metal, which might be the reason for lower methanation activity. The most obvious difference between catalysts modified with K and Rh/A and Rh,Ni/A is the presence of different formate species, which are located on different places on the catalyst surface and named here F1 and F2. Their specific reactivity was examined in further experiments and is described in the next section.

4.1.4 *Operando* DRIFTS/MS study: determination of adsorbates reactivity in CO₂ hydrogenation over rhodium catalysts with isotopic transient technique

From the above described experiments, we know that in CO₂ hydrogenation some formates (F1) are formed through reduction of hydrogen carbonates, which are located preferentially on the alumina support. However, the reactivity of the different formates type F1 and F2, which are most probably present on the alkali-support interface, was not clear. To unravel formate reactivity and their role in the reaction, further experiments with transient methods using isotopically labelled CO₂ were carried out. The idea behind that technique is to monitor the relative exchange rates of different surface species and hence their reactivity by applying IR spectroscopy and mass spectrometry, since the frequency of a band is directly correlated to the reduced mass of the vibrating molecule. Bands from reactive molecules change faster than those of unreactive species, which are also named spectator species. The theoretical basics are described in Chapter 2.4.2 and elsewhere [125-126].

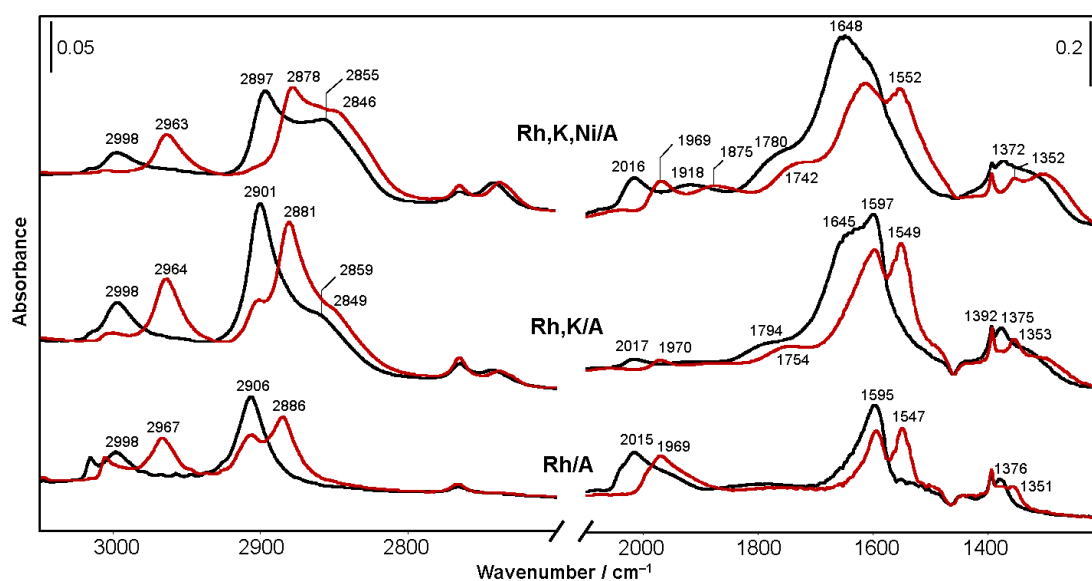


Figure 15. *In situ* DRIFTS spectra of selected Rh catalysts after 30 min exposure to $^{12}\text{CO}_2/\text{H}_2/\text{He}$ (black) and $^{13}\text{CO}_2/\text{H}_2/\text{He}$ (red) at 300 °C.

For this purpose, the Rh catalysts were exposed to the normal gas mixture of $^{12}\text{CO}_2/\text{H}_2/\text{He}$ at 300 °C and after reaching steady-state, the feed was switched to the isotopically labelled $^{13}\text{CO}_2/\text{H}_2/\text{He}$ mixture. To follow the possibly fast changes, FTIR spectra were recorded in short intervals and evolving gases were monitored directly by MS. From Figure 15 it is evidenced that all bands of C-containing species shift to lower wavenumbers after 30 min of exposure to the labelled feed due to the replacement of ^{12}C by ^{13}C in the adsorbed species. This means that all surface species are involved somehow in the reaction. However, to discriminate between main intermediates and spectator species, the exchange rates of surface and gas-phase species have to be determined. The time-dependent changes are therefore displayed in Figure A. 8 and the intensities of the respective bands of the surface species were measured and plotted exemplarily for Rh/A and Rh,K,Ni/A in Figure 16. It is obvious that the exchange of Rh- ^{12}CO /Rh- ^{13}CO bands (2016/1969 cm^{-1}) is very fast and complete after 2 min. Also the formyl bands as shown in Figure 15 (1780/1742 cm^{-1} and 1794/1754 cm^{-1}) are quickly exchanged.

Compared to this fast exchange, the behavior of formates is different, which can be seen in Figure 16. There, formate bands at 2910–2850 cm^{-1} were selected for calculation of the band intensity, because the bands in the O–C–O region stretching region are overlapping with carbonate bands, which makes the assignment difficult. While the ^{12}C -containing formates on Rh,K,Ni/A are exchanged very fast after switching to the labelled feed, those on Rh/A are only slowly and not completely replaced by their isotopomers. Simultaneous MS measurements revealed that ^{13}CO is immediately formed over Rh,K,Ni/A, which could not be observed over Rh/A. Instead, $^{13}\text{CH}_4$ was detected promptly and also constantly (Figure 17) on Rh/A, which is in agreement with catalytic testing results (Figure 12).

By evaluating the time-dependent changes in the spectra and the MS data in Figure 17, it seems, that over Rh,K,Ni/A ¹³CO formation proceeds at a time scale similar to the disappearance of ¹²C-containing formates, suggesting that formates are potential intermediates in CO formation. In contrast, the time formates need for the exchange on Rh/A is longer than the ¹³CH₄ evolution takes (MS data). On the other hand, the replacement of Rh-¹²CO by its isotopomer proceeds in a similar time scale like methane formation. These findings suggest that carbonyls are main intermediates in CH₄ formation and not formates. Moreover, the already mentioned fast exchange of formyl bands (1780/1742 cm⁻¹) observed on Rh,K,Ni/A also correlates with the rate of ¹³CO formation measured with MS. Hence, formyl species has to be assumed to be main reaction intermediates.

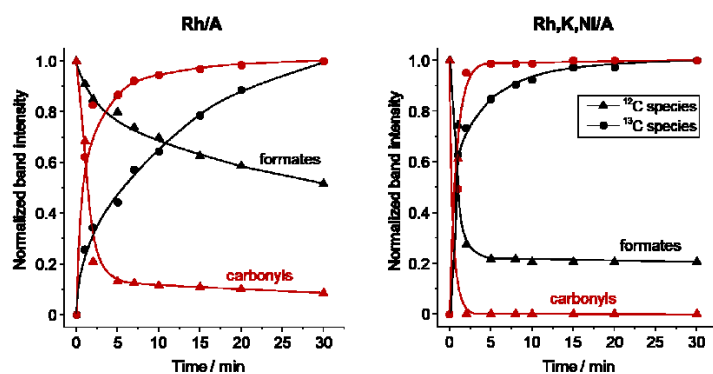


Figure 16. Time-dependent normalized band intensities of ¹²C-containing and ¹³C-containing Rh carbonyl and formate species recorded on Rh/A and Rh,K,Ni/A catalysts at 300 °C after switching from ¹²CO₂/H₂/He = 1/1/3 to the respective ¹³CO₂/H₂/He feed.

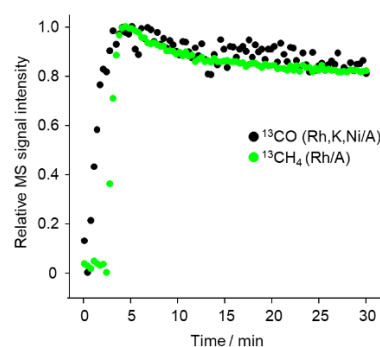
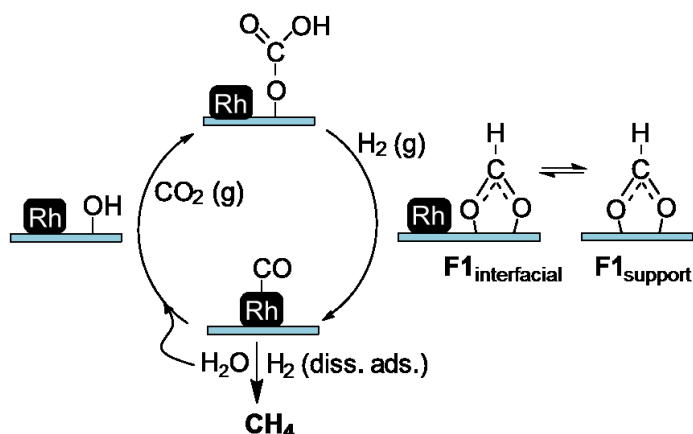


Figure 17. Online-MS signals of product formation over Rh/A and Rh,K,Ni/A after switching from ¹²CO₂/H₂/He to ¹³CO₂/H₂/He at 300°C, corresponding data to IR spectra in Figure A. 8.

4.1.5 Proposed reaction mechanism for CO₂ hydrogenation over different supported Rh catalyst, modified with K and Ni

From the different experiments the following assumptions can be drawn concerning the possible reaction mechanism of CO₂ hydrogenation over modified Rh catalysts. During CO₂ adsorption in the absence of hydrogen, no dissociative adsorption was observed, instead hydrogencarbonates and monodentate carbonates were formed on Rh/A and Rh,Ni/A as well as on the pure alumina support (Figure 14). On Rh,K/A and Rh,K,Ni/A, additional bands of bidentate carbonates and monodentate carbonates species were found. Upon subsequent hydrogen admission after CO₂ adsorption, the evolution of methane, Rh carbonyl bands and formate bands was detected, but only when Rh was present. This suggests that Rh is necessary for dissociative hydrogen adsorption and thus, activation, while the support and the K and Ni modified support are responsible for CO₂ fixation. The following steps in Scheme 5 represent the reaction of the activated hydrogen with the already present hydrogen carbonates, forming formates (F1) on the support and adsorbed CO on the Rh particles.



Scheme 5. Identified species and proposed reaction mechanism for CO₂ hydrogenation over Rh/A and Rh,Ni/A.

eter, the formates of type F1_{interfacial} can migrate away from the active sites and are then stably adsorbed as formates type F1_{support} as detected by DRIFTS (Figure 15). The other minor pathway is, that CO is formed, which can be subsequently hydrogenated on the Rh particle to methane.

In case of K-containing catalysts, DRIFTS experiments in complete hydrogenation feed (CO₂:H₂:He = 1:1:3) revealed that beside the F1 type formates, also another group of formates (F2) could be detected (Figure 13). These F2 formates were not present in any case on the Rh/A and Rh,Ni/A catalysts. These formates are not as stable as F1 formates, since they vanish during He flushing after reaction, also at 250 °C. This implies a possibly higher reactivity of F2 formates compared to F1 formates, which seem rather inactive.

Potassium also influences the Rh carbonyl formation. This was demonstrated in experiments under hydrogenation feed (Figure A. 6). While geminal dicarbonyl Rh⁺-(CO)₂ species are present on Rh/A and Rh,Ni/A at 250 °C, Rh,K,Ni/A and Rh,K/A show already linear carbonyl Rh⁰-CO species, which were formed on the other catalysts at higher temperatures. We assume that potassium affects the adsorbates formation in two ways: (i) by a local polarization of the Rh particle, which partially enhances the electron density and (ii) covering of surface alumina OH groups, which hinders Rh⁺ formation by reaction of Rh⁰ with these hydroxyl groups. The second argument is also underlined by the finding, that hydrogen carbonates were not visible on the K-containing catalyst upon CO₂ dosing (Figure 14), instead hydrogen carbonates are only formed on available OH groups on the support [82]. It was also proved that the intensity of Rh-carbonyl bands of K-containing catalysts at 350 °C was distinctly lower than those of Rh/A and Rh,Ni/A. This suggests an influence of Ni and particular K on the strength of CO adsorption. Thus, the lower coverage of CO on Rh,K,Ni/A and Rh,K/A is an indication of the lower stability of those carbonyls, as was already described in literature [83, 162]. This means, in turn, that consecutive reactions like methanation are hindered as well, which is in line with the experimental findings, since Rh,K/A and Rh,K,Ni/A produce mainly CO and Rh/A and Rh,Ni/A mostly CH₄.

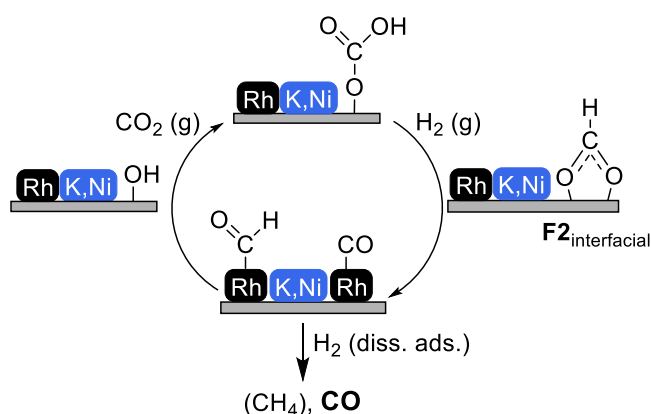
These mechanistic suggestions are in accordance with experimental findings and conclusions discussed in literature for other catalyst systems [123, 143, 160-161]. This proposed reaction mechanism implies that the close vicinity of support-bound hydrogen carbonates to the metal adsorbed hydrogen is needed to transform the hydrogen carbonate into formate. After formate formation, which primarily occurs on the Rh-alumina perim-

The isotopic transient experiments revealed for Rh/A, that the formation of ¹³CH₄, monitored by MS, proceeds at a similar time scale like the exchange of ¹²C-containing Rh carbonyls, visualized by DRIFTS. This indicates that carbonyls are the main reaction intermediates in methanation (Scheme 5). Because methanation proceeds very fast, simultaneous CO formation was not observed on Rh/A. However, formates were replaced slowly and incompletely by their isotopomers as monitored by DRIFTS. This leads to the conclusion, that formates are only spectator species in methanation over Rh/A.

On the other hand, formate species (F2) on the Rh,K,Ni/A catalyst show a faster exchange after switching to the isotopically labelled feed. Also, formyl and carbonyl exchange was fast. Both, ¹³C-containing formyl and formate bands exhibit the same time scale in exchanging, like ¹³CO formation occurs. Therefore, these species are probably main reaction intermediates for carbon monoxide formation (Scheme 6). However,

¹³CH₄ was also observed in the beginning of the reaction, but its concentration decreased over time, while ¹³CO formation was constant. Meaning, both reactions could proceed via the same intermediates and are competing for the same sites.

It is worth mentioning that in contrast to formates F1 on Rh/A, the formates F2 on Rh,K,Ni/A play a role in the reaction. Apparently, potassium influences the reactivity of those formates, being intermediates for CO formation. Moreover, formyl species are only present on the K-containing catalysts and are also active intermediates, but it is not totally clear, if they are important for CH₄ or CO formation pathway, since the rates of ¹³CH₄ and ¹³CO formation are nearly the same in the beginning and the exchange rates of ¹³C-containing formyl and carbonyl species are also comparable. Considering the fact, that formyl species were found to be main reaction intermediates in methanation of CO and CO₂ over Ru/Al₂O₃ [124], we assume that over Rh,K,Ni/A and Rh,K/A they are also rather intermediates in methanation than in carbon monoxide synthesis.



Scheme 6. Identified species and proposed reaction mechanism for CO₂ hydrogenation over Rh,K,Ni/A.

4.1.6 Summary of results for CO₂ hydrogenation over modified Rh catalysts

The above described experiments revealed that the CO₂ hydrogenation proceeds differently over the four catalysts. While Rh/A and Rh,Ni/A produced mainly methane, particularly after the high temperature treatment, carbon monoxide was preferentially formed over alkali promoted catalysts Rh,K/A and Rh,K,Ni/A (Figure 12). The high temperature treatment increased the activity of all Ni containing catalysts, by reducing the probably spinel type NiAl₂O₄ surface covering layer, as was demonstrated by TPR experiments (Figure A. 7), but decreased the activity of the other catalysts (Rh/A and Rh,K/A).

By applying *in situ* and *operando* spectroscopic experiments, comprising transient methods and SSITKA-type exchange techniques, reaction mechanisms were proposed for both methanation over Rh/A and Rh,Ni/A (Scheme 5) as well as CO formation over the K-containing catalysts (Scheme 6) [150]. It was found for all systems, that no dissociative CO₂ adsorption occurs, but the CO₂ is associatively adsorbed at the support, forming mainly hydrogen carbonates on Rh/A and Rh,Ni/A. Those hydrogen carbonates were not observed on Rh,K/A and Rh,K,Ni/A, but rather bi- and monodentate carbonates. The hydrogen activation and dissociation proceed on Rh particles. This activated hydrogen reacts subsequently with the pre-adsorbed hydrogen carbonates and carbonates to form carbonyls on the Rh and formates at the interface of Rh and alumina support. In case of Rh/A and Rh,Ni/A, those formates migrate to the support and are mainly unreactive and are therefore considered to be spectator species. On the other hand, a second type of formate (F2) has been observed on K-containing catalysts, which was found to be more reactive especially in the CO formation pathway. Additionally, formyl species were detected on Rh,K/A and Rh,K,Ni/A, which seem also to be very reactive, but we assume, more likely in methanation than CO formation. In the beginning of the reaction, methanation and RWGS are competing, but under steady-state conditions, CO formation is preferred.

The influence of the promoters K and Ni on the Rh catalysts performance can be explained by both geometrical and electronic effects. Especially K changes the CO adsorption ability of Rh, due to its polarizing power and thus lowering the adsorption strength of the carbonyls, which could be proofed by examining the carbonyl band position. This leads to the preferential formation of CO, because methanation is hampered. Moreover, K and Ni cover partially the OH groups of the support and therefore hinder the oxidation of Rh particles by hydroxyls, and also decrease the possible adsorption sites for inactive formates (F1) on the alumina support.

4.2 Alkali metal promoted gold catalysts for alcohol formation from CO₂, H₂ and C₂–C₃ olefins

4.2.1 Catalyst preparation and characterization

The superior performance of supported gold catalysts compared to those of cobalt, rhodium and copper was evidenced by Ahlers [24] and shortly discussed in chapter 2.3.1. The modification of the gold catalyst with alkali metals should help to increase the CO₂ conversion as well as the selectivity towards the alcohol 1–propanol or butanol [92]. Although it is debated in literature [97] that Cs has a less positive effect on the reaction compared to K, the preparation and characterization of those catalysts was interesting from a mechanistic point of view and also for the localization of the alkali metal by TEM measurements, since the contrast of Cs due to higher mass is more clearly visible.

The elemental preparation steps of gold nanoparticles with deposition–precipitation (DP) method are depicted in Figure 18 [163–164]. The surface of Brønstedt acidic TiO₂ offers generally many hydroxyl groups, which are important to form Au(OH)₃. Intermediates are probably Ti–[O–Au(OH)₃][–] complexes [165]. On the other hand, SiO₂ is an obviously less acidic support and has less hydroxyl groups to anchor the gold complex on the surface. Therefore, the DP method often leads to an incomplete precipitation of gold. ICP–OES measurements confirm this assumption (Table 5). Most SiO₂ – based catalysts do not reach the calculated 2 wt % of gold loading, whereas those based on TiO₂ do.

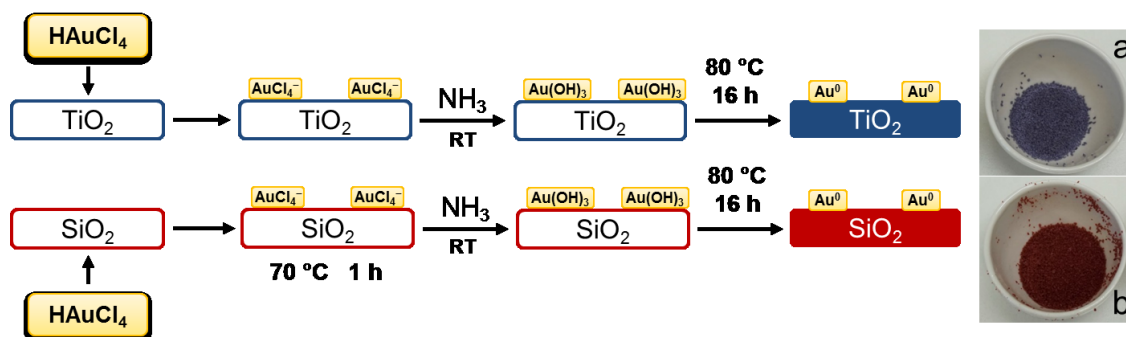


Figure 18. Principal intermediate stages in gold deposition precipitation from chloroauric acid in water and fresh, calcined catalysts (a) 2K,Au/TiO₂ (b) 2K,Au/SiO₂.

The pH value applied during preparation strongly influences the size of the formed Au particles [166–168]. Gold particles distinctly larger than 5 nm are deposited at a pH smaller than 6, while the size can be adjusted to less than 5 nm, when pH is raised to higher than 7. Hence, to ensure the formation of small gold particles, the pH was set to 10 for catalyst preparation. The Au NP size determined from TEM measurements is listed in Table 6.

With ICP–OES only the total amount of elements could be determined, but not if they are on the surface or in the bulk material. Therefore, TEM analysis was carried out, to reveal where alkali metal ions or oxides and gold particles are located. Figure 19 shows selected images of fresh TiO₂ based catalyst with and without cesium. Gold nanoparticles are general-

ly faceted like metallic gold, but it cannot be excluded that single gold atoms are also present on the surface of the support. The gold particle surface of the catalyst without cesium is smoother than that in the presence of cesium. This indicates that alkali metals induce mobility of gold atoms, which can move from the large gold particles to other support sites. This was already described in literature [86]. Gold single atoms are expected to be highly active *e.g.* for hydrogen activation [85]. This migration of single Au atoms from the larger Au NP also leaves more coordinatively unsaturated sites on the latter, which should also be active sites [164]. Especially hydrogen activation needs unsaturated sites [121, 169]. Cesium atoms are visible as small bright spots all on the surface, the support and also the gold particle. In some cases, an accumulation of cesium was found at the perimeter of gold and support.

Table 5. Gold and alkali metal loading of fresh and used SiO₂ and TiO₂ based catalysts for alcohol formation, used ones from 1-propanol formation.

Catalyst		Gold / wt %			Alkali metal / mol %		
		calculated	measured with ICP-OES		calculated	measured with ICP-OES	
			fresh	used		fresh	used
Au/SiO ₂	1.5 K	2	1.4	—	1.5	1.4	—
	5.0 K	2	1.1	1.3	5.0	4.6	4.6
	6.2 K	2	1.3	—	6.2	5.6	—
	1.9 Cs	2	1.4	—	1.9	—	—
	5.0 Cs	2	1.1	1.1	5.0	—	—
Au/TiO ₂	—	2	2.0	—	0.0	—	—
	2.0 K	2	2.3	—	2.0	1.9	—
	5.0 K	2	1.6	1.5	5.0	4.9	5.3
	6.0 K	2	2.3	—	6.0	5.7	—
	2.4 Cs	2	2.2	—	2.4	—	—
	5.0 Cs	2	0.4	—	5.0	—	—
	5.9 Cs	2	2.1	—	5.9	—	—

Comparing the catalysts on the basis of SiO₂ and TiO₂ supports (Figure 20), TEM measurements showed that gold particles on TiO₂ are often associated with the structure of the support, so that the gold nanoparticles were sometimes not stabilized in the characteristic face centered cubic (fcc) structure [170], but grew between or along the oxide layers. This observation was already described in literature and can be explained by the strong metal-support interaction (SMSI), which also influences the particle nucleation and growth during preparation [171-172]. This interaction is more pronounced on TiO₂ than SiO₂. Moreover, the size of gold NPs varies with the support and the amount of alkali metal promoter. For the highly cesium doped gold catalysts in Figure 20, it is obvious that the mean gold particle size is smaller on TiO₂ than on SiO₂. However, both average particle sizes are smaller than 6 nm, which should offer a large number of active gold-support sites on the perimeter interface [171].

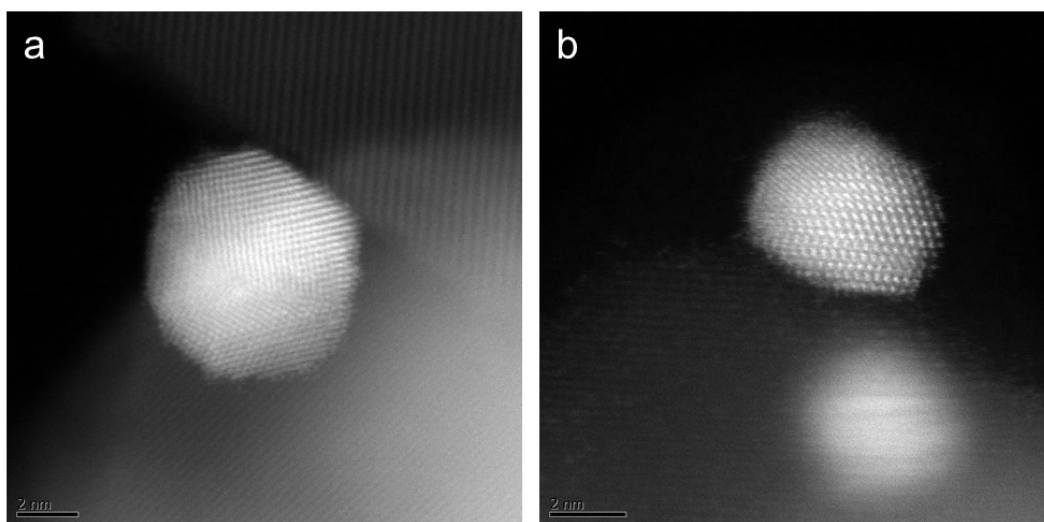


Figure 19. HR-TEM images of fresh (a) Au/TiO₂ and (b) 5.9Cs,Au/TiO₂.

Selected catalysts were additionally analyzed by powder XRD and the size of gold crystallites was calculated by means of Scherrers equation (Eq. 3.1). The results of this evaluation are listed in Table 6. While the gold particle size on SiO₂-based catalysts ranges from 4.9 to 7 nm, independent on alkali metal loading, the size of gold particles on TiO₂-based catalysts seems to be more influenced by the alkali metal presence (Figure 21). The fresh TiO₂ based catalysts were all analyzed by XRD (Figure A. 10), but only very broad reflexes for gold could be detected which are additionally overlaid by titania reflections, therefore the calculation of the NP size via Scherrers equation was not possible. However, this in turn evidenced that the gold particles are very small on TiO₂, in most cases smaller than gold particles, which were prepared on the amorphous SiO₂ support, where sharp Au reflections enabled the size determination (Figure A. 9). Since XRD measurement of Au NPs on TiO₂ showed that the average size is small, the corresponding TEM analysis for the 5K,Au/TiO₂ sample (Figure 21b) can be assumed to be not representative for the entire catalyst. This is of course a typical problem with particle size determination by TEM, because only a randomly selected and small part of the sample is analyzed and evaluated.

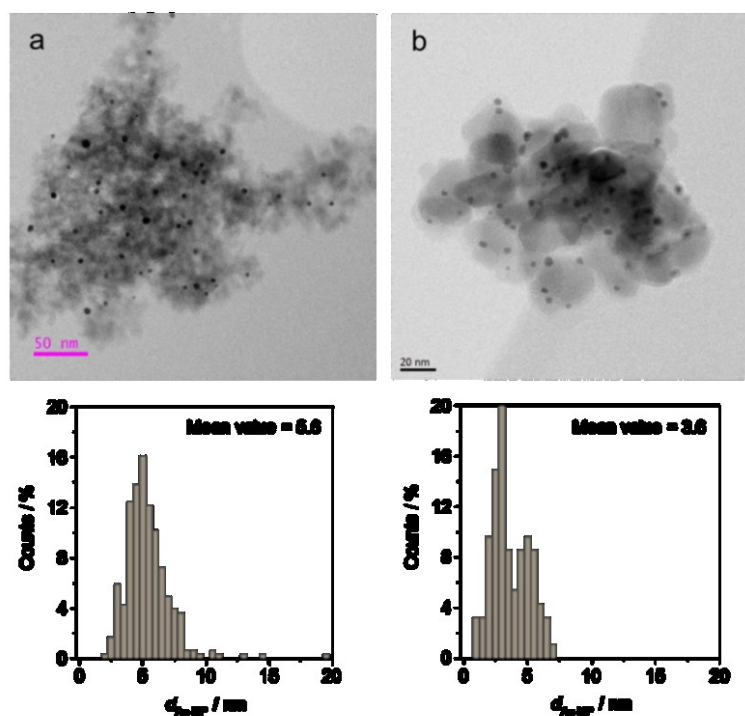
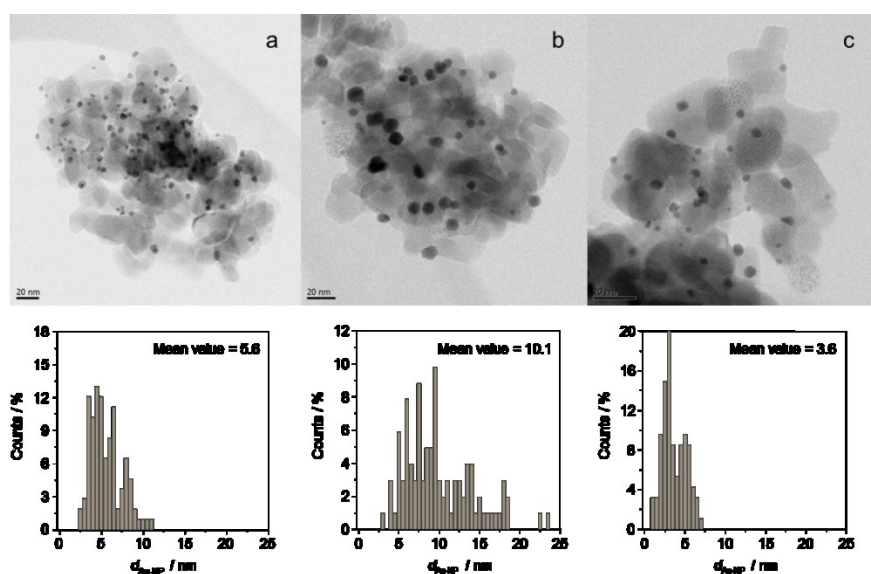


Figure 20. ABF-TEM images and gold particle size distribution of fresh (a) 5Cs,Au/SiO₂ and (b) 5.9Cs,Au/TiO₂.

Table 6. Fresh and used alkali containing gold catalysts for alcohol synthesis and their surface areas and Au NP sizes, determined by TEM and XRD.

Catalyst		$S_{\text{BET}} / \text{m}^2 \text{g}^{-1}$	$S_{\text{BET}} / \text{m}^2 \text{g}^{-1}$	$d_{\text{Au NP}} / \text{nm}$		$d_{\text{Au NP}} / \text{nm}$	
		fresh	used	fresh	used	fresh	used
Au/SiO ₂	2 K	256	187	4.9	—	6	—
	5 K	223	32	6.1	—	7	5
	2 Cs	243	156	5.5	—	5	—
	5 Cs	221	31	5.4	—	5	5
Au/TiO ₂	—	56	—	5.6	—	—	—
	2 K	55	51	—	—	—	—
	5 K	45	48	(10.1)	(8.2)	—	7
	2 Cs	52	49	—	—	—	—
	5 Cs	46	44	3.6*	4.6*	—	—

* Values for 5.9 mol % Cs

**Figure 21.** ABF-TEM images and the respective gold particle size distribution of (a) Au/TiO₂, (b) 6K,Au/TiO₂ (c) 5.9Cs,Au/TiO₂.

TEM imaging and X-ray diffraction revealed no obviously sintering of the gold particles during reaction as concluded from comparison of fresh and used catalysts. The used samples exhibited equal or sometimes also smaller (*e.g.* 5K,Au/SiO₂) gold particle sizes (Table 6). The reaction-induced decrease in the size is again an indication for the mobilization of gold atoms by alkali metals and possibly creation of coordinatively unsaturated Au sites.

Additionally, the surface area of the catalysts was determined using nitrogen adsorption and evaluation according to the theory of Brunauer, Emmett and Teller [133]. Table 6 lists the obtained results, S_{BET} values for the pure supports are reported in Table 3. The surface

area of silica (315 m² g⁻¹) decreased stronger upon gold deposition than that of titania, which exhibited a surface area of 58 m² g⁻¹ before preparation of the catalysts. Generally, S_{BET} decreases with higher alkali metal loading. Most often, the surface area decreased slightly during reaction. But surprisingly, S_{BET} values of the highly K and Cs loaded SiO₂ catalysts drastically declined. They were even smaller than for the respective TiO₂ samples after the same treatment. A more extensive discussion will follow in chapter 4.2.3.

4.2.2 Catalytic testing of modified Au catalysts in 1-propanol synthesis at 20 bar

In the following, the influence of temperature, feed composition and also the contact time on the catalysts performance is presented and discussed. Table 7 lists the usually applied notations for the real feed compositions.

Table 7. Correlation between different feed notations.

H ₂ /(CO ₂ + C ₂ H ₄)	CO ₂ :H ₂ :C ₂ H ₄
0.4	1:2:4
0.5	1:1:1
0.75	1:3:3

For every support material (TiO₂ anatase and SiO₂) one catalyst with low as well as high alkali metal loading was tested. Because Ahlers [24] found that Au/TiO₂ and Au/SiO₂ without alkali metal modification showed only RWGS activity and poor hydroformylation activity, so that most often no 1-propanol formation was detected, those catalysts were not examined in the reactor tests. Figure 22 depicts the obtained yields of 1-propanol, calculated on the basis of CO₂, over different alkali modified Au/TiO₂ and Au/SiO₂ catalysts at 200 °C and 20 bar with three different feed compositions.

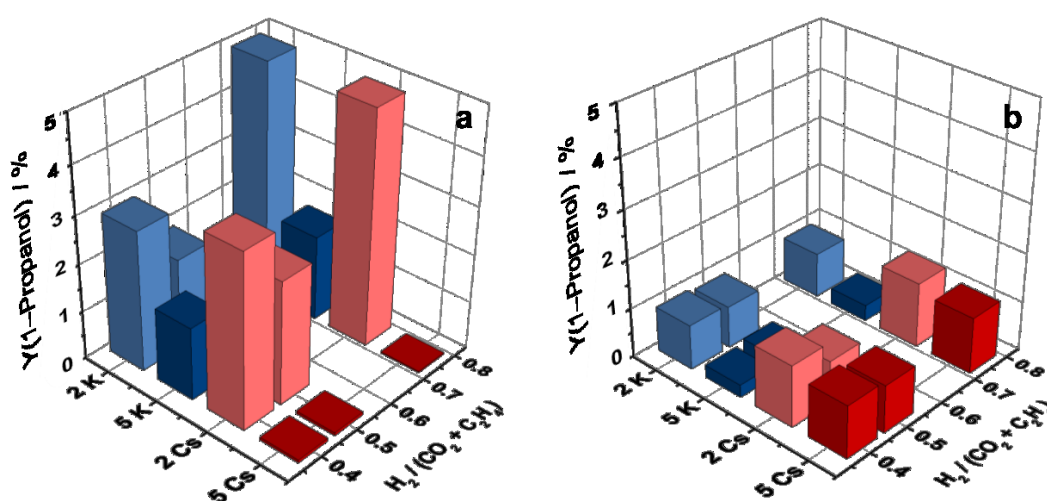


Figure 22. Yield of 1-propanol (derived from CO₂) over different alkali metal modified (a) Au/TiO₂ and (b) Au/SiO₂ catalysts and varied feed compositions, calculation on CO₂ basis (T = 200 °C, p = 20 bar, τ = 43 g_{Cat}·min·L⁻¹).

Influence of the support

Titania based catalysts produced mainly a higher amount of 1-propanol than catalysts with SiO_2 as support, which is exemplarily shown for 200 °C in Figure 22. The highest 1-propanol yield of 5% was reached over 2K,Au/TiO_2 and 2Cs,Au/TiO_2 with a CO_2 conversion of 6.5% and 5.5% (Figure 24), respectively, in the $\text{CO}_2:\text{H}_2:\text{C}_2\text{H}_4:\text{N}_2$ feed of 1:3:3:1. Only the highly loaded Cs-Au/ TiO_2 sample obtained low 1-propanol yield and also selectivity and was therefore least active sample. Instead of 1-propanol, mainly CO was produced as depicted in Figure 23. Besides those two products also the intermediate aldehyde 1-propanal was formed in small amounts, which is an indication of the good hydrogenation ability of the catalysts. The less aldehyde is measured, the higher is the hydrogenation performance to form the alcohol. Traces of *n*-butane, propane, acrolein and *n*-pentane were also observed sometime. CO_2 based selectivity (Figure 23) does not show a support dependent trend. Contrarily, the ethene based 1-propanol selectivity (Figure A. 11) is in the 1:1:1:1 feed on SiO_2 -based catalysts higher as on the TiO_2 -based samples. This underlines the expectation, that ethene hydrogenation can be suppressed over silica-based catalysts. The calculation of ethene based selectivity is important, because this molecule is the more expensive educt, which should preferably be transformed into the desired product to achieve an economic viable process.

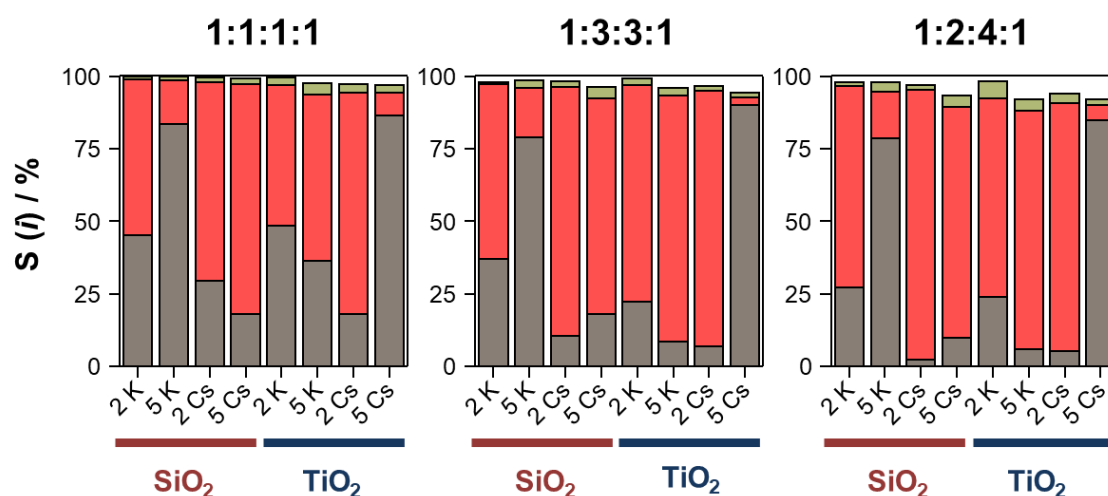


Figure 23. Selectivity of CO (grey), 1-propanol (red) and 1-propanal (green) at different feed compositions ($\text{CO}_2:\text{H}_2:\text{C}_2\text{H}_4:\text{N}_2$), calculation on CO_2 basis ($T = 200$ °C, $p = 20$ bar, $\tau = 43$ $\text{g}_{\text{Cat}} \cdot \text{min} \cdot \text{L}^{-1}$)

Influence of the alkali metal promoter

Generally, the yield of 1-propanol was higher over the low alkali metal loaded catalyst, irrespective of the support, but this goes not in every case along with highest selectivity (Figure 23). Silica supported catalysts with cesium outperform their counterparts with potassium in term of 1-propanol selectivity. Such a clear distinctive effect of the promoters on the selectivity was not established for titania-supported gold catalysts.

Promoting the Au/SiO_2 or Au/TiO_2 catalysts with alkali metal promoters principally leads to a higher CO_2 conversion, when a low amount of the promoter was added. Interestingly, the two Au/TiO_2 samples with 2 mol % of K or Cs exhibited the highest CO_2 conversion (Figure 24), regardless of the feed composition, reaching a maximal conversion of 6.6 % at 200 °C. For titania-based catalyst with 5 mol % of alkali metal, a strong decrease in the conversion was observed possibly due to too strong adsorption of CO_2 or covering of active sites, e.g. perimeter between gold and support, by the alkali metal. It could also be confirmed that increasing concentrations of alkali metals resulted in a decrease in ethene conversion (Figure 25). Comparing the influence of K and Cs, commonly K-containing catalysts exhibit a higher conversion of both CO_2 and ethene than the Cs-containing ones with the same molar percentage. These experiments underline the findings of Sordelli *et al.* [97], who found that the activity of propene hydroformylation catalysts decreased with decreasing polarizing power of the alkali metal.

Influence of the feed composition

The feed composition was found to be important for the performance of the catalysts in alcohol formation. Especially the 1-propanol yield and conversion of CO_2 , which is depicted in Figure 24, over Au/TiO_2 catalysts was obviously changed by the ratio of reactants, while the results for the Au/SiO_2 catalyst were not strongly altered. This might be related to the higher capacity of TiO_2 to “store” CO_2 at the surface, so that lower partial pressures of CO_2 do not lead to a decreased activity. This behavior is further discussed in chapter 4.2.6 and 4.2.7. As expected, the conversion of CO_2 increased markedly with increasing H_2/CO_2 ratio, which is realized in the 1:3:3:1 feed. This is caused by facilitating the RWGS reaction with rising hydrogen partial pressure.

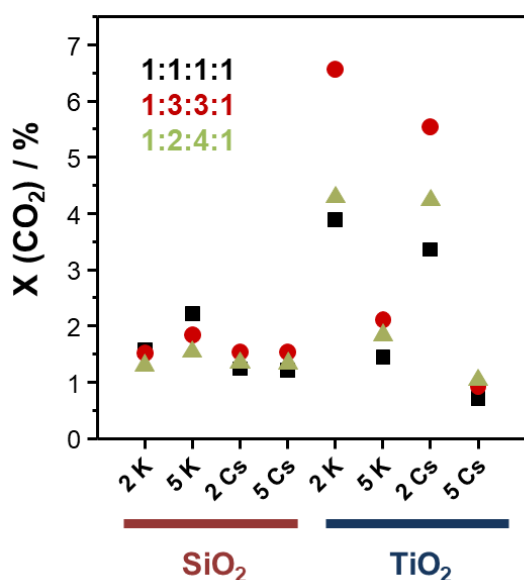


Figure 24. Conversion of CO_2 over different alkali modified Au/SiO_2 and Au/TiO_2 catalysts at 200 °C under different $\text{CO}_2:\text{H}_2:\text{C}_2\text{H}_4:\text{N}_2$ feeds ($p = 20$ bar, $\tau = 43$ $\text{g}_{\text{Cat}} \cdot \text{min} \cdot \text{L}^{-1}$).

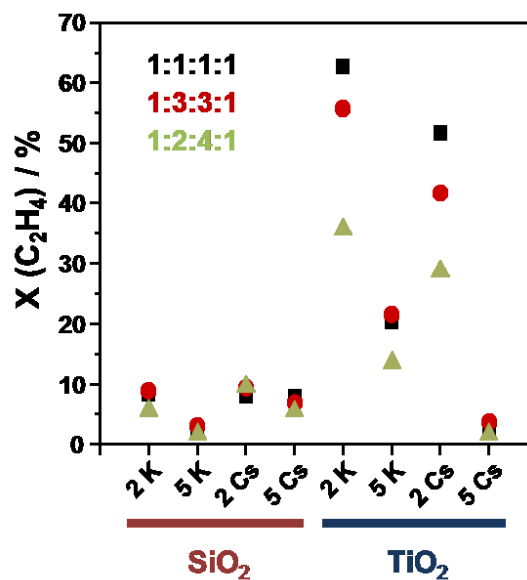


Figure 25. Conversion of ethene over different alkali modified Au/SiO_2 and Au/TiO_2 catalysts at 200 °C under different $\text{CO}_2:\text{H}_2:\text{C}_2\text{H}_4:\text{N}_2$ feeds ($p = 20$ bar, $\tau = 43$ $\text{g}_{\text{Cat}} \cdot \text{min} \cdot \text{L}^{-1}$).

The 1:2:4:1 ($\text{CO}_2\text{:H}_2\text{:C}_2\text{H}_4\text{:N}_2$) feed was used to suppress the undesired side-reaction of ethene hydrogenation by reducing the ratio of $\text{H}_2/\text{C}_2\text{H}_4$. This reaction was responsible for the high ethane selectivity based on ethene as shown in Figure A. 11. Ahlers [24] reported a selectivity towards ethane with more than 90 % in case of the TiO_2 (anatase) catalysts. As one attempt to decrease the “loss” of valuable ethene due to this side-reaction, SiO_2 was tested as support. Thus, the maximal 1-propanol selectivity based on C_2H_4 of 14 % was there obtained over 14.7 wt % $\text{K}_2\text{Au}/\text{SiO}_2$ [24].

Principally, it was therefore aspired to decrease the undesired conversion of C_2H_4 . The gained results for ethene conversion of the newly prepared catalysts are shown in Figure 25. As expected, ethene conversion was markedly lower over Au/SiO_2 catalysts than over Au/TiO_2 catalysts. Simultaneously, the selectivity towards 1-propanol on ethene basis was also found to be higher over the silica based catalysts than titania based (Figure A. 11). Nevertheless, it did not exceed 6% for the $5\text{K}_2\text{Au}/\text{SiO}_2$ or 2% for $2\text{Cs}_2\text{Au}/\text{TiO}_2$, respectively in the 1:1:1:1 feed. These catalysts showed also the best propanol selectivity calculated on ethene basis. Generally, the catalysts with 5 mol % alkali metal loading obtained a higher propanol selectivity than those with 2 mol %, except $5\text{K}_2\text{Au}/\text{TiO}_2$.

Surprisingly, ethene based selectivity to 1-propanol (Figure A. 11) could not be improved by changing the feed to $\text{CO}_2\text{:H}_2\text{:C}_2\text{H}_4\text{:N}_2 = 1:2:4:1$ although this feed composition decreased the ethene conversion (Figure 25). Generally, it has turned out, that the highest selectivity on ethene basis could be achieved under the 1:1:1:1 feed. On the other hand, CO_2 based selectivities were mostly higher when using the 1:2:4:1 feed (Figure 23).

4.2.2.1 Impact of temperature on catalytic activity

Due to different temperature requirements for optimal conversion and selectivity of RWGS reaction and hydroformylation, the effect of temperature was also studied for the combination of RWGS; hydroformylation and hydrogenation to form 1-propanol. Normally, RWGS is carried out at more than 400 °C, because thermodynamically, CO formation is favoured at higher temperatures. Below 400 °C methane formation is more pronounced (cf. Figure 4). For hydroformylation, lower temperatures were found to be optimal [91, 93]. Figure 26 illustrates the obtained CO_2 and ethene conversions as well as the selectivity to 1-propanol as a function of the reaction temperature. The selectivity was calculated based on CO_2 as well as ethene. Because the 1:1:1:1 feed composition was proved to be the most selective feed regarding ethene transformation, this feed was selected for further experiments. The respective 1-propanol yields for 225 °C are depicted in Figure 27 and for 250 °C in Figure 28.

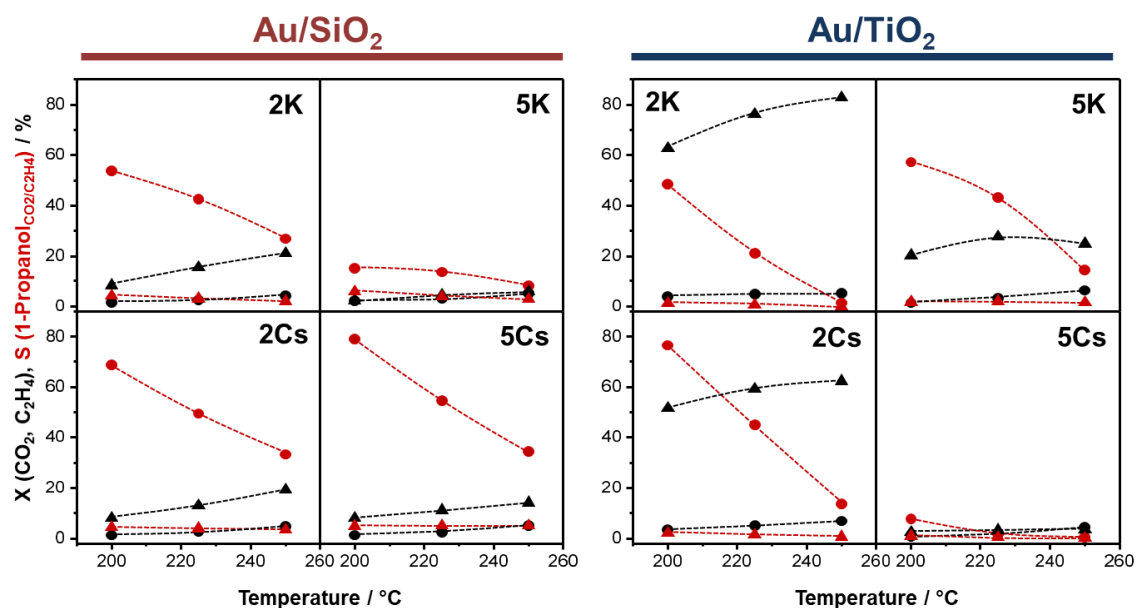


Figure 26. Influence of temperature on conversion (black) of CO₂ (●) and C₂H₄ (▲) as well as selectivity to 1-propanol calculated on the basis of CO₂ (●) and C₂H₄ (▲); (CO₂:H₂:C₂H₄:N₂ = 1:1:1:1, p = 20 bar, τ = 43 g_{Cat}·min·L⁻¹).

As expected, rising temperatures increase the conversion of CO₂ and C₂H₄. Generally, CO₂ conversion does not exceed 5% on silica based catalysts and 7% on titania-based ones at 250 °C. On the other hand, ethene conversion has to be discussed separately in dependence on the support materials. As already mentioned in the previous section, silica based catalysts exhibit an apparently lower conversion, which is in any case not higher than 20%. Contrarily, the 2 mol % alkali metal loaded Au/TiO₂ catalysts showed an ethene conversion of more than 50%.

Although the conversion moderately changed over most of the samples, the selectivity to 1-propanol calculated on CO₂ basis drastically decreased with increasing temperature. This effect is most pronounced over 2Cs,2Au/TiO₂ (Figure 26) on which the selectivity dropped from 77 to 14%. Nevertheless, the highest 1-propanol yield of 2.25% was obtained over this catalyst at 225 °C, as depicted in Figure 27. This value is comparable to the yield obtained at 200 °C, which was 2.5% (Figure 22). However, at higher temperatures the yield of 1-propanol dropped drastically to 0.9% for the TiO₂-based catalysts (Figure 28). This was not observed for SiO₂-based catalysts, there the yield changed only moderately. The Cs promoted samples display even better yields at 250 °C around 1.7%, which are however, lower than those obtained over 2Cs,2Au/TiO₂ at 200 °C.

In general, it was detected that with rising temperature, CO (Figure A. 12) and ethane formation become dominant instead of 1-propanol formation. This means that probably the adsorption of the intermediately formed CO is not strong enough at higher temperatures to enable hydroformylation. Moreover, ethene is predominantly hydrogenated, because more adsorption sites at the gold particles are available for hydrogen activation, which are normally covered by adsorbed CO. A similar effect was discussed also for CO₂ hydrogenation with either CO or CH₄ as product [55].

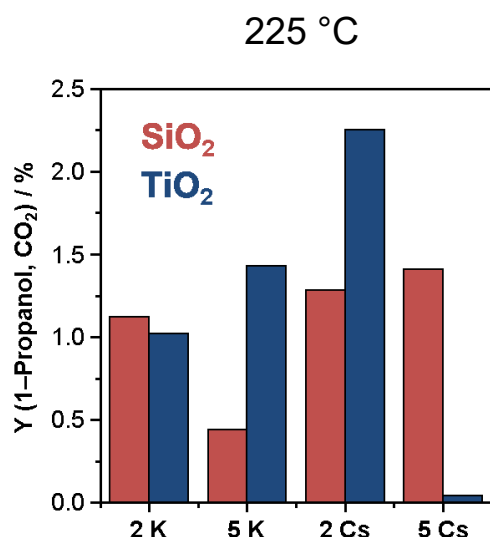


Figure 27. Yield of 1-propanol, calculated on CO₂ basis, obtained over different alkali modified Au/SiO₂ and Au/TiO₂ catalysts at 225 °C with feed of CO₂:H₂:C₂H₄:N₂ = 1:1:1:1, (p = 20 bar, τ = 43 g_{Cat}·min·L⁻¹).

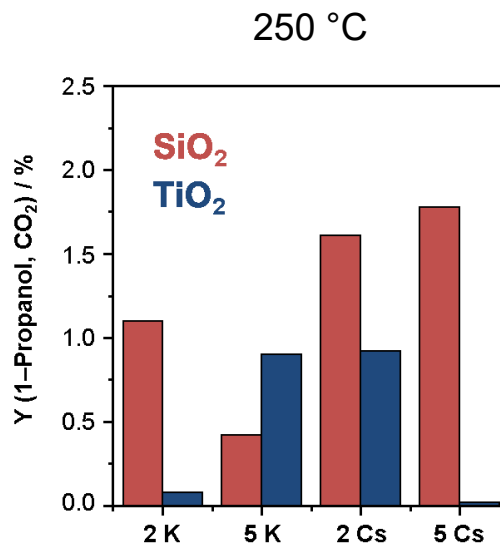


Figure 28. Yield of 1-propanol, calculated on CO₂ basis, obtained over different alkali modified Au/SiO₂ and Au/TiO₂ catalysts at 250 °C with feed of CO₂:H₂:C₂H₄:N₂ = 1:1:1:1, (p = 20 bar, τ = 43 g_{Cat}·min·L⁻¹).

4.2.2.2 Impact of contact time on catalysts activity

To study the reaction pathways of product formation, catalytic tests were carried out at different contact times to achieve different degrees of conversion of feed components. Figure 29 illustrates the influence of contact time on product selectivity over Cs modified catalysts, comparing the feeds CO₂:H₂:C₂H₄:N₂ = 1:1:1:1 and 1:2:4:1. Generally, with rising contact time the conversion of CO₂ and ethene increases over all catalysts independent of the admitted feed.

Most often, a nearly constant selectivity to 1-propanol, independently from contact time, was found, being lower than CO or 1-propanol selectivity. Hence, it can be concluded that this molecule is rapidly hydrogenated at the Au NPs and therefore, is an intermediate of alcohol formation from CO₂, hydrogen and ethene. This is in accordance to the findings of Ahlers *et al.* [24-25], who proposed such reaction pathway for the alcohol formation, too.

It is also a general trend that the 1-propanol selectivity increases with increasing contact time, but the extent of the increase and therefore the rate of propanol formation is different over the various catalysts and also dependent on the feed composition. While the Cs,Au/SiO₂ catalysts exhibit a strong dependence on the contact time, the changes are rather small over the Cs,Au/TiO₂ samples. Unfortunately, the 1-propanol selectivity of the 5Cs,Au/TiO₂ catalyst was also low at long contact times. On the other hand, the titania catalyst with lower Cs loading exhibited a good 1-propanol selectivity already at low contact times (74% with 1:2:4:1 feed), which is an indication for fast propanol formation rates over this sample.

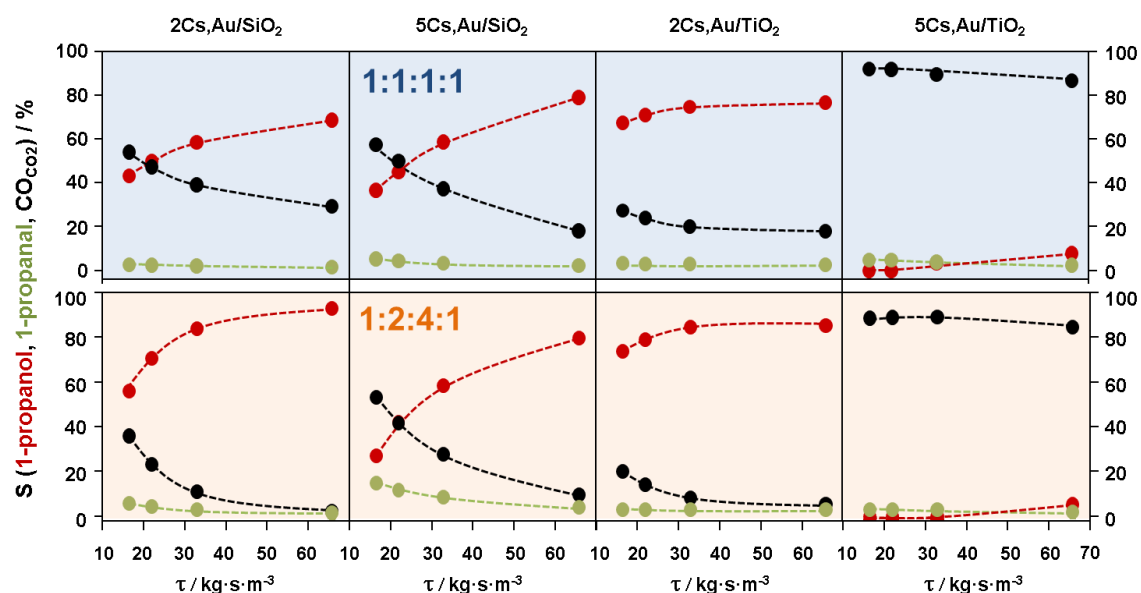


Figure 29. Selectivity to 1-propanol (red), 1-propanal (green) and CO (black) calculated on CO_2 basis over Au/SiO_2 and Au/TiO_2 catalysts promoted with Cs versus contact time τ ; the upper row in $\text{CO}_2:\text{H}_2:\text{C}_2\text{H}_4:\text{N}_2=1:1:1:1$ feed and the lower row in $1:2:4:1$ feed ($p = 20$ bar, $T = 200$ °C).

However, with rising contact time, the 1-propanol selectivity reaches a constant level of around 85% with 1:2:4:1 feed. For the 2Cs,Au/TiO_2 catalyst, the feed composition does not change the formation rate of propanol, because the slope and shape of the selectivity curves are the same for both feed compositions, only the absolute value of 1-propanol selectivity is higher for the 1:2:4:1 feed as already discussed in the former sections.

In contrast, it is evident from the first two graphs of Figure 29 that the rate of propanol formation over Cs,Au/SiO_2 catalysts is influenced by the feed. In particular the 1-propanol selectivity over the 2 mol % Cs,Au/SiO_2 sample increased faster with rising contact time in the 1:2:4:1 feed than in the 1:1:1:1 mixture. This result suggests that the possible higher *in situ* CO concentration in the 1:2:4:1 feed facilitates a faster hydroformylation. The correlation between CO concentration and possible ethene reactions with hydrogen (*e.g.* hydrogenation, homologation) was already discussed in literature [104-105, 173]. The authors describe that higher CO concentration on the surface of the catalyst inhibits the ethene hydrogenation and enhances hydroformylation. This effect seems to be more pronounced over SiO_2 than over TiO_2 , as the presented results suggest. Another notable point is that over the samples loaded with 5 mol % Cs, the hydrogenation of the aldehyde is slower at short contact times than on the catalysts loaded with 2 mol % Cs. This means that higher alkali metal concentrations possibly cover the Au NPs to some extent and hinder probably the activation of hydrogen or ethene.

Similar results were obtained for K doped catalysts. Therefore, these results are not discussed here. The silica based samples exhibited a stronger dependence of catalysts performance on the contact time than those based on titania and the reaction rates were higher in the 1:2:4:1 feed than in 1:1:1:1 feed.

4.2.3 Influence of time on stream on catalysts surface and Au nanoparticles

By inspecting the catalyst particles after reaction, it was found, that the color of those samples, which were prepared with 5 mol % of alkali metal, changed during reaction as depicted in Figure 30. In this figure, the fresh and used 5K,Au/SiO₂ is exemplarily shown. Many particles of the used samples partly lost their color and are merely pale red instead of dark red. The same changes were observed for the 5 mol

% K samples and also the TiO₂ catalysts. Those catalysts with 2 mol % alkali metal loading remained their pristine color. However, it was already demonstrated, that the amount of gold and alkali metals does not change during the reaction, as measured by ICP–OES (Table 5). Also the size of the gold nanoparticles is not altered, as could be proved by TEM and XRD (Table 6). The color of catalysts is influenced by different properties, for example the size of nanoparticles, their oxidation state, but also the support, its reducibility and dielectric constant. This can affect the plasmon resonance band of the Au and can change the color of the catalyst. The different colors of fresh TiO₂ and SiO₂ samples, which are blue or red, respectively, are most likely affected by the support, due to the influence of the Au NP size and dispersion [121, 163].

Furthermore, the surface area of the highly alkali metal loaded SiO₂ samples decreased strongly during the reaction, as has been noted earlier (Table 6). To study these effects, additional TEM measurements have been performed and are presented for TiO₂ in Figure 31 and for SiO₂ in Figure 32.

By comparing fresh and used TiO₂ catalysts in Figure 31, it is obvious that the fresh Au particles have a flat surface, only few uncoordinated sites are visible. On the other hand, the used samples display a roughened surface, which has many defect sites. Also single gold atoms migrated away from the big nanoparticle, forming single sites. This indicates that the active catalyst surface is generated during activation or reaction.

Moreover, the formation of a carbon containing layer over alkali promoted gold catalysts was found after reaction, which can be well observed in the bright field images of 6K,Au/TiO₂ and 5.9Cs,Au/TiO₂. This might be stemming from decomposition of ethene. Generally, the samples with a higher alkali metal amount have a distinctly higher tendency to form such a layer. It can often be observed and confirmed by EDX measurements that Cs accumulates in that carbon layer (Figure 31, f). Furthermore, it was found that these layers sometimes possess a starting short range order, the lattice plane of which show the distance typical for graphite (3.4 Å) [48]. This is exemplarily shown for the 5Cs,Au/SiO₂ catalyst in Figure 32. Pellegrini *et al.* [174] also reported on the formation of such a layer on K doped Pd/SiO₂ catalysts. They found, that rising alkali metal loadings lower the number of accessi-

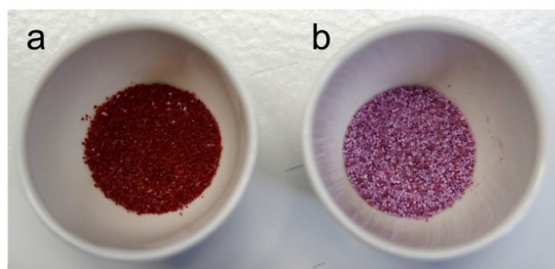


Figure 30. Comparison between (a) fresh and (b) used 5K,Au/SiO₂.

ble Pd atoms, by forming an encapsulating phase deriving from mobilized support material during reduction. So it seems possible also for the Au/SiO₂ samples that higher alkali metal loadings cause a migration of support atoms, leading to a phase formation with a markedly lower surface area.

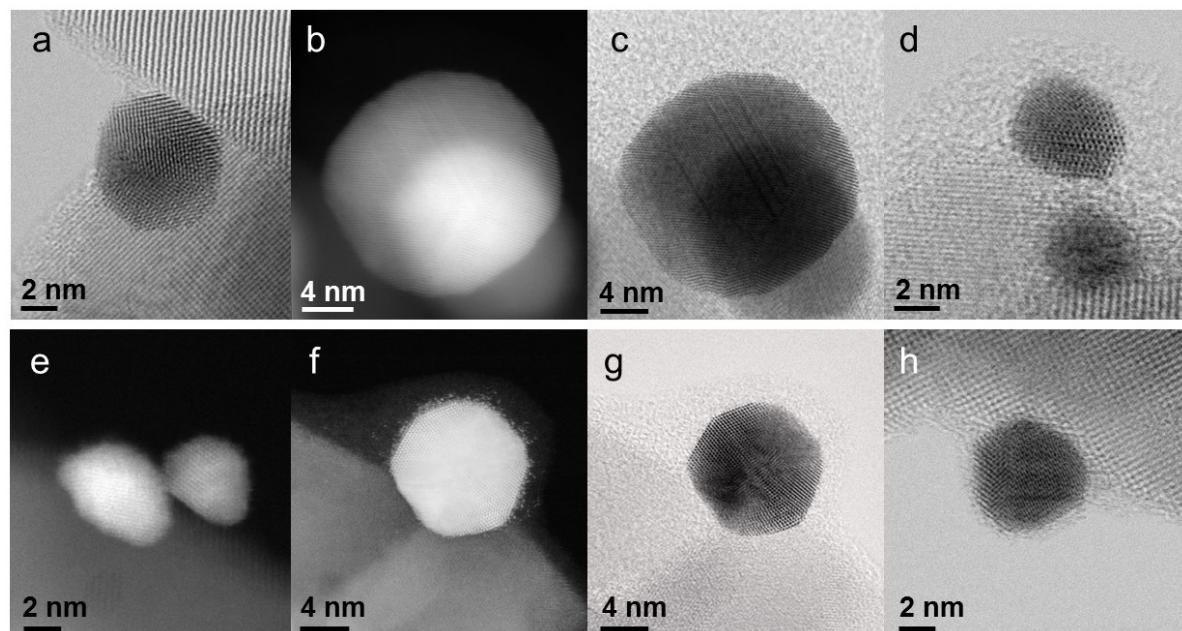


Figure 31. HR-TEM images of fresh (a-d) and used (e-h) TiO₂ catalysts; (a,e) Au/TiO₂, (b-c, f-g) 6K,Au/TiO₂ (d,h) 5.9Cs,Au/TiO₂.

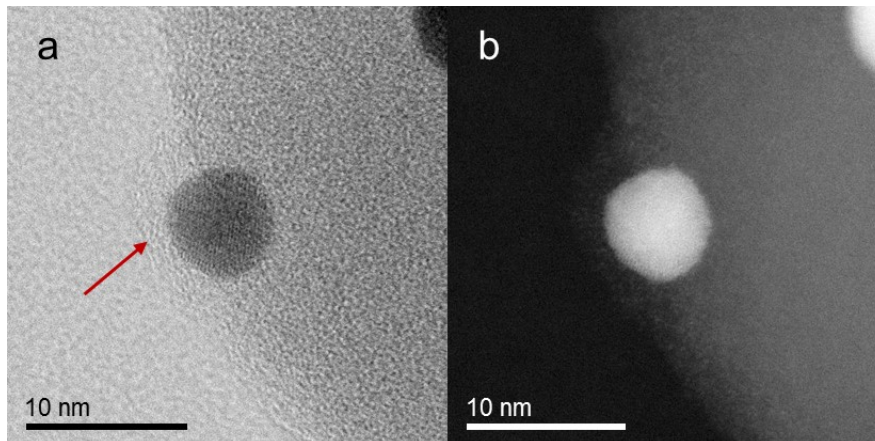


Figure 32. HR-TEM images of 5Cs,Au/SiO₂ used in propanol synthesis in (a) annular bright field and (b) high-angle annular dark field mode, the red arrow points to the area of carbon over layer on Au NP, which possesses a starting short range order.

This point is difficult to discuss for the TiO₂ based catalysts, because their surface is generally small. However, it seems unlikely, that TiO₂ is rearranged upon alkali metal doping, because the crystallite state of the support is energetically advantageous and also the SMSI effect between gold and TiO₂ leads often to a distinct covering of the gold particle by the support, which stabilises both TiO₂ and gold [172].

4.2.4 *In situ* CO adsorption at low temperature

The oxidation and coordination state of Au NP as well as its accessibility was examined by *in situ* FTIR spectroscopic monitoring of CO adsorption at low temperatures. The interaction of the probe molecule with the gold atoms is only weak and adsorption is reversible [175]. This is one reason why the measurements are carried out under liquid nitrogen cooling. Principally, CO adsorption on gold is a well-explored field, because gold is often and effectively used in CO oxidation [117, 170, 176-183]. This in turn means that CO can change the oxidation state of Au [184-186], which would hinder the correct interpretation of the results if CO adsorption is operated as a characterization tool. To avoid a reactive adsorption the adsorption was carried out at low temperature.

In contrast to the Rh catalysts studied in Chapter 4.1.3, CO is adsorbed on Au predominantly in a linear form. The position of the carbonyl vibration of adsorbed CO is sensitive to the strength of the bonding between Au and CO and ranges typically from 2000 to 2170 cm^{-1} [170]. Bands of CO adsorbed on metallic Au particles are referred to be observable at around 2100 cm^{-1} [121, 182]. CO on negatively charged Au would vibrate at lower wavenumbers, while (partial) positively charged Au would give rise to CO bands at higher wavenumbers [187].

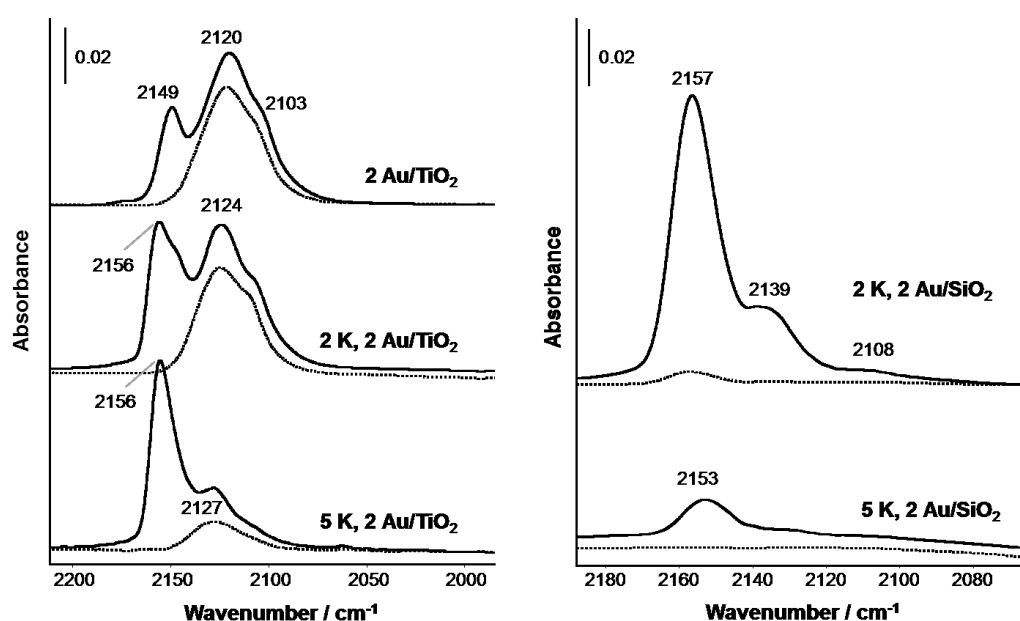


Figure 33. FTIR spectra of CO adsorption on fresh Au/TiO₂ (left) and Au/SiO₂ (right) catalysts with different K loadings. Solid lined spectra were taken after five pulses of 5 vol % CO in He, dashed lines show spectra after subsequent evacuation ($p = 1$ bar, $T = -160$ °C).

The spectra obtained for CO adsorption on the fresh K doped Au/TiO₂ and Au/SiO₂ catalysts are displayed in Figure 33. For a clearer presentation of the CO adsorption bands, the respective spectra recorded after cooling to -160 °C under inert gas were subtracted from the original spectra. Clearly visible are the differences between the two supports as well as the impact of the potassium content on position and intensity of the CO bands. The Au/TiO₂ sample exhibits three carbonyl bands at 2103, 2120 and 2149 cm^{-1} . With rising po-

tassium content, these bands shift to higher wavenumbers. Simultaneously, the band intensity at 2103 cm⁻¹ decreases while the one at 2156 cm⁻¹ increases. The band at around 2103 cm⁻¹ can be assigned to metallic Au⁰ [121, 182], the intensity of which decreases with a higher amount of potassium. The band, which shifts from 2120 to 2127 cm⁻¹ in dependence on K content from Au/TiO₂ to 5K,Au/TiO₂ most probably stems from partially positively charged Au particles [188]. Their intensity is not altered with only 2 mol % of K, but decreased when 5 mol % K is used for doping the sample. The band at around 2156 cm⁻¹ which increased in intensity with higher alkali metal loading is arising from the interaction of CO with support OH groups possibly via a hydrogen bond type coordination [189-190].

From these findings it can be concluded, that potassium doping may cause a slight oxidation or at least an electron shift from the Au particles to the semiconducting TiO₂ or oxygen atoms. This can be understood, because pre-treatment has been carried out only in inert gas atmosphere before CO adsorption and calcination of the sample proceeded in ambient air, which apparently leads to the oxidation of the sample. Moreover, it was found that the samples with Cs (Figure A. 13) exhibit a larger proportion of Au⁰ compared to the respective K doped samples. This could be an evidence that the polarizing power of the alkali metal, which is larger for K, plays a role for the oxidation state of the Au. Moreover, the decrease of the Au⁰–CO bands at higher alkali metal loading is a sign that alkali metals cover the surface of the gold and, thus, occupy sites, which are no longer available for CO adsorption. This confirms the results obtained by TEM measurements described in chapter 4.2.1. The increase of band intensity for CO adsorbed on OH groups (2156 cm⁻¹) of titania also supports the assumption, that the Au particles are partly covered by TiO₂, induced by the SMSI effect or by increasing OH concentrations due to the alkali metals present. The normally preferred adsorption on Au is here compensated by alternative adsorption on the OH groups. The same effect can be observed for the Cs loaded Au/TiO₂ catalysts (Figure A. 13), but the coverage of the Au NP is more strongly visible for the 5 mol % Cs,Au/TiO₂ compared to the 5 mol % K sample, so that mainly bands of CO adsorbed on OH groups are recorded and only weak bands for CO adsorbed on gold. This might be the reason, why those catalysts exhibit such a poor activity in alcohol formation as described in the previous chapters. The adsorption of CO on those hydroxyl groups is not very stable referring to the spectra recorded after evacuation, where they vanished on all samples.

The largest band on the SiO₂-based samples at 2157/2153 cm⁻¹ (Figure 33) is usually ascribed to CO adsorbed on isolated silanols [178] and the less intense band at 2139 cm⁻¹ is most probably stemming from CO adsorbed on Au^{δ+} while the small shoulder at 2108 cm⁻¹ arises from CO at Au⁰ sites [188]. In general, the adsorption of CO on the silica samples is less stable than on titania and fewer Au sites are involved in the adsorption process. This can also be observed in CO-TPD (temperature programmed desorption) experiments, which were carried out with fresh and used catalysts (Figure 34).

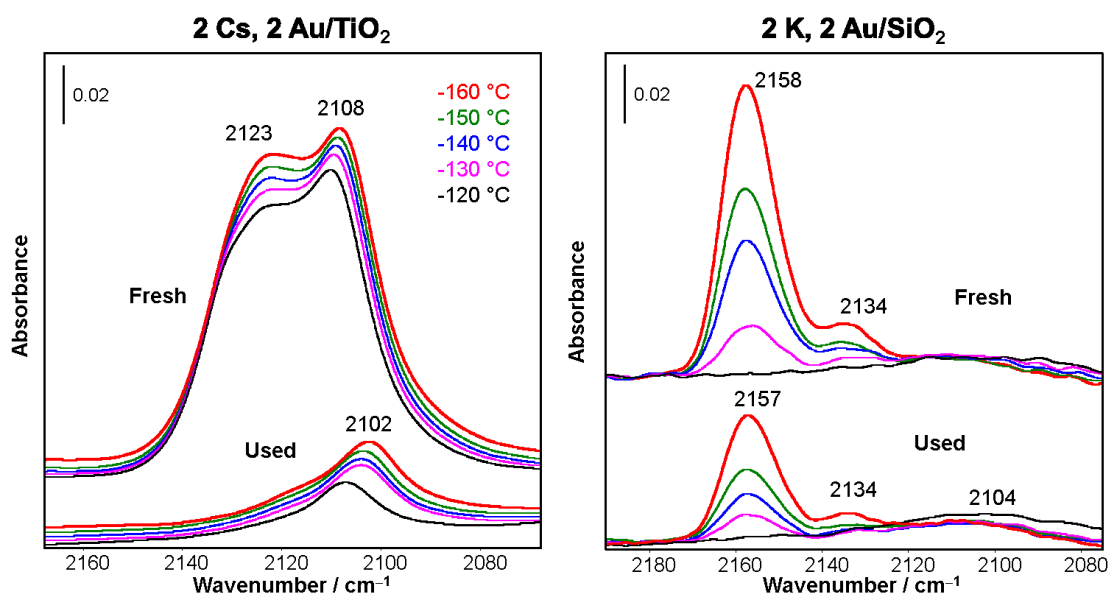


Figure 34. FTIR spectra of CO adsorption and subsequent desorption from $-160\text{ }^{\circ}\text{C}$ to $-120\text{ }^{\circ}\text{C}$ over fresh and used samples of $2\text{Cs}, 2\text{Au}/\text{TiO}_2$ and $2\text{K}, 2\text{Au}/\text{SiO}_2$. ($p = 1\text{ bar}$).

Furthermore, it is also worth mentioning that in the used samples, independently of the support, the intensity of bands of CO adsorbed on gold is weaker than those of the fresh samples. However, it can be observed that on the used catalysts, gold is more or less in the metallic state, which is indicated by the band at 2103 cm^{-1} on the titania sample. On silica, as already described, mainly bands of CO adsorbed on silanol groups are apparent.

4.2.5 Study of the influence of different pre-treatments on CO adsorption and simultaneous thermal analysis

Ahlers *et al.* [24] revealed that a special feed ($\text{CO}_2:\text{H}_2:\text{C}_2\text{H}_4:\text{N}_2 = 4:2:1:1$) is necessary for activation of the catalyst, but it was not clear what happened during this process. Therefore, this process was studied by FTIR spectroscopy and by simultaneous thermal analysis (TG–DSC/MS). The experiments covered three pre-treatments, to compare how the catalyst surface and the adsorbates change during exposure to the different gas atmospheres. CO adsorption followed these pre-treatments, in order to determine the oxidation state of gold and its accessibility. The first experiment was carried out under He at ambient pressure, in which the catalyst was heated to $200\text{ }^{\circ}\text{C}$, in analogy to the experiments presented in the previous chapter. The other two experiments included heating to $250\text{ }^{\circ}\text{C}$ in a mixture of 10% CO_2 and 10% H_2 , diluted with inert gas, prior to the low temperature CO adsorption. The difference between these experiments was the applied pressure, under which the pre-treatment was carried out. One experiment was done at ambient pressure directly in the low temperature cell and the second experiment was executed at 10 bar in the high-pressure IR cell from ISRI.

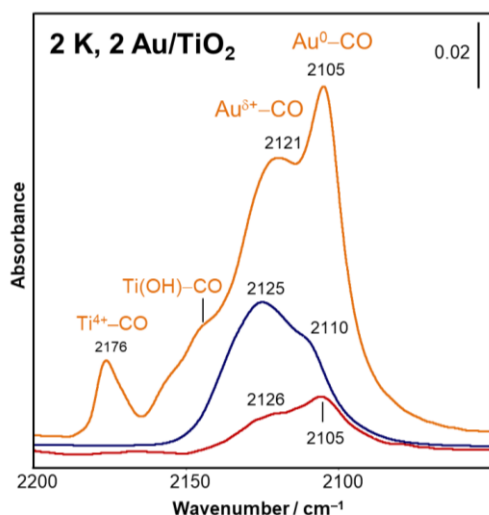


Figure 35. FTIR spectra of CO adsorption on 2K,2Au/TiO₂ catalyst with different pre-treatments: He, 200 °C (blue), 10%CO₂+H₂+He, 250 °C, 1 bar (yellow), 10%CO₂+H₂+N₂ at 10 bar, 250 °C (red). Spectra were taken after dosing of 5 vol % CO in He at -160 °C, subsequent evacuation and heating to -150 °C.

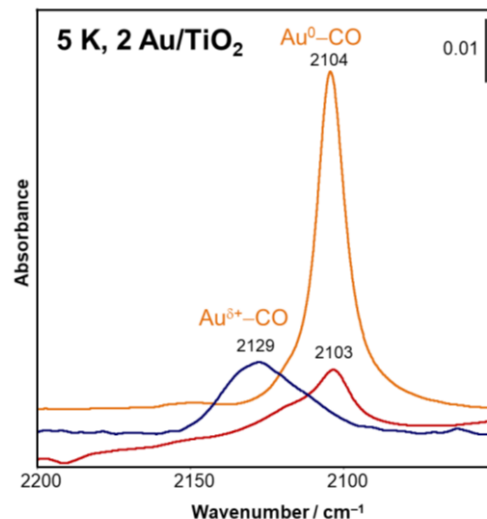


Figure 36. FTIR spectra of CO adsorption on fresh 5K,2Au/TiO₂ catalyst with different pre-treatments: He, 200 °C (blue), 10%CO₂+H₂+He, 250 °C, 1 bar (yellow), 10%CO₂+H₂+N₂ at 10 bar, 250 °C (red). Spectra were taken after dosing of 5 vol % CO in He at -160 °C, subsequent evacuation and heating to -150 °C.

Figure 35 and Figure 36 illustrate the FTIR spectra of low temperature CO adsorption on 2K and 5K,Au/TiO₂ samples. Together with the inert gas pre-treated sample, also the spectra for ambient pressure CO₂+H₂ pre-treatment and the external CO₂+H₂ pre-treatment at 10 bar are shown. Both methods obviously alter the surface properties of the catalysts. The activation with CO₂+H₂ at ambient pressure (yellow lines in Figure 35 and Figure 36) results in the reduction of the Au NP (2103 cm⁻¹), more pronounced on the sample loaded with 5 mol % K, but also partly visible for the sample with 2 mol % K (considering the different scales). This effect is also apparent for the SiO₂-based catalyst, for which the spectra are displayed in Figure A. 14.

Corma *et al.* [191] have found in a study comprising XPS, IR spectroscopy and DFT calculations, that the hydrogen activation ability of catalysts directly increases with rising amounts of such coordinatively unsaturated Au⁰ sites. Therefore, activation in CO₂+H₂ might lead to an enhanced hydrogen dissociation ability of the gold catalysts.

Moreover, the total intensities of the bands of CO adsorbed on gold increase on 2K,Au/TiO₂ after activation at ambient pressure (*cf.* Figure 33, left). This can be an indication for the enhanced accessibility of the gold by this activation procedure in CO₂+H₂ at 1 bar. Interestingly, the 2K,Au/TiO₂ catalyst pre-treated at 1 bar exhibits a band at 2176 cm⁻¹, which was not observed in any other experiment or with another sample. This band arises from CO adsorbed on coordinatively unsaturated Ti⁴⁺ [182, 190, 192-193]. A general intensity loss of CO adsorption bands could be found, when the samples were pre-treated under CO₂+H₂ at elevated pressure (red lines in Figure 35 and Figure 36). Independently of the amount of potassium, bands of CO adsorbed on gold (2102 cm⁻¹) have only low intensity.

For explaining these findings, also other adsorbate species present on the samples and their changes during pre-treatment experiments should be taken into account. Therefore, Figure 37 depicts the spectra of 2K,Au/TiO₂ in the spectral region of OH and CH groups as well as the region where formates and carbonates can be detected. The same is presented for 5K,Au/TiO₂ in Figure 38. For comparison, also the basic spectra of the blank catalyst without any treatment are shown in grey. On the fresh sample, a large O–H stretch band of hydrogen-bound water on hydroxyl groups of titania appears between 3000 and 3600 cm⁻¹ [194-195]. The corresponding bending vibration is visible at 1632 cm⁻¹. Moreover, bands of uncoordinated carbonate can be seen around 1405 cm⁻¹ as well as carboxylates at 1566 and around 1360 cm⁻¹ [117]. After heating in He, the large water bands disappear, but on the other hand, after cooling to -160 °C and CO pulsing, the bands at 3478/3364 cm⁻¹ indicate strongly coordinated water traces on cationic sites [192, 195-196] or OH groups on Au at the interface to the support [197].

The uncoordinated carbonate has vanished, and adsorbed hydrogen carbonate species are now present on the surface, indicated by the bands at 1580, 1469, and 1264 cm⁻¹ as well as bidentate carbonate species (1606 and 1299 cm⁻¹) [120, 123]. These species were formed just by transformation of the carboxylate and carbonate species present on the surface before the treatment and not upon CO adsorption, because their intensity does not change after the heating in He and cooling to -160 °C.

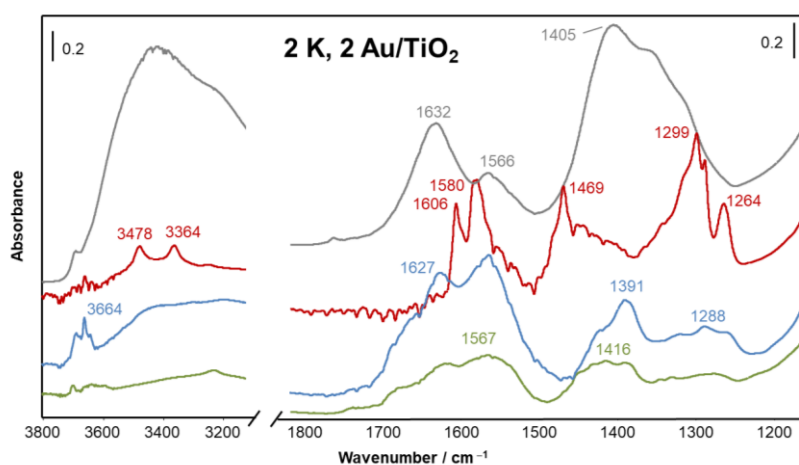


Figure 37. FTIR spectra in the ν OH/CH and ν OCO region of 2K,2Au/TiO₂ during CO adsorption experiments with different pre-treatments: (red) He at 200 °C, (blue) CO₂+H₂+He, 250 °C, 1 bar, (green) CO₂+H₂+N₂ at 10 bar, 250 °C. Spectra were taken after five pulses of 5 vol % CO in He and subsequent evacuation ($p = 1$ bar, $T = -160$ °C) except the grey spectra, which shows the pure catalysts without any treatment at RT.

It was also observed for the other pre-treatments that the CO adsorption does not alter the adsorbed carbonate species. However, the transformation of carboxylates and carbonates was different under the treatment in CO₂+H₂ atmosphere compared to the inert gas treatment. Most obvious is the decrease of the band at 1405 cm⁻¹, which was ascribed to uncoordinated carbonate (Figure 37, grey spectra). On the other hand, the bands at 1566 and 1391 cm⁻¹ become more prominent (Figure 37, blue spectra), which can probably be assigned to monodentate carbonates [82, 123] or formates on TiO₂ [198] or on Au particles. The latter

one were found to be fairly stable also under heating up to 300 °C [87]. Furthermore, bidentate carbonates are evidenced by the bands at 1627 and 1288 cm⁻¹ (Figure 37, blue spectra) [120]. The high pressure CO₂+H₂ pre-treatment (Figure 37, green spectra) principally leads to the decrease of all bands, but the adsorbate species seem to be similar to those in the normal pressure CO₂+H₂ pre-treatment.

In the fresh sample with 5 mol % K (Figure 38), a small band at 1766 cm⁻¹ is more intense than in the fresh catalyst with 2 mol % K (Figure 37). This band originates from alkali nitrates, which were presumably not decomposed during calcination at 250 °C in air or during heating in He (red line in Figure 38) [199]. The presence of alkali nitrates was also confirmed by powder XRD measurements, which are shown in Figure A. 9 and Figure A. 10. Logically, the reflections and also the IR bands of nitrates are more intense in case of higher alkali metal loading. However, it can be seen that the nitrates were degraded in the CO₂+H₂ feed, more effectively in the high-pressure experiment, but also at ambient pressure as indicated by the green and blue spectra in Figure 38.

Moreover, it was evidenced that the nitrates were faster decomposed on the TiO₂-catalysts than on the SiO₂-based ones (Figure A. 15) and also at elevated pressures. The capability of TiO₂-based metal catalysts to reduce nitrates, for example in waste water, was already demonstrated in literature [200]. It can therefore be assumed that the Au/TiO₂ catalysts can also reduce the remaining nitrates with CO, which was formed *in situ* during CO₂+H₂ pre-treatment.

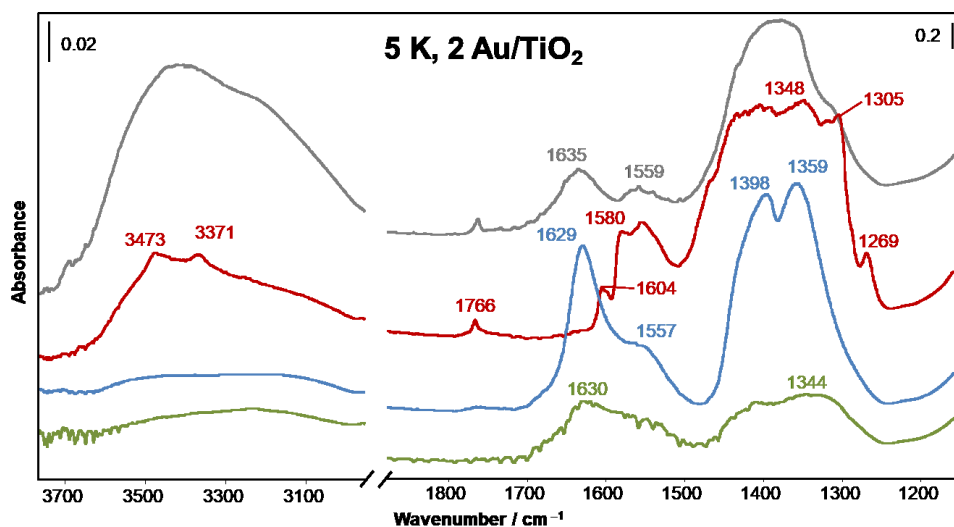


Figure 38. FTIR spectra in the νOH/CH and νOCO region of 5K,2Au/TiO₂ during CO adsorption experiments with different pre-treatments: (red) He at 200 °C, (blue) CO₂+H₂+He, 250 °C, 1 bar, (green) CO₂+H₂+N₂ at 10 bar, 250 °C. Spectra were taken after five pulses of 5 vol % CO in He and subsequent evacuation (*p* = 1 bar, *T* = -160 °C) except the grey spectra, which shows the pure catalysts without any treatment at RT.

Beside the nitrates, different carbonate and carboxylate species can be detected in the region 1269–1604 cm⁻¹ (Figure 38). Furthermore the broad band in the νOH-stretching region indicates that heating in He did not completely remove the water from the surface. The two bands at 3473 and 3371 cm⁻¹ show most probably OH groups, which are located at Au^{δ+}

support perimeter sites [197] or other cationic sites [192]. When the catalyst pre-treatment before CO adsorption is carried out under $\text{CO}_2 + \text{H}_2$ feed at ambient pressure, both bidentate ($1629/1398\text{ cm}^{-1}$) and monodentate carbonates and formates ($1557/1359\text{ cm}^{-1}$) are formed. The intensity of those bands is higher compared to the $2\text{K}, 2\text{Au}/\text{TiO}_2$ sample (Figure 37), which indicates the favorable formation of carbonate species from CO_2 at catalysts with a higher alkali metal loading and their stabilization. It is very likely that carbonates and formates are directly bound to the alkali metal or bridging K and the support, as demonstrated in Table 1 for bidentate formates on $\text{K}/\text{Al}_2\text{O}_3$ [82]. The activation at elevated pressure again results in low carbonate band intensity, similar to the findings for the $2\text{K}, 2\text{Au}/\text{TiO}_2$ sample (Figure 37). However, more bidentate carbonates were present on the $5\text{K}, 2\text{Au}/\text{TiO}_2$ catalyst than monodentate carbonates and formates, which were the dominant species on the $2\text{K}, 2\text{Au}/\text{TiO}_2$ catalyst. The same trend can be observed for the SiO_2 -based catalysts, but in that case only the alkali carbonates and formates are visible with bands at 1359 and 1394 cm^{-1} (not shown). $\nu(\text{CH})$ bands of formates could not be observed in any case. However, their presence is often discussed in literature just on the basis of $\nu(\text{OCO})$ bands, because usually the intensity of $\nu(\text{CH})$ bands is very low [51, 87]. Therefore it is assumed that formates are present, but monodentate carbonates are more abundant.

For a deeper understanding of the activation process, also simultaneous thermal analysis combining TG/DSC and MS was carried out in air as well as in a mixture of CO_2 and H_2 . Figure 39 shows the TG and DSC curves and MS profiles of the mass/charge (m/z) traces of 15, 18 and 30 for titania and silica catalysts with 5 mol % of K. Both samples show a relatively constant mass loss with increasing temperature. The formation of the $m/z = 30$ species, which is most probably assignable to NO, seems generally to be accompanied by an exothermic process. However, on the SiO_2 sample, the slightly endothermic line in the beginning indicates, that some energy is needed to start the reaction. In contrast, an immediate exothermic heat flow is accompanying the formation of the $m/z = 30$ species over $5\text{K}, \text{Au}/\text{TiO}_2$. Moreover, on both samples, the formation of a species with $m/z = 15$ can be detected, when the signal of NO decreased.

Regarding the feed composition of CO_2 and H_2 and the proven activity of both catalysts for RWGS reaction, it can be assumed that the $m/z = 15$ species is the signal of methane. Furthermore, the previous FTIR spectroscopic studies revealed that the nitrates were decomposed during $\text{CO}_2 + \text{H}_2$ pre-treatment, in which CO was most likely formed. Hence, two possible reaction pathways can be discussed for NO formation: (i) the probably reduction of nitrates by *in situ* formed CO formed in the RWGS reaction or (ii) direct reduction of nitrates by hydrogen. In both cases, it seems logic that the formation of methane is first initiated when one of the educts (CO/H_2) is no longer necessary for nitrate reduction. The accompanying water formation following the $m/z = 18$ trace, confirms the methane formation, since water is a side-product.

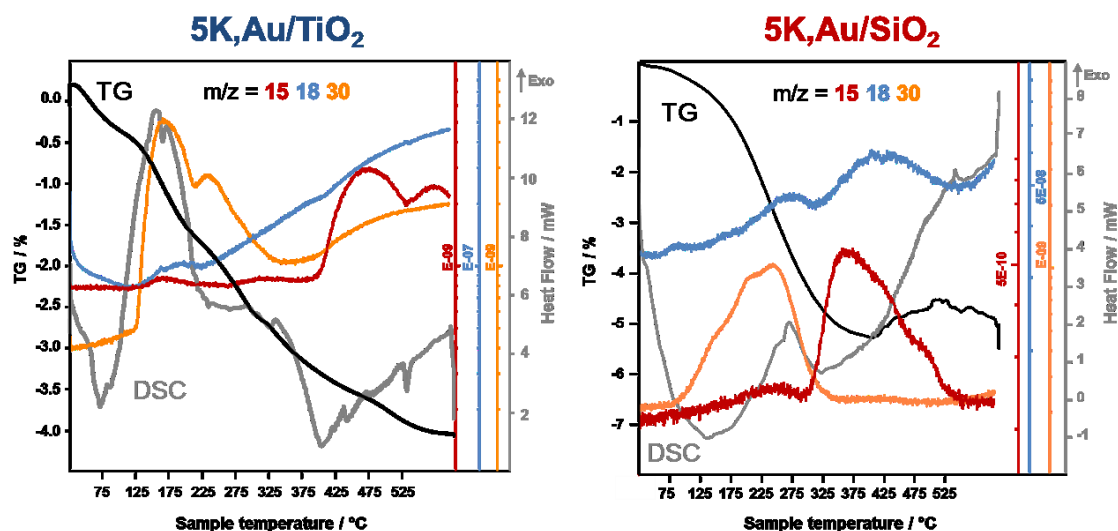


Figure 39. Simultaneous thermal analysis (TG-DSC-MS) of 5K,Au/TiO₂ and 5K,Au/SiO₂ in a gas mixture of 20% CO₂ + 20% H₂ + He (heating rate = 5 K min⁻¹).

The simultaneous thermal analysis of the same samples in air revealed that the decomposition of nitrates started at higher temperatures and results also in other species (Figure A. 17). The formation of a $m/z = 15$ species was not observed, which supports the assumption, that this fragment can be related to methane, the formation of which is not expected in the absence of hydrogen. Instead, traces of $m/z = 44$ and 46 were detected, which might be related to N₂O and NO₂, respectively, but the 44 trace could also be assigned to CO₂. Over the titania based sample, the simultaneous appearance of NO, N₂O and also NO₂ at around 275 °C indicate the stepwise reduction of the nitrate. On 5K,Au/SiO₂ also water, NO and N₂O traces can be measured, but the formation starts at higher temperature compared to the titania sample.

Conclusions on different activation procedures

The previously described experiments revealed that the activation process with CO₂ and H₂ has an influence on the gold oxidation state and also on the adsorbate species formed on the support and alkali metal surface. It is principally necessary to reduce the catalyst before the reaction, because the Au NPs are to a large extent in a partially positive state after calcination in air, indicated by the Au^{δ+}–CO band around 2125 cm⁻¹ (Figure 33). Because hydrogen activation is known to occur on Au⁰, a reducing activation procedure is needed. Moreover, it could be observed, that the addition of alkali metals increase the amount of hydroxyl groups, which were found to be important for RWGS reaction [60, 85]. On the other hand, a too high alkali metal loading decreased the number of accessible Au adsorption sites, most probably because the alkali metals cover the Au NP surface. This effect is visible for TiO₂ and also SiO₂, although the surface area of SiO₂ is much larger. In principle, the adsorption of CO on Au/TiO₂ samples is stronger than on SiO₂, irrespective of the alkali metals (K or Cs) and their loading. This might be related to larger Au NP on SiO₂, which have less corner and edge sites favoring the adsorption [121, 170] as confirmed by TEM measurements

(Chapter 4.2.1). On the other hand, the energetically more favorable situation on TiO_2 due to the semiconductor property facilitates the adsorption in distributing electron density from CO σ -donation on the Au particle or supports the π -backdonation from reduced Au into the $2\pi^*$ orbital of CO [84, 170].

Another important effect of the activation is the reduction of nitrates remaining from preparation, which proceeds more easily over the TiO_2 samples. The simultaneous thermal analysis of the highly potassium loaded samples in CO_2+H_2 gas atmosphere (Figure 39) indicates that either CO or hydrogen reduce the potassium nitrate species forming NO. The reduction of nitrogen oxides by CO to form NO was already found for gold catalysts [201]. Furthermore, the activity of other noble metal catalysts for such a reaction was also proven [202-203]. There, the authors claim that the reduction of nitrate directly proceeds at the active metal (*e.g.* Pt) forming nitrites and finally nitrogen. So it can also be conceived that nitrates in the neighborhood of gold are reduced, possibly assisted by hydrogen.

Moreover, the restructuring of carbonate and carboxylate species on the surface of the catalysts under pre-treatment in CO_2 and H_2 may play a role for activation of the catalysts. The fresh potassium containing gold catalysts were covered with uncoordinated carbonate and carboxylates. During activation with CO_2 and hydrogen these species disappeared, while mainly mono- and bidentate carbonates were formed. The titania-based catalyst with 2 mol % potassium showed a higher amount of adsorbed monodentate carbonate compared to the 5 mol % potassium containing sample, where mainly bidentate carbonates were adsorbed. Generally, the high-pressure pre-treatment leads to a reduced intensity of all adsorbate bands, which points to a restructuring of the catalysts surface.

4.2.6 Mechanistic *in situ* and *operando* studies at high pressure

For elucidating the reasons for the different catalytic performances and also for gaining mechanistic insight into the alcohol formation from CO₂, H₂ and C₂H₄ over the alkali modified gold catalysts, *in situ* and *operando* studies at high pressure were carried out.

To get a first overview of the surface species of the fresh and heated samples, Figure 40 displays the spectra of all catalysts, which were later studied in the *in situ* and *operando* experiments. All titania based catalysts showed a band at around 1637 cm⁻¹ in their fresh state at ambient temperature, which can be assigned to the bending vibration of adsorbed water molecules [194–195, 204]. The corresponding band on SiO₂ appears at 1632 cm⁻¹. Moreover, on all silica catalysts, also without alkali metals, two bands are visible at 1985 and 1873 cm⁻¹, which arise from a combination of Si–O vibration bands of the support and virtually do not change during the experiments [205]. Generally, in the not presented OH/CH stretching region of fresh catalysts, water bands are measurable, which disappear after heating (*cf.* Figure 37/Figure 38).

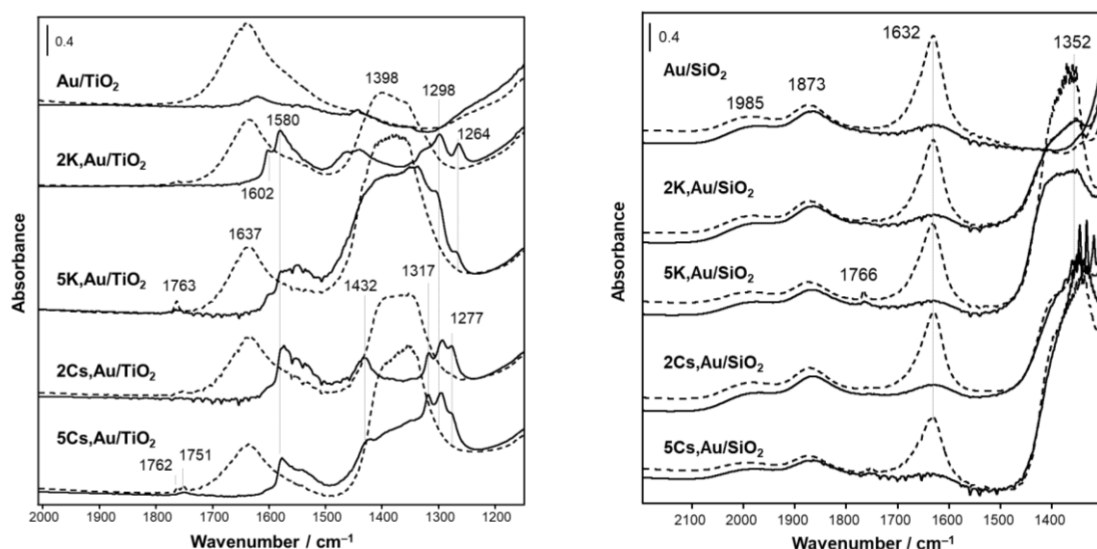


Figure 40. FTIR spectra of Au/TiO₂ (left) and Au/SiO₂ (right) catalysts: fresh and untreated at room temperature (dashed line) and after heating in N₂, 250 °C, 1 bar (solid line).

Beside the bands of adsorbed water, also broad bands of uncoordinated carbonate and carboxylate species arise on TiO₂ catalysts between 1310 and 1400 cm⁻¹ [117]. These bands are principally larger on samples with a higher alkali metal loading, most likely caused by the increased basicity of the surface, where atmospheric CO₂ easily adsorbs, or by the presence of alkali carbonates [206]. The transformation of those surface species during heating in inert gas was already discussed in the previous chapter. In short, hydrogen carbonates, bidentate carbonates and monodentate carbonates are formed on TiO₂ samples loaded with 2 mol % alkali metal.

Again, the 5 mol % loaded samples showed obviously more intense bands between 1300 and 1400 cm⁻¹ also after heating. This suggests that these carbonate and carboxylate species

are more stable and could not be transformed or removed during heating in inert gas. Presumably, a reductive feed is necessary for that. On the samples containing 5 mol % K or Cs typical combination bands of nitrates are observable in the region around $1751\text{--}1766\text{ cm}^{-1}$ [199]. The broad and intense bands between 1300 and 1400 cm^{-1} most probably also arise from nitrates.

4.2.6.1 Operando FTIR/GC experiments with long-term exposure

For gaining insight into the product formation over the prepared alkali metal modified gold catalysts, operando FTIR/GC experiments were carried out at $200\text{ }^{\circ}\text{C}$ and 10 bar pressure using a feed of $\text{CO}_2\text{:H}_2\text{:C}_2\text{H}_4\text{:N}_2 = 1\text{:}1\text{:}1\text{:}1$. A pre-activation was executed for several hours at $250\text{ }^{\circ}\text{C}$ in a CO_2 rich feed, similar to that in the catalytic reactor test (Chapter 4.2.2). The obtained spectra of TiO_2 based catalysts after activation and during feed exposure as well as after flushing with nitrogen after the reaction are displayed in Figure 41.

These three catalysts exhibited different performances in the catalytic tests. While the 2Cs,Au/TiO_2 sample presented the highest yield (*cf.* Figure 22) and selectivity to 1-propanol (CO_2 based, *cf.* Figure 23), 2K,Au/TiO_2 provided the second highest yield, but medium selectivity. As already discussed, the 5Cs,Au/TiO_2 sample was the one, which almost produced no 1-propanol and only small amounts of CO , with a low overall conversion of CO_2 as well as ethene. The FTIR experiments should now help to determine the reasons for this behavior.

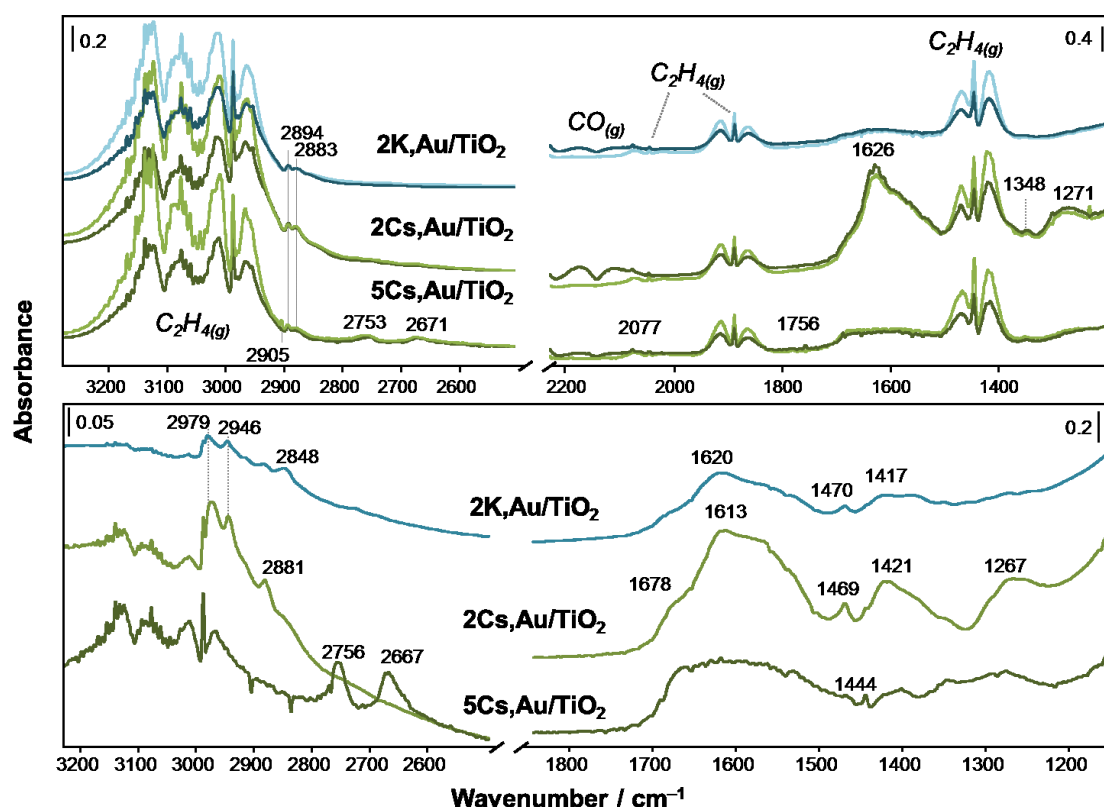
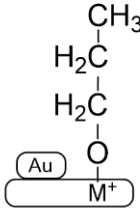
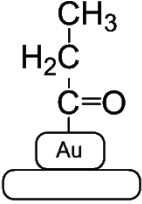
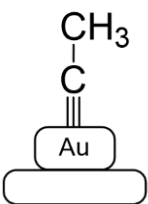


Figure 41. FTIR spectra of Au/TiO_2 catalysts in high-pressure *operando* study of 1-propanol synthesis, Top: after 14 h in activation feed with $\text{CO}_2\text{:H}_2\text{:C}_2\text{H}_4\text{:N}_2 = 4\text{:}2\text{:}1\text{:}1$ at $250\text{ }^{\circ}\text{C}$ (dark spectra) and after 5 h in feed of $1\text{:}1\text{:}1\text{:}1$ at $200\text{ }^{\circ}\text{C}$ (bright spectra), ($p = 10\text{ bar}$, total flow rate = $6.6\text{ ml}\cdot\text{min}^{-1}$), Bottom: spectra recorded after reaction and flushing with nitrogen at $200\text{ }^{\circ}\text{C}$, $p = 1\text{ bar}$.

After 14 h in activation feed, bands of gaseous ethene dominate all spectra in the CH–stretching region between 2905 and 3200 cm^{−1}, with additional bands centered at 2046, 1889 and 1445 cm^{−1} [207]. Besides, bands of the ethene hydrogenation product ethane are visible on all catalysts at 2894 and 2883 cm^{−1} [95, 103]. Moreover, bands of gaseous CO can be observed with different intensities, where the 2Cs,Au/TiO₂ catalyst produced the highest amount of gas phase CO during activation. It has to be mentioned, that carbonyl bands on gold or on the support cannot be observed, because the concentration is most likely very low, as it is directly consumed in hydroformylation reaction, or CO desorbs into the gas phase at these high temperatures. The activation also led to the decomposition of the nitrates, which could be clearly seen by bands around 1763 cm^{−1} on the fresh samples (Figure 40).

Moreover, the most striking difference in the spectra of 2Cs,Au/TiO₂ compared to the other two catalysts are the bands at 1626 and 1271 cm^{−1}, which can be attributed to bidentate carbonates [123]. On the 2K and 5Cs containing catalysts, carbonate or carboxylate species are practically not detectable after activation. Since these species were present on the fresh and also on the heated samples (Figure 40), it can be stated that the activation reduces these species on the surface. The highly cesium loaded sample also displays two bands in the CH–stretching region at 2671 and 2753 cm^{−1}, which might stem from alkali formates or formates that bridge Cs and the support [82]. However, since there are rather broad bands, in the ν(OCO) region, a proper correlation is not really reliable. Furthermore, a small band arises at 1348/1351 cm^{−1}, most intensively on the 2Cs,Au/TiO₂ sample, but it is also present on the others. That band possibly originates from a symmetrical deformation vibration of the CH₃ group of ethylidyne species (Scheme 7), which is often referred to be a spectator species that is slowly hydrogenated to form ethane [95, 103].

			
cm ^{−1}	2971, 2946, 2889, 1462, 1398	1678	2878, 1339
	Propoxy group	Acyl/Propionyl group	Ethylidyne group
Ref.	[208-210]	[91, 99-100]	[95]

Scheme 7. Possible adsorbate species in ethene hydroformylation and hydrogenation with corresponding band positions.

The observation of other intermediates of hydroformylation or at least adsorption of ethene is difficult in the complete feed due to the strong and dominating bands of gas phase ethene, which appear in the same wavenumber region. Therefore, also the spectra recorded after subsequent nitrogen exposure are shown in the lower part of Figure 41. The bands at 2979, 2946 and 2881 cm^{-1} detected on the surface of the TiO_2 -based catalysts with 2 mol % alkali metal, are vibrations of an adsorbed propoxy group, formed by 1-propanol adsorption (Scheme 7) [208-210]. Logically, the most active catalyst with 2 mol % Cs displays the most intense bands for this species. On the other hand, on the 5Cs,Au/ TiO_2 catalyst, bands of that adsorbate species could not be observed, but two bands at 2756 and 2667 cm^{-1} occur, stemming from of a C–H stretching vibration, possibly of formate origin [82]. Furthermore, the shoulder at around 1678 cm^{-1} can be assigned to the C=O stretching of a propionyl group and is visible on all samples [99-100]. Additionally, the small bands, which arise also on all catalysts between 1444 and 1470 cm^{-1} might stem from a propoxy group [208].

The same measurements were performed with two silica based catalysts with 2 mol % of K or Cs, respectively. These catalysts exhibited similar conversions of CO_2 and ethene in the catalytic tests, but the 1-propanol selectivity was higher over the 2Cs loaded sample. The FTIR spectra recorded during activation, long-time experiments and nitrogen flushing are displayed in Figure 42. According to the spectra obtained for titania-based catalysts, gas phase ethene bands (assigned in the figure) are mainly visible in the spectra measured in acti-

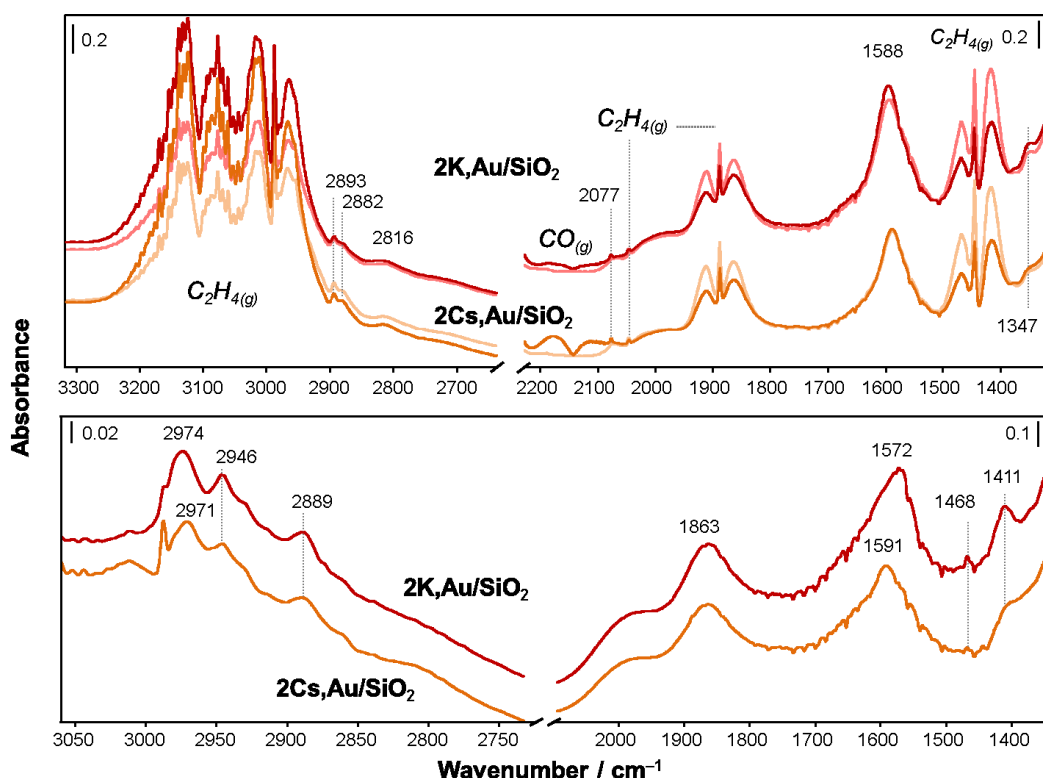


Figure 42. FTIR spectra of Au/ SiO_2 catalysts in high-pressure *operando* study of 1-propanol synthesis, Top: after 15 h in activation feed with $\text{CO}_2\text{:H}_2\text{:C}_2\text{H}_4\text{:N}_2 = 4\text{:}2\text{:}1\text{:}1$ at 250 °C (dark spectra) and after 5 h in feed of 1:1:1:1 at 200 °C (bright spectra), ($p = 10$ bar, total flow rate = $6.6\text{ ml}\cdot\text{min}^{-1}$), Bottom: spectra recorded after reaction and flushing with nitrogen at 200 °C, $p = 1$ bar.

vation feed and the normal reaction feed with CO₂:H₂:C₂H₄:N₂ = 1:1:1:1. Also here, the ethene hydrogenation product ethane is detectable with its bands at 2893 and 2882 cm⁻¹. Moreover, the band of gas phase CO can be measured in the activation feed, with a higher intensity over the catalysts with 2 mol % Cs, than over the potassium modified one, similar to the findings for the titania catalysts. Furthermore, on both samples, the bands at 1588 and 2816 cm⁻¹ indicate the presence of formates [82, 87, 143]. The shoulder at 1347 originates possibly from remaining alkali nitrates [199].

After flushing the cell with nitrogen and lowering the pressure to 1 bar, the large $\nu_{\text{as}}(\text{OCO})$ band of formate is shifted from 1588 to 1572 cm⁻¹ on the 2K,Au/SiO₂ catalyst and to 1591 cm⁻¹ on the 2Cs,Au/SiO₂ sample. This shift might be related to a different surrounding of the adsorption site and also due to a stronger (higher ν) or weaker (lower ν) binding of one of the oxygen atoms of the OCO unit to the surface [211]. Moreover, the band at 1411 cm⁻¹ becomes visible, which is either a vibrational mode of the formate or of a carbaceous species [212-213]. As was already discussed for the titania samples, also on the SiO₂ based catalysts, bands in the C–H stretching region were recorded at 2974, 2946 and 2889 cm⁻¹, which most probably originate from a propoxy group [208-209]. The two bands at around 2000 and 1863 cm⁻¹ are stemming from support Si–O vibrations and are not important for the reaction [205]. An additional small band at 2077 cm⁻¹ can always be measured during high-pressure experiments, originating from CO₂. That band is also detectable when the empty cell is filled and pressurized with CO₂ only and therefore does not represent any adsorbate in this experiment and also does not play a role in the reaction.

Simultaneously to the IR measurements, the exit gas stream was analysed with GC in analogy to the catalytic test. The results of these measurements and the respective data from the catalytic test in the reactor are listed in Table 8. Unfortunately, neither 1-propanol nor 1-propanal have been detected. Therefore, for comparing the performance of the catalysts in the *operando* spectroscopic experiments, only CO₂ conversions and CO yields were taken as a measure. But also those values were most often apparently lower than the values from the catalytic test.

Possible reasons for the different values of *operando* measurements and catalytic tests may be for example the different shape of the catalyst and its position in relation to the gas stream. The catalyst was filled into the reactor as particles for the catalytic tests, so that the reactant gas mixture can flow through the catalyst bed, which enables an intimate contact between the reactants and the catalyst surface. In contrast, the catalyst was pressed into a thin wafer during the FTIR spectroscopic experiments, so that the IR beam can pass through the sample, but this pressing decreased the surface area of the catalyst and a gas flow through the sample is not very likely.

Table 8. Comparison of values for CO₂ conversion and CO yield between catalytic test (Hector reactor) and *operando* IR/GC coupling.

Catalyst	Condition CO ₂ :H ₂ :C ₂ H ₄	X (CO ₂) / %		Y (CO) / %	
		Catalytic test	<i>Operando</i> IR/GC	Catalytic test	<i>Operando</i> IR/GC
2K,Au TiO ₂	Activation 4:2:1; 250 °C	5.6	0.3	5.5	–
	Normal Feed 1:1:1; 200 °C	3.9	–	1.9	–
2Cs,Au TiO ₂	Activation 4:2:1; 250 °C	5.9	1.0	5.6	0.02
	Normal Feed 1:1:1; 200 °C	3.4	–	0.6	–
5Cs,Au TiO ₂	Activation 4:2:1; 250 °C	2.5	1.7	2.4	0.2
	Normal Feed 1:1:1; 200 °C	0.7	0.3	0.6	0.2
2K,Au SiO ₂	Activation 4:2:1; 250 °C	3.5	5.5	3.2	–
	Normal Feed 1:1:1; 200 °C	1.1	–	0.7	–
2Cs,Au SiO ₂	Activation 4:2:1; 250 °C	5.2	0.2	4.4	0.2
	Normal Feed 1:1:1; 200 °C	2.3	0.3	0.1	0.3

Discussion of results from *operando* experiments with long-term exposure

The FTIR spectroscopic measurements during activation and long-term exposure of the catalysts to the normal feed revealed some differences concerning the supports and the kind of alkali metal modification. First of all, it could be evidenced, that the treatment in a CO₂ rich feed with hydrogen and less ethene at 250 °C caused decomposition of nitrates, which were still present after preparation and calcination. Furthermore, carboxylate and uncoordinated carbonates were removed from the fresh catalysts (*cf.* Figure 40) and bidentate and monodentate carbonates and formates were formed. This activation led to an enhancement of catalyst activity as already described [24]. Since particularly gas phase ethene dominated the spectra under real reaction conditions, the inspection of product and adsorbate formation was difficult, and adsorbates could only be analysed after flushing the cell with nitrogen. Unfortunately, it means that a real *operando* monitoring of surface species is not possible in the high-pressure setup, since educt bands are overlaying the interesting adsorbate bands and changes during reaction are difficult to observe. However, after removal of the gas phase, potential intermediates like propoxy and propionyl groups could be detected, which

give hints for a probable mechanism of alcohol formation. On the surface of the most productive catalysts 2Cs,Au/TiO₂ an apparently high amount of carbonate and during activation an appreciable CO formation was found. Contrarily, the least active 5Cs,Au/TiO₂ catalyst exhibited bands of alkali metal associated formates. On the silica-based samples, besides educt bands, mainly formates were visible, which were stable upon nitrogen flushing. Surprisingly, also the propoxy adsorbates could be measured thereafter. The differences between silica samples modified with K and Cs were not that obvious, compared to the titania-based samples.

Moreover, it has to be stated that quantitative product analysis with this particular FTIR cell was not successful. There are distinct discrepancies between catalytic tests and *operando* spectroscopic measurements. This is mainly due to the fact, that the catalysts were not particle like, but pressed into discs so that the gas stream cannot flow through the bed. Therefore, the contact between gas phase and catalyst surface was only short. The interaction of gas molecules and catalytically active sites was thus restricted and as a consequence, reactor-like performance could not be realized. Moreover, formed products may not reach the analysing GC, because of possible condensation in the lines. These lines, visible in Figure 10, were principally heated. On the other hand, they were very thin to minimize the volume, and it was difficult to wrap around the stiff heating band without any gap. Thus, it is possible that there were some spots with lower temperature. Additionally, the design of the cell was not perfectly fitting the requirements, because the cooling part around the sample holder also covered the outlet line (*cf.* Figure 11), which can also cause product condensation. Hence, in order to judge the performance of the catalysts, catalytic test results from the reactor had to be taken into account.

4.2.6.2 Step-by-step exposure to the feed components of 1-propanol synthesis

To evaluate the role of the feed components, the stepwise reaction was studied under high pressure. In general, after reducing the catalyst sample in a mixture of hydrogen and nitrogen at 250 °C for at least 30 min, the sample was exposed to $\text{CO}_2 + \text{H}_2 + \text{N}_2$ atmosphere also at 250 °C. Hence, the activity of the catalysts in the RWGS reaction was investigated by monitoring the CO evolution and also the formation of adsorbates from CO_2 and H_2 . Since adsorbate formation upon CO_2 and H_2 exposure was already discussed in chapters 4.2.5 and 4.2.6.1, only a short summary is given here. On titania-based catalysts, mainly monodentate carbonates and also bidentate carbonates were formed when the catalyst was modified with a low amount of alkali metal (*cf.* Figure 35). Bidentate carbonates and also formates cover preferentially the surface of titania-based catalysts with 5 mol % K/Cs (*cf.* Figure 36). Only formates were found after $\text{CO}_2 + \text{H}_2$ exposure to silica-based catalysts (*cf.* Figure 42).

After adsorption of $\text{CO}_2 + \text{H}_2$, ethene was filled into the IR cell, to prove if it interacts with these adsorbed species. In general, it can be observed that ethane is formed (2894, 2881 cm^{-1}) upon ethene exposure (Figure A. 18) [95, 214]. These bands grow in the first 30 min by reaction of gas phase ethene with previously adsorbed and thus activated hydrogen on the catalyst surface, most probably on gold nanoparticles. After 30 min, the intensity of these bands decreases again, which indicates, that hydrogen is consumed and hydrogenation of ethene is stopped. The adsorption of ethene itself cannot be observed, because only the gas phase bands are visible. However, it is also known from literature [207, 215-216] that ethene adsorption can only be observed at low temperature. The published results of olefin adsorption on oxide surfaces and also metal cations were obtained under liquid nitrogen cooling, which means the adsorption is often not very strong [217]. Therefore it is not surprising that no adsorption bands of ethene are observable at 200 °C.

On the other hand, it is interesting how the bands of formate and carbonate species behave on the two catalysts during ethene feeding. The bands at 1555, 1626 and 2853 cm^{-1} , ascribable to bidentate carbonates and formates on the 2Cs,Au/ TiO_2 catalyst, further increased after switching the feed from $\text{CO}_2 + \text{H}_2 + \text{N}_2$ to $\text{C}_2\text{H}_4 + \text{N}_2$. This might possibly result from residual CO_2 traces in the afferent lines. On the other hand, the formate band at 1591 cm^{-1} on the 2Cs,Au/ SiO_2 catalyst decreased slightly. This leads to the conclusion that the carbonates and formates on the TiO_2 sample are not directly reacting with ethene. Formates on SiO_2 might interact with ethene or they are principally not that stable and decompose under flushing with ethene and nitrogen. The complete set of spectra with $\text{CO}_2 + \text{H}_2$ mixture, subsequent C_2H_4 adsorption and hydrogenation and also reaction with complete feed of both catalysts with 2 mol % Cs is moreover displayed in Figure A. 19. The stability or reactivity of the formate and carbonate bands can also be observed in this figure.

In another experiment, ethene adsorption on 2Cs,Au/ TiO_2 was performed without previous $\text{CO}_2 + \text{H}_2$ exposure (Figure 43). Instead, the catalyst was only heated in nitrogen for 60 min at 250 °C. In this case, as expected, the carbonate species on the catalyst surface are different to those in the previous experiment (*cf.* Figure A. 18). Besides, the bidentate car-

bonate bands at 1572 and 1295 cm^{-1} also a band at 1432 cm^{-1} can be observed, which indicated free carbonate species [120]. Because the $\nu_{\text{as}}(\text{OCO})$ bands appear at lower wavenumbers compared to the ones after $\text{CO}_2 + \text{H}_2$ pre-treatment (1626 and 1271 cm^{-1}), it can be stated, that these species are less strongly adsorbed on the surface. This is underlined by the observation that the intensity of the respective bands decreases under C_2H_4 flow. However, a direct reaction of ethene with these carbonate species can be ruled out, since no plausible products are formed. Obviously, the adsorbed carbonate species are removed under release of CO_2 . In subsequent ethene hydrogenation feed, those carbonates were transformed into formates (1590, 2852 cm^{-1}) due to the presence of hydrogen [143]. Simultaneously, ethene was hydrogenated to ethane, but most probably independently from the transformation of the carbonates into formates, as evidenced by the assigned bands in the figure. In general, formates were always formed when CO_2 and hydrogen were present in the feed. Their formation seems to be also independent of other reactants. This is further confirmed by the spectra recorded under the complete feed. Bidentate carbonate species were also dominantly formed here (1630 cm^{-1}) on the 2Cs,Au/TiO_2 sample.

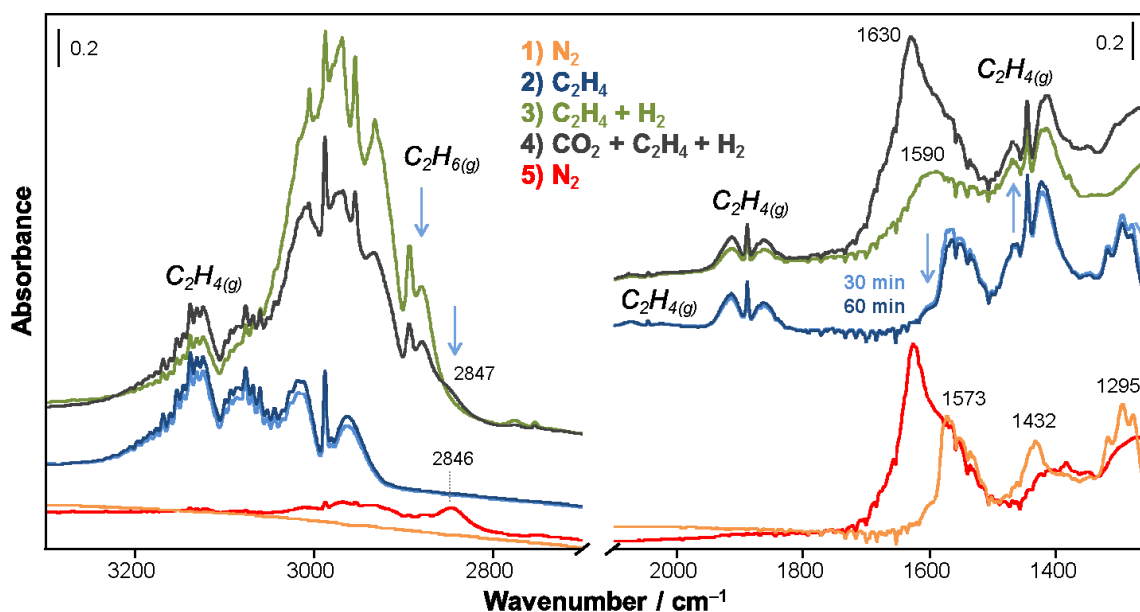


Figure 43. FTIR spectra of ethene adsorption (blue), ethene hydrogenation (green) as well as complete feed (grey) and subsequent nitrogen flushing at 1 bar, pre-treatment only in nitrogen (yellow) at 250 °C for 60 min on 2Cs,Au/TiO_2 ($T = 200$ °C, $p = 10$ bar).

The comparison of the different formed adsorbates on the catalysts is hindered by the presence of gas phase ethene. Therefore, the removal of the gas phase at the end of the experiment should help to detect the stable adsorbate species, which evolve during exposure to $\text{C}_2\text{H}_4 + \text{H}_2$ and subsequent feeding with $\text{CO}_2 + \text{H}_2 + \text{C}_2\text{H}_4$. The resulting spectra are displayed in Figure 44.

The most obvious difference here is that bands of formate species are more intense on TiO_2 -catalysts than on SiO_2 -based ones. On Au/SiO_2 , only Si–O combination bands (1864 and 1975 cm^{-1}) [205] and adsorbed water at 1631 cm^{-1} can be seen. The catalysts modified

with alkali metals also display small bands at 1602 cm^{-1} , which most probably stem from formates [83, 87]. Furthermore, nitrate bands at 1764 cm^{-1} are still present on the 5K,Au/SiO₂ catalyst. Au/TiO₂ exhibits generally non intensive bands at 1619, 1547, 1444 and 1361 cm^{-1} . They arise from mono- and bidentate carbonates [123]. Although the catalytic tests with this catalyst resulted in only small amounts of 1-propanol or 1-propanal formation [24], bands of propoxy groups are visible in the highlighted area with bands at 2970, 2955, 2940, 2929, 2883 and 2877 cm^{-1} (*cf.* Scheme 7) [208-209, 212]. So in general, alkali metals appear not to be highly important for the formation of these species.

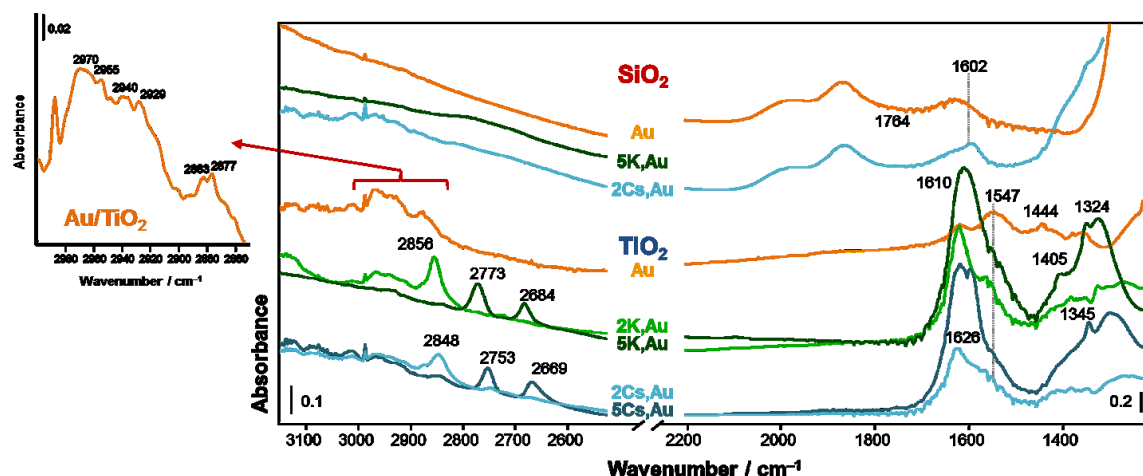


Figure 44. FTIR spectra of Au catalysts after CO₂+H₂ exposure, ethene hydrogenation and reaction in CO₂:H₂:C₂H₄ = 1:1:1 for 60 min at 10 bar and subsequent nitrogen flushing ($T = 200\text{ }^{\circ}\text{C}$, $p = 1\text{ bar}$).

Anderson *et al.* [209] discussed the formation of alkoxy species over Rh/SiO₂ and concluded that they are in fact adsorbed on the surface of the support, but the noble metal is necessary to build this molecular ensemble. It can thus be assumed, that these species are adsorbed on the titania or silica support, respectively, and gold assists in the formation of those species. However, the bands of these alkoxy species in the CH-stretching region are apparently more intense on the Au/TiO₂ sample without alkali metal modification than on the titania-based catalysts with 2 mol % potassium or cesium. This might be an indication that the presence of alkali metals facilitates the desorption or further reaction of these species, forming 1-propanol or 1-propanal. This fact is most probably the reason for the different catalytic behavior.

On the other hand, in the spectra of the highly alkali metal loaded catalysts bands of these species have only very low intensity or are not detectable. This can have two reasons: i) they desorb very fast or ii) they were not formed. The latter explanation seems more plausible, because the alcohol yields, especially over the 5Cs,Au/TiO₂, were the lowest of titania based samples in the catalytic tests (*cf.* Figure 22).

By comparing the spectra of titania-based catalyst, also different types of formates are observable. In general, for the titania-based samples with 2 mol % K or Cs, one $\nu(\text{CH})$ band is visible at $2856/2848\text{ cm}^{-1}$, while on the catalysts with 5 mol % K or Cs, two $\nu(\text{CH})$ bands

at 2773+2684/2753+2669 cm⁻¹ are observable. As expected from the different masses of potassium and cesium, the bands on samples modified with cesium appear at lower wavenumbers. It has been found by Millar *et al.* that for potassium [83, 218] and cesium formates [219] formed on doped Cu/SiO₂ catalysts, two $\nu(\text{CH})$ bands are observed, which typically arise at lower wavenumbers compared to the respective copper formate bands, which were additionally present. Therefore, on the 5 mol % alkali containing catalyst in our experiments, alkali metal formates dominate over formates, which are located on the support. The respective $\nu(\text{OCO})$ stretching and $\delta(\text{CH})$ deformation vibrational bands can be observed below 1700 cm⁻¹. On the Cs₅Au/TiO₂ catalysts, bands of formate species located at cesium oxide are present at 1598 and 1345 cm⁻¹ [153, 219], while the bands at 1626/1618, 1555 (shoulder), ~1388 (shoulder) and 1298/1270 cm⁻¹ are stemming from bidentate carbonates.

The splitting $\Delta\nu$ of the two vibrational modes of the bidentate carbonates is not only determined by the coordination mode (bidentate, monodentate, etc.), but also by the polarizing power of the coordinating cation [120, 213]. Generally, coordination to a highly polarizing ion results in a larger splitting of the bands of carbonates and vice versa. Under this consideration, the bands at 1626/1618 and 1298/1270 cm⁻¹ point to the coordination of carbonates to Ti⁴⁺ support centers and the two less intensive shoulders at 1555 and 1388 cm⁻¹ are most probably originating from bidentate carbonates adsorbed on single valence alkali metals [82]. These adsorbates can also be observed for the 5K₅Au/TiO₂ catalyst. On the 2 mol % alkali metal loaded samples, mainly bidentate carbonate species are formed adsorbed on the titania support, but as a minor fraction also carbonates coordinated to the alkali metals can be found. Moreover, only very weak bands of formates coordinated to the alkali metals can be detected. Instead, the $\nu(\text{CH})$ bands at 2856 cm⁻¹ on 2K₅Au/TiO₂ or 2848 cm⁻¹ on 2Cs₅Au/TiO₂ indicate the presence of formates, which are present on the support.

4.2.7 Interaction of educts with the catalyst surface determined by TAP experiments

For a more detailed investigation of the adsorption behavior of the reactants, time resolved pulse experiments were carried out in a TAP-2 reactor. Therefore, a mixture of the respective feed component or carbon monoxide and an inert gas was pulsed over the catalyst, which was filled in the reactor as particles, in analogy to the catalytic reactor tests. The gas traces, which left the reactor, were monitored by on-line MS. All experiments were carried out at 200 °C and under vacuum, so that no other gases interfere in the interaction between reactants and the catalyst surface. All experimental response signals were transformed into a dimensionless form as suggested in [136] to exclude the effect of diffusivity of gas-phase components on the shape of transient responses. Figure 45 and Figure 46 show the dimensionless response signals after pulsing of a H_2 :Ar mixture in the ratio 1:1 over fresh and used SiO_2 and TiO_2 samples, respectively. The grey Ar signal displays the signal shape characteristic for simply diffusion and is called standard diffusion response.

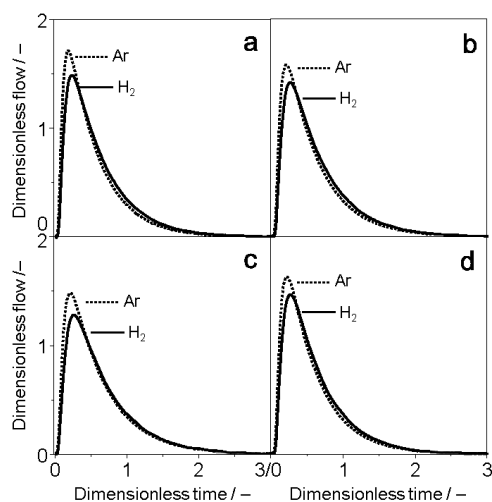


Figure 45. Dimensionless response signals after pulsing of H_2 :Ar = 1:1 over fresh (a) and used (c) 2Cs,Au/SiO_2 as well as fresh (b) and used (d) 2K,Au/SiO_2 at 200 °C.

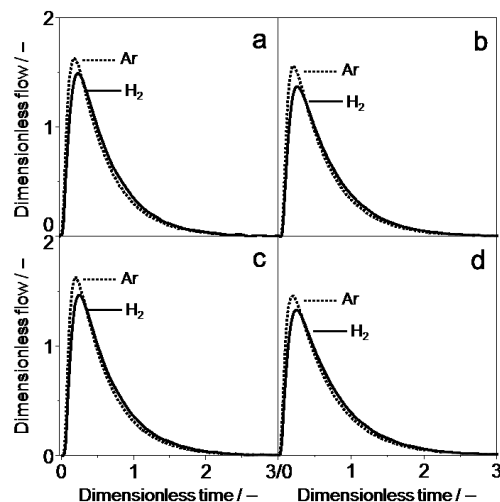


Figure 46. Dimensionless response signals after pulsing of H_2 :Ar = 1:1 over fresh (a) and used (c) 2Cs,Au/TiO_2 as well as fresh (b) and used (d) 2K,Au/TiO_2 at 200 °C.

It is clearly seen in Figure 45 and Figure 46 that the hydrogen response crosses the response of argon. According to the theory of the TAP reactor [136-137], this is a fingerprint of reversible hydrogen adsorption. In case of irreversible adsorption, the hydrogen curve would lie under the argon curve and would not cross it.

There were obviously no major differences between SiO_2 - and TiO_2 -based catalysts or the kind of alkali metal used for modification of the catalysts. Furthermore there were also no big changes, if the fresh or used catalyst was measured (Figure 45 and Figure 46). It can be seen that hydrogen weakly adsorbs on the surfaces.

In contrast, significant differences were observed between SiO_2 (Figure 47) and TiO_2 -based (Figure 48) samples in the measurements with CO_2 . The curve of the response signal

of CO₂ over used SiO₂ samples (Figure 47 c,d) is comparable to that of hydrogen, discussed above, which means, that CO₂ reversibly adsorbs on these samples. On the other hand, the CO₂ response signal of the corresponding fresh catalysts reaches its maximum at a lower flow than the Ar curve (Figure 47 a,b), but still crosses the latter. Therefore, a stronger, but nevertheless reversible adsorption of CO₂ was observed over fresh Au/SiO₂ catalysts. This finding indicates that the properties of the SiO₂–based catalysts markedly changed during reaction, so that the activation of CO₂ becomes more difficult. This might be related to the formation of stable formates, as seen by long–term IR spectroscopic experiments (Figure 42), which accumulate on the surface and probably hinder further CO₂ activation.

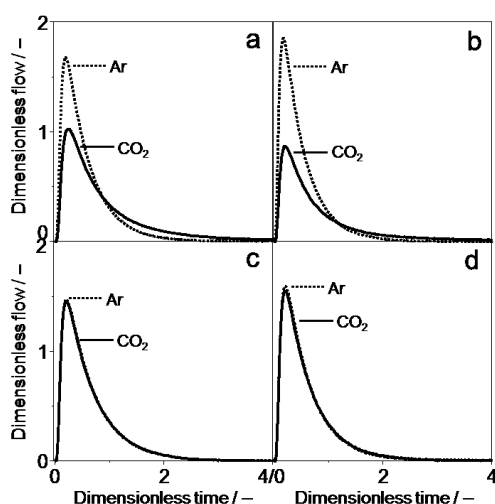


Figure 47. Dimensionless response signals after pulsing of CO₂:Ar = 1:1 over fresh (a) and used (c) 2Cs,Au/SiO₂ as well as fresh (b) and used (d) 2K,Au/SiO₂ at 200 °C.

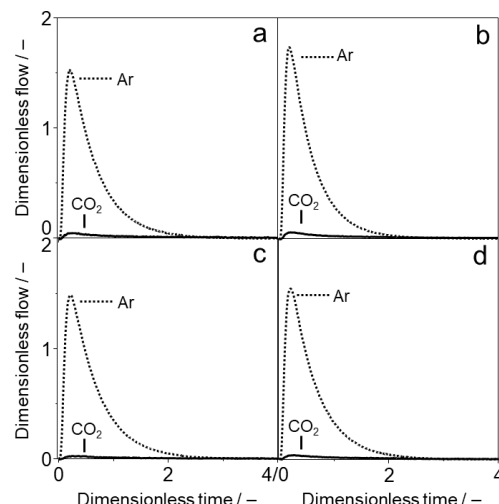


Figure 48. Dimensionless response signals after pulsing of CO₂:Ar = 1:1 over fresh (a) and used (c) 2Cs,Au/TiO₂ as well as fresh (b) and used (d) 2K,Au/TiO₂ at 200 °C.

The response signals of CO₂ on TiO₂–based catalysts (Figure 48) look quite different. The maximum flow is very low and no intersection point can be found between the CO₂ and Ar line, irrespective of the use of fresh or used samples. This indicates a very strong and irreversible CO₂ adsorption on both fresh and used TiO₂–catalysts. This finding confirms also the results from IR spectroscopic experiments, where stable carbonates and formates were formed under exposure to CO₂ (*cf.* Figure 41). However it should be noted here, that the ability of TiO₂ to adsorb and possibly also activate CO₂ still persists after long–term use in catalysis (Figure 48 c,d), which seems to make TiO₂ a superior support compared to SiO₂. It is worth mentioning that no reductive pre–treatment was carried out prior to the adsorption experiments with the used samples, which could remove the carbonate or formate species from the surface, which were formed during catalytic testing.

Furthermore, also CO adsorption experiments were carried out to test the interaction of the catalysts with this intermediate, the activation of which is important for hydroformylation. The obtained response signals are shown in Figure 49 and Figure 50. Principally, the reversible adsorption of CO is less strong than that of CO₂, and also slightly weaker than that of hydrogen. Furthermore, the used samples display commonly a slightly weaker adsorption than the fresh catalyst, irrespective of the used support and alkali metal. This is in accordance with the IR spectroscopic CO adsorption experiments carried out at low temperature (*cf.* Figure 34). One exception is the used 2Cs,Au/SiO₂ catalyst, which shows a similar behavior, equal to the fresh sample. This constant CO adsorption ability might be important for good selectivity and activity in the reaction, as can be seen in the catalytic test, where this SiO₂-catalyst was the one with the highest 1-propanol selectivity (*cf.* Figure 23) and yield (*cf.* Figure 22). However, these experiments indicate, that hydrogen is possibly preferentially adsorbed on the catalysts in comparison to CO, which explains the good hydrogenation activity. Moreover, the decreased ability of used samples to adsorb CO also means that the CO adsorption might be the key point for deactivation in long-term experiments. It has to be enabled, that the adsorption sites are free for CO activation and not blocked by formates, for example.

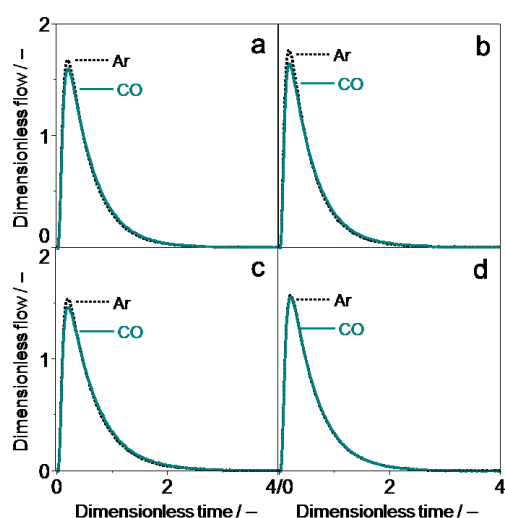


Figure 49. Dimensionless response signals after pulsing of CO:Ar = 1:1 over fresh (a) and used (c) 2Cs,Au/SiO₂ as well as fresh (b) and used (d) 2K,Au/SiO₂ at 200 °C.

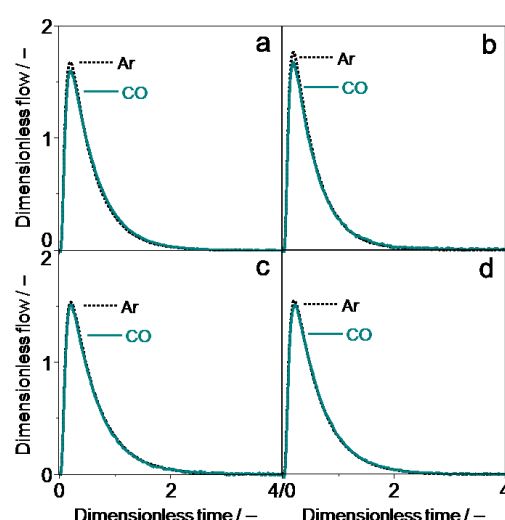


Figure 50. Dimensionless response signals after pulsing of CO:Ar = 1:1 over fresh (a) and used (c) 2Cs,Au/TiO₂ as well as fresh (b) and used (d) 2K,Au/TiO₂ at 200 °C.

Finally, ethene adsorption experiments were also performed (Figure A. 20 and Figure A. 21) and showed that the interaction of ethene with all catalysts was generally very weak. This result was expected at 200 °C, as already discussed for IR spectroscopic experiments in chapter 4.2.6.2, where also no adsorption bands of ethene could be observed.

4.2.8 Structure–reactivity relationship in 1–propanol synthesis over modified Au catalysts

The experimental results discussed in the previous chapters revealed that the dopant (potassium or cesium) as well as the supporting material (TiO_2 or SiO_2) influence the performance of the Au-containing catalysts. In the catalytic tests, higher yields of 1–propanol could be obtained using titania-based catalysts, especially the 2Cs,Au/TiO_2 catalyst performed superior to all others (*cf.* Figure 22). Also the 2K,Au/TiO_2 sample exhibited good results. Principally, a lower alkali metal loading on titania-supported gold catalysts resulted also in higher conversions of both CO_2 and ethene. However, in case of selectivity (*cf.* Figure 23), the 2 mol % K loaded Au/ TiO_2 sample was not one of the most selective catalysts. Both low and highly cesium loaded silica samples and also the 2Cs,Au/TiO_2 catalyst produced 1–propanol with higher selectivity based on CO_2 calculation. On the other hand, all silica based catalysts suppressed the ethene hydrogenation, which results in a good selectivity to 1–propanol on ethene basis. In the following paragraphs, an attempt will be made to correlate structural properties of the catalysts, determined by *in situ* and *operando* IR spectroscopic experiments and also other methods, with reactivity.

Influence of support and mechanistic considerations

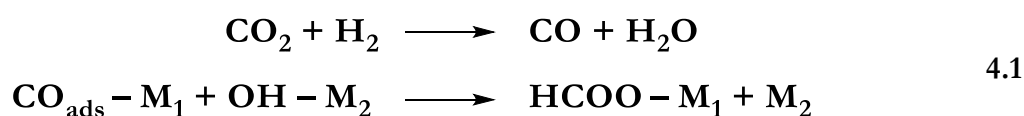
In general, the support material influences the shape and property of gold active metal and accordingly the interaction of feed components and reaction products. TEM measurements and low temperature CO adsorption experiments revealed that the support influences the size and oxidation state of the Au NP. Gold particles deposited on TiO_2 grow often associated with the support structure. During reaction, titania forms a permeable capsule around the gold, which hinders sintering of the gold particles. This effect is obviously favoured by the strong metal–support interaction between Au and TiO_2 . Therefore, Au NPs on TiO_2 are mostly smaller than on SiO_2 , although some samples also exhibited larger particles, but that seems to be rather caused by the presence of alkali metals. Freshly prepared and calcined samples predominantly exhibited oxidised gold particles, which could be (partly) reduced during exposure to $\text{CO}_2 + \text{H}_2$ or presumably also in the activation feed ($\text{CO}_2\text{:H}_2\text{:C}_2\text{H}_4 = 4\text{:2:1}$) at 250 °C. The accessibility of gold for reactants as examined by CO adsorption was mostly greater on TiO_2 than on SiO_2 , while the adsorption of CO was very weak on SiO_2 . It might be probable, that the semiconducting property of TiO_2 enables the stronger adsorption of CO on Au, by donating electron density, which increases the stability of Au–C bond. Moreover, such Au sites, which are able to adsorb CO, are also active in the dissociative adsorption of hydrogen [197]. This is furthermore the reason, why higher CO concentrations on the surface were found to suppress hydrogenation of olefins as stated in literature [105], because CO hinders hydrogen to be activated.

During *in situ* and *operando* IR spectroscopic measurements, where CO_2 and hydrogen were exposed to the catalyst sample, adsorbed carbonates were never detected on the silica based catalysts, while on titania based catalysts different carbonate species evolve, depending on the conditions and feed composition used. Principally, CO_2 can react both as acid or base

and possible adsorption sites are surface oxygen, hydroxyl groups or coordinatively unsaturated sites [117]. Titanium dioxide is a redox active solid and offers different adsorption sites, for example coordinatively unsaturated and therefore Lewis acid Ti^{4+} or basic OH groups [220]. It is moreover possible, that under reducing conditions, oxygen vacancies are formed in the titania structure, where CO_2 can also adsorb. Contrarily, on amorphous silica, mainly OH groups are responsible for CO_2 adsorption via hydrogen bonding [221]. In general, a weak adsorption of CO_2 on different silica and silica based catalysts was described in numerous studies [69, 143]. This might be the reason for the lower CO_2 activation of SiO_2 -based catalysts. This goes along with a lower amount of accessible Au sites for CO adsorption and consequently H_2 activation.

Although Ti^{4+} and Au^0 sites can stabilize ethene interaction by formation of π -complexes [222], such complex formation can be excluded under the conditions used (Figure 43). However, it can be assumed that short-lived species were present, because ethane is formed as observed. Otherwise, it can be assumed that ethene does not directly adsorb on the surface, but interacts with species adsorbed on Au, for example hydrogen. In homogeneous catalysis a concerted outer-sphere mechanism is discussed for hydrogenation of aldehydes, which was recently also assumed for the gas-phase conversion of propene to butanol via tandem hydroformylation and hydrogenation [94].

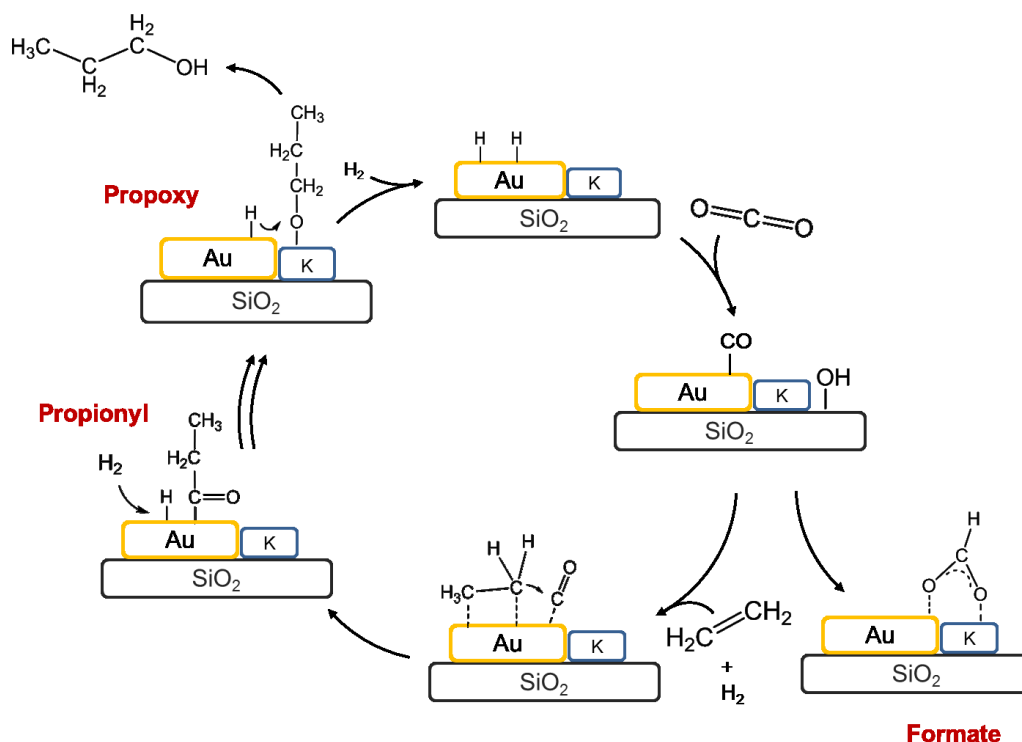
During reaction with carbon dioxide, hydrogen and ethene, formation of adsorbates was also different over SiO_2 and TiO_2 based catalysts. On SiO_2 catalysts, mainly formates were present, which were formed under participation of Au from CO_2 and hydrogen. These formates are most probably located at the interface of gold and alkali metals or in the near surrounding and are not very stable [83]. Thus it was observed in stepwise experiments, that they nearly disappeared after nitrogen flushing (Figure 44). Formates and also carbonaceous species formed on TiO_2 based catalysts do not directly react with ethene. Moreover, the direct reduction of CO_2 on the noble metal is very likely and was already observed over Rh/ SiO_2 samples [55, 223]. Formates are then formed from *in situ* generated CO, according to equation 4.1 proposed by Bianchi *et al.* [224].



Moreover, it was found for homogeneous catalysts that formates can act as hydrogen donor for aldehyde hydrogenation, while olefins were not hydrogenated by H-formate [225]. This can explain the lower ethene hydrogenation over SiO_2 -based catalysts compared to TiO_2 -based ones.

Regarding the hydroformylation reaction, there was no propionyl band visible in the experiments with SiO_2 (*cf.* Figure 42), which was observed in other studies and proposed as intermediate [95]. However, propoxy groups were present in long-term FTIR spectroscopic studies, which should be formed from propionyl species. It can therefore be stated that the propionyl intermediate is very reactive on the SiO_2 samples so that the intensity of respective bands is very low. The band at 1468 cm^{-1} (*cf.* Figure 42), which is most probably stemming

from the $\delta_{\text{as}}(\text{CH})$ vibration of the propoxy group, is more intense on the 2K,Au/SiO_2 catalyst after flushing with nitrogen, than on the 2Cs,Au/SiO_2 sample. Because the 2K,Au/SiO_2 catalyst was a catalyst with a lower selectivity towards 1-propanol, it might be that the product is stronger adsorbed on catalysts modified with potassium, which lowers the yield and selectivity of 1-propanol. The proposed reaction mechanism of this overall reaction, forming 1-propanol from CO_2 , H_2 and ethene is displayed in Scheme 8. It can be seen there, that CO_2 is directly reduced on the Au, forming carbonyl species on the latter, while the oxygen might be captured by the basic alkali metal or cationic support sites. Then, ethene is activated on the gold under assistance of adsorbed hydrogen species, in preparation for hydroformylation. The formation of stable formates from CO, possibly in the neighbourhood of alkali metals and in presence of OH groups, is proceeding in parallel. These formates most probably do not directly take part in the formation of propanol. The propionyl group is then formed by reaction of activated ethene with CO and is still attached to the gold. After further hydrogen activation, this propionyl group, which virtually represents the aldehyde, is hydrogenated to form the propoxy group and further the alcohol.



Scheme 8. Proposed reaction mechanism of 1-propanol formation from CO_2 , ethene and hydrogen over alkali modified Au/SiO_2 catalysts.

Generally, as already stated, carbonate species are more abundant on TiO_2 surfaces, also on the most active and selective 2Cs,Au/TiO_2 catalyst. Therefore it is assumed, that the majority of bidentate carbonate, which was the most abundant carbonate species, is adsorbed on the support apart from the active sites for hydroformylation/ CO_2 hydrogenation and does not hinder the reaction. On the other hand, if it is in vicinity of Au particles, it might react with hydrogen to form CO as it was stated for Pt/CeO_2 catalysts [73].

Elucidation of the role of formates, which were present in two different forms, namely adsorbed on the support and gold only (F_{Au}) and bound to the alkali metal ($F_{K/Cs}$), is a more critical issue and is therefore discussed in more detail in the next paragraph.

On the role of alkali metals

Besides the supporting material, also the nature and amount of alkali metal influences the catalytic activity and 1-propanol selectivity. However, the effects are complex and have to be differentiated.

In general, the presence of alkali metals improved the mobility of gold atoms during activation and reaction, so that single atoms can be detached from larger particles and therefore enhance the number of defect sites. The latter were proved to be more active, for example for CO adsorption or RWGS reaction [85-86]. However, this effect can only be observed for low alkali metal loadings. At higher loadings, the Au particles tend to grow. CO adsorption experiments showed that Au particles were reduced after exposure to $CO_2 + H_2$ mixture. The correlation between Au nanoparticle size, determined by TEM measurements, and valence state of Au particles, determined by CO adsorption (band intensity of Au^0-CO at 2105 cm^{-1} and $Au^{\delta+}-CO$ around 2025 cm^{-1}), as well as the relation to catalytic properties of the catalysts are displayed in Figure 51 and Figure 52.

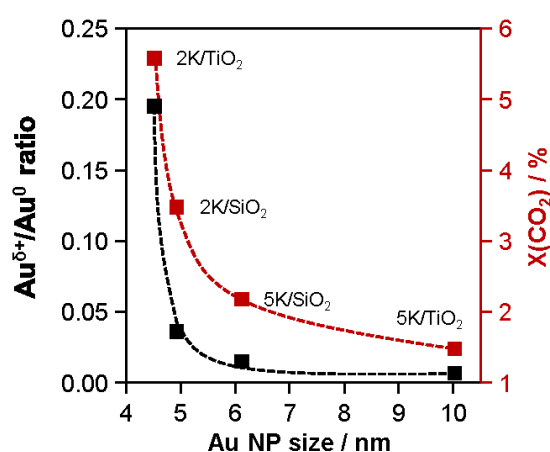


Figure 51. Correlation of Au NP size with the ratio of $Au^{\delta+}/Au^0$, determined by CO adsorption after pre-treatment in CO_2+H_2 at 1 bar (integrated area of CO bands), and conversion of CO_2 at 200 °C in $CO_2:H_2:C_2H_4:N_2 = 1:1:1:1$ feed ($p = 20$ bar).

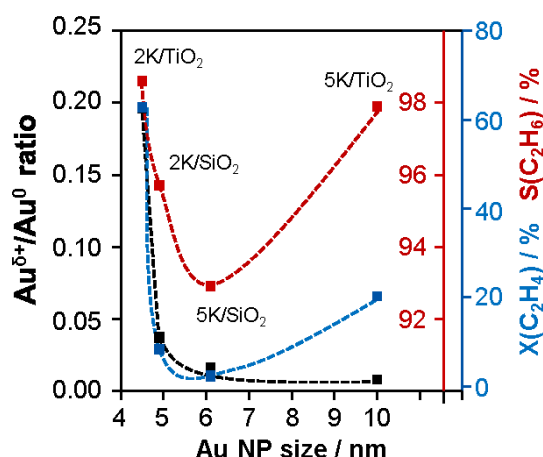


Figure 52. Correlation of Au NP size with the ratio of $Au^{\delta+}/Au^0$, determined by CO adsorption after pre-treatment in CO_2+H_2 at 1 bar (integrated area of CO bands), and conversion of C_2H_4 and selectivity to C_2H_6 at 200 °C in $CO_2:H_2:C_2H_4:N_2 = 1:1:1:1$ feed ($p = 20$ bar).

It can generally be concluded that the amount of $Au^{\delta+}$ sites decreases when the Au nanoparticles grow. This directly correlates with the decline of CO_2 conversion. It is widely accepted that larger particles exhibit less corner and edge sites and tend to be more metallic in character [163], whereas small particles offer many coordinatively unsaturated sites, which can obviously be oxidized easier (e.g. by CO_2), but also re-reduced by hydrogen, as examined by CO adsorption and different pre-treatments. As can be seen from Figure 51 the Au NP

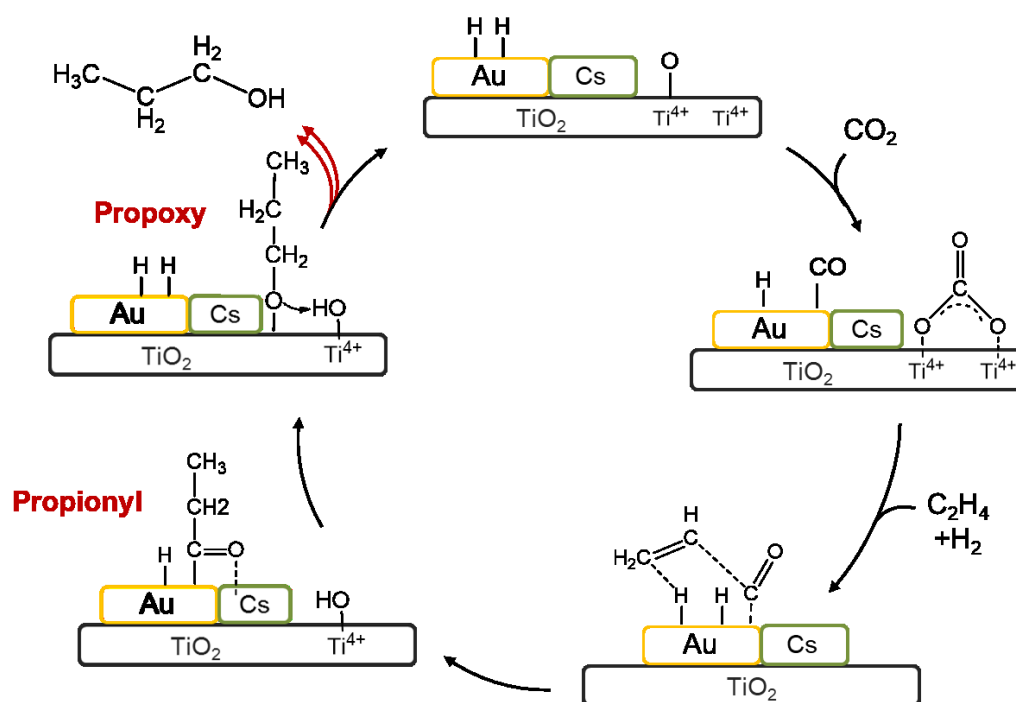
size increases with increasing alkali metal amount, leading to larger particles for catalysts with 5 mol % potassium, so that the positive effect of alkali metal modification concerning dispersion of Au and, thus, activity in CO₂ reduction, is compensated by covering of active sites at higher loadings, especially on low surface area TiO₂. The trend for ethene conversion is in principle the same (Figure 52), namely that the conversion falls with increasing Au NP size, but over the 5K,Au/TiO₂ catalyst it reached again a higher value. Naito *et al.* [106] stated that alkali metals themselves do not interfere in olefin adsorption, so it might mostly be the effect of the support, that plays a role here.

The influence of the amount of alkali metals in RWGS/hydroformylation/hydrogenation pathway was nicely visible in the *in situ* IR experiments. Principally, formation of carbonate species was enhanced by adding alkali metal, since on the pure Au/TiO₂ only small bands of them can be detected, and on Au/SiO₂ nearly no CO₂ adsorption occurred. This clearly indicates that alkali metal addition on silica catalysts is essential for this reaction. While on catalysts with 2 mol % of K or Cs, formates were only formed on TiO₂ and nearby the Au particles (F_{Au}), 5 mol % containing samples were covered with alkali metal bound formates (F_{K/Cs}), which are probably unreactive and block active sites. The coverage of Au nanoparticles in particular with the bulkier cesium atoms and corresponding formates was evidenced by CO adsorption experiments, and this is surely the reason why this catalyst is nearly inactive. Formates of type F_{Au} can be regarded as minor, but active intermediate in CO formation on Au/TiO₂ catalysts. That is concluded from the fact, that bands of this species were visible in the stepwise reaction after CO₂/H₂ exposure and subsequent feeding with C₂H₄/CO₂/H₂, but not over the 2 mol % samples in the long-term exposure test. It seems that they are formed in the beginning of the reaction, but with time, their concentration on the surface decreases. However, the major pathway for CO formation might be the direct reduction of CO₂ on Au. Formyl species, like in RWGS on potassium modified Rh catalysts, could not be detected.

By comparing the Au/TiO₂ catalyst with the two alkali promoted titania catalysts with 2 K and 2 Cs, it is evident that the intermediately formed propoxy species were more stably adsorbed on the unmodified sample, which indicates that the product desorption is easier on the doped catalyst. On the other hand, the propionyl species is stabilized in the presence of alkali metals (Scheme 9). The same has been identified for silica supported Pd and Rh catalysts used in hydroformylation of propene [226]. Furthermore, it seems to be the case that propoxy species more readily desorb from cesium modified catalysts than from potassium modified ones, which enhances their catalytic activity.

The reaction scheme for titania-based catalysts (Scheme 9) shows that CO is in principal directly formed on Au from CO₂, but in contrast to the silica-based catalysts, also carbonate species (mono- and bidentate) were created on the TiO₂, which might act as CO reservoir. However, in case of higher alkali metal content, the amount of especially bidentate carbonates increases, which can block active sites and leads then to inactivity. The next steps, ethene activation and hydroformylation on gold as well as the hydrogenation of the intermediate propionyl and propoxy groups most likely proceeds similar to silica-based catalysts. On the other hand, the already described formates F_{Au} and F_{K/Cs}, the formation of which is de-

pendent on the abundance of alkali metals, strongly affect the propanol formation in blocking active sites. Chelating alkali metal formates ($F_{K/Cs}$) are most probably the species, which hinder the alcohol production the most.



Scheme 9. Proposed reaction mechanism of 1-propanol formation over 2Cs,Au/TiO₂.

The stepwise IR experiments moreover showed that over the catalysts loaded with 5 mol % alkali metal, it is more difficult to reduce the nitrates. Especially on the silica catalysts, also after reaction, bands of nitrates were still present and can lower the activity.

In conclusion, it has been shown by FTIR spectroscopic and TAP experiments that the TiO₂-support enables the CO₂ activation, which is further increased by alkali metal modification. The latter is quite essential for the activation of the greenhouse gas on SiO₂-based catalysts and also for desorption of the product 1-propanol, which was stably adsorbed on non-modified gold catalysts. Cesium was discovered to increase desorption to a higher extent than potassium and, thus, leads most often to higher propanol yields and selectivities over the catalysts modified with this alkali metal. On the other hand, high alkali metal loadings also promote the formation of stable formates and carbonates, which block active sites, for example for CO adsorption, as shown by TAP experiments with used catalysts. Lower alkali metal loadings also favor the formation of formates, but in this case, they were more reactive and, thus, they do not hinder the 1-propanol synthesis.

4.2.9 Catalytic testing of modified Au catalysts in butanol synthesis at 8 bar

This chapter comprises the results obtained from catalytic testing of the prepared catalysts in the butanol synthesis from carbon dioxide, hydrogen and propene at 8 bar. For comparison, also results of testing the 1-propanol synthesis with ethene as a feed olefin at this lower pressure will be discussed. It has to be mentioned that the catalyst samples tested at 8 bar were not identical with those from the tests at 20 bar. Therefore, the alkali metal concentrations were slightly different. Moreover, *in situ* FTIR studies are presented to gain insight, if the hydroformylation/hydrogenation reaction with propene proceeds differently compared to that of ethene.

As already mentioned in the introduction, the experiments with propene to produce 1-butanol and *iso*-butanol are carried out with 8 bar pressure, because the vapor pressure of propene is only around 10 bar at room temperature. Therefore, the experiments could not be performed at the same pressure as the ethene experiments (20 bar). To compare the results of both reactions, additional 1-propanol formation experiments were carried out at 8 bar.

In Figure 53, the conversions of CO_2 as well as ethene or propene, respectively, are shown over different modified gold catalysts. Compared to the experiments at 20 bar (Figure 24), the conversion of CO_2 is slightly lower in the propanol synthesis at 8 bar (Figure 53, c). The general behavior of the catalysts at 8 bar is comparable to that at 20 bar. Thus, the very active $2\text{Cs}_3\text{Au}/\text{TiO}_2$ catalyst at 20 bar is also the most active one at 8 bar. However, the CO_2 conversion is lowered from circa 5.5% to 3.8% in the 1:3:3:1 feed. Moreover, the silica based catalysts are still less active than the low alkali metal loaded titania catalysts, but their activity did not decrease that strongly at reduced pressure. Vice versa, a more striking effect of the lower pressure can be observed for the ethene conversion, which decreased on all samples (*cf.* Figure 25). This effect was most obvious on the titania-based catalysts, where the ethene conversion of the $6\text{K}_3\text{Au}/\text{TiO}_2$ catalysts decreased from 22% to 5.5% (1:3:3:1 feed) and over $2\text{Cs}_3\text{Au}/\text{TiO}_2$ from 42% to 12.2%.

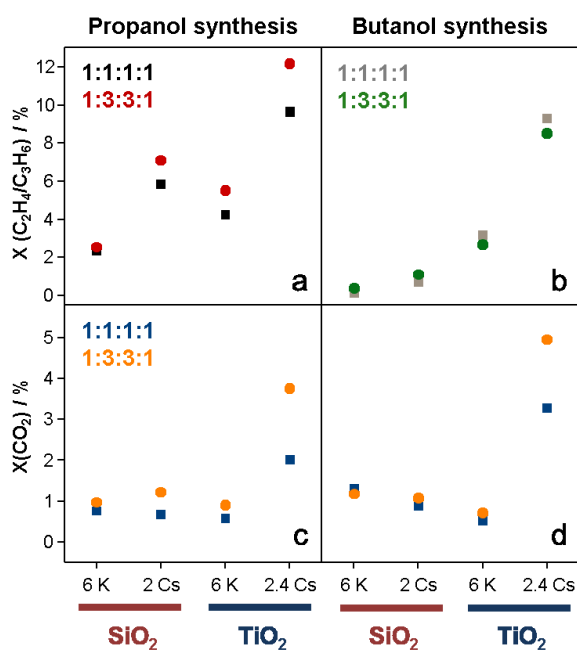


Figure 53. Conversion of ethene (a) or propene (b) and CO_2 in propanol (c) and butanol (d) synthesis, respectively, with different feeds of $\text{CO}_2:\text{H}_2:\text{C}_2\text{H}_4/\text{C}_3\text{H}_6:\text{N}_2$ ($p = 8$ bar, $T = 200$ °C, $\tau = 43$ $\text{g}_{\text{Cat}} \cdot \text{min} \cdot \text{L}^{-1}$).

Furthermore, it was found that the conversion of CO_2 practically did not change, regardless of the used olefin (Figure 53 c,d). Only for the 2.4Cs,Au/ TiO_2 catalyst, a slight increase of about 1% has been determined in the butanol formation feed. Major differences become evident for the conversion of the olefin. In general, the conversion of propene was lower than that of ethene over all samples, but particularly the silica-based catalysts displayed a very low value of around 1% for the K loaded or 2% for the Cs loaded sample only. Such low propene conversion was already described in literature for the hydroformylation of propene over Rh/ SiO_2 catalysts [97]. However, it was also found, that it can be increased by working at higher pressures, but also using a higher H_2 and CO to propene ratio [93]. In this case, propene conversion reaches 40% at 210 °C and 50 bar pressure in liquid phase.

Due to the low conversion over silica catalysts, also the yield of *n*-butanol and *iso*-butanol together was less than 0.2% as depicted in Figure 54. But although the conversion was higher over the titania catalysts, the yield of butanols using titania catalyst was also considerably lower compared to the propanol yield obtained at 8 bar, as displayed in Figure 55. The influence of the feed can clearly be observed, reaching always higher yields using the 1:3:3:1 feed. Compared to the experiments at 20 bar (*cf.* Figure 22), only half of the 1-propanol yields were obtained. This suggests that higher pressures are needed to enhance the alcohol formation from CO_2 , H_2 and ethene.

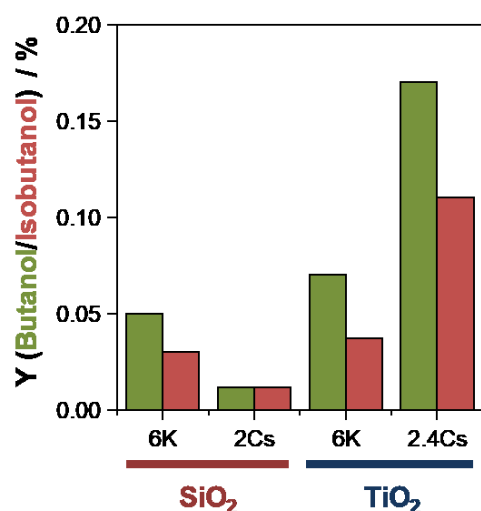


Figure 54. Yield of 1-butanol (green) and *iso*-butanol (red), calculated on CO_2 basis, at 8 bar over different Au/ SiO_2 and Au/ TiO_2 catalysts with feed of $\text{CO}_2:\text{H}_2:\text{C}_3\text{H}_6:\text{N}_2 = 1:1:1:1$ ($T = 200\text{ }^\circ\text{C}$, $\tau = 43\text{ g}_{\text{Cat}}\cdot\text{min}\cdot\text{L}^{-1}$).

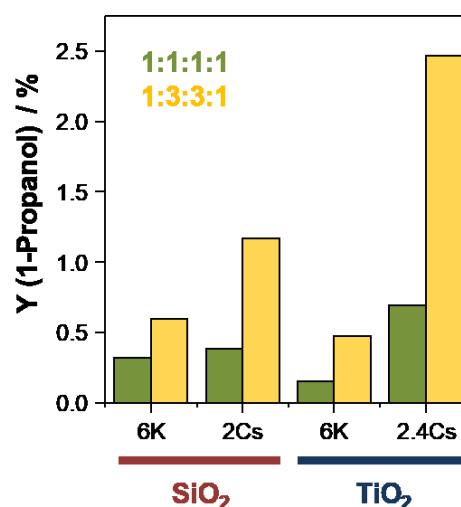


Figure 55. Yield of 1-propanol, calculated on CO_2 basis, at 8 bar over different Au/ SiO_2 and Au/ TiO_2 catalysts at varied feeds of $\text{CO}_2:\text{H}_2:\text{C}_2\text{H}_4:\text{N}_2$ ($T = 200\text{ }^\circ\text{C}$, $\tau = 43\text{ g}_{\text{Cat}}\cdot\text{min}\cdot\text{L}^{-1}$).

In the hydroformylation with propene, both 1-butanol and *iso*-butanol were formed (Figure 54). Moreover, the amount of the linear alcohol was mostly higher than that of the branched one. This is also reflected by the obtained selectivity in the experiments at 8 bar, calculated on CO_2 basis (Figure 56). While the propanol selectivity at 8 bar was always higher than 50 %, and reached even 96% for the 2Cs,Au/ SiO_2 catalyst, the highest 1-butanol selec-

tivity with 8.2 % was obtained over 6K,Au/TiO₂. In reaction with propene, carbon dioxide and hydrogen at 8 bar, CO was the dominating product over all catalysts.

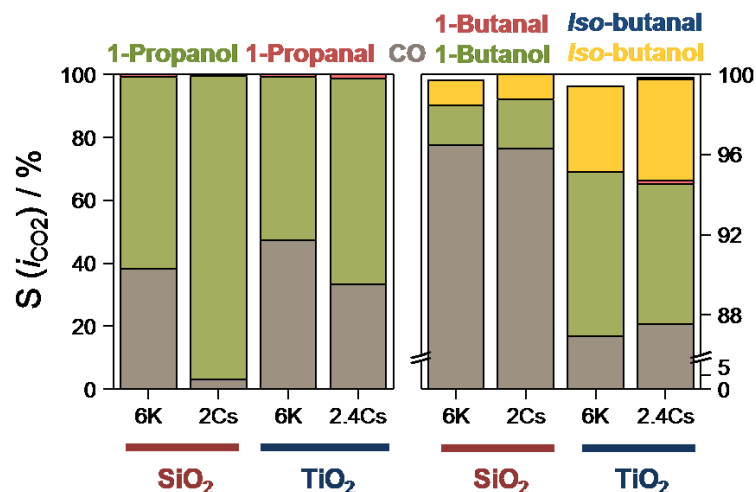


Figure 56. Selectivity to obtained products in alcohol synthesis, calculated on CO₂ basis, at 8 bar with a feed of CO₂:H₂:C₂H₄/C₃H₆:N₂ = 1:3:3:1 (T = 200 °C, τ = 43 g_{Cat}·min·L⁻¹).

Because the butanol synthesis by an advanced tandem hydroformylation–hydrogenation route with heterogeneous catalysts was investigated for the first time, no literature data is available for comparison. Only in the hydroformylation with CO and propene, the chemoselectivity towards linear or branched aldehyde was discussed [91, 94, 97, 106, 226]. In most

cases, the linear aldehyde was preferentially formed, which might be related to a lower activation energy. This was also discussed for alkali metal promotion. For example on silica supported Rh and Pd catalysts, sodium modification was found to enhance the turnover frequency of propene hydroformylation, sometimes also the rate of hydrogenation, but with a lower factor [97, 226].

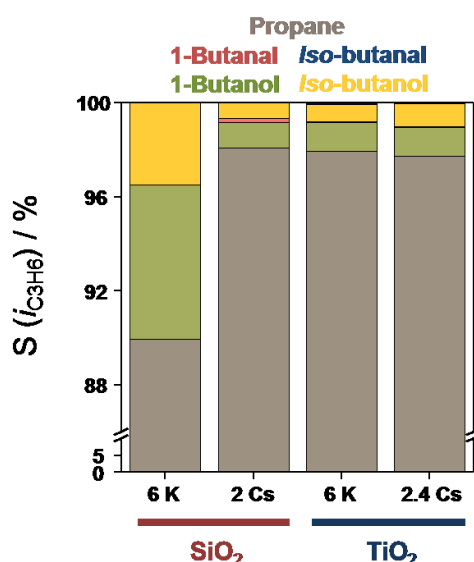


Figure 57. Selectivity to obtained products in alcohol synthesis, calculated on C₃H₆ basis, at 8 bar with a feed of CO₂:H₂:C₃H₆:N₂ = 1:1:1:1 (T = 200 °C, τ = 43 g_{Cat}·min·L⁻¹).

In the experiments discussed here, hydrogenation of the olefin as the most undesired side-reaction is responsible for the loss of the majority of propene (Figure 57). Thus, the selectivity towards propane from propene always reached more than 89%. Comparable selectivities were obtained in the propanol synthesis (cf. Figure A. 11). However, the potassium modified silica catalysts showed again the highest selectivity to the *n*-alcohol, as it was already demonstrated for the experiments with ethene. Obtained selectivity in 1:3:3:1 feed is displayed in Figure A. 16.

4.2.10 *In situ* FTIR studies of butanol formation

In the following section, results of *in situ* FTIR spectroscopic measurements of butanol synthesis at 8 bar are discussed, which were also carried out in the high-pressure cell. Spectra of four selected catalysts are displayed in Figure 58. They were pre-reduced in 10% H₂/N₂ flow and subsequently pre-treated with CO₂+H₂/N₂. Afterwards the samples were exposed to the C₃H₆/CO₂/H₂ mixture for butanol synthesis for 2 h. For clarity, only the spectra at the end of the exposure to the butanol synthesis gas mixture are shown for each catalyst.

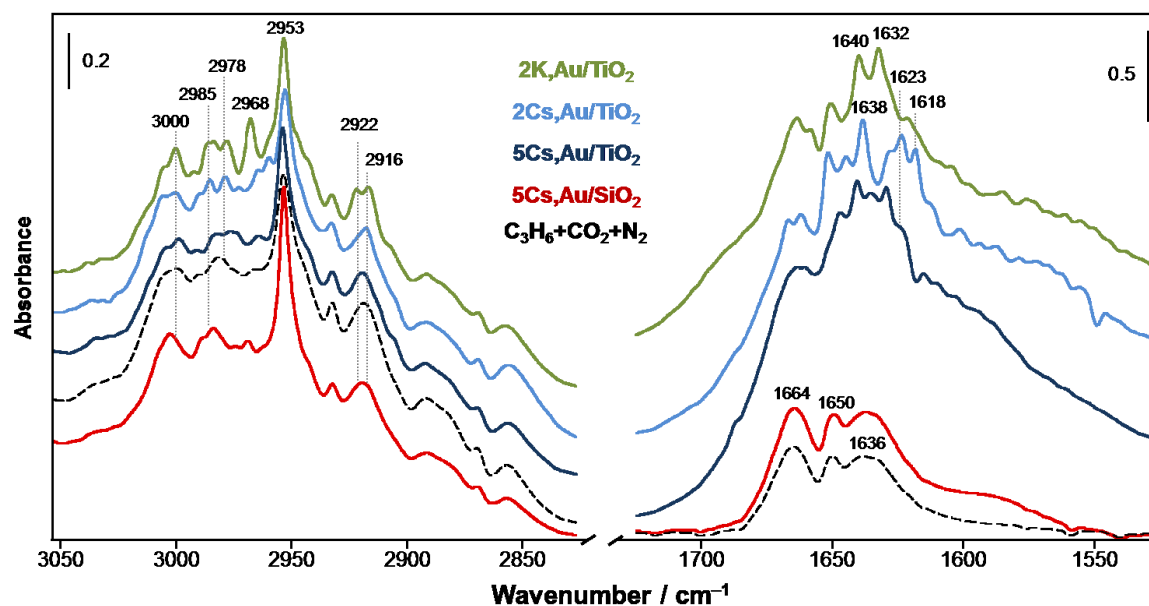


Figure 58. Normalized FTIR spectra of four selected catalysts after 2 h in CO₂:H₂:C₃H₆ = 1:1:1 stream (T = 200 °C, p = 8 bar) and spectra of C₃H₆ + CO₂ in the empty cell (black dashed line)

To distinguish between gas phase propene bands and newly developed bands, probably from adsorbed species, Figure 58 contains also the gas phase spectrum of propene measured at 8 bar in the empty cell. Adsorption of propene on solid surfaces often results in the shift of the vibrational bands to lower wavenumbers [215-216, 227-228]. From this literature, it can be expected that the interaction of propene with the catalysts might be stronger compared to ethene, where a distinct adsorption could not be observed. However, propene adsorption is hardly detectable on the gold catalysts. Differences between TiO₂- and SiO₂-based catalysts can be observed only in the lower wavenumber region in Figure 58. While the 5Cs,Au/SiO₂ catalyst showed nearly the same bands, which were observed for gas phase propene, over titania-based catalysts bands arise, which might point to an adsorption of propene to the surface.

Davydov [215] proposed two possible adsorption classes for non-dissociative propene adsorption on metal oxide surfaces. These are i) coordination via hydrogen bonds or ii) as a π -complex with a metal center. The latter form of adsorption is most stable, when the metal is in a low-valence state, meaning Me⁰ or in this case Au⁰-propene complexes should be more stable than for example the coordination to Ti⁴⁺ centers. On the other hand, propene

adsorption through hydrogen bonds is expected to occur on surface oxygen atoms, but this binding type is said to be noticeably weaker than π -complexes. Under this consideration, it seems probable that on catalysts with only 2 mol % of alkali metal the olefin adsorption might be stronger, because CO adsorption (*cf.* Figure 35 and Figure 36) proved that the amount of Au⁰ in particular, but also the number of accessible Au sites in general is higher on these samples. This assumption supports moreover the finding that the activation, which creates the Au⁰ adsorption sites, is mandatory.

It was furthermore predicted by Panayotov *et al.* [227] that propene first adsorbs on Au–TiO₂ interface sites, before binding to coordinatively unsaturated sites of Au. For determination of the type of adsorption, the position of $\nu(\text{C}=\text{C})$ band is most often used. In case of a π coordination to Au sites, this band is expected to arise at around 1550 cm⁻¹ [228], while a binding to titania would result in a band at 1635 cm⁻¹ [215]. Unfortunately, the interpretation of the spectra in Figure 58 is difficult, because gas phase propene (1665, 1650 and 1637 cm⁻¹) is present and overlays the bands of possibly adsorbed propene. Nonetheless, it can be stated that the olefin interacts more strongly with the TiO₂-based catalysts compared to the SiO₂-based catalyst, because the C=C double bond, which arises at 1650 cm⁻¹ in gas phase, is not shifted and therefore not influenced on the SiO₂-based catalyst. This means, if propene adsorbs on the 5Cs,Au/SiO₂ catalyst, it is only a weak and most probably molecularly interaction.

In contrast to this behavior, propene interaction with the titania-based catalysts resulted in various new bands for example at 1631, 1624, 1619, 1609 and 1593 cm⁻¹. The band at 1631 cm⁻¹ might arise from propene adsorbed on Ti⁴⁺ sites [228], where the others might result from interaction of propene with Au–TiO₂ interface, different Au NP sites, or also interaction with the alkali metal ions. However, a detailed assignment would be very speculative.

As already observed in the ethene experiments, gas phase olefin bands are mostly covering bands of adsorbate species during exposure to the feed. Therefore the spectra recorded after nitrogen flushing after 4 h in butanol synthesis feed are displayed in Figure 59. The most intensive band on all titania catalysts is the band around 1621 cm⁻¹, which might consist of different species, because it exhibits various shoulders. Comparing the spectra after nitrogen flushing in butanol synthesis with those after the same treatment in the propanol synthesis (*cf.* Figure 44), the bands around 1621 cm⁻¹ are here generally more intense, pointing to a higher coverage of the surface with stable adsorbates. For example on 2K,Au/TiO₂, a broad band is visible at around 1678 cm⁻¹. This band probably stems from $\nu(\text{C}=\text{O})$ vibration of an acyl group, which is in this case more stable on the surface of the 2K,Au/TiO₂ sample than on cesium modified samples. This probable butanoyl group can be suggested as intermediate in 1-butanol formation in accordance to the propionyl group in propanol formation.

Sometimes, bands at 1600 cm⁻¹ are ascribed to C–C–O asymmetric stretching of enolate like species that could here be formed from interaction of hydroformylation product butanal with OH groups on the surface [229]. Molecular butanal adsorption cannot be proved, because no band between 1700 and 1750 cm⁻¹ can be observed, what would be a sign for the

aldehyde C=O stretching vibration [230]. As already discussed for the experiments earlier, bands at 1620 and 1252/1254/1275 cm^{-1} can also be attributed to bidentate carbonates [123]. Furthermore, the band at 1564 cm^{-1} , which is more intense on the titania catalysts with 2 mol % of alkali metal, than on silica or with 5 mol % of alkali metal, might either relate to a monodentate carbonate (together with the band at 1386 cm^{-1}) or formate species or to butanal adsorbed in a carboxylate like coordination to the support Ti–O pair [100].

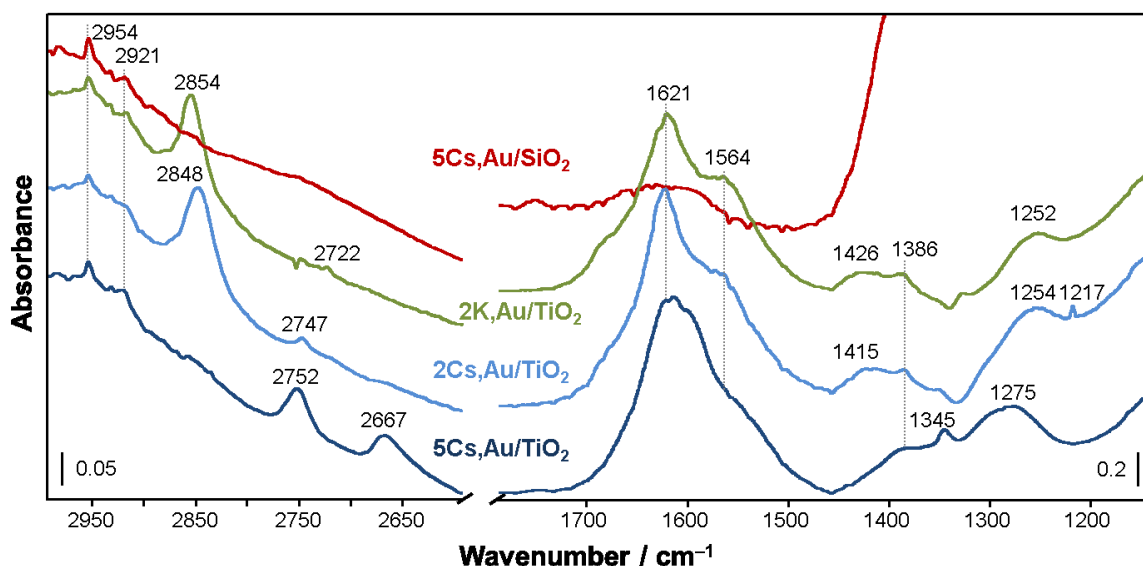


Figure 59. FTIR spectra of gold catalysts in nitrogen flow after 4 h in $\text{CO}_2 + \text{H}_2 + \text{C}_3\text{H}_6 = 1:1:1$ feed for butanol synthesis ($p = 8$ bar, $T = 200$ °C).

What can be safely stated is the presence of stable formates on the titania catalyst after nitrogen flushing, due to the bands at 2854/2848 cm^{-1} and 2752/2667 cm^{-1} . It was already described that those at higher wavenumbers are assignable to titania- or gold-coordinated formates and those at lower wavenumbers can be assigned to cesium bridged formates, respectively. The intensity and also band position is quite similar to that obtained in the propanol synthesis feed. Therefore, it is assumed that the formation of formates is not interfered by olefins.

4.2.11 Conclusion of butanol synthesis over modified Au catalysts

The interaction of propene with the catalysts was stronger compared to ethene on titania-based gold catalysts. Adsorption of propene was observed on all TiO₂ catalysts, clearly indicated by a shift of the $\nu(\text{C}=\text{C})$ vibrational band of propene from 1650 cm⁻¹ to lower wavenumbers and different new bands in the region 1550–1650 cm⁻¹. This is in accordance with the catalytic tests (*cf.* Figure 54), where titania-based gold catalysts exhibited higher yields of butanol than silica-based. It was furthermore observed that the 2.4Cs,Au/TiO₂ sample gave higher propene conversion and butanol yield compared to the 6K,Au/TiO₂ catalyst and also the silica catalysts. A possible explanation for this behavior might be the higher amount of hydroxyl groups on the TiO₂ support of the 2.4Cs,Au/TiO₂ catalyst, which are probably covered by potassium on the 6K,Au/TiO₂ catalyst. It was found in literature [222] that the adsorption of propene is favored by formation of hydrogen bonds with those OH-groups. However, from the results obtained, a more detailed description of structure–reactivity relationship in butanol synthesis is not possible. For gaining more insight into the reaction, long-time testing with an effective activation procedure might give rise to a differentiated picture of adsorbates and intermediates in butanol formation.

In addition, overall activity of gold catalysts in butanol synthesis was not as high as 1-propanol formation. It might be possible that the adsorption of 1-butanol or *iso*-butanol is too strong to achieve higher yields. On the other hand, thermodynamic restrictions might be responsible for the low butanol formation. The illustration of Gibbs free energy (Figure 60) shows that both CO₂ hydrogenation by RWGS reaction as well as propene hydroformylation are endergonic at 200 °C. To become exergonic, RWGS reaction requires higher temperature. In contrast, hydroformylation would readily proceed at temperatures lower than 192 °C. Therefore, it is energetically complicated to combine these reactions and catalyst design is not only responsible for low selectivity and yield of butanol. To reach optimal activity, it would probably be easier to separate the CO₂ hydrogenation from hydroformylation in two reactors, which should be operated at different temperatures. The CO, formed in the first reactor at high temperature can then directly be fed into the second reactor, where it is used to produce the aldehyde and thus, also the alcohol. The hydrogenation of the aldehyde was found not to be limited by temperature in our tests.

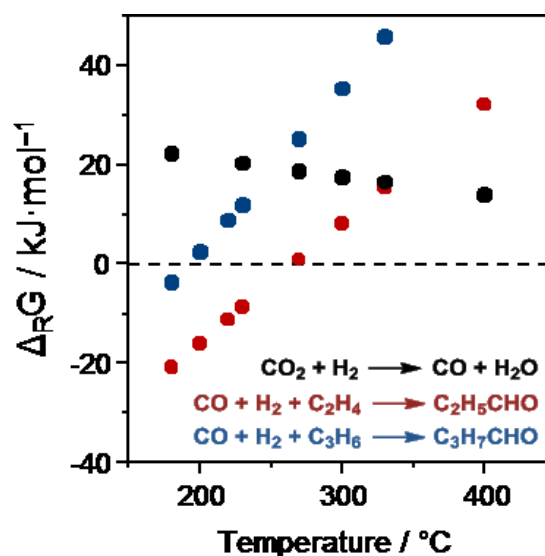


Figure 60. Reaction energy of RWGS reaction, ethene and propene hydroformylation in dependence of temperature.

5 Summary and Outlook

The value-adding transformation of CO₂ was studied in this thesis for three different reactions over supported rhodium- or gold-containing catalysts additionally promoted by alkali metals in form of nitrate or oxide. The hydrogenation of the greenhouse-gas over alumina (A) supported rhodium catalysts led mainly to the formation of CO, when the catalysts are modified with potassium and to CH₄ in case of Rh/A and Rh,Ni/A. In that reaction, a maximum CO₂ conversion of 11% was reached at 350 °C over Rh/A, which was further increased to ~12% over Rh,Ni/A and Rh,K,Ni/A after a high-temperature treatment at 750 °C, which reduced the Ni species on the catalysts surface.

In situ and *operando* FTIR spectroscopic experiments revealed that different carbonates, formates as well as Rh-carbonyl species were present on the catalysts surface during reaction. The alkali metal doping influenced principally the reactivity of the formed adsorbates, but also their creation and desorption properties. On catalysts without potassium, CO₂ adsorbs as hydrogen carbonate on surface OH-groups. These hydrogen carbonates are transformed into carbonyls and formates (F1) by activated hydrogen on the Rh-support interface. These F1 formates are not very reactive, as experiments with isotopically labelling of CO₂ showed, because they could migrate away from the interface, which is potentially the active site. The carbonyls are relatively strong adsorbed on Rh particles on Rh/A and Rh,Ni/A catalysts compared to the catalysts modified with K. This enables further hydrogenation to methane. Therefore, carbonyls are main reaction intermediates in methanation.

In contrast, doping with potassium weakens the CO adsorption, which hinders methanation and increases CO selectivity. The formation of CO on catalysts modified with alkali metals proceeds probably via carbonates, which were formed upon exposure to CO₂. Moreover, formates (F2) are also formed on samples with K, but are more reactive than F1 formates and possibly play a role in CO formation. Besides, also reactive formyl (HCO⁻) species were present on samples with alkali metal. It seems likely that these formyls are intermediates in methanation.

CO₂ transformation into 1-propanol or 1-butanol/2-butanol over alkali modified gold catalysts was also examined. The influence of support material, the kind of alkali metal and its concentration on catalysts performance and the reaction pathway was studied. Catalytic tests showed that higher 1-propanol yields were obtained over titania-based catalysts in calculation on CO₂ basis, reaching a maximum yield of 6% with 2Cs,Au/TiO₂. The respective selectivity was highest over the catalysts with 2 mol % Cs, 5Cs,Au/SiO₂ and 5K,Au/TiO₂, but it changed markedly with the feed composition. Considering the higher price of ethene, selectivity calculated on this basis is also highly important. In this case, silica-based catalysts showed mostly higher selectivities. However, also the feed composition plays a role, because undesired ethene hydrogenation, which lowered the selectivity, could be suppressed by using an appropriate feed (CO₂:H₂:C₂H₄:N₂ = 1:1:1:1).

Alkali metals obviously influence the conversion of both CO₂ and ethene. The highest conversions were obtained over the two titania-based catalysts with 2 mol % of K and Cs,

respectively. While all other catalysts could only convert 1–2% of CO₂, 2K₂Au/TiO₂ reached 6.6% and 2Cs₂Au/TiO₂ 5.5% CO₂ conversion at 200 °C in the CO₂:H₂:C₂H₄:N₂ = 1:3:3:1 feed. Although this conversion could principally be increased by raising the temperature, this would lead to decreased 1-propanol selectivities due to the fact that the hydroformylation is thermodynamically not preferred at high temperatures.

The alkali metals and also the support material influenced the size and shape of gold nanoparticles as was evidenced by TEM and XRD measurements. Generally, the deposition of Au on SiO₂ resulted in slightly larger particles compared to the use of TiO₂, but averaged size was mainly between 4 and 7 nm. Moreover, Au gained enhanced mobility in presence of K or Cs so that single atoms can be separated from the larger clusters, forming more active single sites. Furthermore, the modification with alkali metals resulted in a better reducibility of the gold particles during activation in presence of CO₂ and H₂ as evidenced by FTIR spectroscopic monitoring of low-temperature CO adsorption. These experiments also indicated that the gold particles on catalysts with a low alkali metal loading are easier accessible for CO and thus, also for the reactants. This fact explains the often higher activity of these samples. On the other hand, Au particles were partially covered on samples with higher alkali metal loading, which was further proved by investigation of the used samples. There, a carbonaceous film could be observed by TEM imaging, in which the alkali metals migrated into, what deactivates the catalysts.

The activation process in a reaction feed with high amount of CO₂ and H₂ compared to ethene was found to be necessary for high activity of the catalysts. A thorough investigation of that process by FTIR spectroscopy and simultaneous thermal analysis (TG/DSC/MS) revealed that beside the reduction of residual nitrates, also the restructuring of carbonate species on the surface of the catalysts provoked the activation for 1-propanol synthesis. The reduction of nitrates was possibly initiated by *in situ* formed CO.

Operando high-pressure FTIR spectroscopic experiments with over-night activation procedure prior to testing of the CO₂:H₂:C₂H₄:N₂ = 1:1:1:1 feed showed that bidentate and monodentate carbonates as well as formates were formed on titania-based catalysts, whereas only formates were present on the silica catalysts. Moreover, the formation of formates is strongly influenced by the amount of alkali metal. Support bound formates, possibly in the vicinity of Au, were mainly found on the samples with 2 mol % of alkali metal, but with higher concentration of K or Cs, the formates were often coordinated to the alkali metals. The latter were probably not reactive and block active sites.

Possible intermediates in 1-propanol formation from CO₂, H₂ and ethene were found to be besides CO, propionyl and propoxy groups as shown in the proposed mechanisms (Scheme 8 and Scheme 9). While the ethene adsorption could, as expected, not be observed at applied temperatures, propoxy species have been observed after nitrogen flushing, especially at catalysts without alkali metals. Due to the lower intensity of propoxy bands on catalysts with 2 mol % of K or Cs, it is assumed that alkali metals enhance the desorption of the product. Unfortunately, the formation of products (*e.g.* 1-propanal, 1-propanol) could not be observed with GC, which was coupled to the IR cell. Therefore, the development of a

new and more suitable setup should be forced for future *operando* experiments at high-pressure.

Moreover, testing of butanol synthesis from propene, carbon dioxide and hydrogen with gold catalysts only gave rise to low yields and selectivities. Principally, titania-based catalysts exhibited higher yields than silica-based ones in this reaction, but the obtained product amount was apparently lower than that obtained in the propanol synthesis at the same pressure. Furthermore, the linear alcohol 1-butanol is more difficult to produce, since the formation of branched *iso*-butanol occurs simultaneously. Therefore, in the experiments carried out, the yield and selectivity of 1-butanol was only slightly higher than that of *iso*-butanol.

Unfortunately, it was not possible to extract a detailed reaction mechanism or influences of catalysts components from FTIR spectroscopic experiments, but it might be assumed that the mechanism proceeds similar to that proposed for propanol synthesis. However, it was confirmed that the formation of formates also occurs in this feed composition and is most probably independent from the olefin. Moreover, it might be the case that propene adsorbs slightly stronger on TiO_2 -based catalysts than SiO_2 -based.

Nevertheless, the principle of carbon chain elongation executing both ethene and propene hydroformylation with *in situ* generated CO from CO_2 was proofed to be feasible. It can be imagined that these reactions are implemented in the future in a carbon neutral catalytic cycle [7] to produce olefins and alcohols from CO_2 and H_2 only (Figure 61). This scenario could start with ethene formation from methanol-to-olefin process [231-232], and sustainable hydrogen generation, for example from water-splitting [233-234]. Moreover, dehydration of 1-propanol could yield propene, which can be again integrated into the cycle to form butanol, and so on.

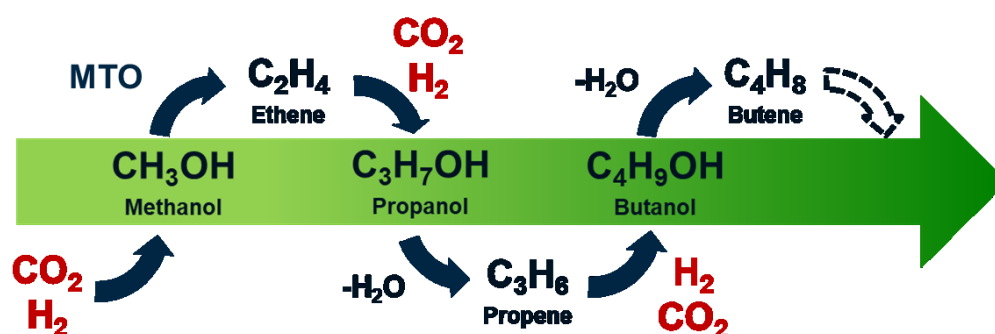


Figure 61. Possible future reaction scheme for alcohol and olefin production from CO_2 and H_2 , MTO = methanol-to-olefin process.

For future experiments, it will be important to improve the cell design and coupling of the high-pressure FTIR cell with the online product analyzing device, which could also be an MS instead of GC, because the product formation can then be monitored more directly. Moreover, the cell should be designed in a way that the dead volume is minimized, in order to decrease the disturbing contribution of gas phase olefin bands.

Furthermore, it might be interesting to study ethene and propene adsorption at lower temperature, because information on where and how these olefins adsorb on the catalysts surface could not be obtained in the experiments carried out in this thesis at 200 °C.

For determining the reactivity of certain adsorbates and intermediates in alcohol formation, it could also be helpful to carry out experiments with isotopically labeled molecules, in analogy to the experiments with the rhodium catalysts in CO₂ reduction. Then also the origin of carbon atoms can be clarified, which would be especially interesting in the 1- and 2-butanol synthesis.

Finally, it might be possible to enhance the alcohol production from CO₂, H₂ and olefins by irradiating the Au/TiO₂ catalysts with light, when taking the special semiconductor properties of TiO₂ into account.[41, 121] Then it might be possible to increase RWGS activity of the catalysts, as was already demonstrated in literature [13, 87, 235-236], and adjust the reaction temperature more suitable for hydroformylation.

6 Literature

- [1] *International Energy Outlook 2016*, DOE/EIA-0484(2016), Washington, USA **2016**, [https://www.eia.gov/forecasts/ieo/pdf/0484\(2016\).pdf](https://www.eia.gov/forecasts/ieo/pdf/0484(2016).pdf), (2017, December 5).
- [2] *Communication from the commission to the European Parliament, the Council, the European economic and social Committee and the Committee of the regions, Energy Roadmap 2050* COM(2011) 885 final, Brussels **2011**, <http://eur-lex.europa.eu/legal-content/EN/TXT/HTML/?uri=CELEX:52011DC0885&from=EN>, (2017, November 24).
- [3] C. Ampelli, S. Perathoner, G. Centi, *Phil. Trans. R. Soc. A* **2015**, 373, 20140177
- [4] E. A. Quadrelli, G. Centi, J. L. Duplan, S. Perathoner, *ChemSusChem* **2011**, 4, 1194-1215.
- [5] I. Dimitriou, P. Garcia-Gutierrez, R. H. Elder, R. M. Cuellar-Franca, A. Azapagic, R. W. K. Allen, *Energy Environ. Sci.* **2015**, 8, 1775-1789.
- [6] M. Peters, B. Köhler, W. Kuckshinrichs, W. Leitner, P. Markewitz, T. E. Müller, *ChemSusChem* **2011**, 4, 1216-1240.
- [7] F. S. Zeman, D. W. Keith, *Phil. Trans. R. Soc. A* **2008**, 366, 3901-3918.
- [8] A. Al-Mamoori, A. Krishnamurthy, A. A. Rownaghi, F. Rezaei, *Energy Technol.* **2017**, 5, 834-849.
- [9] E. Favre, *Chem. Eng. J.* **2011**, 171, 782-793.
- [10] N. von der Assen, P. Voll, M. Peters, A. Bardow, *Chem. Soc. Rev.* **2014**, 43, 7982-7994.
- [11] P. Styring, E. A. Quadrelli, K. Armstrong, *Carbon dioxide utilisation: closing the carbon cycle*, Elsevier, Amsterdam, **2014**.
- [12] W. Wang, S. P. Wang, X. B. Ma, J. L. Gong, *Chem. Soc. Rev.* **2011**, 40, 3703-3727.
- [13] E. V. Kondratenko, G. Mul, J. Baltrusaitis, G. O. Larrazabal, J. Pérez-Ramírez, *Energy Environ. Sci.* **2013**, 6, 3112-3135.
- [14] D. J. Darensbourg, J. R. Andreatta, A. I. Moncada, in *Carbon Dioxide as Chemical Feedstock*, (Ed.: M. Aresta), WILEY-VCH Verlag GmbH & Co. KGaA, Weinheim, **2010**, pp. 213-248.
- [15] M. Usman, W. M. A. W. Daud, H. F. Abbas, *Renewable Sustainable Energy Rev.* **2015**, 45, 710-744.
- [16] D. Pakhare, J. Spivey, *Chem. Soc. Rev.* **2014**, 43, 7813-7837.
- [17] W. Pan, C. Song, in *Carbon Dioxide as Chemical Feedstock*, (Ed.: M. Aresta), WILEY-VCH Verlag GmbH & Co. KGaA, Weinheim, **2010**, pp. 249-266.
- [18] G. Prieto, *ChemSusChem* **2017**, 10, 1056-1070.
- [19] H. T. Luk, C. Mondelli, D. C. Ferre, J. A. Stewart, J. Perez-Ramirez, *Chem. Soc. Rev.* **2017**, 46, 1358-1426.

-
- [20] S. S. Ail, S. Dasappa, *Renewable Sustainable Energy Rev.* **2016**, *58*, 267-286.
- [21] M. Baerns, A. Behr, A. Brehm, J. Gmehling, K.-O. Hinrichsen, H. Hofmann, U. Onken, R. Palkovits, A. Renken, *Technische Chemie*, 2nd ed., WILEY-VCH Verlag & Co. KGaA, Weinheim, **2013**.
- [22] A. Goguet, F. Meunier, J. P. Breen, R. Burch, M. I. Petch, A. F. Ghenciu, *J. Catal.* **2004**, *226*, 382-392.
- [23] A. Iles, A. N. Martin, *J. Cleaner Prod.* **2013**, *45*, 38-49.
- [24] S. J. Ahlers, *Neuartige Synthese von 1-Propanol aus CO₂ mit C₂H₄ und H₂ an heterogenen Anhaltigen Katalysatoren*, Dissertation, Universität Rostock, Rostock, **2016**.
- [25] S. J. Ahlers, U. Bentrup, D. Linke, E. V. Kondratenko, *ChemSusChem* **2014**, *7*, 2631-2639.
- [26] S. J. Ahlers, R. Kraehnert, C. Kreyenschulte, M. M. Pohl, D. Linke, E. V. Kondratenko, *Catal. Today* **2015**, *258*, 684-690.
- [27] S. J. Ahlers, M. M. Pohl, J. Radnik, D. Linke, E. V. Kondratenko, *Appl. Catal., B* **2015**, *176*, 570-577.
- [28] S. J. Ahlers, M. M. Pohl, M. Holena, D. Linke, E. V. Kondratenko, *Catal. Sci. Technol.* **2016**, *6*, 2171-2180.
- [29] E. M. Green, *Curr. Opin. Biotechnol.* **2011**, *22*, 337-343.
- [30] S. Maiti, G. Gallastegui, S. J. Sarma, S. K. Brar, Y. Le Bihan, P. Drogui, G. Buelna, M. Verma, *Biomass Bioenergy* **2016**, *94*, 187-200.
- [31] X. D. Xu, J. A. Moulijn, *Energy Fuels* **1996**, *10*, 305-325.
- [32] A. J. Hunt, E. H. K. Sin, R. Marriott, J. H. Clark, *ChemSusChem* **2010**, *3*, 306-322.
- [33] R. E. Krupp, *Geologische Kurzstudie zu den Bedingungen und möglichen Auswirkungen der dauerhaften Lagerung von CO₂ im Untergrund*, **2010**, http://ccs-protest.de/20101118_klima_energie_ccs_studie.pdf, (2018, February 26).
- [34] J. M. Matter, M. Stute, S. Ó. Snæbjörnsdóttir, E. H. Oelkers, S. R. Gislason, E. S. Aradóttir, B. Sigfusson, I. Gunnarsson, H. Sigurdardóttir, E. Gunnlaugsson, G. Axelsson, H. A. Alfredsson, D. Wolff-Boenisch, K. Mesfin, D. F. d. l. R. Taya, J. Hall, K. Dideriksen, W. S. Broecker, *Science* **2016**, *352*, 1312-1314.
- [35] S. Zhang, D. J. DePaolo, *Acc. Chem. Res.* **2017**, *50*, 2075-2084.
- [36] S. Kara, *Das zweite Wendland: CO₂-Endlager*, *Die Zeit* **2010**, *47*.
- [37] C. J. Keturakis, F. Ni, M. Spicer, M. G. Beaver, H. S. Caram, I. E. Wachs, *ChemSusChem* **2014**, *7*, 3459-3466.
- [38] A. E. Creamer, B. Gao, *Environ. Sci. Technol.* **2016**, *50*, 7276-7289.
- [39] M. Ashley, C. Magiera, P. Ramidi, G. Blackburn, T. G. Scott, R. Gupta, K. Wilson, A. Ghosh, A. Biswas, *Greenhouse Gases: Sci. Technol.* **2012**, *2*, 419-444.
- [40] A. Otto, T. Grube, S. Schiebahn, D. Stolten, *Energy Environ. Sci.* **2015**, *8*, 3283-3297.

- [41] Y. Izumi, *Coord. Chem. Rev.* **2013**, 257, 171-186.
- [42] L. Zhang, Z.-J. Zhao, J. Gong, *Angew. Chem. Int. Ed.* **2017**, 56, 11326-11353; *Angew. Chem.* **2017**, 129, 11482-11511.
- [43] J. Gao, Y. Wang, Y. Ping, D. Hu, G. Xu, F. Gu, F. Su, *RSC Adv.* **2012**, 2, 2358.
- [44] D. Kim, J. Resasco, Y. Yu, A. M. Asiri, P. D. Yang, *Nat. Commun.* **2014**, 5, 4948.
- [45] J. Klankermayer, S. Wesselbaum, K. Beydoun, W. Leitner, *Angew. Chem. Int. Ed.* **2016**, 55, 7296-7343; *Angew. Chem.* **2016**, 128, 7416-7467.
- [46] A. Álvarez, A. Bansode, A. Urakawa, A. V. Bavykina, T. A. Wezendonk, M. Makkee, J. Gascon, F. Kapteijn, *Chem. Rev.* **2017**, 117, 9804-9838.
- [47] T. D. Veras, T. S. Mozer, D. D. R. M. dos Santos, A. D. Cesar, *Int. J. Hydrogen Energy* **2017**, 42, 2018-2033.
- [48] E. Riedel, *Anorganische Chemie*, 2nd ed., de Gruyter, Berlin/New York, **1990**.
- [49] Y. A. Daza, J. N. Kuhn, *RSC Adv.* **2016**, 6, 49675-49691.
- [50] M. D. Porosoff, B. H. Yan, J. G. G. Chen, *Energy Environ. Sci.* **2016**, 9, 62-73.
- [51] P. Panagiotopoulou, *Appl. Catal., A* **2017**, 542, 63-70.
- [52] J. Kehres, J. W. Andreasen, F. C. Krebs, A. M. Molenbroek, I. Chorkendorff, T. Vegge, *J. Appl. Crystallogr.* **2010**, 43, 1400-1408.
- [53] H. Sakurai, A. Ueda, T. Kobayashi, M. Haruta, *Chem. Commun.* **1997**, 271-272.
- [54] V. Kyriakou, A. Vourros, I. Garagounis, S. A. C. Carabineiro, F. J. Maldonado-Hódar, G. E. Marnellos, M. Konsolakis, *Catal. Commun.* **2017**, 98, 52-56.
- [55] H. Kusama, K. K. Bando, K. Okabe, H. Arakawa, *Appl. Catal., A* **2000**, 197, 255-268.
- [56] G. A. Mills, F. W. Steffgen, *Catal. Rev.: Sci. Eng.* **1974**, 8, 159-210.
- [57] P. Frontera, A. Macario, M. Ferraro, P. Antonucci, *Catalysts* **2017**, 7, 59.
- [58] D. Li, N. Ichikuni, S. Shimazu, T. Uematsu, *Appl. Catal., A* **1998**, 172, 351-358.
- [59] K. K. Bando, K. Soga, K. Kunitomi, H. Arakawa, *Appl. Catal., A* **1998**, 175, 67-81.
- [60] X. Yang, X. Su, X. Chen, H. Duan, B. Liang, Q. Liu, X. Liu, Y. Ren, Y. Huang, T. Zhang, *Appl. Catal., B* **2017**, 216, 95-105.
- [61] C.-S. Chen, W.-H. Cheng, S.-S. Lin, *Appl. Catal., A* **2003**, 238, 55-67.
- [62] M. D. Porosoff, J. W. Baldwin, X. Peng, G. Mpourmpakis, H. D. Willauer, *ChemSusChem* **2017**, 10, 2408-2415.
- [63] S. Brosda, C. G. Vayenas, J. Wei, *Appl. Catal., B* **2006**, 68, 109-124.
- [64] B. Miao, S. S. K. Ma, X. Wang, H. Su, S. H. Chan, *Catal. Sci. Technol.* **2016**, 6, 4048-4058.
- [65] A. Karelovic, P. Ruiz, *J. Catal.* **2013**, 301, 141-153.
- [66] D. Widmann, R. J. Behm, *Angew. Chem. Int. Ed.* **2011**, 50, 10241-10245.

-
- [67] L. C. Wang, D. Widmann, R. J. Behm, *Catal. Sci. Technol.* **2015**, 5, 925-941.
- [68] L. C. Wang, M. Tahvildar Khazaneh, D. Widmann, R. J. Behm, *J. Catal.* **2013**, 302, 20-30.
- [69] D. Martin, D. Duprez, *J. Phys. Chem.* **1996**, 100, 9429-9438.
- [70] J. J. Benitez, R. Alvero, I. Carrizosa, J. A. Odriozola, *Catal. Today* **1991**, 9, 53-60.
- [71] H. C. Wu, Y. C. Chang, J. H. Wu, J. H. Lin, I. K. Lin, C. S. Chen, *Catal. Sci. Technol.* **2015**, 5, 4154-4163.
- [72] A. Westermann, B. Azambre, M. C. Bacariza, I. Graca, M. F. Ribeiro, J. M. Lopes, C. Henriques, *Appl. Catal., B* **2015**, 174, 120-125.
- [73] A. Goguet, F. C. Meunier, D. Tibiletti, J. P. Breen, R. Burch, *J. Phys. Chem. B* **2004**, 108, 20240-20246.
- [74] P. A. Ussa Aldana, F. Ocampo, K. Kobl, B. Louis, F. Thibault-Starzyk, M. Daturi, P. Bazin, S. Thomas, A. C. Roger, *Catal. Today* **2013**, 215, 201-207.
- [75] Y. X. Pan, C. J. Liu, Q. F. Ge, *J. Catal.* **2010**, 272, 227-234.
- [76] N. Ishito, K. Hara, K. Nakajima, A. Fukuoka, *J. Energy Chem.* **2016**, 25, 306-310.
- [77] B. Liang, H. Duan, X. Su, X. Chen, Y. Huang, X. Chen, J. J. Delgado, T. Zhang, *Catal. Today* **2017**, 281, 319-326.
- [78] T. Hyakutake, W. van Beek, A. Urakawa, *J. Mater. Chem. A* **2016**, 4, 6878-6885.
- [79] N. Tien-Thao, M. H. Zahedi-Niaki, H. Alamdari, S. Kaliaguine, *J. Catal.* **2007**, 245, 348-357.
- [80] M. Amoyal, R. Vidruk-Nehemya, M. V. Landau, M. Herskowitz, *J. Catal.* **2017**, 348, 29-39.
- [81] R. W. Dorner, D. R. Hardy, F. W. Williams, H. D. Willauer, *Energy Environ. Sci.* **2010**, 3, 884-890.
- [82] A. Iordan, M. I. Zaki, C. Kappenstein, *Phys. Chem. Chem. Phys.* **2004**, 6, 2502-2512.
- [83] G. J. Millar, C. H. Rochester, K. C. Waugh, *J. Chem. Soc. Faraday Trans.* **1992**, 88, 1477-1488.
- [84] G. Blyholder, *J. Phys. Chem.* **1964**, 68, 2772-2777.
- [85] M. Yang, S. Li, Y. Wang, J. A. Herron, Y. Xu, L. F. Allard, S. Lee, J. Huang, M. Mavrikakis, M. Flytzani-Stephanopoulos, *Science* **2014**, 346, 1498-1501.
- [86] A. P. Farkas, F. Solymosi, *J. Phys. Chem. C* **2009**, 113, 19930-19936.
- [87] G. Halasi, A. Gazsi, T. Bánsági, F. Solymosi, *Appl. Catal., A* **2015**, 506, 85-90.
- [88] D. Iruretagoyena, X. Huang, M. S. P. Shaffer, D. Chadwick, *Ind. Eng. Chem. Res.* **2015**, 54, 11610-11618.
- [89] T. M. Powell, W. F. Giauque, *J. Am. Chem. Soc.* **1939**, 61, 2366-2370.
- [90] G. M. Torres, R. Frauenlob, R. Franke, A. Börner, *Catal. Sci. Technol.* **2015**, 5, 34-54.

- [91] M. Lenarda, L. Storaro, R. Ganzerla, *J. Mol. Catal. A: Chem.* **1996**, *111*, 203-237.
- [92] A. Fusi, R. Psaro, C. Dossi, L. Garlaschelli, F. Cozzi, *J. Mol. Catal. A: Chem.* **1996**, *107*, 255-261.
- [93] L. Alvarado Rupflin, J. Mormul, M. Lejkowski, S. Titlbach, R. Papp, R. Gläser, M. Dimitrakopoulou, X. Huang, A. Trunschke, M. G. Willinger, R. Schlögl, F. Rosowski, S. A. Schunk, *ACS Catal.* **2017**, *7*, 3584-3590.
- [94] D. G. Hanna, S. Shylesh, P. A. Parada, A. T. Bell, *J. Catal.* **2014**, *311*, 52-58.
- [95] N. Sivasankar, H. Frei, *J. Phys. Chem. C* **2011**, *115*, 7545-7553.
- [96] N. Navidi, J. W. Thybaut, G. B. Marin, *Appl. Catal., A* **2014**, *469*, 357-366.
- [97] L. Sordelli, M. Guidotti, D. Andreatta, G. Vlaic, R. Psaro, *J. Mol. Catal. A: Chem.* **2003**, *204*, 509-518.
- [98] T. Hanaoka, H. Arakawa, T. Matsuzaki, Y. Sugi, K. Kanno, Y. Abe, *Catal. Today* **2000**, *58*, 271-280.
- [99] S. S. C. Chuang, S. I. Pien, *J. Mol. Catal.* **1989**, *55*, 12-22.
- [100] E. J. Rode, M. E. Davis, B. E. Hanson, *J. Catal.* **1985**, *96*, 574-585.
- [101] I. Horiuti, M. Polanyi, *Trans. Faraday Soc.* **1934**, *30*, 1164-1172.
- [102] M. W. Balakos, S. S. C. Chuang, *J. Catal.* **1995**, *151*, 253-265.
- [103] M. K. Ko, H. Frei, *J. Phys. Chem. B* **2004**, *108*, 1805-1808.
- [104] K. J. Williams, A. B. Boffa, M. Salmeron, A. T. Bell, G. A. Somorjai, *Catal. Lett.* **1991**, *11*, 77-88.
- [105] D. S. Jordan, A. T. Bell, *J. Phys. Chem.* **1986**, *90*, 4797-4805.
- [106] S. Naito, M. Tanimoto, *J. Chem. Soc., Chem. Commun.* **1989**, 1403-1404.
- [107] D. Y. Murzin, A. Bernas, T. Salmi, *J. Mol. Catal. A: Chem.* **2010**, *315*, 148-154.
- [108] X. Liu, B. Hu, K. Fujimoto, M. Haruta, M. Tokunaga, *Appl. Catal., B* **2009**, *92*, 411-421.
- [109] *In situ Spectroscopy of Catalysts*, (Ed.: B. M. Weckhuysen), American Scientific Publishers, Stevenson Ranch, **2004**.
- [110] *In-situ Characterization of Heterogeneous Catalysts*, (Ed.: J. A. Rodriguez, J. C. Hanson, P. J. Chupas), John Wiley & Sons, Inc., Hoboken, NJ, **2013**.
- [111] *In-Situ Spectroscopy in Heterogeneous Catalysis*, (Ed.: J. F. Haw), Wiley-VCH Verlag GmbH & Co. KGaA, Weinheim, **2004**.
- [112] U. Bentrup, *Chem. Soc. Rev.* **2010**, *39*, 4718-4730.
- [113] M. A. Bañares, *Catal. Today* **2005**, *100*, 71-77.
- [114] R. Schlögl, *Angew. Chem. Int. Ed.* **2015**, *54*, 3465-3520.
- [115] J. Ryczkowski, *Catal. Today* **2001**, *68*, 263-381.

-
- [116] J. Sirita, S. Phanichphant, F. C. Meunier, *Anal. Chem.* **2007**, *79*, 3912-3918.
- [117] A. A. Davydov, *Molecular Spectroscopy of Oxide Catalyst Surfaces*, (Ed.: N. T. Sheppard), John Wiley & Sons Ltd, Chichester, **2003**.
- [118] G. Mestl, H. Knözinger, in *Handbook of Heterogeneous Catalysis*, Wiley-VCH Verlag GmbH & Co. KGaA, Weinheim, **2008**.
- [119] J. P. M. Maas, *Spectrochim. Acta, Part A* **1978**, *34*, 179-180.
- [120] G. Busca, V. Lorenzelli, *Mater. Chem.* **1982**, *7*, 89-126.
- [121] D. A. Panayotov, J. R. Morris, *Surf. Sci. Rep.* **2016**, *71*, 77-271.
- [122] G. J. Millar, C. H. Rochester, K. C. Waugh, *J. Chem. Soc. Faraday Trans.* **1991**, *87*, 2785-2793.
- [123] M. Marwood, R. Doepper, A. Renken, *Appl. Catal., A* **1997**, *151*, 223-246.
- [124] S. Eckle, H. G. Anfang, R. J. Behm, *J. Phys. Chem. C* **2011**, *115*, 1361-1367.
- [125] F. C. Meunier, *Catal. Today* **2010**, *155*, 164-171.
- [126] F. C. Meunier, in *Catalysis, Vol. 22*, (Ed.: J. J. Spivey, K. M. Dooley), The Royal Society of Chemistry, Cambridge, **2010**, pp. 94-118.
- [127] S. L. Shannon, J. G. Goodwin, *Chem. Rev.* **1995**, *95*, 677-695.
- [128] Y. Yang, R. S. Disselkamp, J. Szanyi, C. H. F. Peden, C. T. Campbell, J. G. Goodwin, *Rev. Sci. Instrum.* **2006**, *77*.
- [129] D. Tibiletti, A. Goguet, F. C. Meunier, J. P. Breen, R. Burch, *Chem. Commun.* **2004**, 1636-1637.
- [130] E. Marceau, X. Carrier, M. Che, in *Synthesis of Solid Catalysts*, (Ed.: K. P. de Jong), Wiley-VCH Verlag GmbH & Co. KGaA, Weinheim **2009**, pp. 59-82.
- [131] J. A. Cusumano, *Nature* **1974**, *247*, 456.
- [132] F. Somodi, I. Borbath, M. Hegedus, A. Tompos, I. E. Sajo, A. Szegedi, S. Rojas, J. L. G. Fierro, J. L. Margitfalvi, *Appl. Catal., A* **2008**, *347*, 216-222.
- [133] S. Brunauer, P. H. Emmett, E. Teller, *J. Am. Chem. Soc.* **1938**, *60*, 309-319.
- [134] P. Scherrer, *Nachr. Ges. Wiss. Göttingen* **1918**, *26*, 98-100.
- [135] T. J. Collins, *Biotechniques* **2007**, *43*, 25-30.
- [136] J. T. Gleaves, G. S. Yablonskii, P. Phanawadee, Y. Schuurman, *Appl. Catal., A* **1997**, *160*, 55-88.
- [137] J. T. Gleaves, J. R. Ebner, T. C. Kuechler, *Catal. Rev.* **1988**, *30*, 49-116.
- [138] E. V. Kondratenko, J. Pérez-Ramírez, *Catal. Today* **2007**, *121*, 159.
- [139] J. Pérez-Ramírez, E. V. Kondratenko, *Catal. Today* **2007**, *121*, 160-169.
- [140] G. S. Yablonsky, M. Olea, G. B. Marin, *J. Catal.* **2003**, *216*, 120-134.
- [141] J. A. Lercher, C. Gründling, G. Eder-Mirth, *Catal. Today* **1996**, *27*, 353-376.

- [142] In-Situ High-Low Pressure Infrared Reactor, Retrieved from: <http://www.in-situ-research.com/Prods/IRCell.html>, (2018, February 12)
- [143] F. Solymosi, A. Erdöhelyi, T. Bánsági, *J. Chem. Soc., Faraday Trans. 1* **1981**, 77, 2645-2657.
- [144] N. M. Martin, P. Velin, M. Skoglundh, M. Bauer, P.-A. Carlsson, *Catal. Sci. Technol.* **2017**, 7, 1086-1094.
- [145] D. B. Williams, C. B. Carter, in *Transmission Electron Microscopy: A Textbook for Materials Science*, Springer, New York, **2009**, pp. 371-388.
- [146] W. Reschetilowski, *Einführung in die Heterogene Katalyse*, Springer Spektrum, Berlin, **2015**.
- [147] P. Kim, Y. Kim, H. Kim, I. K. Song, J. Yi, *Appl. Catal., A* **2004**, 272, 157-166.
- [148] C. Jiménez-González, Z. Boukha, B. de Rivas, J. J. Delgado, M. Á. Cauqui, J. R. González-Velasco, J. I. Gutiérrez-Ortiz, R. López-Fonseca, *Appl. Catal., A* **2013**, 466, 9-20.
- [149] G. Li, L. Hu, J. M. Hill, *Appl. Catal., A* **2006**, 301, 16-24.
- [150] D. Heyl, U. Rodemerck, U. Bentrup, *ACS Catal.* **2016**, 6, 6275-6284.
- [151] A. Beuls, C. Swalus, M. Jacquemin, G. Heyen, A. Karelovic, P. Ruiz, *Appl. Catal., B* **2012**, 113, 2-10.
- [152] A. Karelovic, P. Ruiz, *ACS Catal.* **2013**, 3, 2799-2812.
- [153] N. Nomura, T. Tagawa, S. Goto, *Appl. Catal., A* **1998**, 166, 321-326.
- [154] F. Solymosi, M. Lancz, *J. Chem. Soc., Faraday Trans. 1* **1986**, 82, 883-897.
- [155] A. Yang, C. W. Garland, *J. Phys. Chem.* **1957**, 61, 1504-1512.
- [156] J. D. Donaldson, J. F. Knifton, S. D. Ross, *Spectrochim. Acta* **1964**, 20, 847-851.
- [157] A. Bansode, B. Tidona, P. R. von Rohr, A. Urakawa, *Catal. Sci. Technol.* **2013**, 3, 767-778.
- [158] P. Gélín, J.-F. Dutel, Y. B. Taârit, *J. Chem. Soc., Chem. Comm.* **1990**, 1746-1747.
- [159] A. Karelovic, P. Ruiz, *Appl. Catal., B* **2012**, 113, 237-249.
- [160] P. Panagiotopoulou, D. I. Kondarides, X. E. Verykios, *Catal. Today* **2012**, 181, 138-147.
- [161] X. Wang, H. Shi, J. H. Kwak, J. Szanyi, *ACS Catal.* **2015**, 5, 6337-6349.
- [162] S. C. Chuang, J. G. Goodwin, I. Wender, *J. Catal.* **1985**, 95, 435-446.
- [163] G. C. Bond, D. T. Thompson, *Catal. Rev.* **1999**, 41, 319-388.
- [164] A. S. K. Hashmi, G. J. Hutchings, *Angew. Chem. Int. Ed.* **2006**, 45, 7896-7936.
- [165] R. Zanella, L. Delannoy, C. Louis, *Appl. Catal., A* **2005**, 291, 62-72.
- [166] M. Haruta, *Catal. Today* **1997**, 36, 153-166.

-
- [167] S. Tsubota, M. Haruta, T. Kobayashi, A. Ueda, Y. Nakahara, in *Studies in Surface Science and Catalysis, Vol. 63*, (Ed.: G. Poncelet, P. A. Jacobs, P. Grange, B. Delmon), Elsevier, **1991**, pp. 695-704.
- [168] F. Moreau, G. C. Bond, A. O. Taylor, *J. Catal.* **2005**, *231*, 105-114.
- [169] L. Stobiński, L. Zommer, R. Duś, *Appl. Surf. Sci.* **1999**, *141*, 319-325.
- [170] A. Villa, N. Dimitratos, C. E. Chan-Thaw, C. Hammond, G. M. Veith, D. Wang, M. Manzoli, L. Pratia, G. J. Hutchings, *Chem. Soc. Rev.* **2016**, *45*, 4953-4994.
- [171] Y. Y. Wu, N. A. Mashayekhi, H. H. Kung, *Catal. Sci. Technol.* **2013**, *3*, 2881-2891.
- [172] H. Tang, Y. Su, B. Zhang, A. F. Lee, M. A. Isaacs, K. Wilson, L. Li, Y. Ren, J. Huang, M. Haruta, B. Qiao, X. Liu, C. Jin, D. Su, J. Wang, T. Zhang, *Sci. Adv.* **2017**, *3*, 1-8.
- [173] E. J. Gibson, R. W. Clarke, *J. Appl. Chem.* **1961**, *11*, 293-299.
- [174] R. Pellegrini, G. Leofanti, G. Agostini, L. Bertinetti, S. Bertarione, E. Groppo, A. Zecchina, C. Lamberti, *J. Catal.* **2009**, *267*, 40-49.
- [175] Y. Iizuka, H. Fujiki, N. Yamauchi, T. Chijiwa, S. Arai, S. Tsubota, M. Haruta, *Catal. Today* **1997**, *36*, 115-123.
- [176] L. Li, X. C. Zeng, *J. Am. Chem. Soc.* **2014**, *136*, 15857-15860.
- [177] E. Rombi, M. G. Cutrufello, C. Cannas, M. Occhiuzzi, B. Onida, I. Ferino, *Phys. Chem. Chem. Phys.* **2012**, *14*, 6889-6897.
- [178] E. Rombi, M. G. Cutrufello, R. Monaci, C. Cannas, D. Gazzoli, B. Onida, M. Pavani, I. Ferino, *J. Mol. Catal. A: Chem.* **2015**, *404-405*, 83-91.
- [179] S. Derrouiche, P. Gravejat, D. Bianchi, *J. Am. Chem. Soc.* **2004**, *126*, 13010-13015.
- [180] F. Boccuzzi, A. Chiorino, S. Tsubota, M. Haruta, *J. Phys. Chem.* **1996**, *100*, 3625-3631.
- [181] Y. Wang, D. Widmann, R. J. Behm, *ACS Catal.* **2017**, *7*, 2339-2345.
- [182] F. Vindigni, M. Manzoli, A. Chiorino, F. Boccuzzi, *Gold Bull.* **2009**, *42*, 106-112.
- [183] F. Boccuzzi, S. Tsubota, M. Haruta, *J. Electron Spectrosc. Relat. Phenom.* **1993**, *64-5*, 241-250.
- [184] K. I. Hadjiivanov, G. N. Vayssilov, *Adv. Catal.* **2002**, *47*, 307-511.
- [185] P. Concepción, S. Carrettin, A. Corma, *Appl. Catal., A* **2006**, *307*, 42-45.
- [186] M. A. P. Dekkers, M. J. Lippits, B. E. Nieuwenhuys, *Catal. Lett.* **1998**, *56*, 195-197.
- [187] M. Chen, D. W. Goodman, *Acc. Chem. Res.* **2006**, *39*, 739-746.
- [188] R. Carrasquillo-Flores, I. Ro, M. D. Kumbhalkar, S. Burt, C. A. Carrero, A. C. Alba-Rubio, J. T. Miller, I. Hermans, G. W. Huber, J. A. Dumesic, *J. Am. Chem. Soc.* **2015**, *137*, 10317-10325.
- [189] F. Boccuzzi, A. Chiorino, M. Manzoli, P. Lu, T. Akita, S. Ichikawa, M. Haruta, *J. Catal.* **2001**, *202*, 256-267.
- [190] K. I. Hadjiivanov, D. G. Klissurski, *Chem. Soc. Rev.* **1996**, *25*, 61-69.

- [191] M. Boronat, P. Concepción, A. Corma, *J. Phys. Chem. C* **2009**, *113*, 16772-16784.
- [192] G. Martra, *Appl. Catal., A* **2000**, *200*, 275-285.
- [193] A. A. Tsyganenko, L. A. Denisenko, S. M. Zverev, V. N. Filimonov, *J. Catal.* **1985**, *94*, 10-15.
- [194] C. E. Nanayakkara, W. A. Larish, V. H. Grassian, *J. Phys. Chem. C* **2014**, *118*, 23011-23021.
- [195] C. Morterra, *J. Chem. Soc., Faraday Trans. 1* **1988**, *84*, 1617-1637.
- [196] I. Onal, S. Soyer, S. Senkan, *Surf. Sci.* **2006**, *600*, 2457-2469.
- [197] M. Manzoli, A. Chiorino, F. Vindigni, F. Boccuzzi, *Catal. Today* **2012**, *181*, 62-67.
- [198] M. C. Holz, K. Tölle, M. Muhler, *Catal. Sci. Technol.* **2014**, *4*, 3495-3504.
- [199] J. Greenberg, L. J. Hallgren, *J. Chem. Phys.* **1960**, *33*, 900-902.
- [200] J. A. Anderson, *Phil. Trans. R. Soc. A* **2018**, 376.
- [201] M. J. Bollinger, R. E. Sievers, D. W. Fahey, F. C. Fehsenfeld, *Anal. Chem.* **1983**, *55*, 1980-1986.
- [202] F. Epron, F. Gauthard, C. Pinéda, J. Barbier, *J. Catal.* **2001**, *198*, 309-318.
- [203] F. Gauthard, F. Epron, J. Barbier, *J. Catal.* **2003**, *220*, 182-191.
- [204] D. J. C. Yates, *J. Phys. Chem.* **1961**, *65*, 746-753.
- [205] S. M. Han, E. S. Aydil, *Appl. Phys. Lett.* **1997**, *70*, 3269-3271.
- [206] H. Ehrhardt, H. Seidel, H. Schweer, *Z. anorg. allg. Chem.* **1980**, *462*, 185-198.
- [207] G. Busca, G. Ramis, V. Lorenzelli, A. Janin, J. C. Lavalley, *Spectrochim. Acta, Part A* **1987**, *43*, 489-496.
- [208] J. E. Bailie, C. H. Rochester, G. J. Hutchings, *J. Chem. Soc. Faraday Trans.* **1997**, *93*, 4389-4394.
- [209] J. A. Anderson, M. W. McQuire, C. H. Rochester, T. Sweeney, *Catal. Today* **1991**, *9*, 23-30.
- [210] G. Mul, A. Zwiijnenburg, B. van der Linden, M. Makkee, J. A. Moulijn, *J. Catal.* **2001**, *201*, 128-137.
- [211] G. Socrates, *Infrared characteristic group frequencies*, 2nd ed., John Wiley & Sons Ltd, Chichester, **1980**.
- [212] E. Finocchio, G. Busca, V. Lorenzelli, V. S. Escribano, *J. Chem. Soc. Faraday Trans.* **1996**, *92*, 1587-1593.
- [213] M. Kantschewa, E. V. Albano, G. Ertl, H. Knözinger, *Appl. Catal.* **1983**, *8*, 71-84.
- [214] J. Kondo, K. Domen, K. Maruya, T. Onishi, *J. Chem. Soc. Faraday Trans.* **1990**, *86*, 3665-3669.
- [215] A. A. Davydov, *Mater. Chem. Phys.* **1985**, *13*, 243-260.

-
- [216] G. Busca, V. Lorenzelli, G. Ramis, V. S. Escribano, *Mater. Chem. Phys.* **1991**, *29*, 175-189.
- [217] J. Kondo, K. Domen, K. Maruya, T. Onishi, *J. Chem. Soc. Faraday Trans.* **1990**, *86*, 3021-3026.
- [218] G. J. Millar, C. H. Rochester, K. C. Waugh, *J. Catal.* **1995**, *155*, 52-58.
- [219] G. J. Millar, C. H. Rochester, K. C. Waugh, *Top. Catal.* **1996**, *3*, 103-114.
- [220] G. Busca, H. Saussey, O. Saur, J. C. Lavalley, V. Lorenzelli, *Appl. Catal.* **1985**, *14*, 245-260.
- [221] A. Ueno, C. O. Bennett, *J. Catal.* **1978**, *54*, 31-41.
- [222] A. A. Efremov, A. A. Davydov, *React. Kinet. Catal. Lett.* **1980**, *15*, 327-331.
- [223] I. A. Fisher, A. T. Bell, *J. Catal.* **1996**, *162*, 54-65.
- [224] H. Kalies, N. Pinto, G. M. Pajonk, D. Bianchi, *Appl. Catal., A* **2000**, *202*, 197-205.
- [225] N. Menashe, E. Salant, Y. Shvo, *J. Organomet. Chem.* **1996**, *514*, 97-102.
- [226] S. Natio, M. Tanimoto, *J. Catal.* **1991**, *130*, 106-115.
- [227] D. Panayotov, M. McEntee, S. Burrows, D. Driscoll, W. Tang, M. Neurock, J. Morris, *Surf. Sci.* **2016**, *652*, 172-182.
- [228] D. M. Driscoll, W. Tang, S. P. Burrows, D. A. Panayotov, M. Neurock, M. McEntee, J. R. Morris, *J. Phys. Chem. C* **2017**, *121*, 1683-1689.
- [229] G. Busca, V. Lorenzelli, *J. Chem. Soc. Faraday Trans.* **1992**, *88*, 2783-2789.
- [230] Y. Yang, F. Lin, H. Tran, Y. H. Chin, *ChemCatChem* **2017**, *9*, 287-299.
- [231] P. Tian, Y. Wei, M. Ye, Z. Liu, *ACS Catal.* **2015**, *5*, 1922-1938.
- [232] D. Chen, K. Moljord, A. Holmen, *Microporous Mesoporous Mater.* **2012**, *164*, 239-250.
- [233] C. Acar, I. Dincer, G. F. Naterer, *Int. J. Energy Res.* **2016**, *40*, 1449-1473.
- [234] M. G. Walter, E. L. Warren, J. R. McKone, S. W. Boettcher, Q. Mi, E. A. Santori, N. S. Lewis, *Chem. Rev.* **2010**, *110*, 6446-6473.
- [235] A. A. Upadhye, I. Ro, X. Zeng, H. J. Kim, I. Tejedor, M. A. Anderson, J. A. Dumesic, G. W. Huber, *Catal. Sci. Technol.* **2015**, *5*, 2590-2601.
- [236] S. N. Habisreutinger, L. Schmidt-Mende, J. K. Stolarczyk, *Angew. Chem. Int. Ed.* **2013**, *52*, 7372-7408.

Appendix

Table A. 1 Substances and their manufacturers used for preparation and experiments.

Substances	Manufacturer
AgNO ₃	Fluka
γ-Al ₂ O ₃	Sasol (Puralox)
Ar 5.0	Air Liquide
C ₂ H ₄ 3.0/3.5 (Hector reactor)	Linde
C ₂ H ₄ 3.5 (TAP)	Air Liquide
C ₃ H ₆ 2.5	Air Liquide
CO ₂ 4.5	Linde
¹³ CO ₂	Linde
CsNO ₃	Alfa Aesar
H ₂ 5.0	Air Liquide
HAuCl ₄ · x H ₂ O (41.12%/37.5%)	ChemPur
He 5.0	Air Liquide
KNO ₃	Alfa Aesar (Rh catalysts) Merck (Au catalysts)
N ₂ 5.0	Air Liquide
NH ₃ solution (25%)	Roth
Ni(NO ₃) ₂ · 6 H ₂ O	Aldrich
RhCl ₃ · 3 H ₂ O (38%)	Acros Organics
RuCl ₃ · 3 H ₂ O (99.9%)	ABCR
SiC	ESK-SIC
SiO ₂	Sigma Aldrich (Davisil)
TiO ₂ (Anatase)	BASF

Table A. 2 Settings for gas chromatograph Varian-3800 used for experiments at 8 bar with ethene and propene.

TCD		FID	
Variable	Value	Variable	Value
Injector	Split/splitless	Injector	Split/splitless
Temperature	200 °C	Temperature	200 °C
Split ratio	5:1	Split ratio	20:1, after 0.3 min 1:1
Pressure		Pressure	
Start pressure	450 kPa for 2.2 min	Start pressure	450 kPa for 0.8 min
Ramp	to 350 kPa in 0.1 min with 150 kPa per min		
Detector			
Temperature	180 °C	Temperature	250 °C
Time constant	Fast	Time constant	fast
Filament temperature	230 °C		
Range	0.5	Range	12
Autozero	on	Autozero	on
Polarity	Positive		
He Makeup flow	22 ml min ⁻¹	He Makeup flow	5 ml min ⁻¹
He reference flow	30 ml min ⁻¹	H ₂ flow	10 ml min ⁻¹
		Air flow	300 ml min ⁻¹

Table A. 3 Oven programme for gas chromatograph Varian-3800 used for experiments at 8 bar with ethene and propene.

Heating rate / K min ⁻¹	Temperature / °C	Time / min
Start	50	0.7
40	130	0.0
80	190	3.1
60	60	0.0

Table A. 4 Settings for gas chromatograph Agilent 7890B used for experiments at 20 bar with ethene and for on-line measurements with FTIR cell.

TCD		FID	
Variable	Value	Variable	Value
Injector	Split/splitless	Injector	Split/splitless
Temperature	250 °C	Temperature	250 °C
Split ratio	10:1	Split ratio	20:1
Pressure		Pressure	
Start pressure	110 kPa	Start pressure	140 kPa
Detector			
Temperature	240 °C	Temperature	250 °C
Polarity	Positive		
He Makeup flow	2 ml min ⁻¹	He Makeup flow	25 ml min ⁻¹
He reference flow	24 ml min ⁻¹	H ₂ flow	30 ml min ⁻¹
		Air flow	400 ml min ⁻¹

Table A. 5 Oven programme for gas chromatograph Agilent 7890B used for experiments at 20 bar with ethene and for on-line measurements with FTIR cell.

Heating rate / K min ⁻¹	Temperature / °C	Time / min
Start	60	1.5
20	70	0.0
40	210	0.0
20	220	2.0
80	80	1.8

Rhodium catalysts for CO₂ hydrogenation:

- Rh is mostly homogeneously and atomically distributed (small bright spots)
- After utilization in the reaction, more agglomerates of Rh were detected

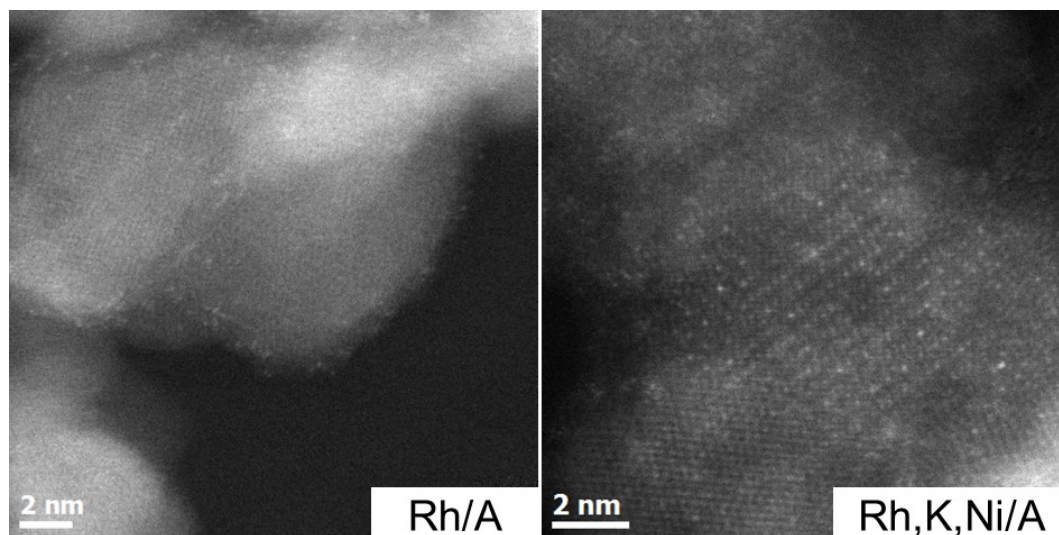


Figure A. 1 STEM images of the fresh Rh/A and Rh,K,Ni/A catalysts. The latter shows a superlattice structure of high contrast atoms forming a surface decoration.

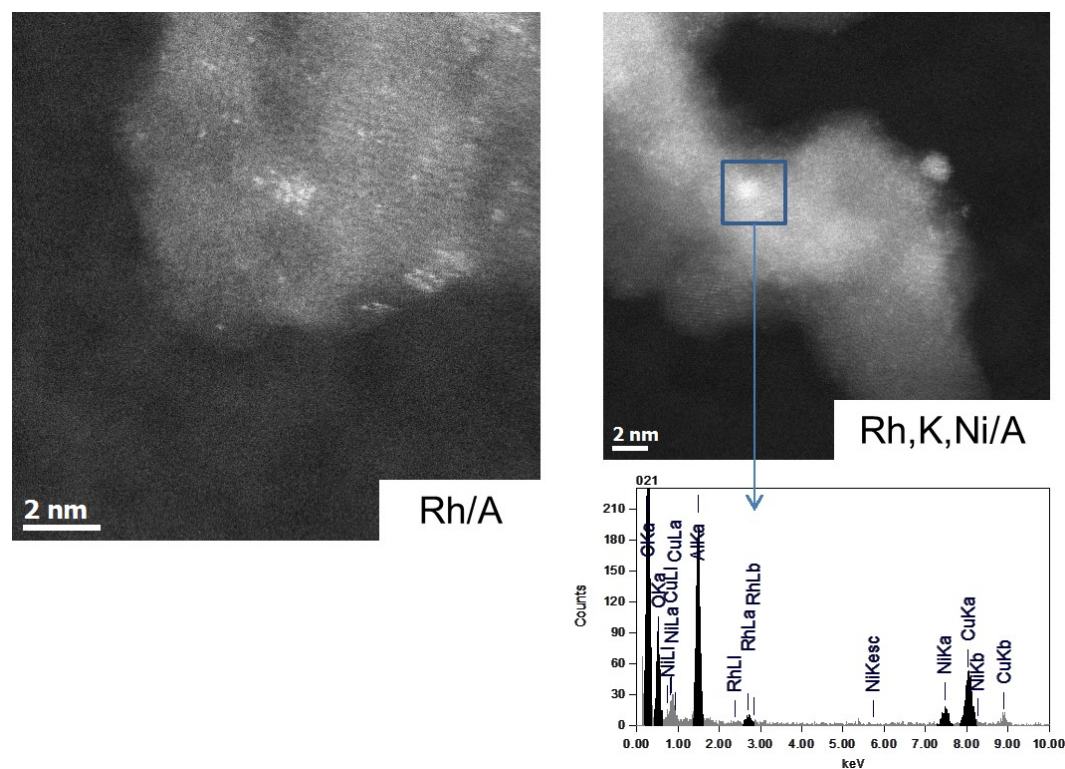


Figure A. 2 STEM images of the Rh/A and Rh,K,Ni/A catalysts after CO₂ hydrogenation reaction showing agglomeration of the Rh particles (*cf.* Figure A. 1). On the right side, EDX analysis detected also particles with both Rh and Ni. Such particles were also found in the Rh,Ni/A catalyst.

Additional catalytic data for CO₂ hydrogenation over Rh catalysts:

Note: the data of the following three diagrams was recorded before high-temperature treatment.

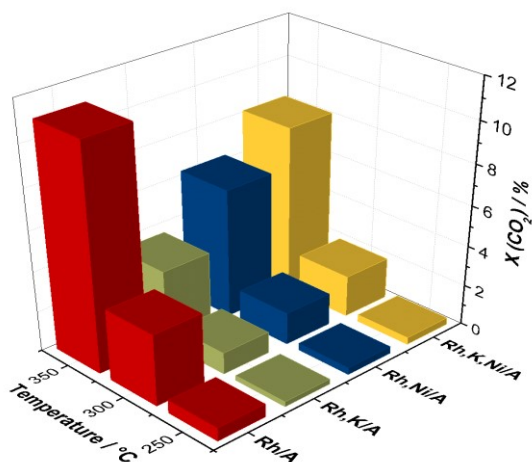


Figure A. 3. Temperature dependent conversion of CO₂ over different rhodium catalysts, reaction condition: $p = 1$ bar, $\tau = 1.67$ g_{cat}·min·L⁻¹, CO₂/H₂/N₂ = 1/1/3.

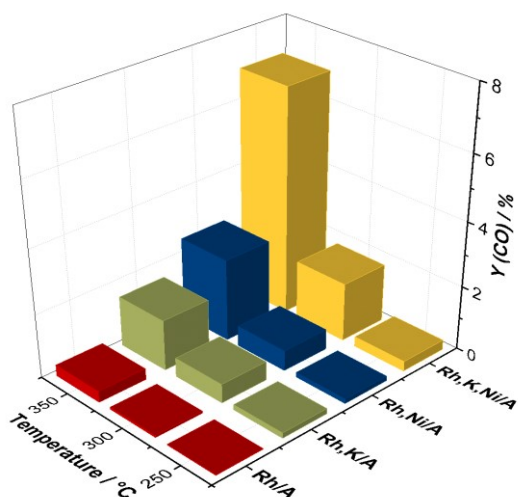


Figure A. 4. Temperature dependent yield of CO over different rhodium catalysts, reaction condition: $p = 1$ bar, $\tau = 1.67$ g_{cat}·min·L⁻¹, CO₂/H₂/N₂ = 1/1/3.

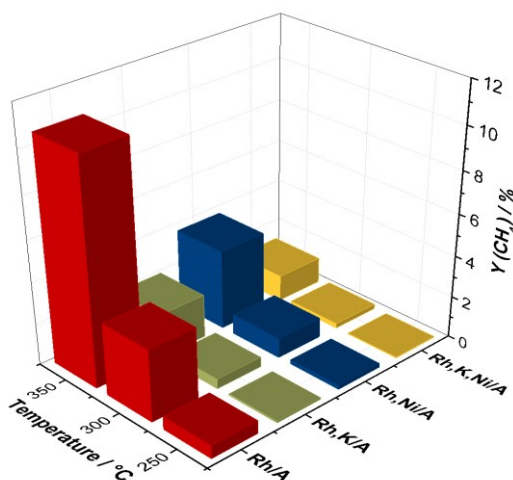


Figure A. 5. Temperature dependent yield of CH₄ over different rhodium catalysts, reaction condition: $p = 1$ bar, $\tau = 1.67$ g_{cat}·min·L⁻¹, CO₂/H₂/N₂ = 1/1/3.

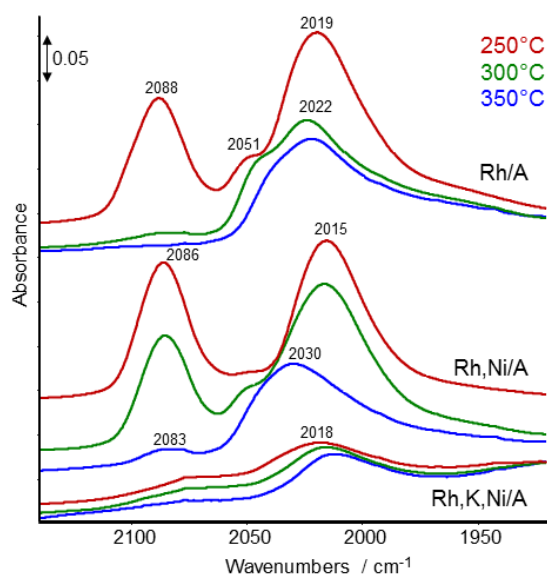
Additional *in situ* DRIFTS spectra of Rh catalysts:

Figure A. 6. *In situ* DRIFTS spectra of CO adsorbed on different Rh catalysts. The spectra were recorded after 30 min admission of the hydrogenation feed ($\text{CO}_2/\text{H}_2/\text{He} = 1/1/3$) at the labelled temperatures.

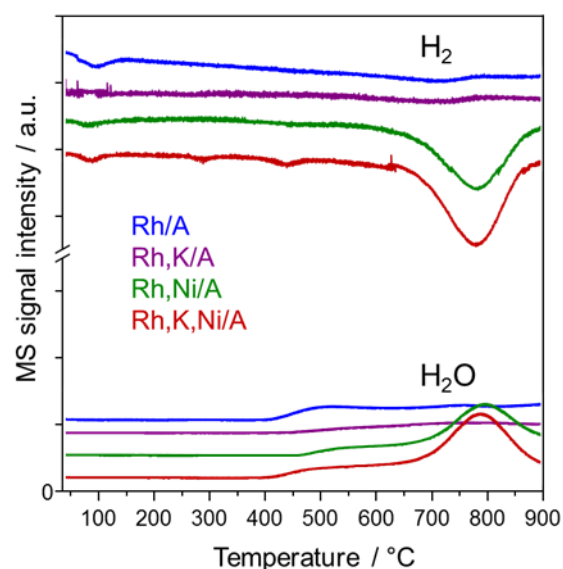


Figure A. 7. Temperature programmed reduction of modified Rh catalysts. Displayed is the hydrogen consumption and water evolution, measured by MS during heating of 50 mg of the sample in a mixture of 5 % H_2 in Ar (heating rate = 10 K/min). The samples were previously heated in Ar up to 700 °C.

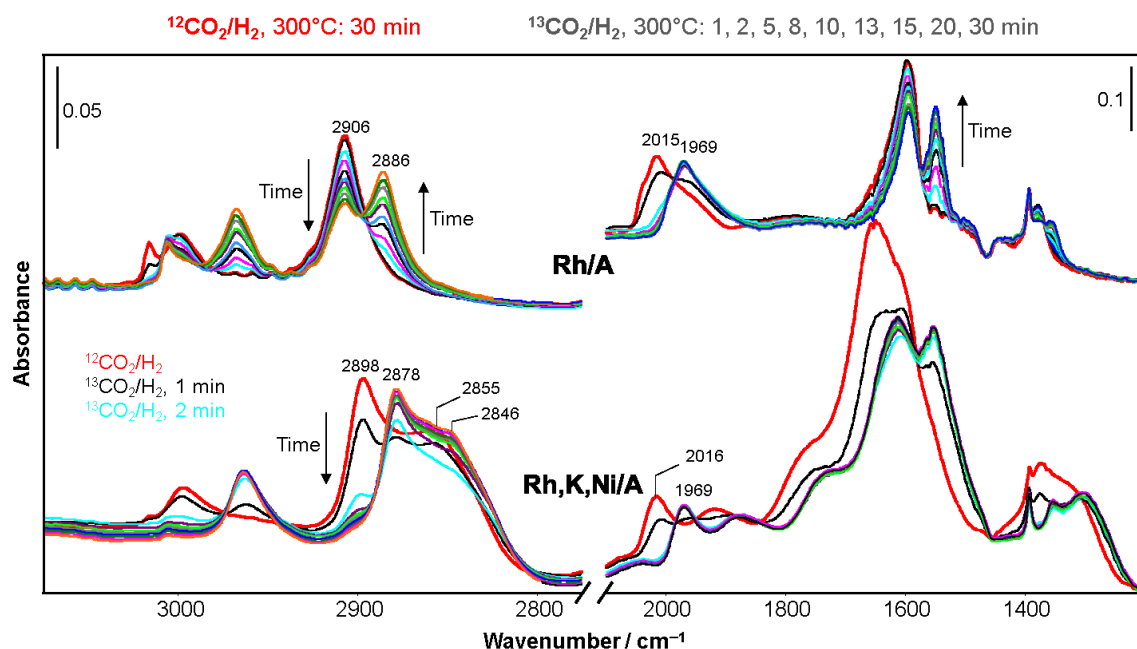


Figure A. 8. Time-resolved *in situ* DRIFT spectra of Rh/A and Rh,K,Ni/A obtained after switching from $^{12}\text{CO}_2/\text{H}_2/\text{He}$ (after 30 min, red) to $^{13}\text{CO}_2/\text{H}_2/\text{He}$ at 300°C (each time multi-coloured).

Additional data of modified Au catalysts:

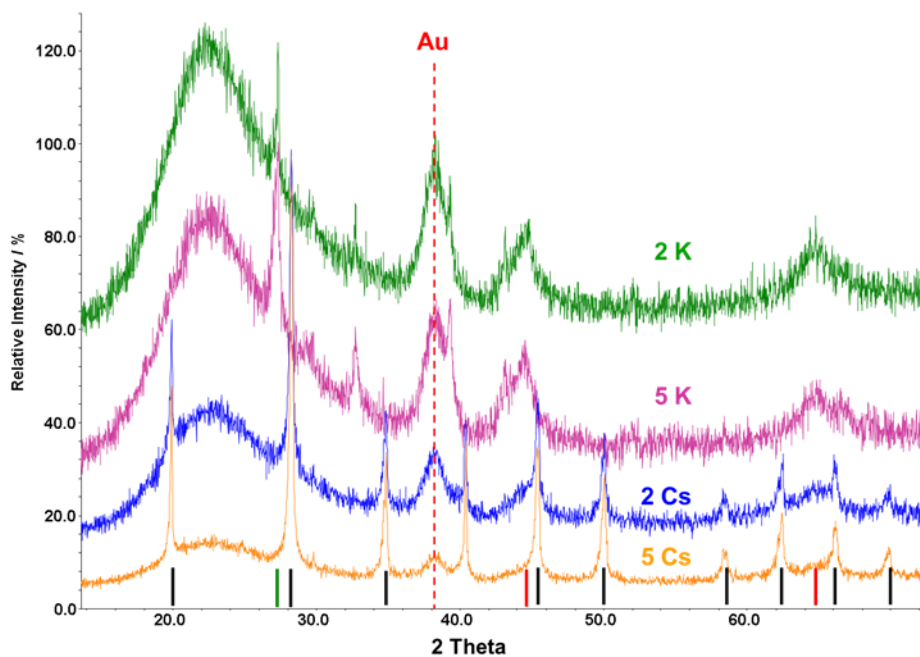


Figure A. 9. Powder XRD pattern of fresh SiO₂ based gold catalysts with different alkali metal loadings, the red dashed line marks the reflex, which was used for gold NP size determination; assignment of reflexes: cubic gold (red), CsNO₃ (black), KNO₃ (green).

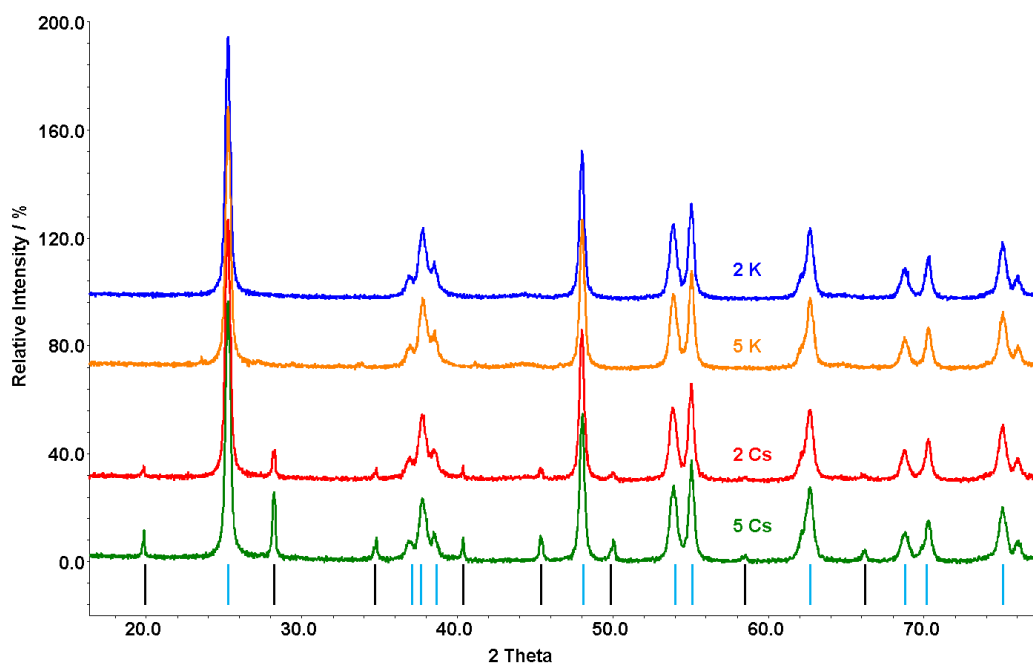


Figure A. 10. Powder XRD pattern of fresh TiO₂ based catalysts with different alkali metal loadings; assignment of reflexes: CsNO₃ (black), TiO₂ anatase (light blue).

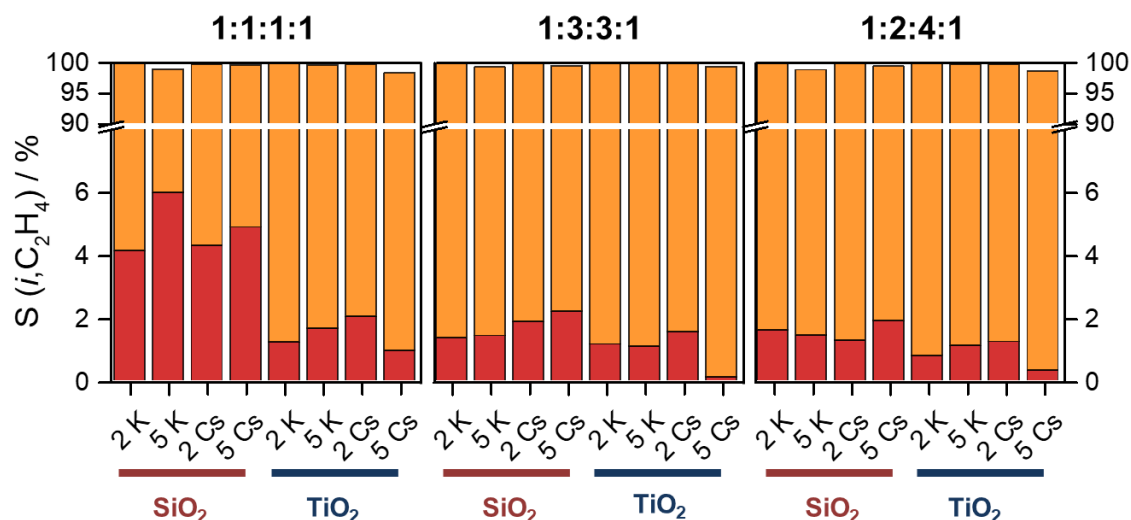


Figure A. 11. Selectivity of 1-propanol (red) and ethane (yellow) obtained over different alkali modified Au/SiO₂ and Au/TiO₂ catalysts at 200 °C with different feed composition of CO₂:H₂:C₂H₄:N₂, ($p = 20$ bar, $\tau = 43$ g_{Cat}·min·L⁻¹).

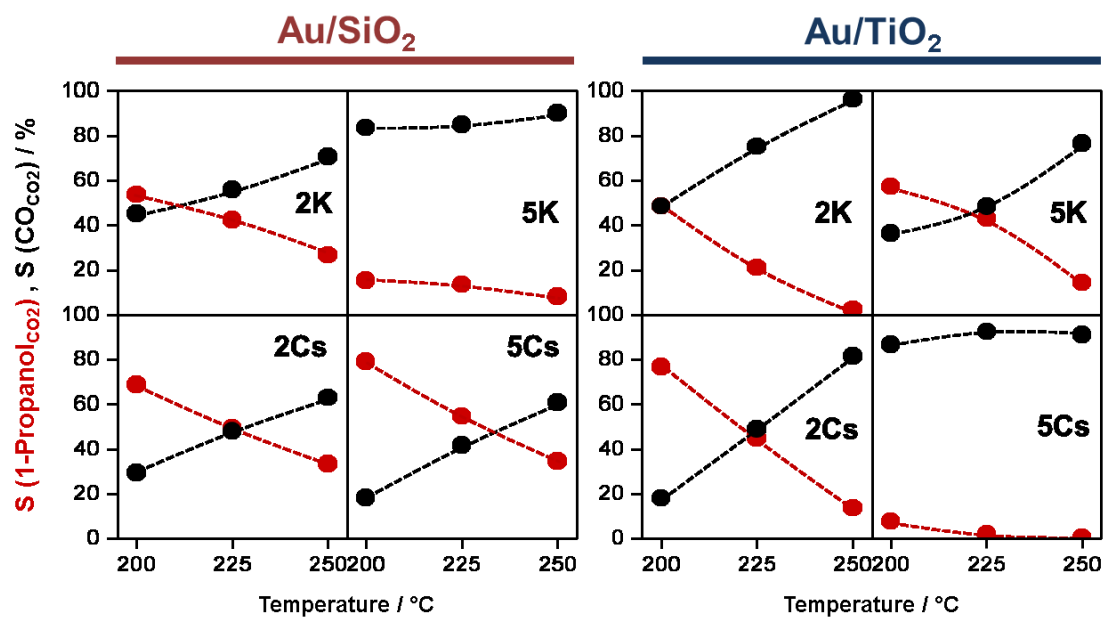


Figure A. 12. Selectivity of 1-propanol (red) and CO (black) calculated on the basis of CO₂ at different reaction temperatures obtained over various alkali modified Au/SiO₂ and Au/TiO₂ catalysts with feed of CO₂:H₂:C₂H₄:N₂ = 1:1:1:1, ($p = 20$ bar, $\tau = 43$ g_{Cat}·min·L⁻¹).

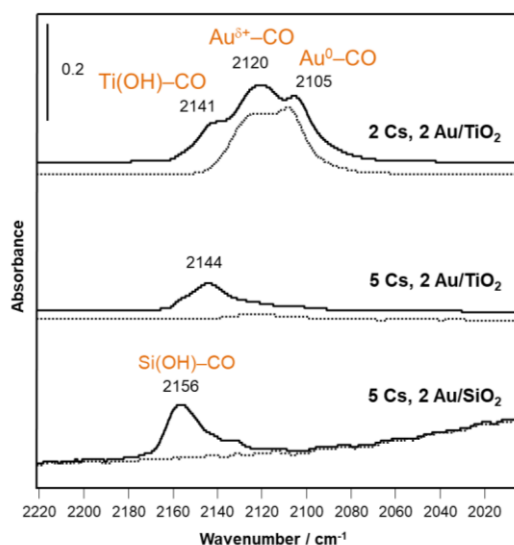


Figure A. 13. FTIR spectra of CO adsorption on fresh Au/TiO₂ and Au/SiO₂ catalysts with different Cs loadings. Solid lined spectra were taken after five pulses of 5 vol % CO in He, dashed lines show spectra after subsequent evacuation ($p = 1$ bar, $T = -160$ °C).

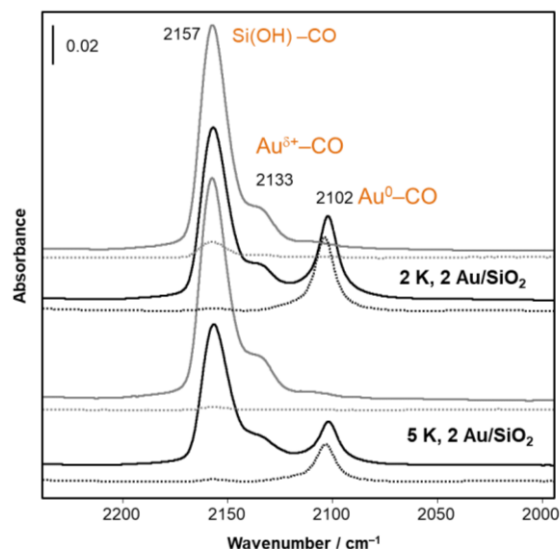


Figure A. 14. FTIR spectra of CO adsorption on 2K and 5K, 2Au/SiO₂ catalysts with different pre-treatments: (grey) in He at 200 °C, (black) CO₂+H₂+He, 250 °C, 1 bar. Solid lined spectra were taken after five pulses of 5 vol % CO in He, dashed lines show spectra after subsequent evacuation ($p = 1$ bar, $T = -160$ °C).

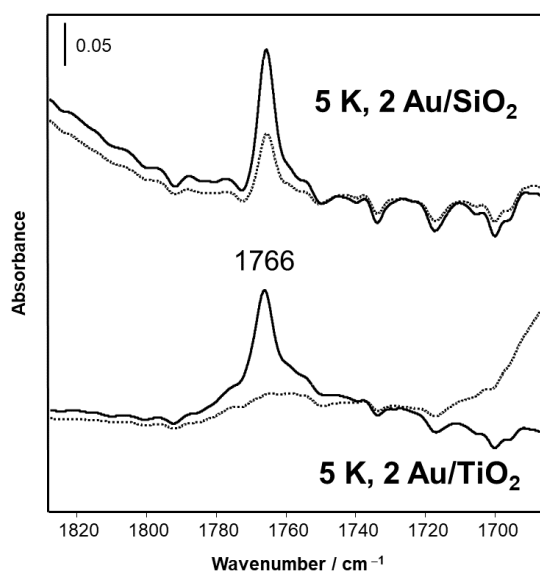


Figure A. 15. FTIR spectra of 5K, 2Au/SiO₂ and 5K, 2Au/TiO₂ catalysts after CO₂+H₂+He pre-treatment at 250 °C, 1 bar and cooling to -160 °C (solid lines) and after five pulses of 5 vol % CO in He (dashed lines).

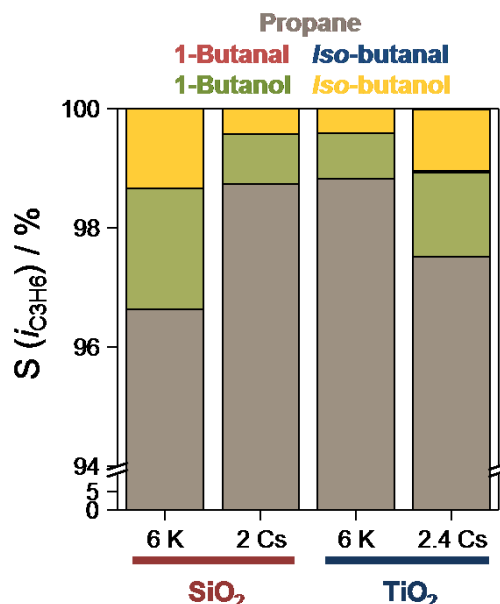


Figure A. 16. Selectivity to obtained products in alcohol synthesis, calculated on C₃H₆ basis, at 8 bar with a feed of CO₂:H₂:C₃H₆:N₂ = 1:3:3:1 ($T = 200$ °C, $\tau = 43$ g_{Cat}·min·L⁻¹).

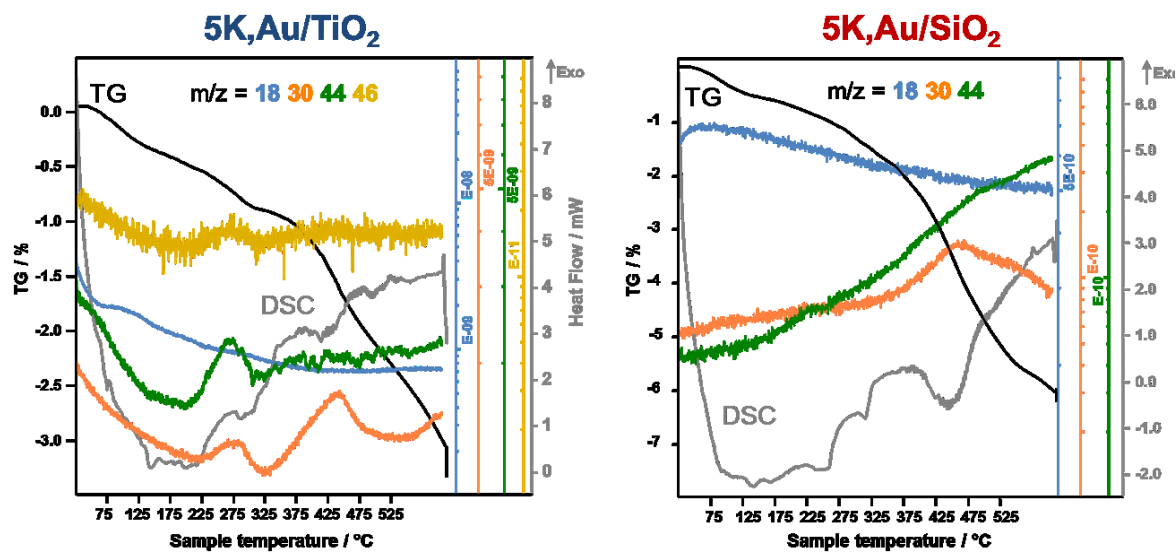


Figure A. 17. Simultaneous thermal analysis (TG-DSC-MS) of 5K,Au/TiO₂ and 5K,Au/SiO₂ in air (heating rate = 5 K min⁻¹).

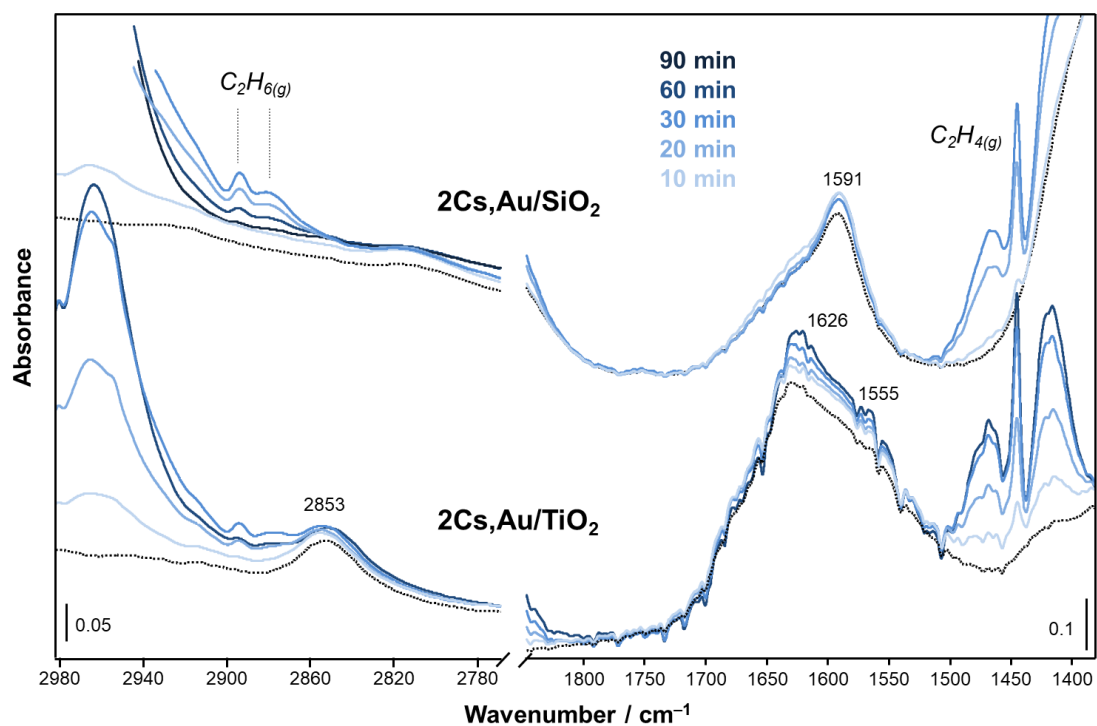


Figure A. 18. High pressure FTIR spectra of time dependent ethane evolution and simultaneous changes in formate/carbonate band region over 2Cs,Au/TiO₂ and 2Cs,Au/SiO₂ in 10% ethene + N₂ flow (blue lines), (200 °C, 10 bar) after 60 min exposure to CO₂+H₂ (dotted black line), (250 °C, 10 bar).

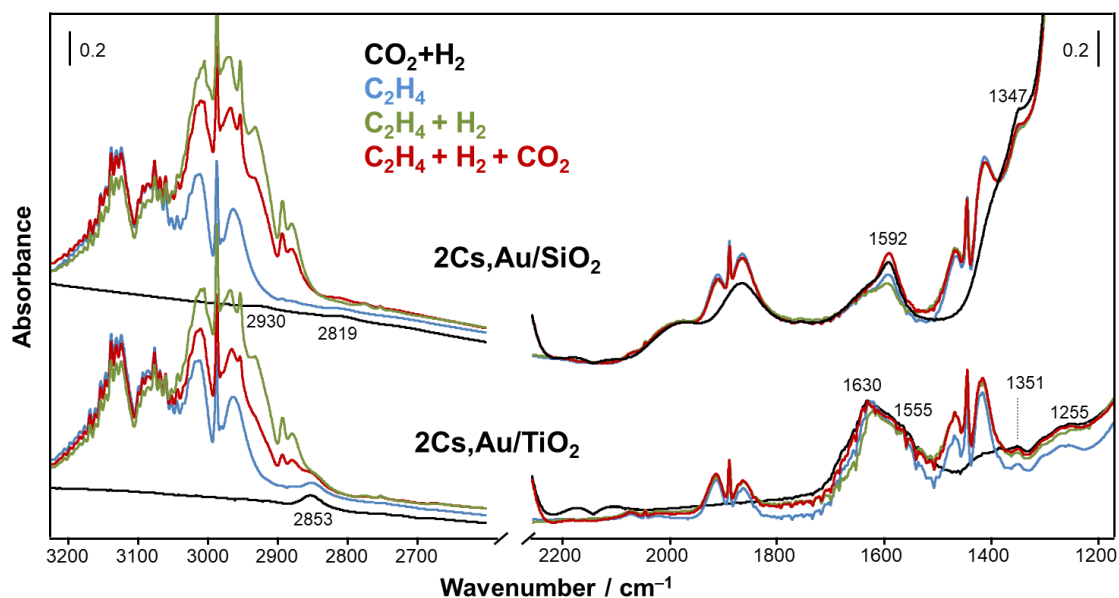


Figure A. 19. FTIR spectra of stepwise reaction procedure over 2Cs,Au/SiO₂ and 2Cs,Au/TiO₂: 1) CO₂+H₂ (250 °C), 2) C₂H₄ (200 °C), 3) C₂H₄+H₂ (200 °C), 4) CO₂+H₂+C₂H₄ (200 °C) spectra are taken after 60 min of exposure (p = 10 bar).

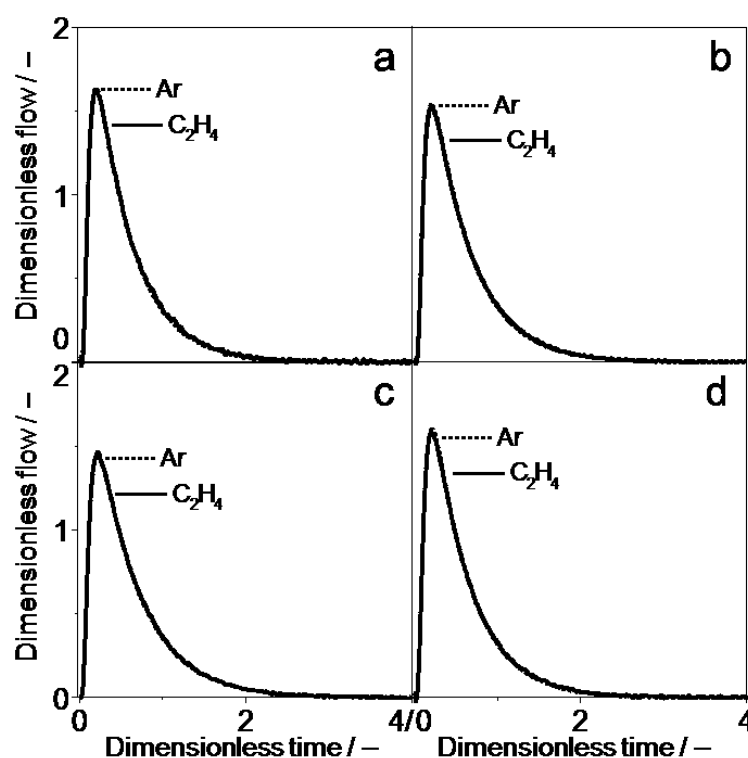


Figure A. 20. Dimensionless response signals after pulsing of C₂H₄:Ar = 1:1 over fresh (a) and used (c) 2Cs,Au/SiO₂ as well as fresh (b) and used (d) 2K,Au/SiO₂ at 200 °C.

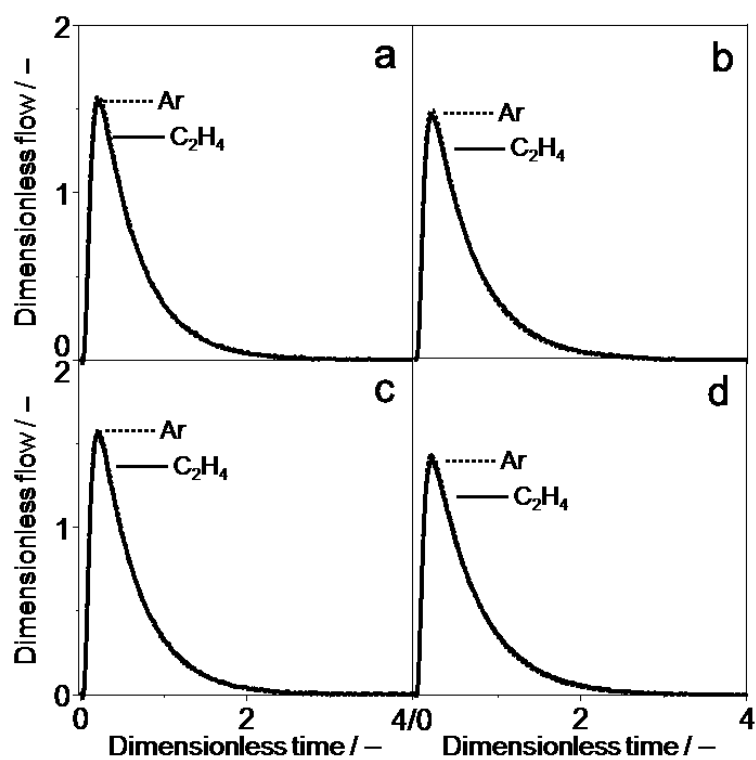


Figure A. 21. Dimensionless response signals after pulsing of $\text{C}_2\text{H}_4:\text{Ar} = 1:1$ over fresh (a) and used (c) 2Cs,Au/TiO_2 as well as fresh (b) and used (d) 2K,Au/TiO_2 at 200°C .

Curriculum Vitae

Lebenslauf

Denise Heyl, M.Sc.

born on the 22nd of August 1990 in Burgstädt, Germany

PhD

- 10/2014–04/2018 Leibniz Institute for Catalysis e.V. at University Rostock
Topic: „Valorization of carbon dioxide: Mechanistic aspects of hydrogenation and hydroformylation reactions over supported alkali modified gold and rhodium catalysts“ supervised by Prof. Dr. Angelika Brückner, Catalytic in situ studies.
- 06/2016 Summer School “Spectrocat” on *in situ* spectroscopy at LCS/ENSICEAN in Caen, France

University Study

- 10/2012–08/2014 Master of Science (Chemistry), University Rostock
Topic: „Operando–FTIR–Untersuchungen zum Einfluss des Trägers auf die Selektivität geträgerter Rh/Ni–Katalysatoren bei der Hydrierung von CO₂“, supervised by Prof. Dr. Angelika Brückner, Catalytic in situ studies (LIKAT).
- 10/2009–09/2012 Bachelor of Science (Chemistry), University Rostock
Topic: „Synthese und Charakterisierung neuer Phosphor–Stickstoff–Verbindungen“ supervised by Prof. Dr. Axel Schulz.

School

- 06/2009 Abitur, Sächsisches Landesgymnasium St. Afra zu Meißen

Scientific contributions

List of publications

1. Denise Heyl, Carsten Kreyenschulte, Vita A. Kondratenko, Ursula Bentrup, Evgenii V. Kondratenko, Angelika Brückner: "*Alcohol synthesis from CO₂, H₂ and olefins over alkali-promoted Au catalysts - a catalytic and in situ FTIR spectroscopic study*", *ChemSusChem* **2018**, DOI: 10.1002/cssc.201801937.
2. Denise Heyl, Uwe Rodemerck, Ursula Bentrup: "*Mechanistic study of low-temperature CO₂ hydrogenation over modified Rh/Al₂O₃ catalysts*", *ACS Catalysis* **2016**, 6 (9), 6275-6284.

Oral presentations

1. Denise Heyl, Stefan J. Ahlers, Ursula Bentrup, Angelika Brückner, Evgenii V. Kondratenko, „*Role of dopant and support in CO₂ conversion into C₃-C₄ alcohols with H₂ and C₂-C₃ olefins over Au catalysts*“, 1st Rohan DAAD SDG Summer School, Rostock (Germany), 2nd – 5th May 2017.
2. Denise Heyl, Stefan J. Ahlers, Ursula Bentrup, Evgenii V. Kondratenko, „*Alcohol formation from CO₂, H₂ and alkenes over supported gold catalysts*“, ZING Conference CO₂ Catalysis, Albufeira (Portugal), 19th – 22nd April 2016.
3. Denise Heyl, Ursula Bentrup, Angelika Brückner, „*Operando-Infrarotspektroskopische Studien zum Einfluss des Trägermaterials und Promotoren auf die Leistung von Rh-Katalysatoren in der CO₂-Hydrierung*“, 18. Norddeutsches Doktorandenkolloquium, Göttingen (Germany), 7th – 8th September 2015.

Poster presentations

1. Denise Heyl, Ursula Bentrup, Evgenii V. Kondratenko, Angelika Brückner, "*High pressure FTIR study of 1-propanol synthesis from CO₂, H₂ and C₂H₄ over Au catalysts promoted with alkali metals*", 6th International Congress on Operando Spectroscopy, Estepona/Málaga (Spain), 15th – 19th April 2018.
2. Denise Heyl, Stefan J. Ahlers, Ursula Bentrup, Angelika Brückner, Evgenii V. Kondratenko, „*Role of dopant and support in CO₂ conversion into C₃-C₄ alcohols with H₂ and C₂-C₃ olefins over Au catalysts: A catalytic and in situ spectroscopic study*“, 13th European Congress On Catalysis (Europacat), Florence (Italy), 27th – 31st August 2017.
3. Denise Heyl, Uwe Rodemerck, Ursula Bentrup, „*Influence of modification on the performance of Rh/Al₂O₃ catalysts in CO₂ hydrogenation: an operando infrared spectroscopic study*“, Spectro Cat Summer School, Caen (France), 27th June – 1st July 2016.
4. Denise Heyl, Ursula Bentrup, Evgenii V. Kondratenko, „*Butanol formation from CO₂, H₂ and propene over supported gold catalysts*“, JCF Frühjahrssymposium, Kiel (Germany), 15th – 19th March 2016.

-
5. Denise Heyl, Uwe Rodemerck, Ursula Bentrup, „*Influence of modification on the performance of Rh/Al₂O₃ catalysts in CO₂ hydrogenation: an operando infrared spectroscopic study*”, 48. Jahrestreffen Deutscher Katalytiker, Weimar (Germany), 11th – 13th March 2015.
 6. Prasanna Rajagopalan, Denise Heyl, Ursula Bentrup: „*Influence of the supporting material on the performance of Rh/Ni catalysts in CO₂ hydrogenation: an operando infrared spectroscopic study*”, ProcessNet-Jahrestagung, Aachen (Germany), 30th September – 2nd October 2014. (Abstract: U. Bentrup, P. Rajagopalan, D. Heyl, *Chem. Ing. Tech.* **2014**, 86, 9, 1633.)
 7. Denise Heyl, Prasanna Rajagopalan, Ursula Bentrup , Angelika Brückner, „*The influence of the supporting material on the performance of Rh/Ni catalysts in CO₂ hydrogenation: an in situ FTIR spectroscopic study*” JCF Frühjahrssymposium, Jena (Germany), 26th – 29th March 2014.